Functional polyoxometalate assemblies
From host-guest complexes to porous frameworks

UNIVERSITY
of
GLASGOW

Carsten Streb

A thesis submitted to the University of Glasgow
for the degree of Doctor of Philosophy

Department of Chemistry
January 2008

Acknowledgements

This project was carried out between January 2005 and December 2007 in the Department of Chemistry at the University of Glasgow. Over this period, many people offered their support and help. In particular I would like to acknowledge:

Prof. Lee Cronin for giving me the opportunity to work on this project. I have highly appreciated his enthusiasm when things were going well and his encouragement when they were not.

Dr. De-Liang Long and **Dr. Eric M. Burkholder** for their expertise as crystallographers and chemists as well as for teaching me the basics of crystallography. I would further like to acknowledge the help of **Dr. Sax Mason** and **Dr. Marie-Hélène Lemée-Cailleau** at the Institut Laue-Langevin and **Prof. Paul Kögerler** at the RWTH Aachen.

Dr. Chris Ritchie for the invaluable discussions on the fields of polyoxometalates, lawn bowls, meteorology and seafood restaurants in Ayrshire.

Dr. Hamera Abbas for her help and advice and for her friendship in the upstairs office…and thanks for the pakoras.

Dr. Geoffrey J T Cooper for his support in the lab and especially for introducing me to the wilderness of the Scottish Highlands and Islands.

Liz Wilson for her support, even when I have been grumpy, and for thorough proof-reading of this thesis.

Graham Newton, **Phil Kitson**, **Scott Mitchell** and **Jennifer S Mathieson** for their advice about the intricacies of life in Scotland and generally for the entertainment provided in the upstairs office.

Oliver Brücher, a dedicated project student who contributed considerably to the successful outcome of this project.

The technical staff of the University of Glasgow for their support, in particular Jim McIver for his help in the lab, Michael Beglan for FAAS analysis and Kim Wilson for elemental analysis.

All the members of the Cronin Empire, past and present who made this project a highly enjoyable experience: It has been a pleasure to work with you all.

"In the realm of ideas everything depends on enthusiasm. In the real world all rests on perseverance"

Johann Wolfgang von Goethe

Dedicated to my parents and to Liz
Thank you for your support

TABLE OF CONTENTS

TABLE OF COMPOUNDS

Compound	Formula
1	$(TEAH)_6[Mo_{36}O_{112}(H_2O)_{14}(TEAH)_2]\cdot 10H_2O$
2	$(TEAH)_4Na_2[Mo_{36}O_{112}(H_2O)_{14}(TEAH)_2]\cdot 28H_2O$
3	$(TEAH)_9Na_2[(H_2O)_4K\subset[H_{12}W_{36}O_{120}]]\cdot 17H_2O$
4	$(TEAH)_9Na_2[(H_2O)_4Rb\subset[H_{12}W_{36}O_{120}]]\cdot 17H_2O$
5	$(TEAH)_9Na_2[(H_2O)_4Cs\subset[H_{12}W_{36}O_{120}]]\cdot 15H_2O$
6	$(TEA)(TEAH)_8Na_2[(H_2O)_4Sr\subset[H_{12}W_{36}O_{120}]]\cdot 17H_2O$
7	$(TEA)(TEAH)_8Na_1Ba_{0.5}[(H_2O)_4Ba\subset[H_{12}W_{36}O_{120}]]\cdot 17H_2O$
8	$(TEAH)_9Na_2[NH_4\subset[H_{12}W_{36}O_{120}]]\cdot 17H_2O$
9	$(TEAH)_{11}[PHEN\subset[H_{12}W_{36}O_{120}]\cdot 17H_2O$
10	$(TEAH)_{11}[4PBA\subset[H_{12}W_{36}O_{120}]\cdot 17H_2O$
11	$TEAH_9Na_1[p\text{XDA}\subset[H_{12}W_{36}O_{120}]]\cdot 17H_2O$
12	$(TEAH)_{10}[DAH\subset[H_{12}W_{36}O_{120}]\cdot 17H_2O$
13	$(GUA)_{12}[Mo_{12}O_{62}H_{11}Na_1P_8]\cdot 11H_2O$
14	$(APY)_{14}[Mo_{12}O_{62}H_9NaP_8]\cdot 13H_2O$
15	$(EN)_6[Mo_{12}O_{62}H_9Na_3P_8]\cdot 18H_2O$
16	$(APY)_5[Mo_5O_{15}H(PO_4)_2]\cdot 5H_2O$
17	$(SPA)_4(BTC)_1[H_{15}Mo_{12}NaO_{62}P_8]\cdot 10H_2O$
18	$([Ag_3(DMSO)_6][Ag_1(DMSO)_3][H_2V_{10}O_{28}])_\infty$
19	$([Ag_3(DMSO)_6][Ag_1(DMSO)_2][H_2V_{10}O_{28}])_\infty$
20	$[Ag(CH_3CN)_4][Ag_2(CH_3CN)_4][H_3W_{12}O_{40}]$
21	$(n\text{-}Bu_4N)_4[H_4W_{12}O_{40}]$
22	$(n\text{-}Pr_4N)_4[H_4W_{12}O_{40}]$

PUBLICATIONS

The following articles and communications were published as a result of work undertaken over the course of this PhD programme.

"Unravelling the Complexities of Polyoxometalates in Solution Using Mass Spectrometry: Protonation versus Heteroatom Inclusion", Long, D.-L., Streb, C., Song, Y., Mitchell, S., Cronin, L., *J. Am. Chem. Soc*, **2008**, 130, 1830-1832.

"Molecular Growth of Polyoxometalate Architectures Based on [-Ag{Mo_8}Ag-] Synthons: Towards Designed Cluster Assemblies", Abbas, H., Streb, C., Pickering, A. L., Neil, A. R., Long, D.-L., Cronin, L. *Cryst. Growth Des.* **2008**, 8, 635-642..

"Modular assembly of a functional polyoxometalate-based open framework constructed from unsupported $Ag^{I\cdots}Ag^{I}$ interactions", Streb, C., Ritchie, C., Long, D.-L., Cronin, L., *Angew. Chem. Int. Ed. Engl.,* **2007**, 46, 7579-7582.

"Engineering porosity in a chiral heteropolyoxometalate-based framework: the supramolecular effect of benzenetricarboxylic acid", Streb, C., Long, D.-L., Cronin, L., *Chem. Commun.,* **2007**, 471-473.

"Influence of organic amines on the self-assembly of hybrid polyoxomolybdenum(V) phosphate frameworks", Streb, C., Long, D.-L., Cronin, L., *Cryst. Eng. Commun.* **2006**, *8*, 629-634.

"Inorganic crown: The host-guest chemistry of a high nuclearity 'Celtic-ring' isopolyoxotungstate $[H_{12}W_{36}O_{120}]^{12-}$", Long, D.-L.; Brücher, O., Streb, C.; Cronin, L., *Dalton Trans.*, **2006**, *23*, 2852-2860.

"Observation and theoretical analysis of the 'sensitive coordination sites' in the isopolyoxomolybdate cluster $[Mo_{36}O_{112}(H_2O)_{14}]^{8-}$, Long, D.-L., Streb, C., Kögerler, P., Cronin, L., *J. Clust. Sci,* **2006**, *17*, 257-266.

ABBREVIATIONS

In addition to standard notation, the following abbreviations were used in this thesis:

4PBA	4-Phenylbutyl amine
APY	2-Aminopyrimidinium
BTC	1,3,5-Benzenetricarboxylic acid
DAH	1,6-Diaminohexane
DMF	Dimethyl formamide
DMSO	Dimethyl sulfoxide
EN	Ethylene diammonium
FT-IR	Fourier-transformation infra-red
GUA	Guanidinium
HPOM	Heteropolyoxometalate
n-Bu	*n*-Butyl
NMR	Nuclear magnetic resonance
n-Pr	*n*-Propyl
OAc	Acetate
Ph	Phenyl
PHEN	Phenethyl amine
POM	Polyoxometalate
*p*XDA	*para*-Xylylene diamine
TBA	Tetra-*n*-butyl ammonium
TEAH	Protonated triethanol amine
TPA	Tetra-*n*-propyl ammonium
UV-VIS	Ultraviolet-visible
XRD	X-ray diffractometry

NOTATION

In line with standard notation, the formulae of cluster compounds will be noted in square brackets, such as $[Mo_{36}O_{112}(H_2O)_{18}]^{8-}$. However, this simple example illustrates that this notation can result in rather long and awkward formulae which do not add to the clarity of the text. Therefore, an abbreviated notation will be introduced where the number and type of metal centres of the cluster is indicated in curly brackets and represents the complete cluster unit. For example, the formula of the cluster unit above, $[Mo_{36}O_{112}(H_2O)_{18}]^{8-}$ will be reduced to $\{Mo_{36}\}$.

In addition, the presence of geometric coordination motifs within one cluster will be indicated using a square bracket notation. For example, an octahedral building unit where six oxygen ligands (O) coordinate to a central transition metal (M) will be noted as $[MO_6]$. In this case, no charge will be assigned since this description illustrates a purely formal structural building unit.

ABSTRACT

The host-guest chemistry of two sets of isopolyoxometalate clusters is investigated. In particular the binding modes of cationic alkali and alkali earth metals through coordinative interactions with the cluster anions $\{Mo_{36}\}$ and $\{W_{36}\}$ were compared and contrasted. It was shown that the ionic radii of the cations are crucial in the isolation of discrete molecules or infinite 3D frameworks. Crystal engineering allowed the introduction of organic amine guest molecules by the formation of a set of intermolecular interactions between the cluster anions and the amine cations. In addition it was shown that by engaging the ammonium guest molecules in additional supramolecular interactions, the framework assembly in the solid state could be directed.

Further investigations focused on the assembly of supramolecular polyoxometalate-based framework materials where organic ammonium cations were used as hydrogen-bond donors. The structural effects of three amines were compared and contrasted and it was established that the use of rigid planar molecules resulted in the formation of 2D networks whereas the use of flexible amines gave supramolecular 1D chains. Based on these results the synthesis of a functional framework was achieved; a three-component approach allowed the formation of a chiral, porous framework which shows structural stability and reversible solvent sorption properties.

In a different approach, the cross-linking of polyoxometalates using transition metal linkers in organic solvents was studied. It was shown that silver(I) cations are highly versatile linking units and allow the linking of $\{V_{10}\}$ cluster anions into 1D zigzag chains and 2D planar networks. The silver units assemble into supramolecular, trinuclear complexes which are supported by bridging organic ligands. Careful choice of the reaction conditions allowed the formation of a 3D framework based on $\{W_{12}\}$ units. The tungstate clusters are cross-linked by dinuclear $\{Ag_2\}$ linkers which are held together by argentophilic silver-silver interactions and result in the formation of a porous framework. The material features reversible sorption capabilities and can be used to sequester small molecules as well as transition metal cations from organic solvents.

1 Introduction

1.1 Supramolecular chemistry – chemistry beyond the molecule

Over the last century, the ability of chemists to control and manipulate the synthesis of complex molecules has changed the world we live in. We can manufacture highly sophisticated natural products to treat diseases, fabricate breathable garments that protect us from the elements and even create non-stick coatings for cooking pots. These achievements are all based on the step-by-step assembly of large molecules by covalently connecting smaller fragments, often using well-known and established reaction mechanisms. However, comparing the methods we use to nature's approach immediately reveals how basic our control beyond the molecular scale still is. In this sense we are only at the beginning of understanding and controlling chemistry at the supramolecular level.

The complexity of structural features we find in nature is not based on strong covalent bonds but is governed by an intricate range of weaker interactions which result in sophisticated yet robust sterical arrangements. A prime example of this assembly principle is the formation of protein structures where a sequence of amino acids - the primary structure – forms hydrogen-bonds and gives rise to local structural motifs such as loops and helices– the secondary structure – which in turn result in a 3D spatial arrangement – the tertiary structure - driven by hydrophobic, π–π and other weak interactions, see Figure 1, top.

The ability to understand and control these non-covalent interactions which lead to the assembly of complex supramolecular architectures has been the driving force for research in areas ranging from traditional organic chemistry to biochemistry and inorganic coordination chemistry. Over the last 50 years more and more sophisticated structures have been discovered which show the versatility of supramolecular chemistry in the formation of novel compounds with remarkable properties such as molecular recognition and structure-specific host-guest interactions. In particular the seminal works of Cram, Lehn and Pedersen which established new areas of research in the field of organic supramolecular architectures have been recognised with the 1987 Nobel Prize for Chemistry, awarded *"for their development of molecules with structure-specific*

interactions of high selectivity".[1] However, over the last decades it has become more and more obvious that polynuclear metal-oxide clusters, polyoxometalates, can serve as model compounds which illustrate the ability of a system to spontaneously form highly ordered assemblies based on comparatively small precursors. It is this intrinsic process, often referred to as *self-assembly* which governs the formation of inorganic clusters ranging from merely six metal centres to structures comprising 368 metals and matching the size of many proteins, see Figure 1.

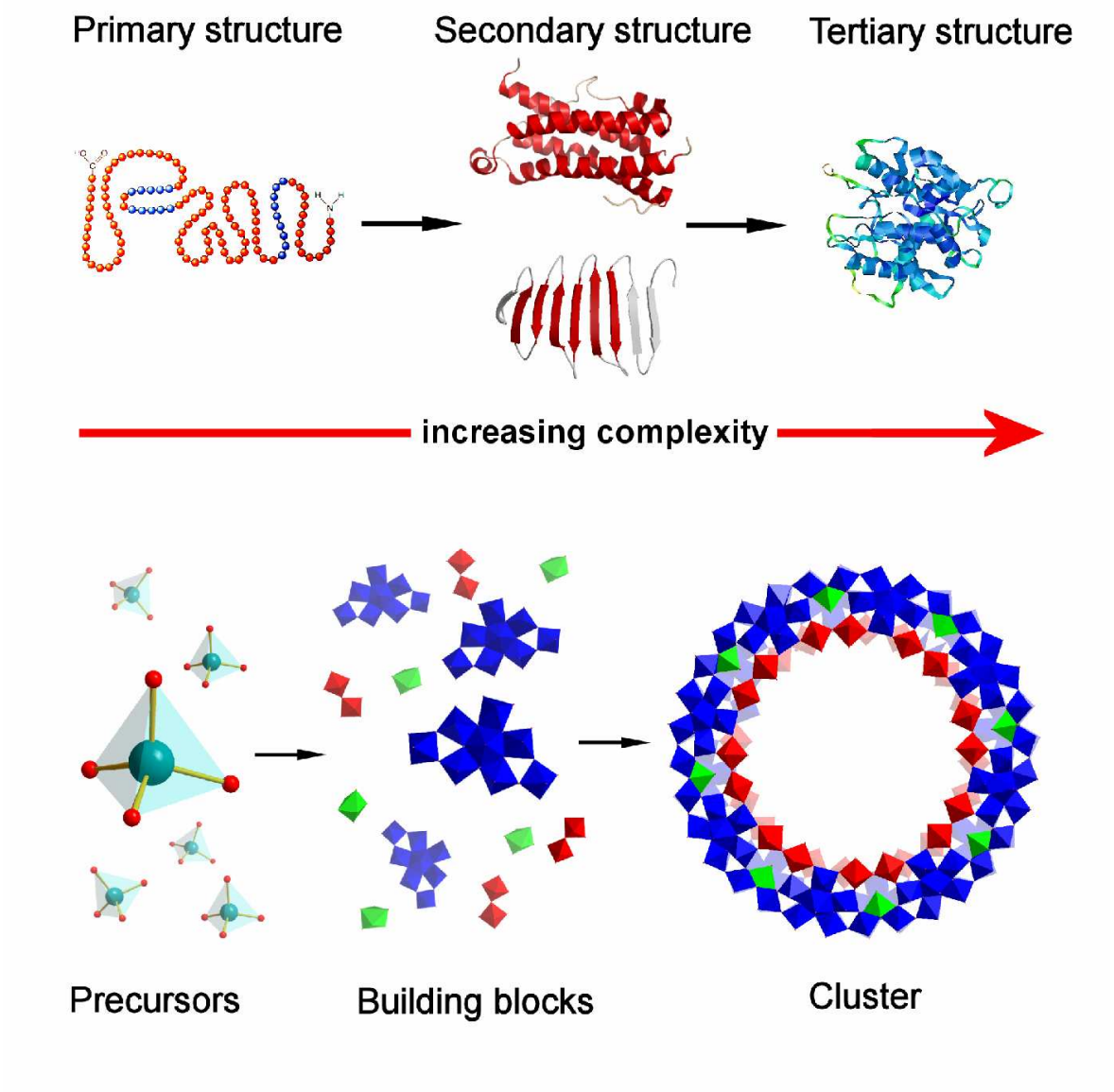

Figure 1: Illustration of the self-assembly of a biological system (top) and the self-assembly of a polyoxometalate cluster (bottom). Both systems are characterised by increasing structural complexity and novel physicochemical properties associated with their structural arrangement. The biological self-assembly is exemplified here by the structure of the enzyme chloroperoxidase (top);[2] the polyoxometalate cluster is a $\{Mo_{176}\}$ giant wheel (bottom).[3]

1.2 Self-assembly and self-organisation – the bottom-up approach

One key subject which underpins the principles of supramolecular chemistry is molecular self-assembly, the intrinsic ability of a system to spontaneously build up large and complex functional structures from a wide range of smaller building blocks *without* any interference or direction from outside. As a result these assemblies feature a higher degree of order and can further exhibit chemical and physical properties which the original building blocks do not possess. It is this dramatic increase in complexity and functionality which makes self-assembled structures one of the most fascinating areas of research in modern inorganic chemistry and materials science. Key to the comprehension of the assembly processes is the understanding of the various intermolecular interactions which determine the final structure. In general terms, it is the so-called "weak" intra- and intermolecular interactions such as Coulomb interactions, hydrogen bonds and dispersive interactions which drive the self-assembly of complex systems and which enable the formation of a multitude of different supramolecular structures. However, especially in the field of inorganic coordination chemistry coordinative bonds play an important role in the assembly of large cluster compounds, owing to their kinetic lability and variable bond strength. In particular the self-assembly of polyoxometalates, anionic transition metal-oxygen clusters is dominated by the formation of coordinative bonds between the electron deficient metal centre and oxygen atoms which act as nucleophilic ligands. Their formation, their properties and applications will be discussed in detail in the following section.

1.3 Polyoxometalates

The ability of oxo anions of molybdenum (VI), tungsten (VI) and vanadium (V) to undergo condensation reactions under acidic conditions is a unique and remarkable property of this class of compounds. It leads to the formation of polynuclear metal-oxide anions whose unrivalled structural and chemical diversity has sparked a tremendous amount of scientific research ranging from first-principles studies[4-12] to industrial applications.[13-19] As a general structural rule, the metal centres (M) coordinate oxygen ligands (O) to form coordination polyhedra of the type $[MO_y]$ (y = 4-7) which in turn can undergo further condensation reactions. As a result a polynuclear anionic molecule $[M_xO_y]^{m-}$ is obtained, see Scheme 1.

Scheme 1: Assembly of mononuclear metal oxide anions into polyoxometalates

$$x\ MO_4^{n-} + z\ H^+ \rightarrow [M_xO_y]^{m-} + z/2\ H_2O$$

As early as 1826 it was noted by *J. J. Berzelius* that the reaction of ammonium molybdate, $(NH_4)_2MoO_4$ with an excess of phosphoric acid leads to the formation of a light yellow crystalline solid.[20] Following these initial reports, several leading scientists amongst them L. Pauling and A. Werner investigated these molybdates and related tungsten-based compounds in an attempt to understand the structure and composition of the material.[21-23] It required yet another major scientific breakthrough to fully elucidate the nature of the reaction product, namely crystal structure determination by X-ray diffraction methods, first discovered by M. v. Laue in 1912[24] and pioneered by W. L. Bragg and W. H. Bragg.[25] This method finally allowed the unambiguous identification and structural characterisation of the cluster compound: In 1933, J. F. Keggin reported the structure of 12-phosphotungstic acid which had been solved by the interpretation of powder-X-ray diffraction images.[26, 27] Since then, this type of compound is often generically referred to as the "Keggin" structure.

Table 1: Timeline of events and discoveries leading up to the first structural characterisation of polyoxometalates

1778	C. W. Scheele	Reports reduced molybdenum oxides: "Molybdenum blue"
1826	J. J. Berzelius	Reports reaction of molybdate and phosphate
1862	M. C. Marignac	Isolates and reports various polyoxotungstates and polyoxomolybdates
1907	A. Miolati A. Rosenheim	Suggest corner-sharing tetrahedra as a structural motif → Miolati-Rosenheim structural hypothesis
1909	A. Werner	Suggests highly linked polyhedra, based on his theory of coordination
1929	L. Pauling	Suggests corner-sharing octahedra based on ionic radii
1933	J. F. Keggin	Structural characterisation of 12-phosphotungstic acid
1948	G. Anderson	Reports crystal structure of $[TeMo_6O_{24}]^{6-}$, → "Anderson-Evans structure"

Almost one hundred years on, the field of polyoxometalate chemistry still relies on crystallographic studies to determine the structure of new clusters and advancements in the field of fast XRD data acquisition and processing are directly reflected in the increasing number of polyoxometalate-related compounds being reported in the literature, see Figure 2. The following chapters will give an overview over the structural diversity of this class of metal oxides, their properties and their applications.

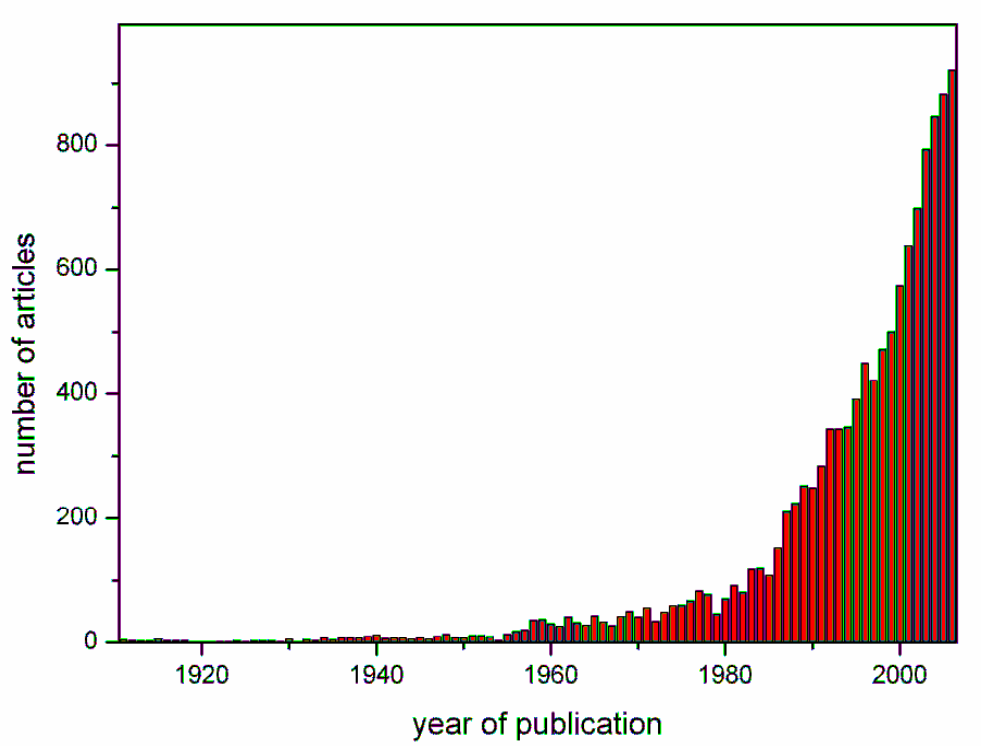

Figure 2: Illustration of the exponential increase in the number of publications containing "polyoxometalate" as a keyword over the last century. Data taken from SciFinder Scholar.

1.3.1 General considerations and structural principles in the formation of POMs

The self-assembly of polyoxometalate clusters in solution can formally be described as a condensation reaction between small metal-oxide building blocks. The most common building blocks are $[MO_6]$ octahedra (M = early transition metal) which are subsequently linked into larger clusters *via* corner- and edge-sharing modes; in other words these octahedra are linked by one or two bridging oxygen ligands respectively. By far the most prominent metal centres in POM chemistry are high-valent molybdenum (V/VI) and tungsten (V/VI) with more and more structures of vanadium (IV/V) niobium (V) and tantalum (V) being published.[28] The abundance of molybdenum- and tungsten-based polyoxometalate is governed by several factors as described below:

The Mo and W metal centres in POMs are typically found in their highest two oxidation states, i.e. fully oxidised (VI) or one electron reduced (V). Therefore they feature empty d-orbitals which allow for strong metal oxide π-bonding in addition to the coordinative bond formed between metal centre and oxygen ligand. This π-bond is formed between an occupied ligand orbital (p_x, p_y) and metal d-orbitals of similar symmetry (d_{xy}, d_{xy}, d_{yz}). As a direct result of this binding mode, the terminal M=O double bonds are characterised by a highly decreased basicity (and nucleophilicity) which in turn limits the growth of the metal-oxide structures and results in the formation of discrete clusters rather than in infinite solid-state structures.[29] Interestingly, this polarisation of the oxygen by the metal centre further results in an extremely weak binding of protons by these terminal oxygen ligands and explains the high acidity of polyoxometalates.[30] Furthermore the structural diversity in both Mo- and W-based POMs is their ability to accept different numbers of oxygen ligands to form coordination polyhedra ranging from tetrahedral [MO_4] to pentagonal bipyramidal [MO_7] units. This versatility is caused by a charge-to-ionic radius ratio which allows the effective binding of oxygen ligands and therefore the assembly of the typical building blocks and subsequent condensation to larger fragments, see Table 2. In contrast, elements such as Cr, Ta and Nb do not exhibit this versatile coordination geometry and consequently are limited in the number of polyoxo anions they are able to form.

Table 2: Comparison of the ionic radii of some typical polyoxo anion-forming metals

Element (oxidation state)	coordination number	Ionic radius / Å[31]	Ratio oxidation state : ionic radius
Mo (V)	6	0.61	8.20
Mo (VI)	6	0.59	10.17
W (V)	6	0.62	8.06
W (VI)	6	0.60	10.00
V (IV)	5	0.53	7.55
V (IV)	6	0.58	6.90
V (V)	5	0.46	10.87
V (VI)	6	0.54	11.11
Cr (V)	6	0.49	10.20
Cr (VI)	6	0.44	13.64
Ta (V)	6	0.64	7.81
Nb (V)	6	0.64	7.81

1.3.2 The Keggin anion – a prototype polyoxometalate

Traditionally, polyoxometalates are synthesised in aqueous media using simple metal-oxide precursors such as molybdenum(VI) oxide, MoO_3 or sodium molybdate, Na_2MoO_4. The acidification of an aqueous solution of these starting materials results in an expansion of the metal coordination shell from 4 to 6, i.e. from a tetrahedral to an octahedral oxygen coordination environment. This in turn enables protonation of the terminal oxygens and facilitates condensation reactions between the particular $[MO_6]$ fragments. As a result, larger structures are self-assembled in solution. The key aspects of these self-assembly principles, and some aspects of symmetry in polyoxometalate chemistry are illustrated in Scheme 2 and Figure 3 using the self-assembly of the α-Keggin cluster $H_3PMo_{12}O_{40}$ as a prime example.

Scheme 2: Formation of the α-Keggin cluster 12-phosphomolybdic acid

$$12\ MoO_4^{2-} + PO_4^{3-} + 27\ H^+ \rightarrow H_3PMo_{12}O_{40} + 12\ H_2O$$

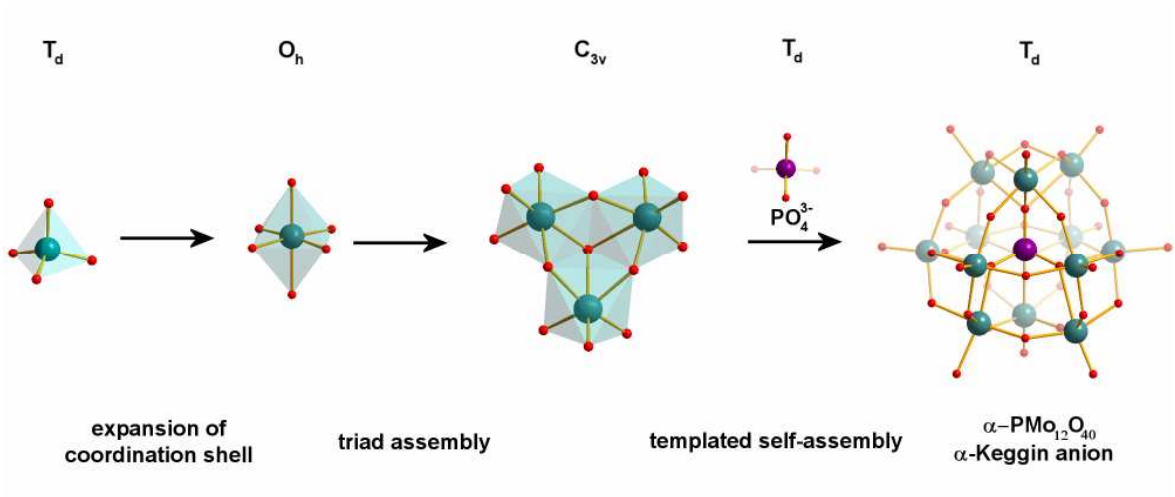

Figure 3: Illustration of the formal self-assembly processes which lead to the formation of the Keggin anion $PMo_{12}O_{40}^{3-}$ A tetrahedral precursor (MoO_4^{2-}) accepts two additional oxo ligands in acidic aqueous solution to form a reactive $[MoO_6]$ intermediate. Trinuclear $[Mo_3O_{13}]$ subunits (triads) are subsequently formed and templating by a tetrahedral heteroanion (PO_4^{3-}) results in the assembly of the tetrahedral Keggin cluster α-$[PMo_{12}O_{40}]^{3-}$. NB: The prefix α refers to the most common isomer of the Keggin anion; for further details see section 1.5.1. Colour scheme: molybdenum: teal, oxygen: red, phosphorus: purple. Indicated above are the idealised point group symmetries of the particular fragments.

The formation of the α-Keggin anion $PMo_{12}O_{40}^{3-}$ exemplifies the complex self-assembly processes of polyoxometalates in aqueous solution. Upon acidification, the tetrahedral molybdate anion can coordinate two additional oxygen ligands and form highly reactive hydrated complexes such as $O[MoO(OH)_4]_2^{2-}$ which can subsequently undergo further reactions.[32-34] These reactive intermediates can normally not be isolated, although several *in-situ* studies using ^{17}O-NMR, ^{183}W-NMR and related techniques provide evidence for their presence.[35-44] In the case of the Keggin cluster, the principal building units are four trinuclear $[M_3O_{13}]$ triads (Figure 3, centre) which are assembled from three edge-sharing $[MO_6]$ octahedra. In the α-Keggin unit, these triads are arranged around a central XO_4^{n-} heteroanion template so that the central μ_3-oxygen ligand of each $[M_3O_{13}]$ fragment links up to the central heteroatom X (X = S, P, As etc). In effect this creates a dodecanuclear metal-oxide anion with tetrahedral symmetry where each metal centre occupies the corner of a truncated tetrahedron, see Figure 4.

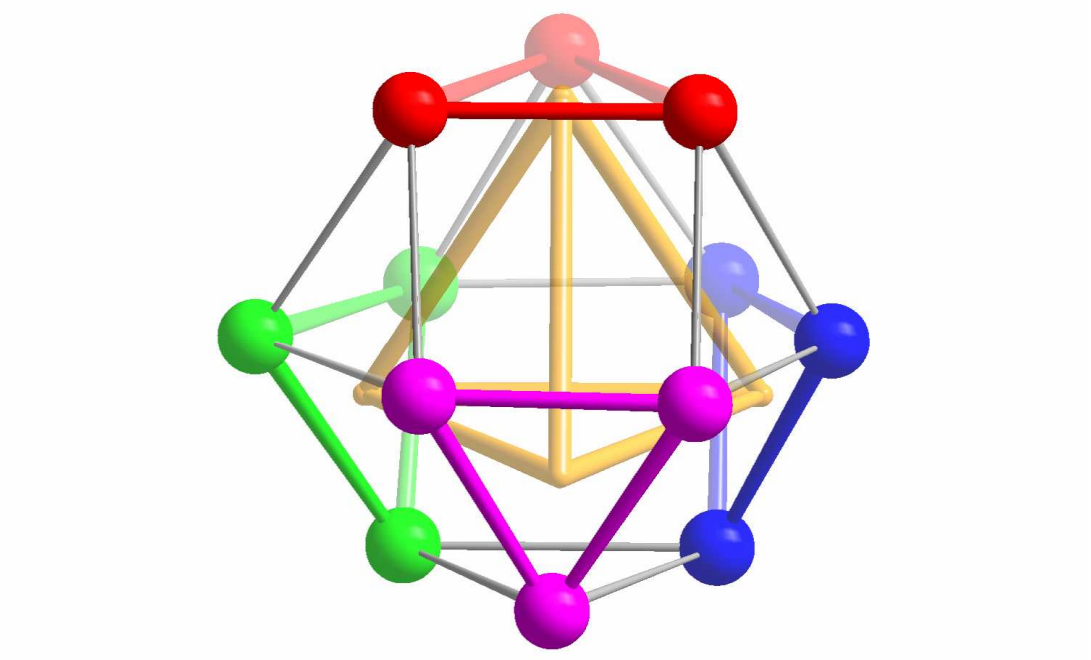

Figure 4: Rationalisation of the Keggin structure. The anion is made up of four independent $[M_3O_{13}]$ triads (red, green, magenta, blue) interconnected by threefold nodes only. The structure exhibits T_d symmetry as indicated by the inscribed tetrahedron (yellow) which is introduced by the central templating anion XO_4^{n-}.

The processes which in this case led to the formation of the α-Keggin structure can be modified and result in a huge diversity of different topologies and various sub-classes of

polyoxometalate clusters. For these reasons a classification system was devised which allows the structural description and categorisation of the various cluster types. This system will be discussed in detail in the following sections.

The composition of all polyoxometalate anions can be expressed by the formula $[X_xM_yO_z]^{n-}$, where M represents the primary metal centre such as Mo, W or V which make up the cluster framework. These high-valent transition metals are often referred to as *addenda* atoms.[28] In case of the Keggin structure introduced above (see 1.3.2), the twelve molybdenum (VI) centres constitute the addenda metals; in other words they are the principal non-oxygen building units of the structure. Clusters which are only composed of addenda centres and oxygen ligands (which can be protonated) are referred to as isopolyoxometalates, thus indicating that there are no additional elements (apart from H) present. A wide range of POMs do however contain additional heteroatoms X which often play a vital structural role, such as the phosphorus (V) in the structure of the Keggin anion $[PMo_{12}O_{40}]^{3-}$, see above. This group of POMs is referred to as heteropolyoxometalates and the heteroatoms observed thus far cover almost the whole range of the periodic table. The following sections will discuss the similarities and differences between isopolyoxo- and heteropolyoxometalates using representative cluster architectures as examples.

1.4 Isopolyoxometalates

The self-assembly of polynuclear oxide clusters of Group 5 and Group 6 metals in aqueous solution can be directed and influenced by a variety of reaction parameters. Factors such as use of inorganic and organic cations, the ionic strength and polarity of the solvent, reaction temperature and pressure will affect the complicated equilibria between various structural types and only detailed knowledge of the reaction system allows the isolation of the desired product.[28,45,46] The major influence on polyoxoanion-formation however is the pH, the concentration of protons in the aqueous reaction mixture. The sensitive equilibrium between acid concentration and strength and polyoxometalate precursors allows fine-tuning of the reaction conditions to isolate the desired cluster type. The following section will illustrate how systematic variation of the reaction conditions results in the formation of various prominent isopolyoxometalate structures.

1.4.1 Isopolyoxo anions of group 5: V, Nb and Ta

1.4.1.1 The ubiquitous $[M_6O_{19}]^{n-}$ Lindqvist cluster

The polyoxo anion chemistry of the group 5 elements is dominated by vanadium in oxidation state +V and + IV. However, one polyoxometalate cluster that can be formed by all group 5 and 6 metals (except chromium) in their highest oxidation state is $[M_6O_{19}]^{n-}$ (M = V^{5+}, Nb^{5+}, Ta^{5+}, Mo^{6+}, W^{6+}, n = 8 (group 5), n = 2 (group 6)). The Lindqvist anion, as this octahedral hexametalate species is also known, is made up from six $[MO_6]$ polyhedra which are all linked in an edge-sharing fashion, see Figure 5. As a result, each metal centre forms one strong M=O terminal bond which is much shorter than the bridging M-O-M bonds. Structurally, each of the six terminal oxygens occupies the corner of an octahedron which demonstrates the high symmetry (O_h) of this cluster. Depending on the nature of the addenda atom, this cluster type shows an intriguing change in reactivity. Whilst the V(V)-based hexavanadate cluster $[V_6O_{19}]^{8-}$ is highly labile and can only by isolated by the use of alkoxides as bridging ligands[47-49] or by coordination of sterically demanding Ru(III), Rh(II) and Ir(I) complexes,[50-52], the Mo(VI)-based cluster shows only limited ability to coordinate to transition metals[53] and the homologue tungsten(VI) compound is not known to coordinate to any transition metal complex at all.

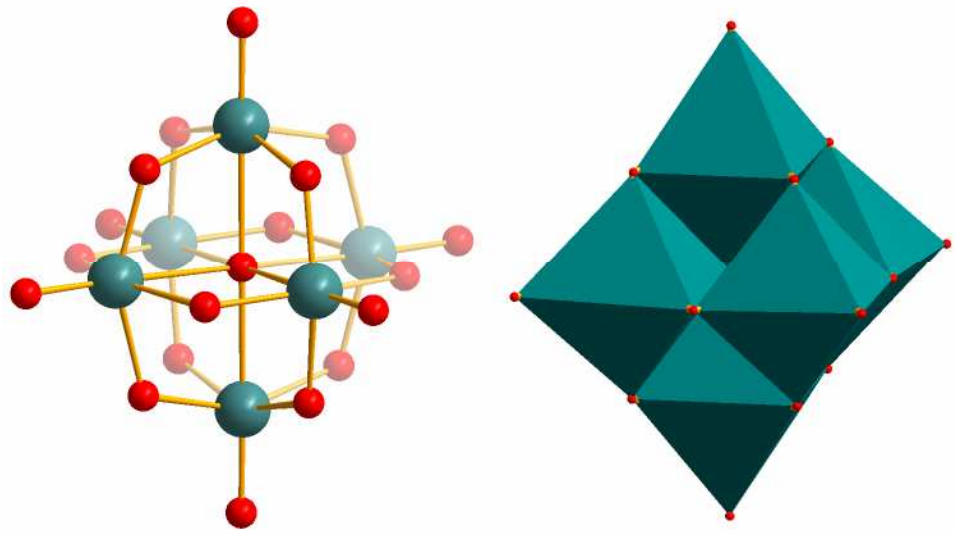

Figure 5: Left: Ball-and-stick representation of the $[M_6O_{19}]^{n-}$ structure (M=V, Nb, Ta, Mo, W) illustrating the assembly of six $[MO_6]$ octahedra into a supramolecular octahedron. Right: Polyhedral representation of the Lindqvist structure, highlighting the exclusively edge-sharing connectivity between the $[MO_6]$ octahedra. Colour scheme: M: teal, O: red. NB: Polyhedral representation of cluster shells can dramatically simplify the structural features.

1.4.1.2 The decavanadate cluster $[V_{10}O_{28}]^{6-}$

One of the most common and most stable V(V) oxo-clusters found in aqueous solution is the decavanadate ion $[H_xV_{10}O_{28}]^{(6-x)-}$ which has been synthesised over a wide range of pH values.[54-56] Depending on the acidity of the solution the cluster can be found in different protonation states and the number of protons per cluster unit can range from x = 1 to 4.[57-63] It is this ability of many iso- and heteropolyoxometalate clusters to act as multibasic acids which allows fine-tuning of the material properties by simply changing the synthesis parameters. In addition, these properties make POMs interesting candidates for various catalytic applications.

Structurally, the $[V_{10}O_{28}]^{6-}$ framework is an extension of the hexametalate structure discussed above. It can be rationalised as two $[V_6O_{19}]^{8-}$ building blocks which are connected by one common set of two $[VO_6]$ octahedra, thus formally losing one $\{V_2\}$ fragment as illustrated in Figure 6. Similar to the hexametalate structure, each V centre forms one formal V=O double bond to a terminal oxygen which results in a displacement of the central atoms towards the terminal oxygens in the $[VO_6]$ coordination polyhedra, see Figure 6, left.

The highly increased stability of the $\{V_{10}\}$ compared with the $\{V_6\}$ unit can be explained by the different ratios of inert non-nucleophilic terminal oxygens O_t to the number of reactive nucleophilic bridging oxygens O_b. In $\{V_6\}$ the ratio $O_b/O_t = 2.167$ whereas in $\{V_{10}\}$ the ratio is decreased to 1.80 and as a result, the overall reactivity of the cluster towards electrophiles reduces considerably. This is further supported by the fact that the vanadium-based Lindqvist cluster $[V_6O_{19}]^{8-}$ requires the presence of alkoxy groups as bridging oxygen donors so as to decrease nucleophilicity and additionally introduce steric bulk which limits the accessibility of the μ_2-oxo sites for potential electrophilic groups.

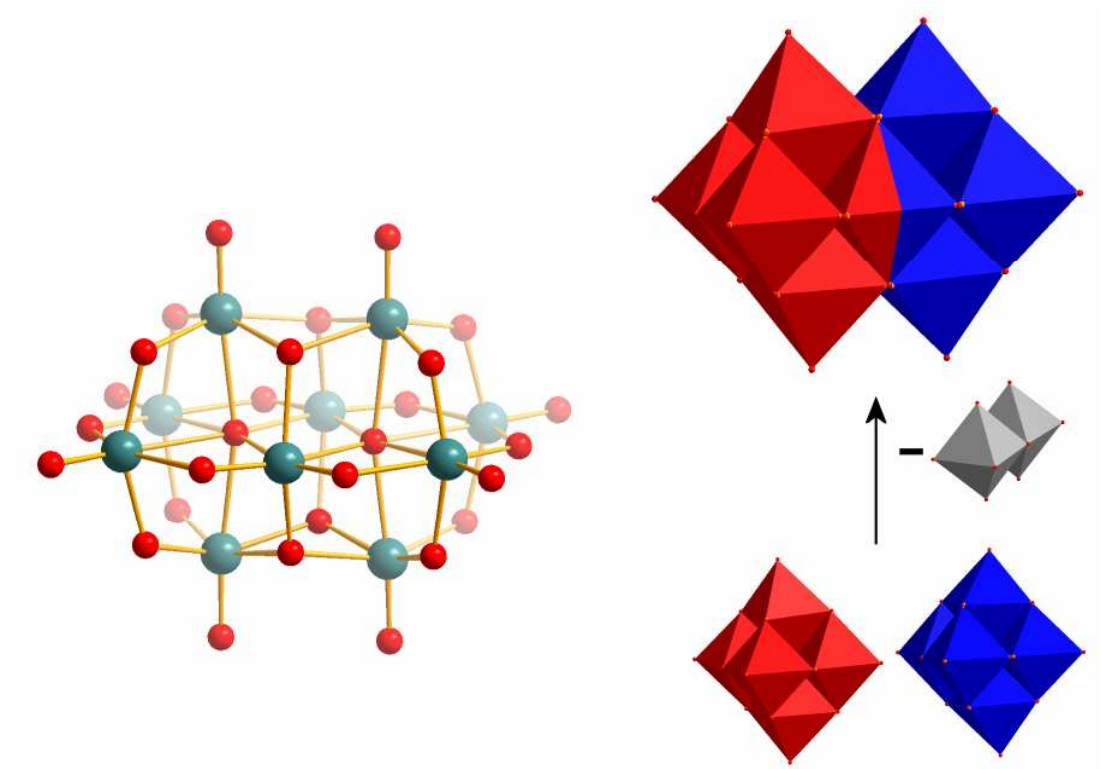

Figure 6: Ball-and-stick representation of the decavanadate ion $[V_{10}O_{28}]^{6-}$ (left), illustrating the displacement of the central V atoms towards the terminal oxygen atoms. Interestingly, the two central oxo ligands act as μ_6-bridges and connect six V centres in an octahedral fashion. They can thus be considered to "template" the structure. Vanadium: green, oxygen: red. Right: Polyhedral representation of the $\{V_{10}\}$ cluster (top) and its formal assembly by fusing two hexavanadate ions. (red and blue, bottom). NB: This is only a formal rationalisation and so far has not been demonstrated synthetically.

1.4.1.3 Host-guest chemistry of polyoxovanadates

The number of isopolyoxovanadates with more than ten metal centres is limited, mainly due to the thermodynamic instability of the cluster structures.[64] However, higher nuclearity clusters can by obtained using hydrothermal synthesis methods which offer access to different pressure and temperature ranges compared to standard syntheses. In polyoxometalate chemistry these methods are often employed to overcome solubility and reactivity problems. In the following example, a hydrothermal synthesis procedure allowed the isolation of a ball-shaped pentadecavanadate species, $[V_{15}O_{36}]^{6-}$. Interestingly, the ball-shaped cluster is partly reduced *in situ* so that the material contains seven V atoms in oxidation state +IV and eight vanadium(V) centres.[65] Several other examples further illustrate that the overall oxidation state of the cluster can be fine-tuned.[51, 65-69] Of particular interest from a supramolecular chemistry perspective is the ability of the cluster

to act as a cage-type host for anions such as chloride. This effect is caused by the distinct coordination environments of the vanadium centres which in contrast to the structures presented thus far are [VO_5] square pyramids rather than [VO_6] octahedra, see Figure 7. As a result, the inside of the {V_{15}} cage features an oxygen-free positively polarised environment in which the chloride ion can interact directly with each of the fifteen vanadium centres ($d_{V\text{-}Cl}$ = 3.3 – 3.5 Å) so that the resulting host-guest relationship of this assembly can be expressed as $Cl^-\subset\{V_{15}\}$.

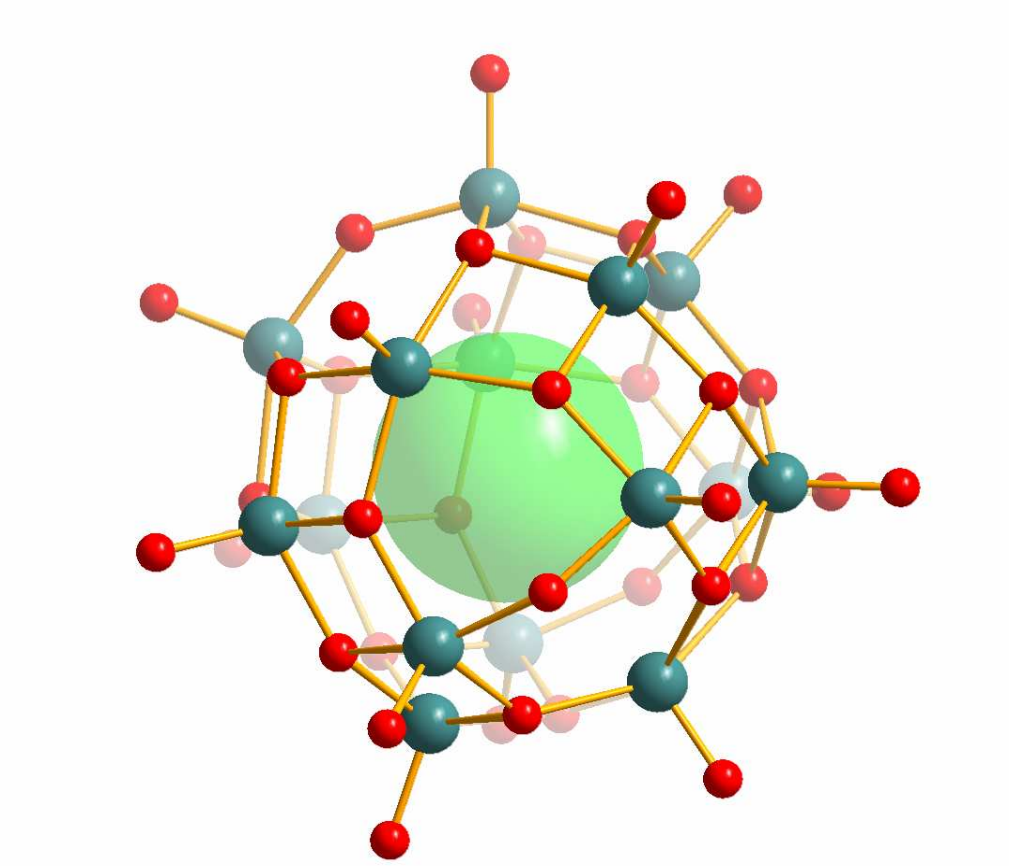

Figure 7: Illustration of the chloride-encapsulating $[V_{15}O_{36}]^{6-}$ cluster with the negatively polarised outer surface and a positively polarised internal cavity. The chloride anion seems to template the structure by arranging the electrophilic [VO_5] units in a way so that they can undergo condensation reactions and eventually form the spherical cluster shell. Colour scheme: V: teal, O: red, Cl: light green sphere.

The chloride anion can template the formation of even larger spherical isovanadates as exemplified by the inclusion complex $Cl^-\subset[V_{18}O_{42}]^{12-}$ which has been synthesised by photochemically reducing a vanadium(V) precursor to V(IV) centres. The shape-selectivity of this molecular recognition process has been taken a step further by employing non-spherical anions such as azide N_3^-, perchlorate ClO_4^- and nitrate NO_3^- to facilitate the formation of elongated host-guest assemblies such as $N_3^-\subset[H_2V_{18}O_{44}]^{4-}$.[70, 71]

The ability to form exchangeable host-guest assemblies by employing open-shell clusters has been illustrated by the dodecanuclear vanadate $[V_{12}O_{32}]^{4-}$ which is synthesised in organic media such as acetonitrile.[72-74] The cluster adopts a bowl-shaped configuration reminiscent of organic cryptands[75] and has demonstrated shape-selective binding of organic nitriles in its cavity, see Figure 8. Similar to the $\{V_{15}\}$-cage presented above, this cluster is constructed from $[VO_5]$ square pyramids rather than from $[VO_6]$ octahedra. This creates a distinct internal coordination environment so that the organic nitrile can interact with all twelve V centres and fill their coordination sphere by long-range V-N interactions ($d_{V\text{-}N}$ = 3.6 – 3.8 Å).

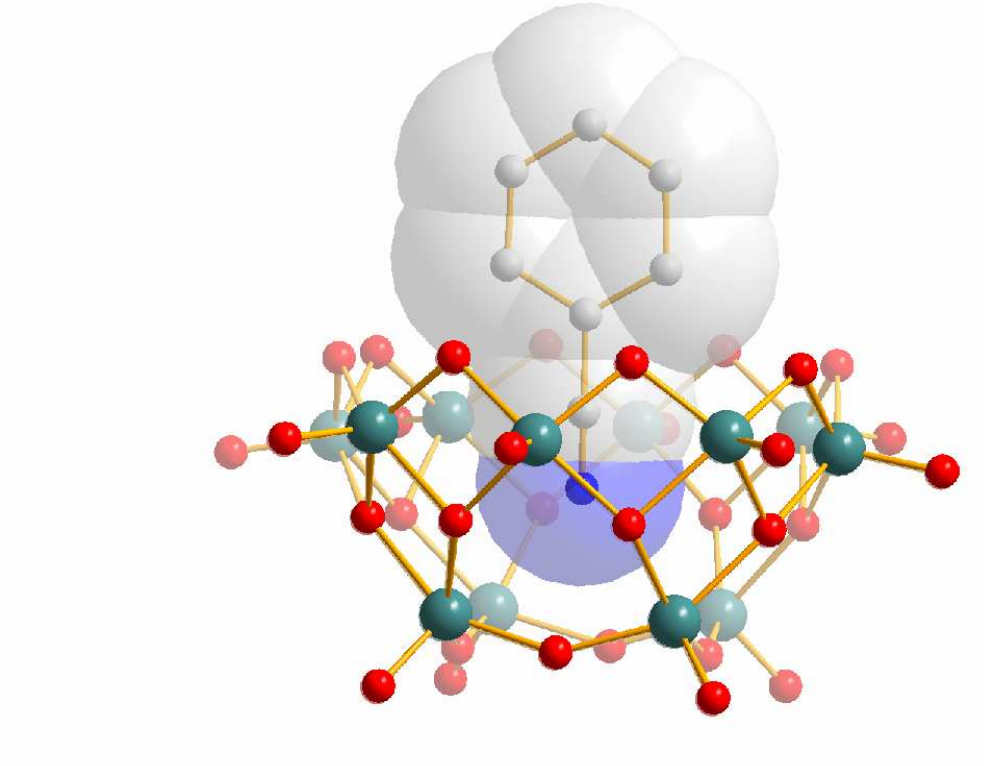

Figure 8: Ball-and-stick representation of the $[V_{12}O_{32}]^{4-}$ structure, illustrating the complexation of a single benzonitrile molecule in the central cavity. The nitrogen donor of the organic nitrile interacts with all 15 vanadium centres through coordinative interactions. Colour scheme: V: teal, oxygen: red, C: grey, N: blue. The actual dimensions of the guest molecule benzonitrile are visualised using a faded spacefilling model.

The ability to "self-template" a structure using tetrahedral VO_4^{3-} anions as central structure directing anions has been demonstrated in the example of a capped Keggin-type isopolyvanadate anion $[V_{15}O_{42}]^{9-}$.[64] As discussed in section 1.3.2 for the original Keggin-type heteroPOM, a tetrahedral central anion facilitates the formation of the cluster cage. Here, the tetrahedral orthovanadate ion VO_4^{3-} enables the condensation of twelve $[VO_6]$ octahedra and results in the formation of the well-known α-Keggin structure (see Figure

9). In addition, two of the square faces of the cluster are capped with "V=O" fragments to yield two square pyramidal [VO_5] moieties. As a result this cluster is a rare example which features only fully oxidised V(V) centres in three different coordination environments and demonstrates the structural versatility of vanadium-based polyoxometalates.

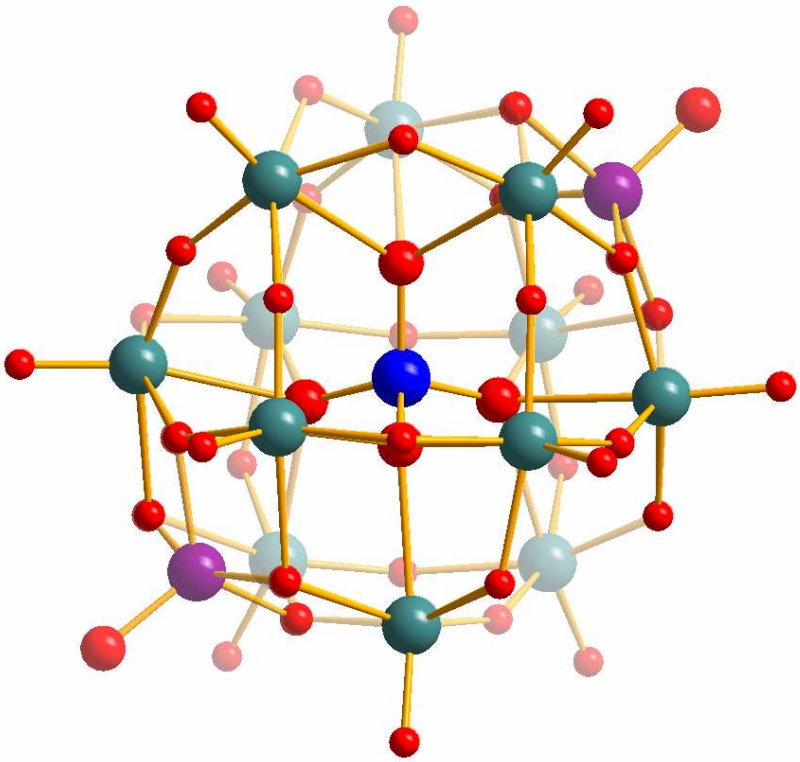

Figure 9: Ball-and-stick representation of the bicapped Keggin-based isopolyoxovanadate $[V_{15}O_{42}]^{9-}$. The three different vanadium coordination environments are highlighted in different colours of the central metal. The central tetrahedron (blue) templates the assembly of the cluster ion. Twelve octahedral vanadium centres (teal) are arranged on the corners of a truncated tetrahedron and resemble the Keggin cluster shell. Two additional V=O units (purple) form square pyramids by interacting with four cluster shell oxo ligands.

In conclusion it has been demonstrated that vanadium-based polyoxometalates feature a varied structural chemistry and can form a range of cluster types with closed and open shell motifs. Furthermore the vanadium centres can adopt different oxidation states and various coordination geometries which subsequently allow the binding of guest molecules

Various other isopolyoxovanadates have been obtained mainly from hydrothermal synthesis and from reactions carried out in organic media. However, these were not considered within the scope of this thesis which focuses on ambient temperature and pressure reactions.

1.4.2 Isopolyoxo anions of Group 6: Mo and W

1.4.2.1 A common heptametalate species: $[M_7O_{24}]^{6-}$

The similarities which are often observed in molybdenum- and tungsten-based heteropolyoxometalate systems are governed by the enormous structural influence of the heteroatoms used (see section 1.5). It is therefore not unexpected that the structural diversity varies to a much larger degree between isopolyoxomolybdates and isopolyoxotungstates compared to the corresponding Mo- and W-based heteroPOM systems. However, at moderate pH values of around 5 to 6, isostructural isopolyoxometalates can be formed in tungstate and molybdate solutions. This is exemplified by the heptametalate cluster $[M_7O_{24}]^{6-}$ (M = Mo (VI), W (VI)) which is often used as a precursor for the assembly of larger architectures[76] and is commonly known as paramolybdate and paratungstate A respectively, see Figure 10.[28,45,76,77]

Structurally, the heptametalate structure is closely related to the decavanadate structure introduced in section 1.4.1 and can be derived from the latter by removing three of the six metal centres in the central belt (see Figure 6). As a result, a very stable cluster structure is obtained where each metal centre can form two short metal-oxygen bonds. Interestingly, even the central metal atom features two short M-O distances rather than adopting a longer bond length typical for μ_2-bridging oxygens, see Figure 10.[77]

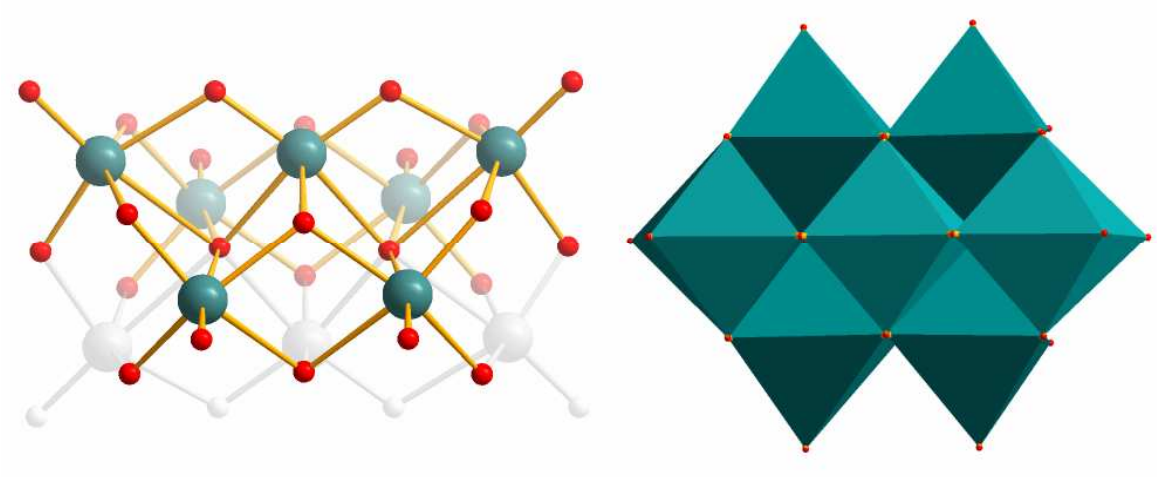

Figure 10: Left: Side view of the $[M_7O_{24}]^{6-}$ structure. The three additional metal centres which relate the $\{M_7\}$ heptametalate to the $\{V_{10}\}$ decavanadate structure are highlighted by faded grey spheres. Further, the presence of two terminal M=O positions on each of the peripheral metal centres is illustrated. Right: Polyhedral illustration of the $\{M_7\}$ framework. Metal centres and $[MO_6]$ octahedra: teal, oxygen: red.

Although isostructural polyoxomolybdates and –tungstates can be formed at medium pH levels of approximately 5 to 6, lowering the pH further results in dramatic changes in the species formed, depending on the metalate in question. This illustrates that although the reactivity of Mo and W might superficially appear similar, they form two distinct sets of cluster types which have to be discussed separately.

1.4.3 Isopolyoxomolybdates

1.4.3.1 Octamolybdate $[Mo_8O_{26}]^{4-}$

At acidic pH levels of pH 3 and lower, molybdate solutions can produce an octanuclear species, β-$[Mo_8O_{26}]^{4-}$.[78-80] This cluster is structurally closely related to the $\{V_{10}\}$ decavanadate (section 1.4.1, Figure 6) and can be derived from this parent anion by removing two apical M=O units so that two sheets of four $[MoO_6]$ octahedra remain, see Figure 11.[77] In effect, these two $[Mo_4O_{13}]^{2-}$ fragments are fused along one common face by sharing eight oxygen atoms which results in an overall rhombohedral structure. The cluster surface features a set of 16 terminal oxygen ligands so that every Mo(VI) centre forms two short $Mo=O_t$ bonds arranged in a *cis*-fashion, see Figure 11. The presence of two terminal (i.e. non-bridging) oxo-ligands is a common motif in isopolyoxomolybdates whereas isotungstates are mostly limited to one free apex (see section 1.4.4).[77]

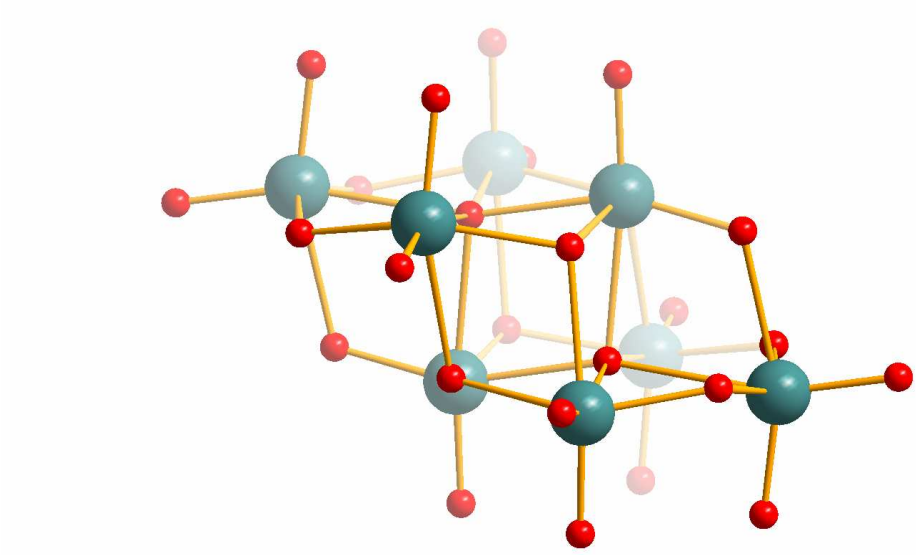

Figure 11: Ball-and-stick representation of the β-$[Mo_8O_{26}]^{6-}$ octamolybdate cluster. Each Mo centre features two terminal oxygens in *cis*-configuration which creates a highly rigid oxygen ligand environment. Colour scheme: Mo: teal, O: red.

This distinct arrangement of Mo centres leads to several intriguing steric consequences and dramatically affects the properties of the cluster because the octamolybdate anion can act as a giant chelator as two neighbouring terminal oxygen atoms form a rigid bidentate coordinating system. Overall, the cluster anion features six sets of chelating terminal oxygen groups which have yielded molecular coordination complexes with transition metals such as Cu^{2+}[53,81-83] and rare earth metals such as La^{3+} and Gd^{3+}.[67,84]

Recently it has been demonstrated that this strategy can be extended by linking β-$[Mo_8O_{26}]^{4-}$ units into a family of related compounds, see Figure 12. A range of infinite 1D chains and 2D networks were assembled starting from monomeric $[(DMSO)_2Ag\{Mo_8\}Ag(DMSO)_2]$ building blocks. It was shown that in these architectures, dimeric $\{Ag_2\}$ fragments link the molybdate clusters by interacting with the bidentate chelators on the cluster. Further investigation allowed the isolation of intermediate compounds in which the formation of the $\{Ag_2\}$ dimers was sterically hindered and thus provided vital information about the mechanism of this supramolecular self-assembly process.[85,86]

It was further established that one control factor in the design of different structural motifs is the use of bulky organic counterions such as tetraalkylammonium cations or tetraphenylphosphonium groups which act as pillaring agents and can separate the structure so as to only allow growth in one direction. As a result, 1D chains rather than 3D infinite frameworks can be obtained. Consequently the use of more flexible counterions can induce the formation of networks with higher dimensionality.

It should be noted that the β-$[Mo_8O_{26}]^{4-}$ structure presented above represents only the most common of seven isomers of the octamolybdate cluster. Different isomers can be synthesised using specific hydrothermal or non-aqueous routes and exhibit varying structures as well as molybdenum coordination geometries (tetrahedral, square pyramidal, octahedral).[87]

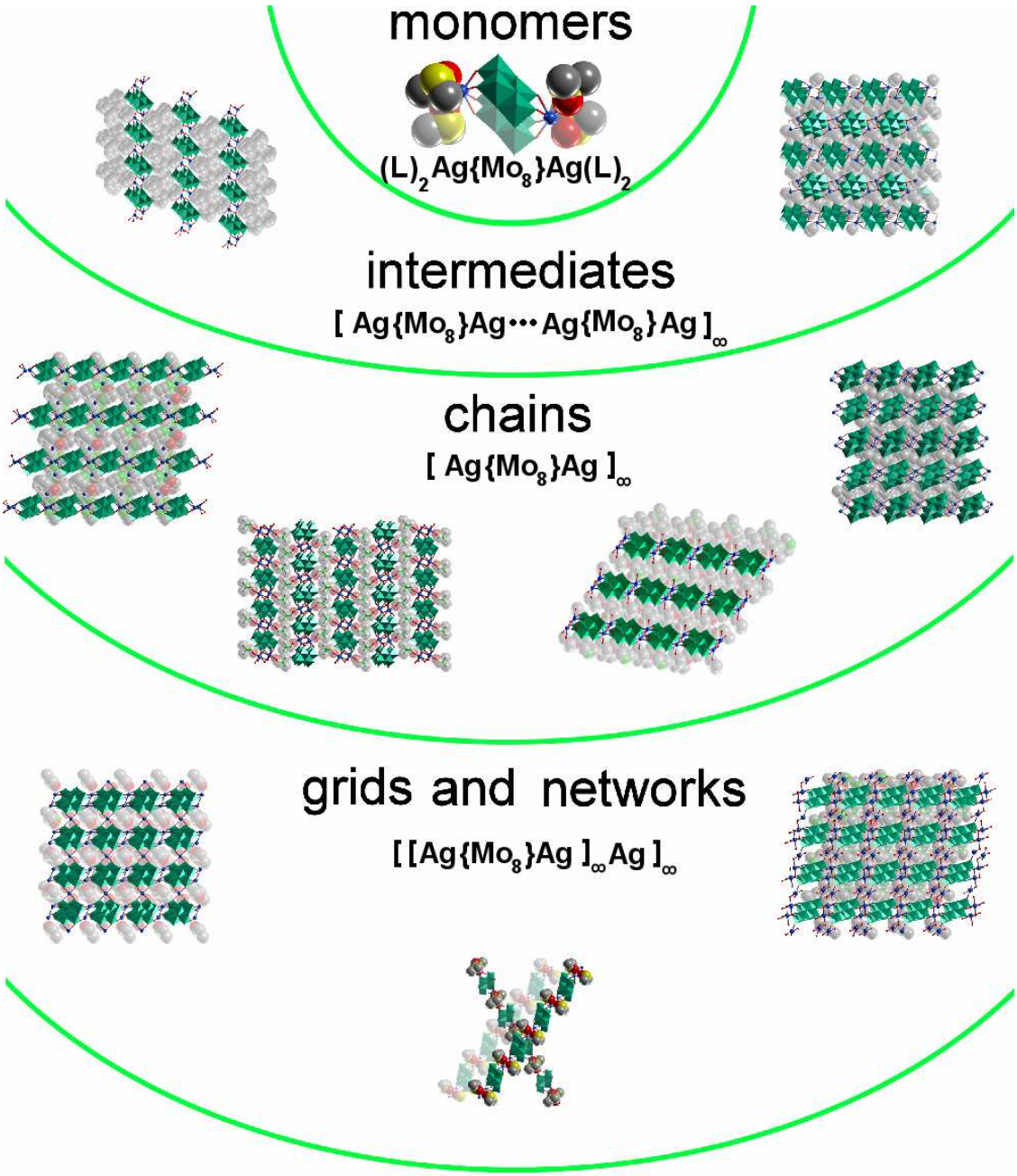

Figure 12: Illustration of the family of related structures which are all based on the secondary building unit $\{Mo_8\}$.[86] From top to bottom the dimensionality of the structures increases, ranging from monomers and intermediates to 1D chains and 2D networks and grids. The common structural unit is an $\{Ag_2Mo_8\}$ fragment where two silver ions coordinate to opposite cluster faces through Ag-O-Mo interactions. These fragments can subsequently grow either by linking of the silver centres with organic bridging ligands or directly though argentophilic Ag-Ag interactions. In addition, the pillaring effect of the organic cations is clearly visible and explains how different bulky counterions can result in different topologies. L: DMSO ligands.

1.4.3.2 The open-shell cluster unit $[Mo_{36}O_{112}(H_2O)_{18}]^{8-}$

At highly acidic pH levels below pH 2, a large isopolymolybdate is formed as the main species in solution.[77] These findings were first reported by Glemser *et al.* in 1973 and the general formula of the metal-oxygen framework was deduced correctly.[88] However, only the full single crystal XRD analysis revealed the true structure of the compound and reported the formula $[Mo_{36}O_{112}(H_2O)_{18}]^{8-}$.[89,90] The cluster is assembled from two identical $\{Mo_{17}\}$ fragments which are related by a centre of inversion. Both halves are linked by two $\{Mo_1\}$ units to form an open-shell ellipsoidal structure. This cluster anion is a prime candidate to exemplify the formal building principles which can be applied to all polyoxometalate structures which will be discussed in detail in the following section.

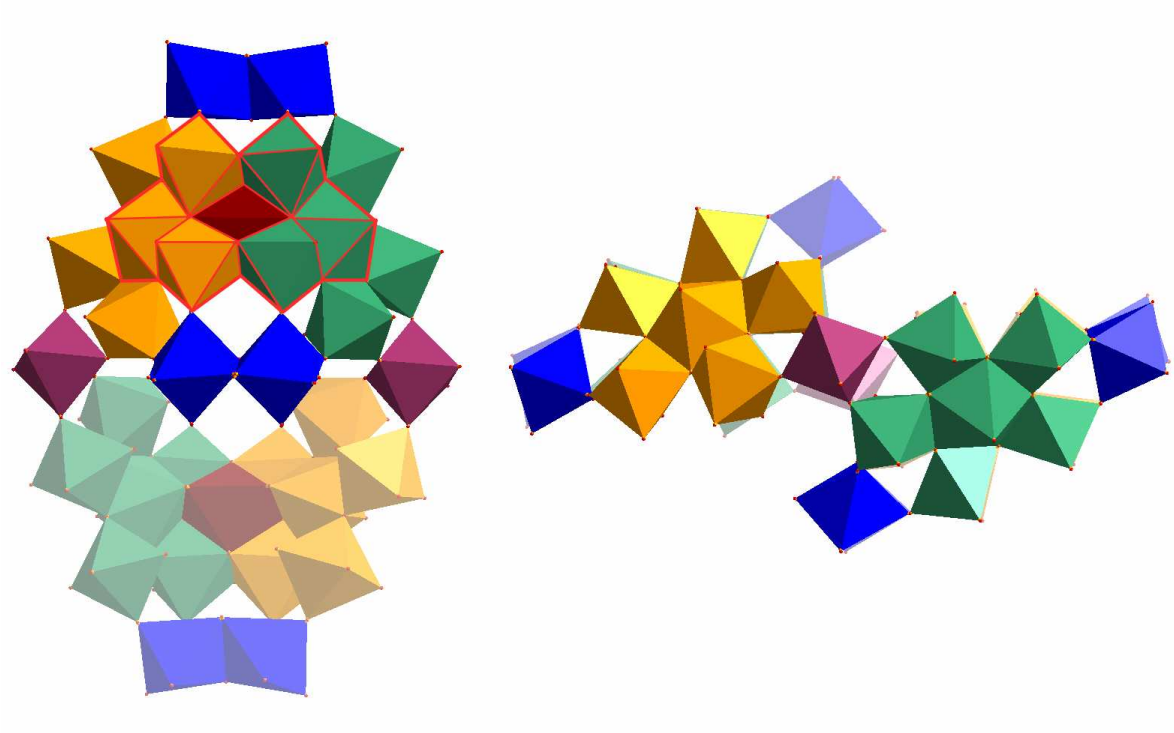

Figure 13: Top view (left) and side view (right) of the $\{Mo_{36}\}$ cluster. Highlighted are the different structural building blocks $\{Mo_1\}$ linkers (purple), $\{Mo_2\}$ dimers (blue), $\{Mo(Mo)_5\}$ pentagonal units (green, orange). Formally, the cluster assembly can be described as the combination of two $\{Mo_{17}\}$ units which are linked *via* two $\{Mo_1\}$ bridges through Mo-O-Mo linking modes. The cluster shell can be rationalised as $\{Mo_{36}\} = \{Mo_1\}_4\{Mo_2\}_4\{Mo(Mo)_5\}_4$. The heptamolybdate structure $[Mo_7O_{24}]^{6-}$ is highlighted using red bold edges in the top view (top left).

Three principal building units can be identified by structural analysis of the $\{Mo_{36}\}$ anion. Structurally the most important unit is a star-shaped pentagonal $\{Mo(Mo_5)\}$ unit in which a central pentagonal-bipyramidal $[MoO_7]$ fragment is fused along its central edges with five $[MoO_6]$ octahedra (orange and green units in Figure 13). These units are ubiquitous as vital building units in the self-assembly of reduced giant "molybdenum blue" species and will be discussed further in section 1.6. In addition, dimeric edge-sharing $\{Mo_2\}$ units (blue units in Figure 13) act as stabilisers and help to increase the stability of the $\{Mo_{36}\}$ framework. Finally, the two symmetrical halves of the cluster are held together by two $\{Mo_1\}$ units which are involved in four corner-sharing Mo-O-Mo bonds. This example demonstrates how a complex structure can formally be rationalised by breaking it down into small building blocks, i.e. $\{Mo_{36}\} = \{Mo_1\}_4\{Mo_2\}_4\{Mo(Mo)_5\}_4$.

It is noteworthy that the two $\{Mo_{17}\}$ section contain the heptamolybdate cluster $[Mo_7O_{24}]^{6-}$ introduced above (see 1.4.2.1) as an integral building unit (highlighted by red edges in Figure 13). This $\{Mo_7\}$ unit is surrounded by four corner-sharing and six edge-sharing $[MoO_6]$ octahedra which results in the formation of the complete $\{Mo_{17}\}$ fragment. This observation might provide an interesting insight in the actual formation mechanism of these structures; it can be speculated that with decreasing pH, increasingly complex assemblies are formed *via* condensation reactions occurring on the surface of smaller clusters which in turn self-organise into larger molecules.[77]

1.4.4 Isopolytungstates

1.4.4.1 Paratungstate B $[H_2W_{12}O_{42}]^{10-}$

After the initial formation of heptanuclear paratungstate A clusters ($[W_7O_{24}]^{6-}$, see section 1.4.2), a slow rearrangement reaction occurs in solution which eventually leads to the formation of a dodecanuclear compound often referred to as paratungstate B.[35,77] The cluster, $[H_2W_{12}O_{42}]^{10-}$ is reminiscent of the Keggin structure in that it features two $[W_3O_{13}]$ triads which form the opposite faces of the structure and are arranged in an antiparallel fashion, see Figure 14. The two $[W_3O_{13}]$ fragments are linked by two sets of edge-sharing $\{W_3\}$ octahedral units which connect the triads *via* corner-sharing modes.

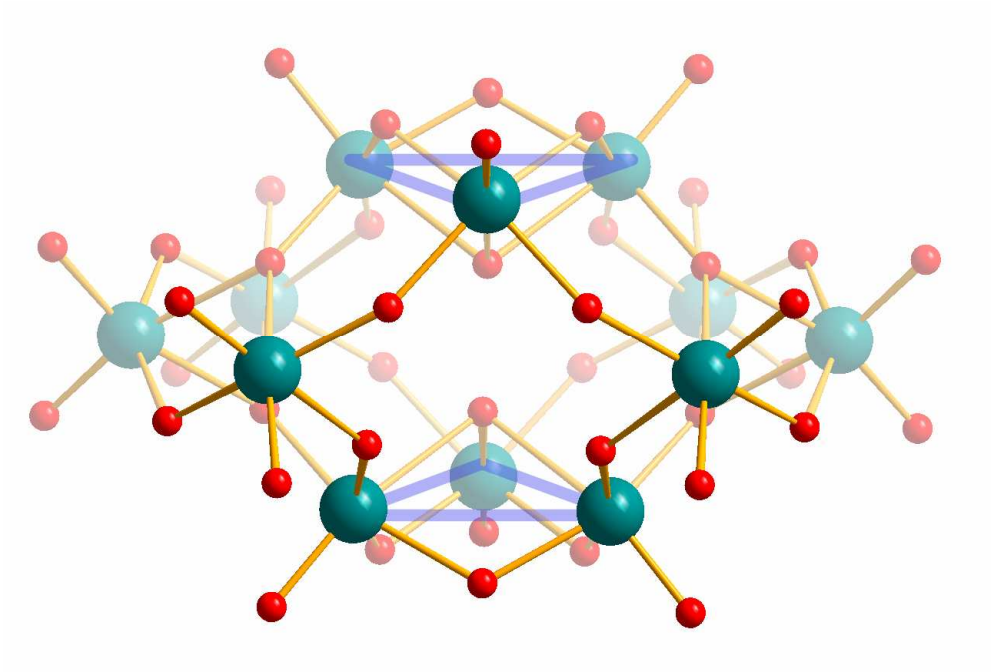

Figure 14: Ball-and-stick representation of paratungstate B, $[H_2W_{12}O_{42}]^{10-}$. The assembly of the cluster is based on the linking of two $[W_3O_{13}]$ triads which are highlighted by blue triangles. The two triad units are linked by trinuclear edge-sharing $\{W_3\}$ linkers. Interestingly, the tungsten centres located on triads feature one terminal W=O bond whereas the linking units exhibit two W=O bonds in a *cis*-arrangement. In addition, the antiparallel orientation of the triads is clearly visible. The central cavity contains two protons. Colour scheme: W: teal, O: red.

It has been successfully demonstrated that this cluster can be utilised as an inorganic scaffold for the construction of supramolecular assemblies. The use of transition metal complexes such as $[Cu(en)_2]^{2+}$as bridging ligands under hydrothermal conditions allowed the formation of infinite 1D chains in which four Cu centres link the clusters by coordination to the terminal oxygen ligands.[91]

Sécheresse *et al.* have demonstrated that paratungstate B can also be used to construct supramolecular frameworks which are linked in three dimensions. In this structure, each $\{W_{12}\}$ paratungstate unit coordinates to ten copper(II) centres *via* W-O-Cu bridges which engage in coordinative interactions to connect to the next isotungstate and thus form an infinite 3D net.[92] The resulting assembly forms layers of infinite copper-bridged paratungstate chain assemblies which are further cross-linked by additional copper(II) units and result in the formation of a 3D network structure.

1.4.4.2 The Metatungstate family

Acidification of an aqueous tungstate solution to pH levels around pH 4 and lower results in the formation of a new set of isotungstate clusters, the metatungstates. The most prominent example illustrates the increased stability of the large tungsten centred octahedra compared with smaller homologues such as vanadium and molybdenum by forming a cluster shell with an internal void. The cluster, α-$[H_2W_{12}O_{40}]^{6-}$ features a metal centre arrangement which is identical to the α-Keggin structure illustrated in Figure 3.[28, 35] However, the central cavity is not occupied by a stabilising tetrahedral template such as PO_4^{3-} but is in essence an internal vacancy which only contains two protons which have no pronounced structural effect.

It has been shown however that this cluster is a promising candidate for the assembly of larger frameworks based on the coordination of soft transition metals such as Cu^{2+}. Thus far, several molecular coordination complexes with multiple transition metals bound to one cluster have been isolated. Typically these compounds are synthesised under hydrothermal conditions using chelating nitrogen-donors such as ethylene diamine[92] or bipyridine-derivatives[53,93] to cap the transition metal centre and isolate discrete molecular structures. Of further interest for applications in energy storage is the ability of the α-metatungstate cluster to be reduced by up to 32 electrons per cluster, a prime example of the rich electrochemistry of polyoxometalate systems.[94]

In highly acidic solutions of pH 1 and below, a highly unusual isotungstate, ψ-metatungstate can be isolated and structurally characterised.[35,51,95] The compound $[H_4W_{11}O_{38}]^{6-}$ comprises 11 fully oxidised W(VI) centres and is composed of three sub-units: The backbone of the cluster is formed by a $[W_4O_{16}]$ "butterfly" unit which is formally derived from a $[W_3O_{13}]$ triad (see section 1.3.2) by addition of a single $[WO_6]$ unit (Figure 15, highlighted in red). This $\{W_4\}$ motif is connected to a non-modified $[W_3O_{13}]$ triad (Figure 15, highlighted in blue) *via* two corner-sharing $[W_2O_{10}]$ dioctahedral units (Figure 15, highlighted in green). Interestingly this cluster has only been observed in the solid state whereas solution studies suggest a composition of $[H_6W_{11}O_{40}]^{6-}$ thus implying that an elimination reaction takes place during the crystallisation where formally one oxo ligand lost from cluster shell.[35]

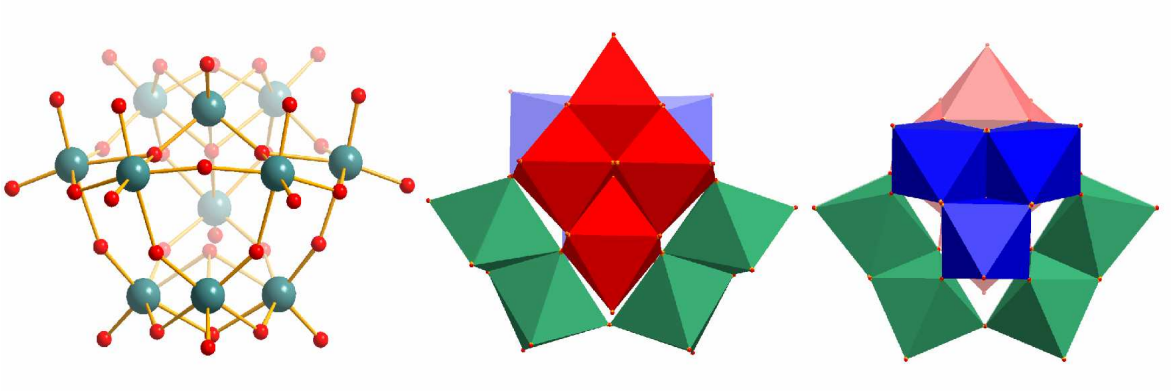

Figure 15: Left: Ball-and-stick representation of ψ-metatungstate $[H_4W_{11}O_{38}]^{6-}$. Front view (middle) and back view (right) of the formal sub-units $[W_4O_{16}]$ (red); $[W_3O_{13}]$ (blue) $[W_2O_{10}]$ (green), illustrating the complex architecture of the cluster in which the two main building blocks$\{W_4\}$ and $\{W_3\}$ are held together by two dioctahedral linking units $\{W_2\}$. The cluster can thus be rationalised as $\{W_{11}\} = \{W_4\}\{W_3\}\{W_2\}_2$. Colour scheme: W: teal, O: red.

Recently, it has been demonstrated by Cronin *et al.* that ψ-metatungstate can be used as a building block to generate the largest isopolytungstate known to date, a $\{W_{36}\}$ assembly[96] which features remarkable host-guest recognition properties. This cluster is however a main part of the present thesis and will be therefore discussed in detail in chapter 3.2.2.

1.5 Heteropolyoxometalates

As already discussed earlier, the chemistry as well as topology of heteropolyoxometalates is governed by the nature of the heteroatom X which is typically introduced to the structure as an oxo-anion XO_y^{n-}. The steric requirements of these anions thus dictate the final structure of the heteroPOMs, their charge and reactivity.[28,45,77] The vast majority of HPOM clusters are templated by tetrahedral anions XO_4^{n-} with central heteroatoms X covering large sections of the periodic table.[77] Specifically however Si, Ge, P As and S are the most frequently observed heteroatoms, most likely due to the straightforward synthesis and structural diversity of the resulting clusters.[77] Amongst the most prominent structures obtained by this templating route are the Keggin and the Wells-Dawson anions and their derivatives which will be discussed in the following section.

1.5.1 The Keggin anion $X_1M_{12}O_{40}^{n-}$

As discussed in section 1.3.2, the Keggin structure is templated by a tetrahedral anion XO_4^{n-} around which twelve addenda atoms, typically Mo or W, are arranged in a tetrahedral fashion. The metal centres form four $[M_3O_{13}]$ triads; every triad being composed of three $[MO_6]$ octahedra which are connected by sharing two edges with their direct neighbours. In turn, these $\{M_3\}$ fragments are linked by corner-sharing modes and connect to the central heteroanion by coordinating to one of the $[XO_4]$ oxygen ligands. Intriguingly, this arrangement allows the formation of structural isomers which are all based on a common parent anion, the α-Keggin structure, see Figure 3 and Figure 4. The β, γ, δ and ε isomers can formally be obtained from the α-Keggin by rotation of 1, 2, 3 or 4 triads respectively by 60 °. These structures are however energetically unfavoured due to an increase in the number of edge-sharing octahedra which results in an increased Coulomb repulsion between the high valence addenda centres.[97, 98] As a result the α-isomer is the Keggin-structure most commonly found with only few examples of the energetically unfavoured β[99], γ[100], δ[101] and ε[102] isomers known. It becomes obvious that an enormous structural and compositional control is achieved due to the number of possible isomers and the variation of addenda and heteroatoms; these features make Keggin anions desirable compounds for studies ranging from electrochemistry[103] and redox-activity[103] to acidity and catalysis.[104] However, the structural variations of Keggin-based assemblies can be taken one step further by creating lacunary clusters, i.e. clusters which are formed by the controlled hydrolysis of their parent compounds and which are structurally characterised by the loss of one, two or three addenda centres.

1.5.2 Lacunary Keggin-derivatives

Increasing the basicity of an aqueous solution of the tungsten-based Keggin-anion $[XW_{12}O_{40}]^{n-}$ under strictly controlled conditions results in the formation of a $[XW_{11}O_{39}]^{(n+4)-}$ cluster which has formally lost one M=O vertex and thus features a structural vacancy.[105] This anion is a typical example of the so-called lacunary polyanions which are formed by partial decomposition of their parent compounds. These lacunary polyanions have sparked a tremendous amount of research[106] due to their promising ability to coordinate secondary transition metals which in turn dramatically alter the

properties of the cluster in fields such as molecular magnetism[107] and POM-based framework assembly.[108] It has been demonstrated that up to three addenda atoms can be selectively removed from the cluster framework, thus resulting in the mono-, di- and trivacant species $[XW_{11}O_{39}]$, $[XW_{10}O_{36}]$, $[XW_9O_{34}]$, see Figure 16.

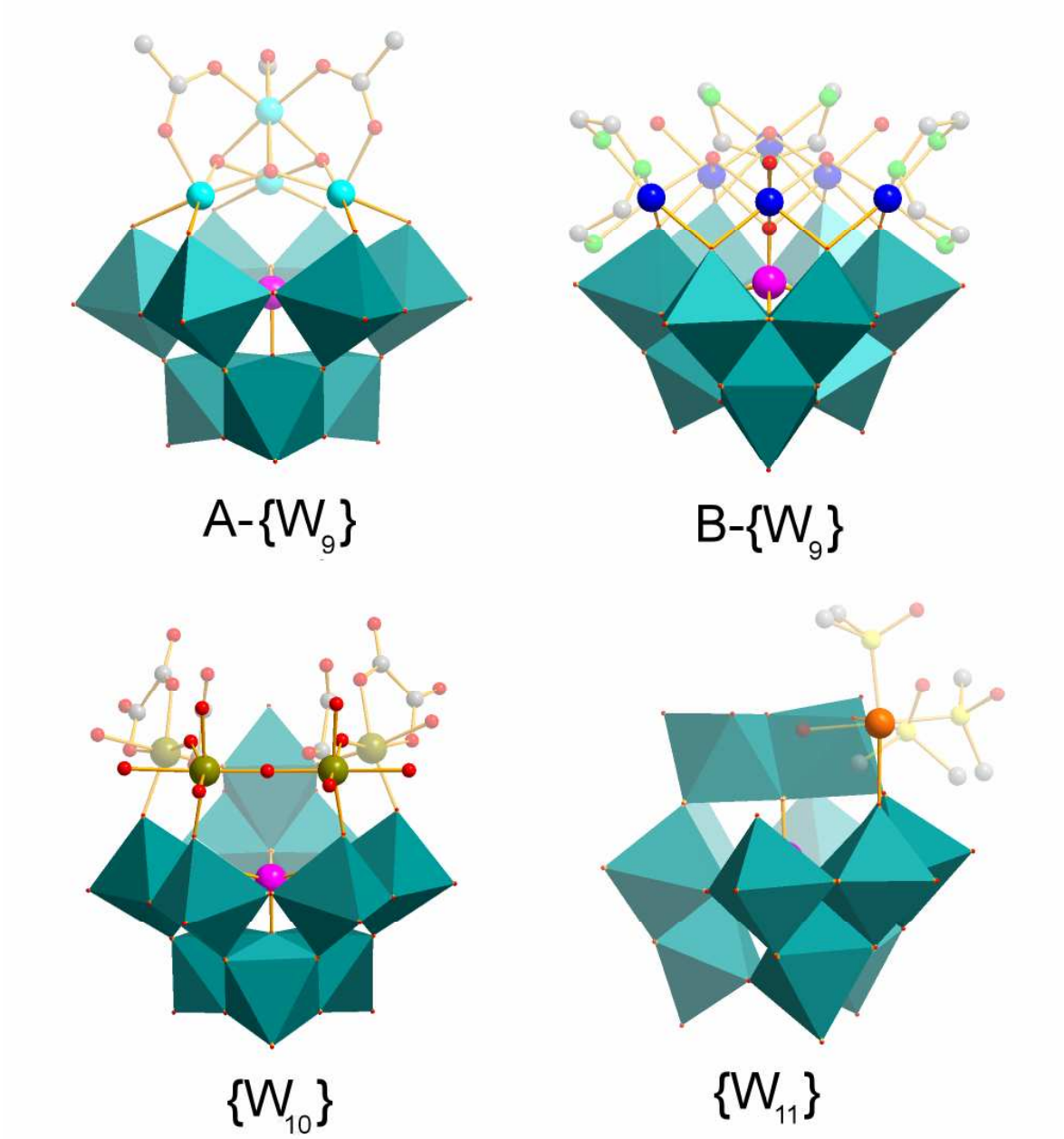

Figure 16: Illustration of the structural variety of Keggin-based lacunary POMs highlighting the diverse coordination environments governed by the number of vacancies and by the type of isomer. Top left: $Co_4[A\text{-}XM_9O_{34}]$[109]; Top right $Ni_6[B\text{-}XW_9O_{34}]$[110]; Bottom left: $Ti_4[XW_{10}O_{36}]$[111]; bottom right: $Ru_1[XW_{11}O_{39}]$.[112] Colour scheme: Ni: blue, Ti: dark yellow, Ru: orange; N: green, O: red, S: yellow, C: grey. Central heteroatom: magenta, lacunary cluster: green polyhedra.

The structural diversity of these lacunary species is enormously increased by a number of possible isomers which are induced by the rotational isomerism described for the α-Keggin structure (see section 1.5.1), but furthermore depend on the relative orientation and connectivity of the internal XO_4^{n-} heteroanion moiety. This phenomenon is particularly pronounced for the trivacant $\{XM_9\}$ cluster which forms a group of four isomers. The main distinction between the two principal structural isomers (A- and B-type) is the $[M_3O_{13}]$ triad which caps the central metal-oxide belt. In the A-isomer, this triad is the well-known edge-sharing moiety which is the basic building unit of the α-Keggin structure (see section 1.3.2). It is connected to the six-membered main belt by six corner-sharing bridges and is directly linked to the heteroatom by a X-O-M coordinative bond, see Figure 16, top left. Consequently all four oxygen atoms of the heteroanion are engaged in coordinative bonds to the cluster framework. In contrast, the B-isomer is capped by an unusual corner-sharing $[M_3O_{13}]$ unit but more importantly the heteroanion features one free oxygen ligand which can coordinate directly to secondary transition metals, see Figure 16, top right. As a result, the coordination modes and hence the physical properties of these two isomers are altered significantly.[109,110] In addition to this structural isomerism, each of the compounds can form two rotational isomers (α and β respectively) by rotation of the triad units around the C_3 axis by 60 °.

In addition to their wide-ranging coordination chemistry these lacunary fragments can also be considered to act as formal building units in the assembly of larger heteropolyoxometalate structures. A prime example of this mechanism is illustrated in the following section.

1.5.3 The Wells-Dawson anion $[X_2M_{18}O_{62}]^{n-}$

The combination of two $[A\text{-}XM_9O_{34}]$ lacunary fragments by sharing six corners results in the formation of α-$[X_2M_{18}O_{62}]^{n-}$, a cluster often referred to as the Wells-Dawson or simply the Dawson anion.[28,45,77,113] The D_{3h} symmetrical cluster is composed of two six-membered central belts formed by three corner-sharing $[M_2O_{10}]$ dioctahedra; each of the two belts encloses a central tetrahedral XO_4^{n-} anion which supports the three $\{M_2\}$ fragments by engaging three of the XO_4^{n-} oxygens in X-O-M coordinative bonds. The top

and bottom of this assembly are capped by two $[M_3O_{13}]$ triads which are linked to the cluster by six corner-sharing modes and by interaction with the central XO_4^{n-} anion *via* one X-O-M coordinative bond. As expected, a number of structural isomers can be obtained by using either the α- or β-type $\{XM_9\}$ fragments or a combination of the two as building blocks. Furthermore, the rotation the $[M_3O_{13}]$ caps relative to one another by 60 ° allows the generation of even more isomeric structures. *A priori* a total of six isomers can be constructed, however, so far only four of these have actually been observed with the α-isomer being the most common, see Figure 17.[114]

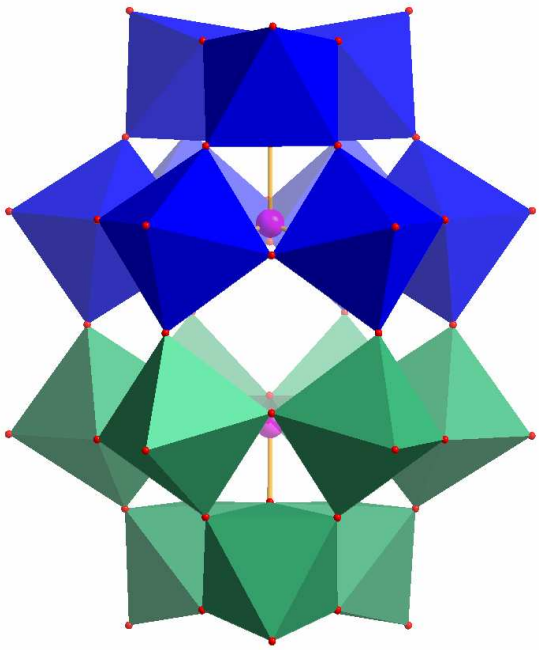

Figure 17: Polyhedral representation of the α-$[X_2M_{18}O_{62}]^{n-}$ Wells-Dawson anion. The two $[XM_9O_{32}]$ fragments which formally assemble the structure are highlighted in green and blue respectively; the two central heteroatoms are illustrated in magenta. The cluster shell can be described as two central six-membered belts which are alternatively linked by edge-sharing and corner-sharing modes. Between the two belts, only corner-sharing modes are observed. The belts are capped (top and bottom) by $[M_3O_{13}]$ triads which interact exclusively *via* corner-sharing links.

To date the majority of studies have focussed on the physical and chemical properties of the phosphorus(V)-based α-$[P_2M_{18}O_{62}]^{n-}$ anion and reported applications range from heterogeneous catalysis[115,116] to photo- and thermochroism in thin films[117,118] to enhanced antibiotic activity.[119,120]

An intriguing example of how to utilise the Wells-Dawson shell as a nano-reactor has been reported by Cronin *et al.* in 2004.[121] A molybdenum-based Dawson framework was constructed which encapsulates two trigonal-pyramidal sulfite SO_3^{2-} anions.

Thermal activation of the compound triggers an intramolecular redox reaction in which the two sulfite moieties are oxidised and form a sulfur-sulfur bond. Simultaneously, two electrons are transferred from the sulfurs to the metal-oxide shell, resulting in the formation of two Mo(V) centres. It has furthermore been shown that this reaction is reversible hence this material can be considered a redox-active molecular switch.

1.5.4 Lacunary Wells-Dawson derivatives

Typically, the Wells-Dawson anions are inert to hydrolysis in acidic conditions of pH 6 and lower.[77] However the controlled increase of the pH to levels higher than pH 6 initially results in the loss of one "M=O" fragment and a monolacunary species $[X_2M_{17}O_{61}]^{(n+4)-}$ is formed. Two isomers of this structure are known depending on the position of the vacancy. The α_2-isomer is formed by loss of one "M=O" fragment from the apical position, i.e. one metal centre is removed from a $[M_3O_{13}]$ triad which caps the cluster. However, a more complicated procedure involving further decomposition and re-assembly of the cluster leads to the formation of the α_1-isomer where the vacancy is created within the central six-membered belt. DFT studies show that this results in an energetically unfavoured structural configuration and the α_1-cluster readily isomerises into the more stable α_2-structure.

Removal of more than one [M=O] fragment from the shell of the Dawson cluster results in the formation of di- and trilacunary species very much analogous to the considerations described for Keggin-based lacuna species, see section 1.5.2. Again, a range of structural and rotational isomers are obtained, the structures of which have been comprehensively discussed in the recent literature.[28,45,77,122]

1.6 Molybdenum blues

The existence of highly reduced molybdenum oxide species was reported as early as 1783 when C. W. Scheele observed the formation of a deep blue solution upon heating molybdenum (VI) oxide, MoO_3, in concentrated nitric acid.[123, 124] However, the structural composition of this complex group of compounds remained unknown until Müller *et al.* reported the structures of a family of giant clusters in the 1990s. These compounds are typically assembled in one-pot reactions under acidic reducing conditions where smaller fragments are formed which then, in turn, condense into larger stable structures.

1.6.1.1 A trigonal ring –shaped {Mo_{57}} cluster

A prime example of this synthetic approach is the formation of a {Mo_{57}} ring obtained by the self-assembly of three {Mo_{17}} units using electrophilic transition metals as linkers.[125-128] The {Mo_{17}} fragments are arranged in a trigonal fashion and are virtually identical to the {Mo_{17}} subunits found in the {Mo_{36}} isopolyoxomolybdate cluster (see section 1.4.3). This trigonal assembly is stabilised by three face-sharing [$Mo^{V}_2O_9$] dioctahedral linking units which link the {Mo_{17}} fragments through corner-sharing modes, see Figure 18. Furthermore, six paramagnetic Fe(III) centres are located between the polyoxometalate subunits and act as linking metal centres. This building-block rationalisation allows the description of the cluster as a combination of fragments: {Mo_{57}} = [{Mo_{17}}$_3${Mo_2}$_3${Fe}$_6$]. Interestingly, a range of structurally identical assemblies were obtained using V(IV) instead of iron(III), resulting in the isolation of pure {V}$_6$ as well as mixed metal [{V}$_x${Fe}$_{6-x}$] clusters. The facile control over the physicochemical properties of the structures was demonstrated by the variation in magnetic interactions depending on the combination of transition metals used.[129] These results illustrate the broad applicability of the key principles of this self-assembly approach, i.e. the linking of fully oxidised POM fragments ({Mo_{17}}) using electrophilic linkers (Fe(III), V(IV), *etc.*) and reduced metalate stabilisers ([$Mo^{V}_2O_9$]) which results in the formation of a wide range of self-assembled, tuneable structures, see Figure 18. [128-130]

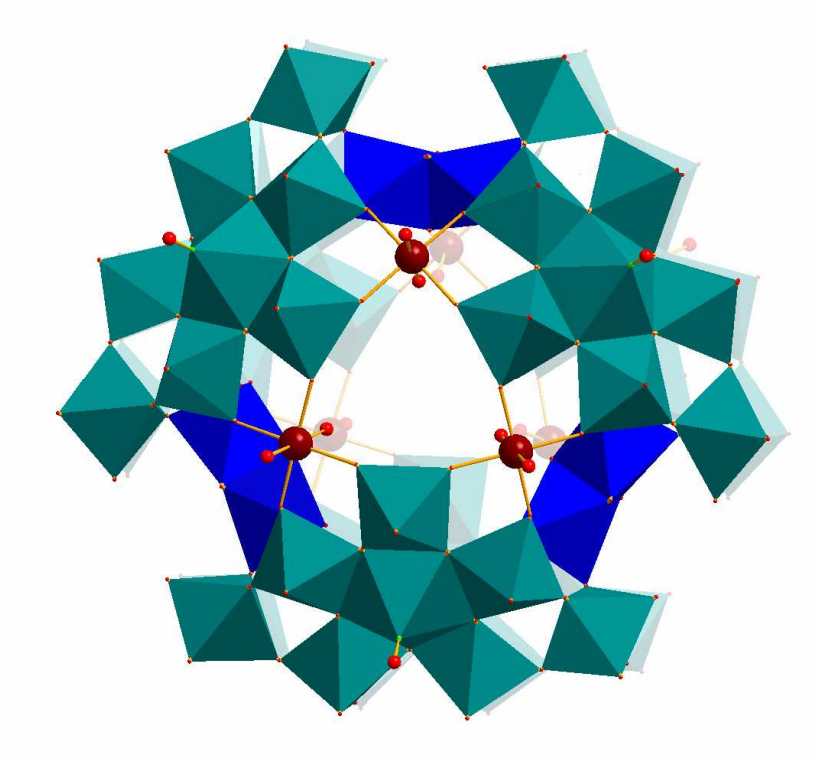

Figure 18: Polyhedral representation of the {Mo_{57}} cluster anion, $[Mo^{VI}_{51}Mo^{V}_{6}Fe_6(NO)_6O_{174}(OH)_3(H_2O)_{24}]^{15-}$ highlighting the self-assembly based on three {Mo_{17}} units (teal), three {Mo_2} linkers (blue) and six Fe^{III} centres (brown spheres). The versatility of the system has been demonstrated by replacing the iron(III) centres with V(IV) centres whilst retaining the overall structure. Oxygen ligands: red spheres, nitrogen ligands: green spheres.

The high degree of synthetic control over the cluster assembly and the inherent potential for manipulating the cluster properties have furthermore been successfully demonstrated by attaching a set of six electrophilic [Mo=O] units to the periphery of the cluster under reducing conditions. This feature allows extension of the metal-oxide framework and further provides a facile route to introducing additional *addenda* atoms. These additional metal units can be removed from the cluster under oxidising conditions and highlight another means of controlling the assembly of molybdenum blue species, namely changing redox-potentials of the reaction system.[130]

1.6.1.2 Giant Wheel structures: {Mo_{154}} and {Mo_{176}}

Applying this general synthetic approach to other reaction systems allows the isolation of a giant wheel-shaped cluster, $[Mo_{154}(NO)_{14}O_{448}H_{14}(H_2O)_{70}]^{28-}$ (={Mo_{154}}) which was formed in a straight-forward one-pot reaction using sodium molybdate as a precursor. The cluster

can alternatively be formulated as a tetradecamer formed by linking fourteen $\{Mo_8\}$ units with monomeric $\{Mo_1\}$ octahedra into a mesoscopic molecule with an external diameter of *ca.* 3.3 nm and an internal cavity of *ca.* 2.0 nm. The $\{Mo_8\}$ fragments are based on pentagonal $\{Mo(Mo_5)\}$ units where five $[MoO_6]$ octahedra are arranged around a Mo-centered pentagonal bipyramid $[MoO_7]$ in a corner-sharing fashion. Two additional $[MoO_6]$ octahedra are attached to the periphery of this pentagon by corner-sharing binding modes to complete the $\{Mo_8\}$ building blocks, see Figure 19.

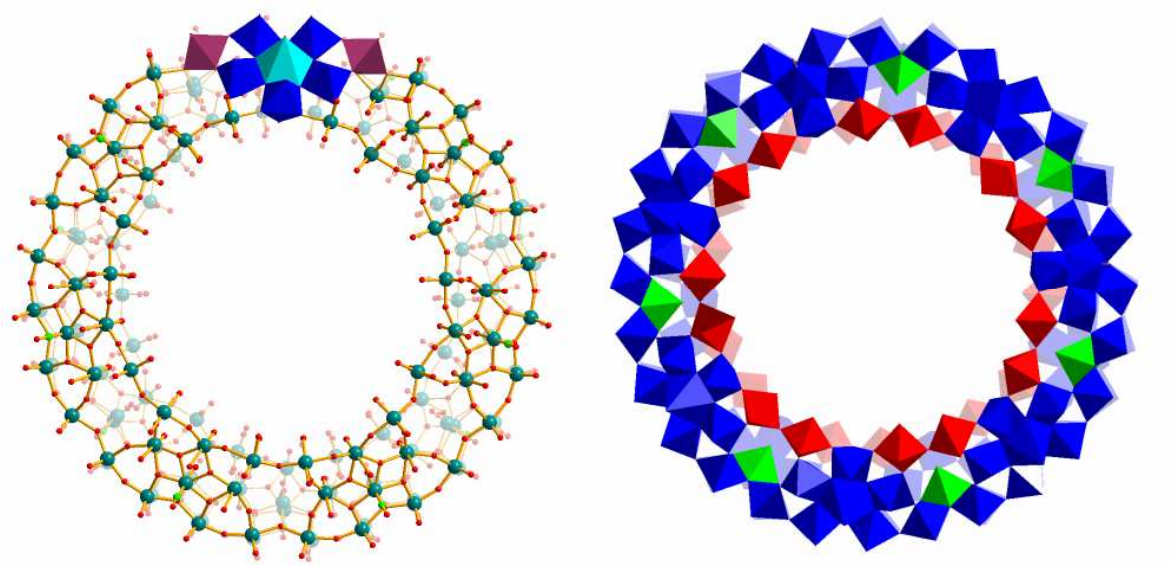

Figure 19: Left: Ball-and-stick representation of the $\{Mo_{154}\}$ wheel structure. The $\{Mo_8\}$ building unit is highlighted by polyhedral representation. Central pentagonal bipyramid: Light blue; edge-sharing $\{Mo_1\}$ units: blue; peripheral $\{Mo_1\}$ linkers: purple. Right: Full polyhedral representation of the $\{Mo_{154}\}$wheel structure illustrating the connectivity of $\{Mo_8\}$ units (blue), $\{Mo_2\}$ dioctahedra (red) and central $\{Mo_1\}$ stabilising units (green). Colour scheme: Mo: green spheres, O: red spheres.

Interestingly identical building units are found in the assembly of the $\{Mo_{36}\}$ isopolyoxomolybdate in section 1.4.3.2 where the pentagonal $\{Mo(Mo_5)\}$ fragments are instrumental in forming the $\{Mo_{17}\}$ subunits. In opposite to the $\{Mo_{36}\}$ and $\{Mo_{57}\}$ structures however, the $\{Mo_8\}$ fragments in the $\{Mo_{154}\}$ wheel do not form $\{Mo_{17}\}$ units, but are arranged as discrete moieties around the equator of the ring-like assembly (Figure 19, right, highlighted in blue). Structural stabilisation is provided by 14 corner-sharing $\{Mo_2\}$ dioctahedral units which form two peripheral rings around the external edges of the structure (Figure 19, right, highlighted in red). Further stabilisation is provided by 14 internal $\{Mo_1\}$ octahedra which act as bridges between the discrete $\{Mo_8\}$ fragments (Figure 19, right, highlighted in green).

It has been demonstrated that in aqueous solution these clusters truly self-organise into spherical nanoscopic vesicles.[131] Aggregation of the discrete wheels leads to the formation of hollow vesicles made up from almost 1200 individual $\{Mo_{154}\}$ clusters which encapsulate a water matrix. This inorganic vesicular structure is characterised by a diameter of *ca.* 45 nm and a molar weight of more than 2.5×10^7 g mol^{-1}. Similar hierarchical self-organisation processes have also been observed using the ball-shaped "Keplerate" type molybdenum blue species (see section 1.6.1.3) and vesicle diameters of up to 80 nm have recently been reported.[132] These initial results, therefore, seem to indicate a general potential for the controlled aggregation of nano- and mesoscopic objects based on large POM clusters.[133, 134]

Müller et al. demonstrated that the concept of self-assembling wheel-like POM clusters based on reactive building blocks can be taken one step further by isolating a cluster made up of 176 Mo centres.[3,135] The ring-shaped $\{Mo_{176}\}$ assembly can be formulated as $[(MoO_3)_{176}(H_2O)_{80}H_{32}]$ and can be structurally described based on the principles elaborated for the $\{Mo_{154}\}$ wheel, see above. The hexadecameric cluster is formed by linking 16 $\{Mo_8\}$ units with 16 $\{Mo_1\}$ bridges along the equatorial plane. Stabilisation along the inner rims is provided by two sets of 8 $\{Mo_2\}$ corner-sharing dioctahedra, see Figure 20.

The truly hexadecameric character of the structure becomes immediately evident in the alternative notation $\{Mo_{176}\} = [\{Mo_8\}\{Mo_2\}\{Mo_1\}]_{16}$. Sterically this assembly results in the formation of a nanoscopic ring with an outer diameter of *ca.* 4.1 nm and an internal solvent-filled cavity of *ca.* 2.3 nm. The host-guest potential of the $\{Mo_{176}\}$ wheel has recently been explored by Aida *et al.* who investigated the supramolecular interactions between the POM cluster and Zn-centered porphyrins.[136] Detailed spectroscopic studies, electron microscopy investigations and mass spectrometry showed that the cluster can incorporate up to three metallated porphyrins which are π-π stacked and whose molecular planes are arranged parallel to the equatorial plane of the $\{Mo_{176}\}$ wheel, see Figure 20.

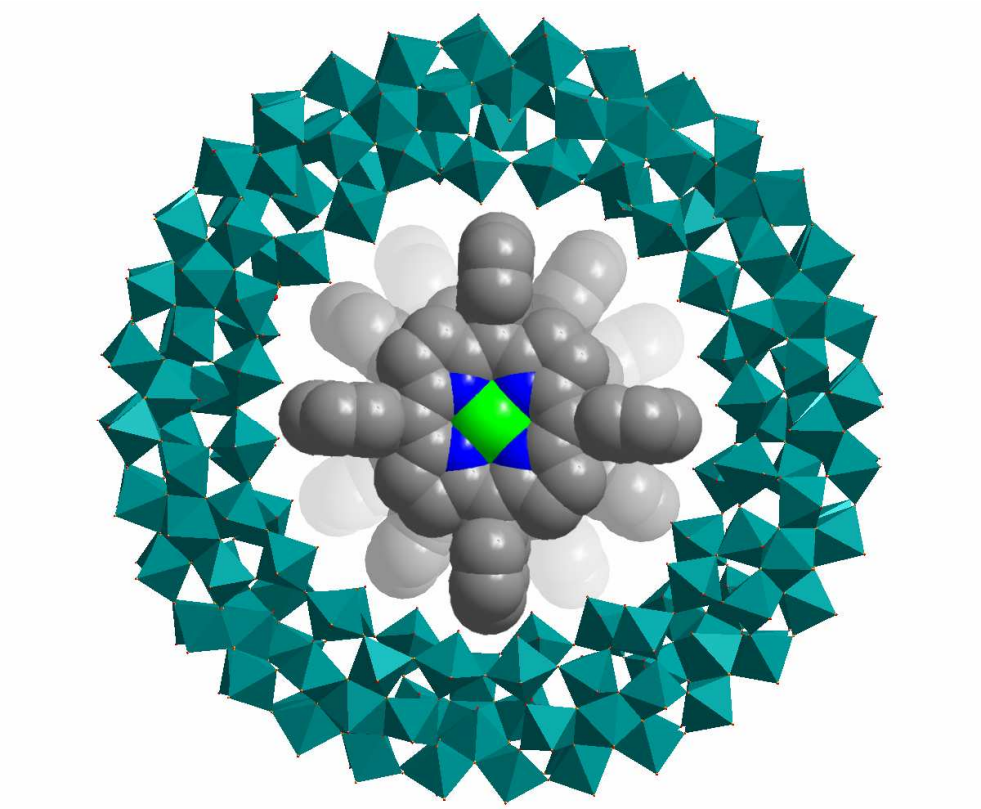

Figure 20: Schematic representation of the host-guest complex formed by the inclusion of three Zn-porphyrin moieties inside the giant wheel $\{Mo_{176}\}$. NB: This illustration is not taken from crystallographic data but has been generated based on the properties of the compound observed by MALDI mass-spectrometry, scanning-tunnelling microscopy, UV/Vis/IR-spectroscopy and titration experiments.

The potential to build even larger molecules based on this wheel structure has been demonstrated by attaching two $\{Mo_{36}\}$ "hub caps" to either side of the $\{Mo_{176}\}$ wheel structure according to the reaction scheme $\{Mo_{176}\} + 2\ \{Mo_{36}\} \rightarrow \{Mo_{248}\}$.[137] As a consequence, the open cavity inside the wheel structure is effectively sealed off. The ability of molybdenum blue species to form fully enclosed spherical cavities has been demonstrated by a whole range of compounds, the so-called Keplerates. Their formation and function will be discussed in detail in the following section.

1.6.1.3 The {M_{132}} Keplerate family

One of the most prominent examples of self-assembled molybdenum blue species is the {M_{132}} Keplerate family. The archetypical all-molybdenum compound $[Mo^{VI}_{72}Mo^{V}_{60}O_{372}(OAc)_{30}(H_2O)_{72}]^{42-}$ can structurally be described as a cluster resembling the fullerene structure with overall icosahedral symmetry.[135] The main building blocks are once again the ubiquitous pentagonal fragments described earlier which are the prototypical structural feature observed in most molybdenum blue species.[29,138,139] A set of 12 pentagonal fully oxidised {(Mo)Mo_5} units are located on the vertices of an icosahedron and are connected by a set of 30 dinuclear {Mo_2} linkers *via* corner-sharing oxygen bridges. These dioctahedral {Mo_2} bridges further reinforce the structure by establishing Mo^{V}-Mo^{V} bonding interactions which are identified by short intermetallic distances of *ca.* 2.6 Å.

Overall this structural arrangement results in the formation of a spherical molecule with an outer diameter of *ca.* 2.9 nm which can be rationalised as {Mo_{132}} = {(Mo)Mo_5}$_{12}${Mo_2}$_{30}$. The spherical character of the {Mo_{132}} cluster becomes immediately evident by studying the packing of the molecules in the crystal lattice. Remarkably the clusters adopt an ABC-type packing which is identical to the cubic close packing (ccp) of atoms in metals such as Cu and Ag.[140]

It was soon realised that the well-defined arrangement of pentagonal units and dioctahedral linkers leads to the formation of hexagonal pores with tuneable pore sizes depending on the detailed structure of the {Mo_2} linkers employed. This ability was demonstrated by cation sequestration experiments which showed that depending on the nature of the cation, the pores can act as ion-sensitive gates and, therefore, represent an unique example of a purely inorganic model for ion transport channels in biological systems. In addition, it was shown that these “pores” can be selectively opened and shut using guanidinium cations as molecular recognition motifs which fit exactly in the centre of the pore and can thus bind strongly to the pore wall through electrostatic and hydrogen-bonding interactions. This feature allows the reversible closing of the shell structure and reveals another intriguing supramolecular ability of these Keplerate structures.[141-144]

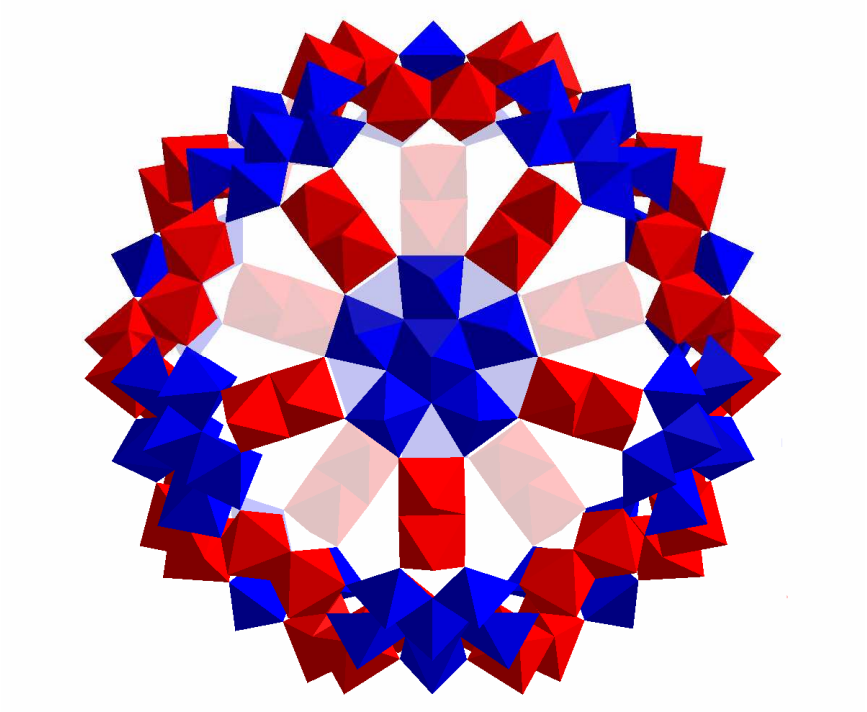

Figure 21: Polyhedral representation of the Keplerate-type $\{Mo_{132}\}$ cluster illustrating the set of 12 five-connected $\{(Mo)Mo_5\}$ pentagonal building blocks (blue) featuring the central pentagonal bipyramidal $[MoO_7]$ fragment. The $\{Mo_2\}$ linking units (red) consolidate the structural integrity by forming Mo-Mo single bonds with typically short interatomic distances $d_{Mo\text{-}Mo}$ = *ca.* 2.6 Å.

The structural diversity of this class of compounds can further be expanded by replacing the dimeric reduced $\{Mo^{V}_2\}$ linkers by monomeric $\{Fe^{III}_1\}$ bridges resulting in an overall formula of $\{Mo^{VI}_{72}Fe^{III}_{30}\}$.[145] In other words, the overall size of the cluster has been reduced to 2.1 nm by decreasing the size of the bridging units and consequently producing a closer arrangement of the pentagonal $\{(Mo)Mo_5\}$ building blocks. This "shrinking" of the cluster combined with the incorporation of paramagnetic Fe^{III} species induces several significant changes in the physical and chemical properties of the structure, especially in relation to the magnetic and redox properties.[138,145,146] Furthermore it has been reported that the fully oxidised $\{Mo_{72}Fe_{30}\}$ cluster can encapsulate reduced Keggin clusters, $[H_2PMo_{12}O_{40}]^{3-}$, and form a supramolecular host-guest complex.[147] This assembly exhibits strong electronic interactions between the reduced Keggin core and the oxidised Keplerate shell as indicated by an unprecedented charge-transfer band in the visible region. Recently, it has been observed that the $\{Mo_{72}Fe_{30}\}$ spheres undergo further condensation reactions in the solid state to form highly condensed frameworks.[148] This process proceeds *via* the formation of Fe-O-Fe bridges between the spheres so that each Keplerate

acts as a four-connected node in this 3D assembly. This phenomenon illustrates the intrinsic ability of polyoxometalates to act as scaffolds for the assembly of rigid 3D frameworks which can subsequently be manipulated to feature highly sought-after chemical and physical functionalities such as acidity and porosity. Several approaches to establish this novel class of functional POM frameworks have been reported and the following section will discuss the various methods employed to date.

1.7 Polyoxometalate-based frameworks

Over the last decade, the assembly of stable supramolecular frameworks has become one of the main challenges for chemists all over the world. In particular the construction of 3D metal organic frameworks (MOFs) which incorporate structural functionality has created an enormous interest in this field of material science.[149-158] The main advantage of MOFs is the enormous structural control which enables chemists to tailor the properties of the material. It is this ability which separates MOFs from purely inorganic materials such as zeolites and AlPOs.[159] However, polyoxometalates in particular have been identified as promising inorganic building blocks for the design of novel framework compounds owing to their structural diversity in combination with their tuneable physical and chemical properties and their discrete molecular nature.

The viability of this strategy has been demonstrated recently by the assembly of an ionic calix[4]arene-linked polyoxometalate framework. Konichi *et al.* used phosphorous-centered tungstate Keggin units, $[PW_{12}O_{40}]^{3-}$ as molecular scaffolds to form a microporous material, see Figure 22.[160] The stability of this framework is provided by non-directed Coulomb electrostatic interactions between the cationic, organic calixarene groups and the anionic POM cluster. However, the sophisticated structural arrangement is further governed by a multitude of weaker interactions; in particular hydrogen-bonding motifs and van-der-Waals interactions seem to arrange the building blocks in such a way as to enclose channels with dimension of *ca.* 6 x 9 Å. Sorption studies demonstrated that the pores can reversibly absorb water molecules as well as *n*-alcohol molecules with varying carbon chain lengths ranging from 2-4.

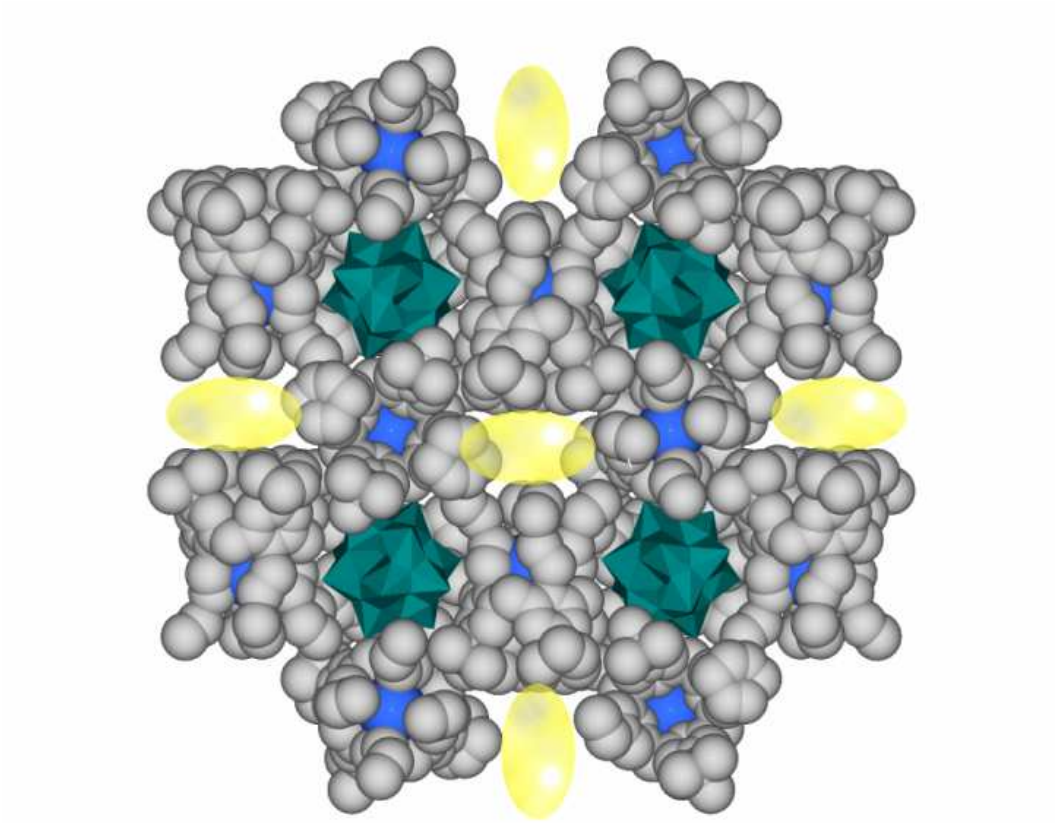

Figure 22: Illustration of the framework assembly of sodium-centered calix[4]arene units and $[PW_{12}O_{40}]^{3-}$ Keggin clusters resulting in the formation of accessible cavities (yellow ellipsoids) with dimensions of *ca.* 6 x 9 Å. Colour scheme: C: grey, Na: light blue, polyoxometalate clusters: green. H, O and solvent molecules were omitted for clarity.

Another successful approach was recently reported by *Wang et al.* who linked molybdenum-based Keggin units with in-situ generated copper iodide clusters, $[Cu_{24}I_{10}(ligand)_{12}]^{14+}$. These $\{Cu_{24}\}$ moieties are stabilised by organic ligands and cross-link the polyoxometalates into a 3D framework with interesting photochemical and electrochemical properties and furthermore feature electrocatalytical reductive capabilities.[161]

The ability to further introduce functionality and selectivity in polyoxometalate-based porous frameworks has been demonstrated by using triangular $[Cr_3(O)(C_2H_5COO)_6(H_2O)_3]^+$ (=$\{Cr_3\}$) macrocations and potassium cations to link $\{PW_{12}\}$ Keggin clusters into several porous frameworks with layered structures.[162] This group of materials features two types of channels which exhibit different degrees of hydrophilicity and as a result can absorb different molecules depending on their polarity. It has been shown that one type of channels preferentially absorbs water molecules whereas the more

hydrophobic pores absorb organic molecules such as small alcohols. The uptake of nonpolar compounds such as dichloromethane is completely excluded thus demonstrating the molecular sieve properties of these compounds.

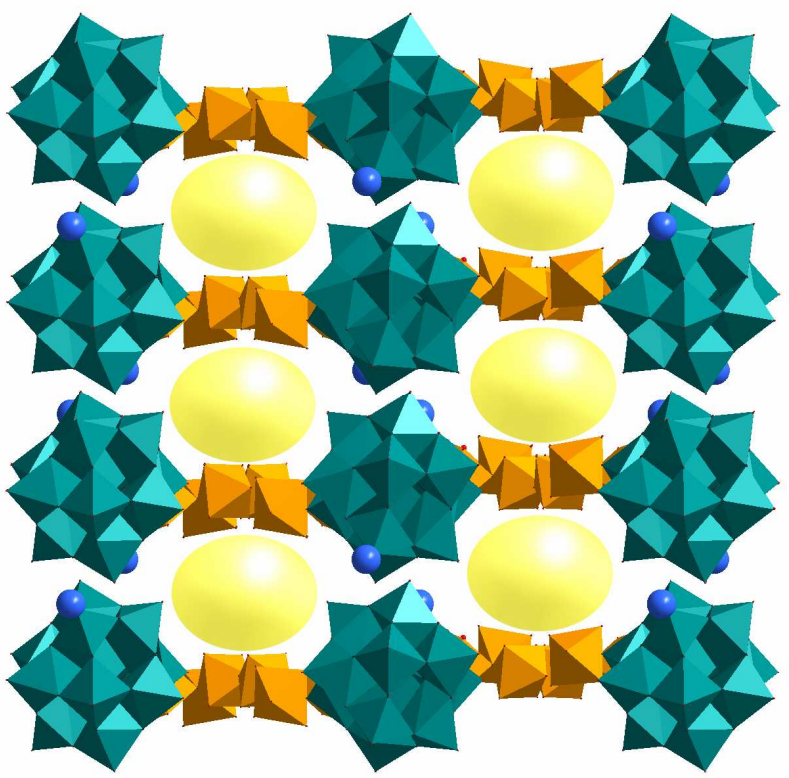

Figure 23: Illustration of the porous structure of the {Cr_3}-linked {PW_{12}} Keggin assembly. The voids in the material are highlighted by yellow spheres, the connectivity of the {Cr_3} cations (orange polyhedra) and Keggin clusters (green polyhedra) shows the formation of a layered structure which is pillared by potassium-ions (blue spheres) in the inter-layer spaces. Organic ligands are omitted for clarity.

The variation of several structural parameters furthermore allows the manipulation of pore size and sorption properties. Changing the inorganic pillaring counterions from potassium to the larger homologue caesium completely switched off the capability of sorbing organic cations but did not affect the uptake of water. In these systems the polarity of the channels could further be fine-tuned by systematically changing the ligands which support the {Cr_3} assembly. Longer carbon chain lengths on these ligands directly affected the solvent uptake and allowed the application of the material as molecular sieves in the separation of azeotrope solvent mixtures.[163-165] It was further demonstrated that very similar frameworks can be assembled using the larger {P_2W_{18}} Wells-Dawson anion and lacunary fragments thereof. The study conclusively showed that the solvent uptake in the pores

could be directly related to the charge on the cluster and therefore gave vital information for further work towards functional polyoxometalate frameworks.[166]

1.8 Perspectives

The range of cluster architectures in the polyoxometalate family is unrivalled in the field of inorganic chemistry. The varied range of accessible coordination modes, oxidation states and the presence of additional heteroatoms which dramatically alter the physical and chemical properties of these compounds allow the formation of a vast range of cluster species. It is this versatility which makes polyoxometalate clusters promising candidates for the synthesis of functional inorganic compounds. In the light of the ever-increasing demand for more sophisticated, multifunctional materials, it becomes evident that polyoxometalates might be the answer to some of the most intriguing scientific questions.

It has been illustrated that polyoxometalate-based materials can combine key properties which are highly sought-after, such as porosity and redox-switchability for the assembly of energy- and gas storage materials or acidity and specific reactivity for the application as “green” industrial catalysts. Over the last decade it has become increasingly evident that polyoxometalate research is diversifying from purely investigating the formation of new cluster compounds to the application of these materials in assembling ever more sophisticated frameworks and solid-state materials with specifically designed properties. This diversification process is still accelerating and is driven by collaborations between researchers from scientific backgrounds ranging from computational prediction of material properties to process-oriented industrial applications.

It is therefore evident that the synthesis polyoxometalate-based materials is still in its infancy and will become increasingly sophisticated by the input and feedback from researchers with very different scientific perspectives. One key feature which is of paramount interest would be the assembly of polyoxometalates and linker units driven by a crystal-engineering approach so that predetermined framework architectures can be designed. This would subsequently allow the formation of a new family of materials with tuneable properties and synergistic functionality which could create a new area in polyoxometalate research.

2 Problem and Objectives

The assembly of larger frameworks based on polyoxometalate building blocks has thus far been typically accomplished by using organic ligands or ligand-supported transition metals as bridges between the anionic clusters. The ability of organic ligands to bind to two or more clusters demands the presence of a ditopic unit which features two distinct binding motifs (often hydrogen-bond donors or positively charged amines) supported by an organic spacer unit. The interactions of these ligands with polyoxometalates is dominated by spacially non-directed Coulomb attraction and further stabilised by weaker, but directed attractive forces such as hydrogen-bonding and van der Waals interactions.

The effect of these organic ligands on the overall framework structure however, is not yet fully understood. Factors such as geometry and rigidity of the ligand, arrangement of the binding motifs, and the ability to interact not only with the clusters, but also with other ligands might play an important role in the directed assembly of functional frameworks. A major part of this study will thus investigate the ability of different amine-based ligands to form framework architectures with polyoxometalates. The effects of the organic ligands on the framework assemblies will be correlated to their structure and chemical properties and their potential for the formation of functional materials will be elucidated. A detailed structural analysis of the range of interactions between the organic ligands and the cluster shells will be the basis for this study and will further allow the development of a working hypothesis to understand which organic groups are particularly promising candidates for the assembly of polyoxometalate-based frameworks.

In addition it will be assessed whether organic groups can be used to introduce functionality directly by the use of more sophisticated ligands. This procedure will facilitate framework modifications by virtue of the organic cations used in the synthesis. In effect this will allow fine-tuning of the properties of the supramolecular assemblies whilst retaining the POM building blocks. In this way, a given reaction system does not require complete adaptation in order to introduce a new functionality but can simply be altered by changing the organic cations used in the synthesis. This approach will help to understand

how framework properties can be introduced by synergistic interactions between the organic linkers and the polyoxometalate building blocks.

The assembly of porous frameworks based on polyoxometalate building blocks is, however, not limited to linking clusters with organic cations. It has been demonstrated that transition metals can coordinate to the outer-shell oxygen environment and thus form potential linking points for framework extension. Often the actual linkage is provided in the form of coordinating ligands which interact with the transition metals on two clusters and thus establish a bridging interaction. However, this concept is only of limited use for the assembly of potentially porous compounds since framework stability is frequently decreased due to the instability of this type of coordination bond. Introducing an all-metal-oxide framework by direct linking of the clusters *via* metal bridges would help to increase the overall stability and the understanding of directed framework assembly based on the principles of self-assembly. However, one major problem which has thus far limited the success of this approach is the large negative charge of polyoxometalate clusters. Any close contact between two clusters would thus have to be compensated for by highly charged cations which in turn limit the type of transition metal that can be used for direct linking of two clusters. The coordination behaviour of common polyoxometalate building blocks will, therefore, be investigated in combination with suitable transition metal linkers which are known to form strong bonds with POM clusters. The challenge is to establish a system which interacts and forms stable frameworks in the absence of coordinating (and thus stabilising) ligands. This approach will allow the use of the metal coordination sites to interact with several POMs and form extended structures rather than only isolated molecular clusters.

Owing to their structural variety, polyoxometalates can form specific interactions with a range of guest molecules and act as selective binding sites for inorganic as well as organic cations. The host-guest complexation behaviour of two isopolyoxo anions, $\{Mo_{36}\}$ and $\{W_{36}\}$, will be studied to understand if these compounds can be used as size-selective hosts in sequestration processes. The potential for the assembly of frameworks based on these compounds will be studied and the effects of varying the ionic radii of guest ions will be rationalised. Furthermore the concepts of “molecular machines” will be applied to the system and initial experiments will elucidate the possibility of creating a hybrid organic-inorganic rotator.

3 Results and Discussion

3.1 Coordination behaviour and host-guest chemistry of isopolyoxometalates

Although polyoxometalates have been known for more than 200 years, the self-assembly processes which lead to their formation in aqueous acidic solution are still not fully understood. This is mainly due to the complexity of the systems in combination with the large range of synthetic parameters that influence cluster assembly in solution. As a result, the effects of ionic strength, solution pH and type of counter cation can often not be rationalised and have to be elucidated by a set of experimental studies. However, although the processes which lead to cluster formation are largely unknown, the general solution behaviour of non-reduced tungstate and molybdate systems is in principle well understood and the cluster types formed can be predicted based on pH, concentration and ionic strength of the aqueous solution. This prior knowledge thus allows the study of a particular polyoxometalate cluster by adjusting the conditions so as to favour the presence and maximise the solution concentration of the desired compound.

A basic prerequisite for the assembly of larger structures based on polyoxometalates is the detailed understanding of the coordination behaviour for a given cluster type. The effects of structural and geometric restraints in combination with the location of the coordination sites allows the pre-determination and, to a degree, the design of a supramolecular assembly. This approach will be exemplified in the following sections by two isopolyoxometalate families, the $\{Mo_{36}\}$ and $\{W_{36}\}$ cluster anions.

3.2 Sensitive coordination sites on a isopolymolybdate $\{Mo_{36}\}$ cluster

While investigating the formation of polyoxomolybdates in highly acidic solutions below pH 1.8 it was observed that, depending on the presence of sodium cations, two types of $\{Mo_{36}\}$ clusters can be formed. Both clusters are based on the archetypal $\{Mo_{36}\}$ structure as introduced in section 1.4.3.2, however the cluster surface is in both cases decorated with coordinating organic ligands which stabilise the framework.

3.2.1 The guest free cluster anion $(TEAH)_6[Mo_{36}O_{112}(H_2O)_{14}(TEAH)_2]\cdot 10H_2O$

Compound **1** was isolated as the oxidation product of a Dawson-type cluster,[121] $[Mo_{18}O_{54}(SO_3)_2]^{6-}$ which undergoes extensive decomposition- and rearrangement processes including the loss of all sulphite heteroanions (SO_3^{2-}) and eventually results in the formation of $(TEAH)_6[Mo_{36}O_{112}(H_2O)_{14}(TEAH)_2]\cdot 10H_2O$ (**1**) where TEAH = protonated triethanol amine $[(C_2H_4OH)_3NH]^+$. The cluster anion $[Mo_{36}O_{112}(H_2O)_{14}(TEAH)_2]^{6-}$ **(1a)** is assembled from two $\{Mo_{17}\}$ sub-units which can be rationalised using a building block approach, see Figure 24.

The main element of each $\{Mo_{17}\}$ sub-unit is a $\{(Mo)Mo_5\}$ assembly which contains a pentagonal bipyramidal $[MoO_7]$ fragment as the central template. Five $[MoO_6]$ octahedra are condensed to the periphery of this fragment by edge-sharing modes along the equatorial belt of the bipyramid, see Figure 24, top. The typical range of Mo-O bond-lengths of this small building block is immediately apparent and reflects the general bonding modes in most polyoxometalates. In detail, three types of Mo-O bonds can be identified, the shortest ones being terminal $Mo{=}O_t$ bonds with a double bond character; here these strong coordinative Mo-O interactions result in characteristic metal-oxygen distances of $d_{Mo=Ot} \sim 1.7$ Å. Due to the π-bonding with empty Mo d-orbitals, these oxygen ligands are only weakly basic and exhibit a decreased nucleophilicity. In addition, bridging oxygens are observed which reinforce the structure by linking the metal centres and feature longer Mo-O distances of *ca.* 2.0-2.2 Å, depending on the number of metal centres connected by one O atom. There are 14 additional water ligands located on the cluster surface which form weak coordinative bonds to molybdenum centres with long bonding distances of $d_{Mo-O} \sim 2.4$ Å.

The assembly of these $\{(Mo)Mo_5\}$ building blocks into the $\{Mo_{17}\}$ subunit occurs *via* structural reinforcement by two $\{Mo_2\}$ dioctahedra and one central $\{Mo_1\}$ octahedron unit which link two pentagonal building units by a combination of edge- and corner-sharing modes, see Figure 24. The resulting fragment features a semi-spherical arrangement with a "pre-determined" linking point (Figure 24, magenta arrows) that allows the connection of two $\{Mo_{17}\}$ fragments *via* two mononuclear $\{Mo_1\}$ octahedra into a $\{Mo_{36}\}$ cluster, according to the formalism: $2\ \{Mo_{17}\} + 2\ \{Mo_1\} \rightarrow \{Mo_{36}\}$. It is interesting to note that the organic modification of this cluster can be achieved by introducing an organic

counterion, protonated triethanol amine (TEAH), into the synthesis of this cluster. The counterion can engage one of its hydroxyl groups as a ligand to replace one terminal water ligand in the periphery of the pentagonal {(Mo)Mo_5} unit and thus form a coordinative C-O-Mo bond to the cluster surface. (d_{Mo-O} = 2.375 Å). It is furthermore intriguing that the C_{2V} symmetry of the cluster fragment is broken by the unsymmetrical attachment of the organic ligand; in other words only one pentagonal {Mo{Mo5}} unit of each {Mo_{17}} unit binds an organic ligand whereas the opposite half remains non-ligated. This observation might be helpful in the design of anisotropic organic-inorganic hybrid materials.

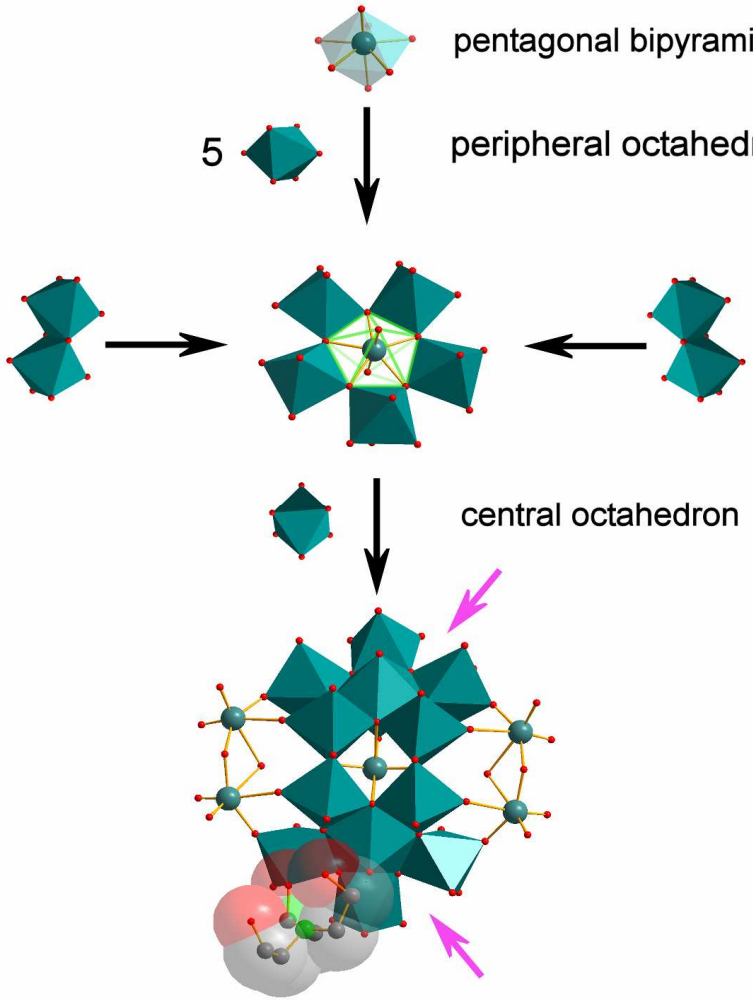

Figure 24: Illustration of the self-assembly of the {Mo_{17}} subunit in **1a**. A [MoO_7] pentagonal bipyramid templates the formation of a pentagonal {(Mo)Mo_5} unit. The five octahedral molybdenum oxide fragments are condensed to the central bipyramid by edge-sharing. The complete {Mo_{17}} subunit is subsequently assembled by linking two {(Mo)Mo_5} units with two dioctahedral {Mo_2} bridges and one central {Mo_1} linker (both illustrated as ball-and stick models in the {Mo_{17}} structure, see bottom). The cluster fragment can employ one TEAH counter cation to replace one apical terminal water ligand with a hydroxyl group, see bottom. Magenta arrows indicate the linking points for assembly of the {Mo_{36}} cluster from two {Mo_{17}} units and two {Mo_1} octahedral linkers. Colour scheme: Mo: teal, O: red, C: dark grey, N: green.

The assembly of two {Mo_{17}} subunits by linkage through two {Mo_1} octahedra results in the formation of the complete cluster anion $[Mo_{36}O_{112}(H_2O)_{14}(TEAH)_2]^{6-}$, **1a**, as illustrated in Figure 25. The {Mo_{36}} cluster can be described as an open-shell assembly which comprises two coordination pockets as potential binding sites for guests with multiple interaction sites provided by terminal oxygen ligands. In addition, the spatial arrangement of the two {Mo_{17}} sub-units encloses a cavity which is surrounded by a 10-membered ring formed by the peripheral molybdenum centers of the cluster anion, see Figure 25.

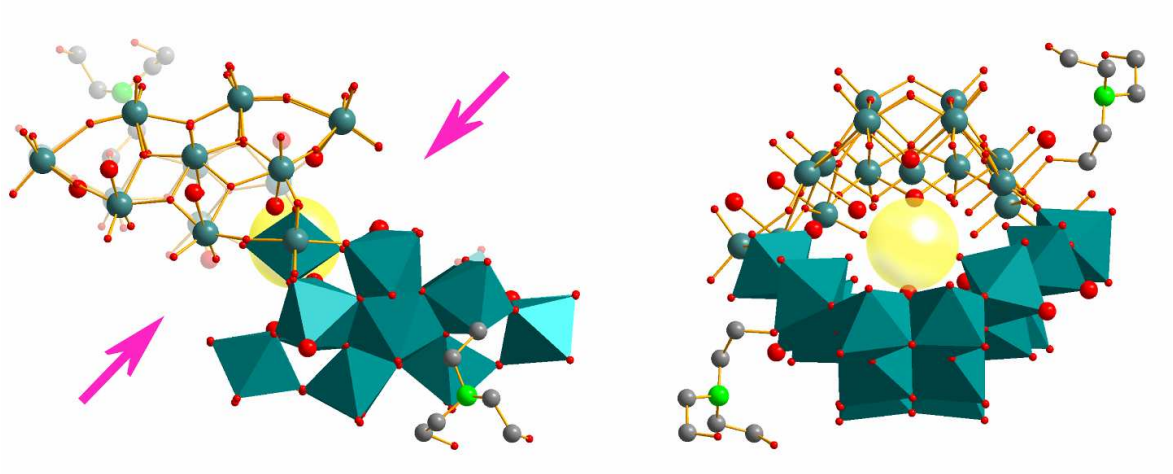

Figure 25: Side view (left) and front view (right) of the cluster anion **1a**. The side view demonstrates the open-shell assembly which provides two potential coordination pockets, highlighted by magenta arrows. The front view illustrates the internal cavity with an approximate diameter of *ca.* 5 Å (highlighted by a yellow sphere). Mo: teal, O: red spheres, C: dark grey, N: green. Water ligands are illustrated as large red spheres.

In the crystal lattice, the cluster anions **1a** form a channel-like arrangement so that the cavities are lined up along the crystallographic *a*-axis, see Figure 26. The cavities in this "guest-free" compound are filled with solvent water molecules which hydrogen-bond to the surrounding cluster oxygen environment. Furthermore, the inter-layer water molecules stabilise the structure by forming an extensive hydrogen-bonding network. The charge of the cluster anions is balanced by six TEAH cations as determined by elemental analysis, FT-IR and thermogravimetry. However, due to a high degree of disorder in the organic ligands, these could not be unambiguously assigned by X-ray crystallography. Remarkably, the minimum spacing between two adjacent cluster anions is d_{min} = 3.495 Å (O10 – O51) which is uncommon considering size and charge of the cluster. This phenomenon however can be explained by the supramolecular effect of the coordinating TEAH ligands. In the lattice, two ligands per cluster unit hydrogen-bond to the adjacent clusters and thus allow closer contacts by establishing attractive interactions, see Figure 26.

It is these interactions which allow a much denser packing along the crystallographic *b*-axis.

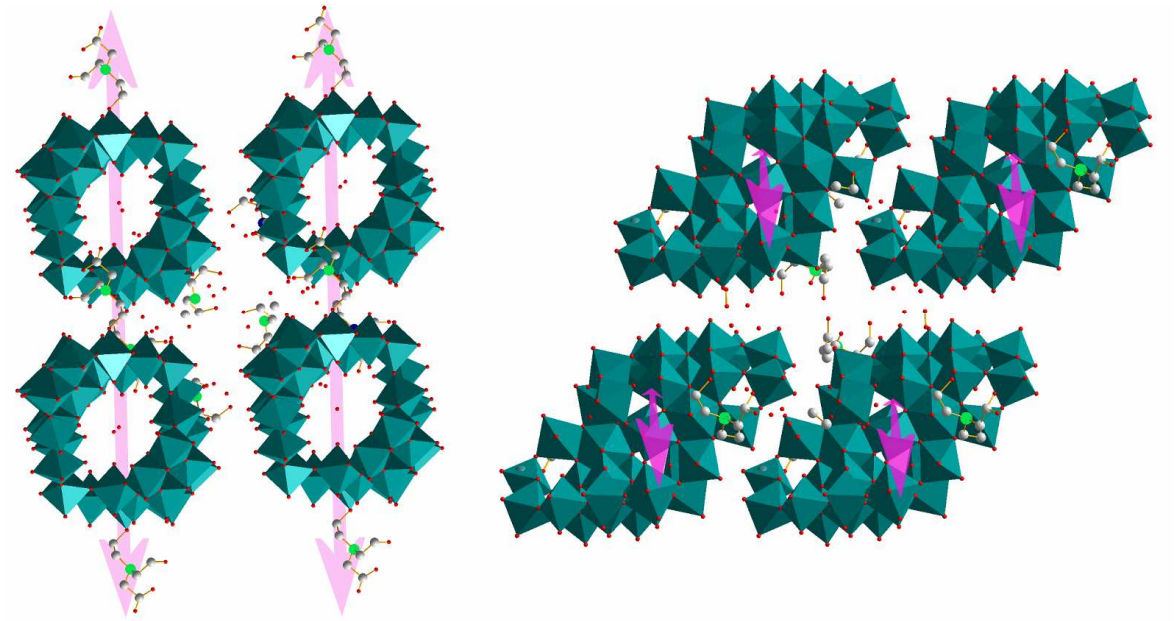

Figure 26: Polyhedral representation of the crystal packing of **1**. View along the crystallographic *a*-axis (left) and along the crystallographic *b*-axis (right) illustrates how the interaction of the TEAH ligands results in close contacts between the cluster anions **1a** (the direction of propagation of the strong hydrogen-bonding interactions is indicated by magenta arrows). Colour scheme: {Mo_{36}}: teal, C: grey, N: green, O: red. Disordered TEAH ligands were omitted for clarity.

3.2.2 The host-guest compound $(TEAH)_4Na_2[Mo_{36}O_{112}(H_2O)_{14}(TEAH)_2]\cdot 28H_2O$

In contrast to compound **1**, the assembly of TEAH-ligand-supported {Mo_{36}} clusters can also be achieved by a straight-forward self-assembly process starting from sodium molybdate as a precursor. This process at pH 1.2 results in an almost immediate crystallisation of compound **2**, $(TEAH)_4Na_2[Mo_{36}O_{112}(H_2O)_{14}(TEAH)_2]\cdot 28H_2O$ (= $(TEAH)_4$**2a**$\cdot 28H_2O$). The polyoxometalate anion **2a** is structurally very similar to compound **1a**, however, analysis of the coordination behaviour of the organic ligand TEAH reveals distinct differences. As demonstrated in **1a,** the cluster anion **2a** can incorporate two TEAH ligands *via* coordination through the hydroxyl oxygen donor. In **2a**, the TEAH cations coordinate closer to the equatorial cluster cavity, resulting in a more central arrangement around the cluster framework, see Figure 27. However, the major difference to cluster **1a** is the coordination of two sodium cations inside each of the two independent binding sites described above. In this host-guest assembly which can be rationalised as $Na_2\subset${Mo_{36}}, the sodium cations are bound to the cluster surface by

forming three Na-O-Mo coordination bonds to terminal Mo=O oxygen ligands. Two medium range Na-O interactions feature average Na-O distances of *ca.* 2.45 Å, while the third Na-O bond is distinctly longer (d_{Na-O} = 2.748 Å) and as a result the sodium is displaced towards one {Mo_{17}} subunit. The coordination motif formed by the three terminal oxygen ligands can geometrically be described as a *mer*-arrangement of these oxygens and is a direct result of their *syn*-planar geometrical relation within the cluster framework, see Figure 27. In other words, these three terminal oxygen atoms form an ideal pre-designed binding site for the sodium atom and allow selective binding of sodium cations. The coordination sphere of the distorted octahedron around each sodium cation is completed by three additional water ligands which feature two medium range (d_{Na-O} ~2.35 Å) and one long range Na-O bonding interaction of d_{Na-O} = 2.698 Å. The intriguing elongation of one Na-(OH_2) bonding distance is a caused by the location of this water ligand inside the cluster cavity. The water molecule can establish an extensive hydrogen bonding network which results in the net force vector pointing away from the Na-O bond and thus results in an increased Na-O distance, see Figure 28. A long-range attractive interaction is observed between the sodium centre and a μ_2-oxygen atom which further stabilises the cation inside the polyoxometalate binding pocket. However, the relatively large distance (d_{Na-O} = 3.022 Å) suggests only weak attractive interactions.

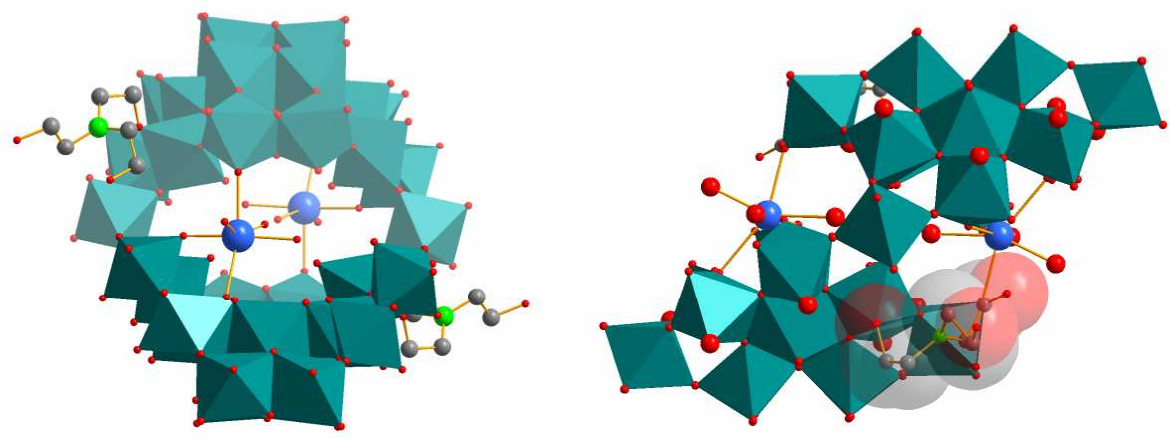

Figure 27: Front view (left) and side view (right) of the cluster anion **2a**, $Na_2[Mo_{36}O_{112}(H_2O)_{14}(TEAH)_2]^{4-}$. The two Na^+ cations inside the open cluster shell are illustrated as light blue spheres. The ligands reside close to the central belt of the cluster, above and below the equatorial plane. [MoO_6] octahedra: teal, O: red spheres, C: dark grey, N: green. Water ligands are illustrated as large red spheres.

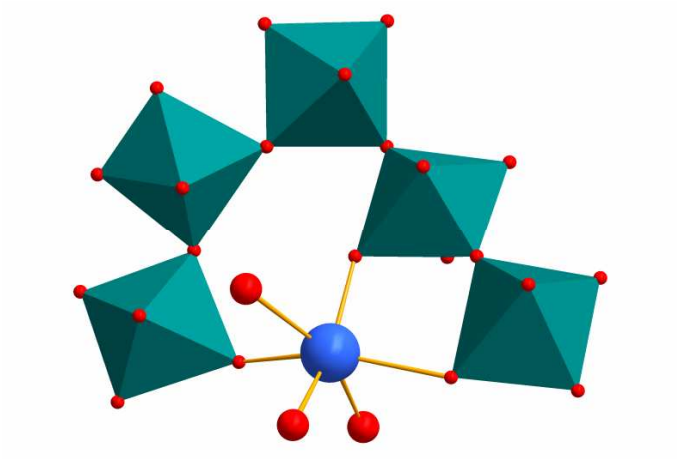

Figure 28: Detailed representation of the coordination environment of the sodium cations, highlighting the *mer*-arrangement of the three water ligands and the three terminal oxygen ligands respectively. Note that the three terminal oxygens form a pre-assembled rigid binding site governed by their location in the cluster framework. [MoO_6] octahedra: teal, O: red spheres, C: dark grey, N: green. Water ligands are illustrated as large red spheres.

In the crystal lattice, the anions **2a** are densely packed in an ABAB fashion which allows the formation of close contacts between neighbouring clusters. However, in opposite to the TEAH-mediated inter-cluster hydrogen-bonding in **1**, this close packing in **2** is a direct result of hydrogen-bonding between the water ligands on the cluster framework and oxygen sites on adjacent {Mo_{36}} clusters. As a result, very close contacts between the cluster surfaces are established with a minimum distance of 2.739 Å (O13-O21). This supramolecular arrangement consequently results in the formation of a hydrogen-bonded, 1D infinite chain which propagates along the crystallographic *a*-axis, see Figure 29.

Notably, the organic ligands in compound **2** do not act as linkers but as "spacer" units which inhibit further interactions of the cluster anion and thus effectively limit framework growth to one dimension, see Figure 29. The resulting chain structure is further reinforced by a network of water molecules which are located between neighbouring clusters within the chains. They stabilise the supramolecular assembly by forming hydrogen bonds between two adjacent clusters and thus bridge distances which are too large to support direct cluster-to-cluster hydrogen bonds.

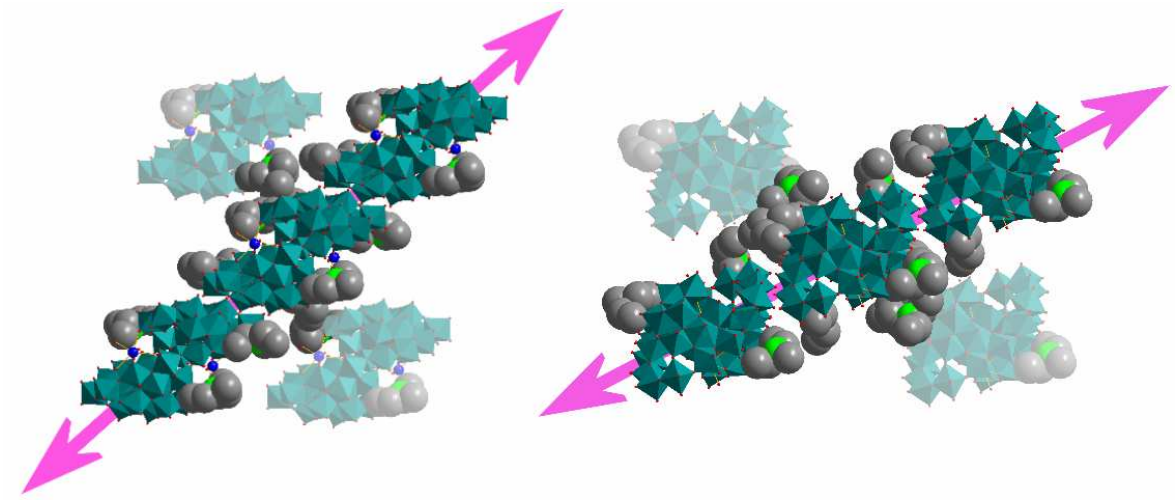

Figure 29: Illustration of the hydrogen-bonded {Mo_{36}} chains in **2**. View along the crystallographic *b*-axis (left) and *c*-axis (right) reveal the close contacts between the cluster anions **2a**. The spacer-effect of the coordinated TEAH ligands is emphasised by space-filling representation of the organic ligands. The hydrogen-bonded chain propagation is highlighted by magenta arrows. {Mo_{36}}: teal polyhedra, O: red, C: grey, N: green, Na: blue. Solvent water molecules and TEAH counterions are omitted for clarity.

The organo-modification of the cluster anions **1a** and **2a** and the resulting effects on supramolecular packing is an intriguing opportunity for the designed engineering of building block properties. Structural comparison of the TEAH-substituted coordination sites in both anions with the unsubstituted parent compound $[Mo_{36}O_{112}(H_2O)_{18}]^{8-}$[88-90] reveals that that in the parent anion these exchangeable positions are always occupied by a weakly bound water ligand ($d_{Mo\text{-}O}$ ~2.3 – 2.4 Å). This structural feature thus allows the fast exchange of the ligand and facilitates substitution of the labile water molecule by the organic TEAH ligand. However, the different binding sites observed in the two cluster anions **1a** and **2a** in combination with the presence of coordinating sodium cations in the case of **2a** require the detailed study of these systems by Density Functional Theory (DFT) computational methods (see section 5.3.3 for details).

In order to explore if the positioning of the two TEAH ligands on the {Mo_{36}} anions is controlled by the coordination of Na^+ cations or whether the coordination sites result from electronic effects intrinsic to the POM framework, DFT calculations on both {Mo_{36}} cluster anions were performed to calculate charge densities. As the role of the sodium cation is limited mostly to charge polarisation, a set of arguments was created based on charge distribution effects. The first aim was to establish whether the actual coordination sites of the sodium cations in **2a** are determined by the location of the TEAH ligand.

However, calculations on **2a** and on **1a** with the $[Na(H_2O)_3]^+$ group removed clearly indicate that the same total charge is observed for the three terminal oxygen ligands which eventually bind the Na^+, regardless of the site of the TEAH coordination. Although the Na^+ cation could also occupy other positions in the interior coordination pockets, all of these sets yield a decreased total charge and thus a decreased electrostatic binding energy, rendering the Na^+ position observed in anion **2a** the local energetic minimum. Further calculations were undertaken to establish the factors which control the binding site of the TEAH ligands in the two anions **1a** and **2a**. The TEAH ligands were thus replaced by water molecules and yielded charge distributions for the molybdenum centres which indicate that the coordination sites of the organic ligands are indeed subject to charge variations. Out of all Mo positions to which water ligands can coordinate, the Mo position to which TEAH binds in **1a** is found to be most electrophilic with a charge of +0.465 in {**1a**+2H_2O}, compared to charges in the range of +0.338 to +0.391 for the remaining Mo(OH_2) positions. For {**2a**+2H_2O}, the spread of Mo charges follows a similar but less pronounced trend; the TEAH-binding Mo centre features a charge of +0.402 compared to charges ranging from +0.339 to +0.369 for the remaining Mo positions that are available for an H_2O-to-TEAH exchange. In summary, the coordination modes of the TEAH ligands in **1a** and **2a** can be understood and predicted on the basis of the electronic structure and charge distribution of the cluster anions. This study further illustrates the effects of organic linking moieties, which can act as stabilising bridging ligands and result in a supramolecular assembly (**1**) based on polyoxometalate clusters. On the other hand, the application of organic TEAH ligands as spacing ligands in **2** highlights their ability to "isolate" POM units and thus restrict structural growth to one dimension.

It has already been reported in the literature that the non-substituted cluster anion, $[Mo_{36}O_{112}(H_2O)_{18}]^{8-}$ can be employed as an inorganic building block for the assembly of a microporous rigid framework structure.[167] The assembly of the cluster anions using diprotonated 4,4'-bipyridine as organic counterions results in the formation of a framework with accessible pores of *ca.* 7 x 5 Å. It was further demonstrated that the solvent water molecules can be desorbed and re-adsorbed without loss of crystallinity. In conclusion a similar approach using organo-substituted {Mo_{36}} clusters might allow the formation of a more sophisticated framework with tuneable pore sizes.

3.3 A family of inorganic {W_{36}} host-guest compounds

3.3.1 The archetypal isopolytungstate K⊂{W_{36}}[96]

As demonstrated above, the use of coordinating cations such as TEAH can result in the formation of novel polyoxometalate host-guest systems with the capability of incorporating inorganic cations. While studying the effect of TEAH in a tungstate-based reaction system, Cronin *et al.* reported the formation of a ring-shaped {W_{36}} cluster, the largest isopolyoxotungstate observed thus far.[96] The cluster shows remarkable similarities to organic crown-ether-type structures and can bind a selection of alkali and alkali earth metals and furthermore forms organic-inorganic hybrid host guest systems. The common structural motif within this family of host-guest complexes is a ring-shaped {W_{36}} isopolyoxotungstate. The structural features of this cluster will be discussed in detail using the archetypal compound **3**, $(TEAH)_9Na_2[(H_2O_4)K\subset[H_{12}W_{36}O_{120}]]\cdot 17H_2O$ (=$(TEAH)_9Na_2[(H_2O_4)K\subset$**3a**$]\cdot 17H_2O$) as an example.[96]

The polyoxotungstate cluster **3a** comprises 36 tungsten centers in oxidation state +VI, which are all coordinated octahedrally by six oxygen ligands. Detailed crystallographic studies reveal that the cluster anion is of approximate C_{3v} symmetry and can be separated into two types of building blocks. Formally, the {W_{36}} framework is assembled from three {W_{11}} units which are linked by three octahedral bridging {W_1} fragments, so that the ring-like structure can be rationalised as {W_{36}} = {W_{11}}$_3${W_1}$_3$.

The spatial arrangement of the three bulky {W_{11}} units results in the formation of a central cavity which contains a single potassium cation. Detailed structural analysis reveals that the K^+ coordination environment is created by a {W_6O_6} assembly with six terminal W=O binding sites pointing into the cluster cavity, see Figure 30.

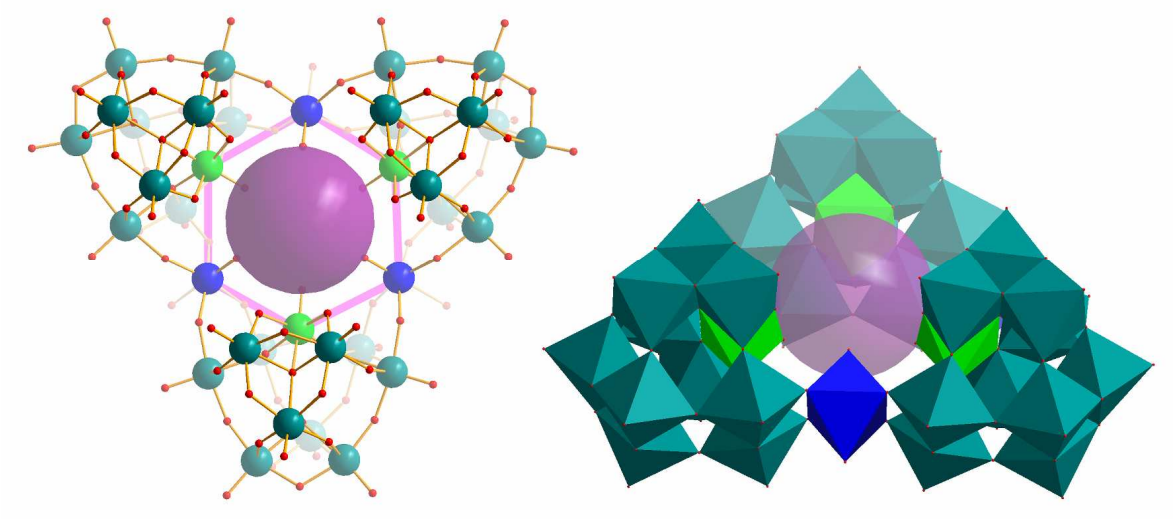

Figure 30: Top view (left) and side view (right) of the ring-shaped host guest complex **3a**, $K\subset[H_{12}W_{36}O_{120}]^{11-}$. The ball-and-stick illustration (left) emphasises the connectivity within the cluster and its assembly from three $\{W_{11}\}$ units (teal) and three $\{W_1\}$ linkers (blue). The potassium cation (purple) is shown in space-filling representation. The six-membered $\{W_6O_6\}$ coordination belt is highlighted by a magenta hexagon.

The coordination environment of the central K^+ cation within the cluster anion is formed by two sets of three terminal oxygen donors extending away from the cluster framework into the central cavity. Three $W{=}O_t$ coordination sites are provided by the set of three $\{W_1\}$ linkers (highlighted as blue polyhedra in Figure 30) which connect two adjacent $\{W_{11}\}$ fragments *via* edge-sharing modes. The remaining three oxygen ligands are located on the apical positions of the $\{W_{11}\}$ subunits and point towards the centre of the cavity (highlighted as green polyhedra in Figure 30).

Detailed analysis of the location of the potassium cation shows that it is virtually centered between the six oxygen donors with uniform bond lengths of $d_{K\text{-}O}$ ~2.75-2.85 Å. However, the potassium cation is displaced to one side of the equatorial plane and can thus coordinate three additional water molecules in this coordination hemisphere ($d_{K\text{-}OH2}$ ~3.01 Å). The opposite, more shielded coordination hemisphere can only bind one water molecule, see Figure 31.

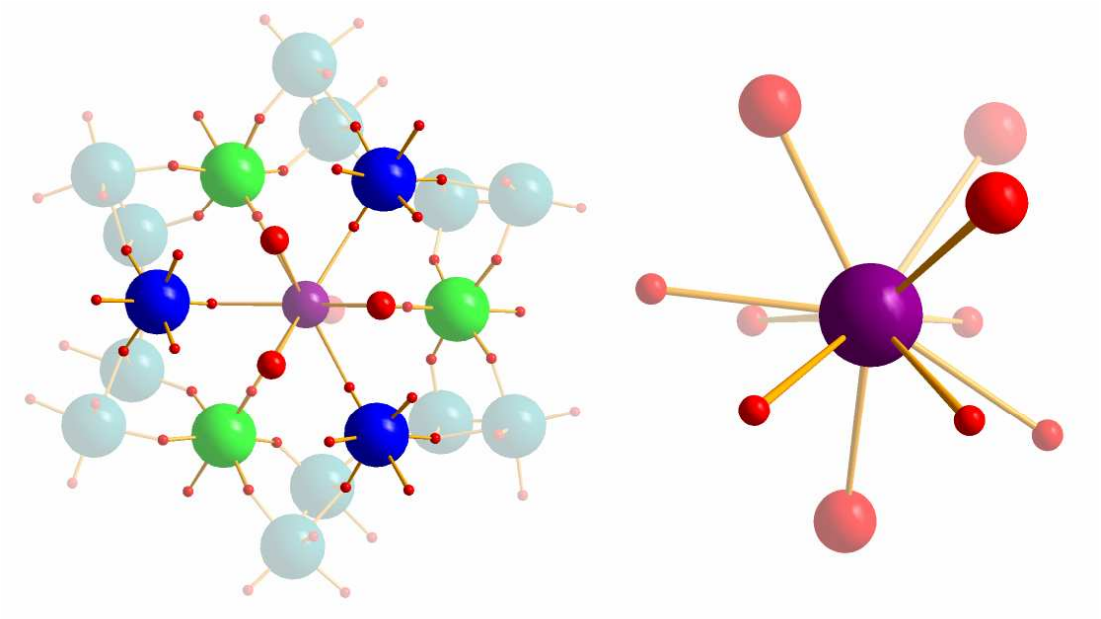

Figure 31: Illustration of the coordination environment of the central potassium ion (left) and detailed illustration of the different types of oxygen and water ligands (right). The potassium cation (purple sphere) in **3a** is coordinated by six terminal oxo ligands (small red spheres) which are located at the $\{W_{11}\}$ subunit (blue) and at the $\{W_1\}$ linker (green). The K^+ is displaced slightly above the equatorial plane formed by the six oxygens. As a result, three water molecules (large red spheres) can access the coordination shell of the potassium cation from above, where only one water molecule can coordinate from below, due to steric hindrance.

Structural analysis of the tungsten-oxide framework of the $\{W_{11}\}$ subunit reveals that the fragment is identical to the cluster shell of ψ-metatungstate, $[H_4W_{11}O_{38}]^{6-}$ (see section 1.4.4.2). The structure can be described as a combination of the well-known $[W_3O_{13}]$ triad with a $[W_4O_{16}]$ fragment in butterfly configuration which are connected by two dioctahedral $\{W_2\}$ linkers so that the whole framework can be rationalised as a set of three subunits: $\{W_{11}\} = \{W_3\}\{W_4\}\{W_2\}_2$.

Notably this $\{W_{11}\}$ can be regarded as a functional building block in the assembly of $\{W_{36}\}$-type molecular hosts. This is because the framework geometry of the $\{W_{11}\}$ cluster results in the facile accessibility of one terminal W=O site which acts as a preferred binding site for the potassium cation as illustrated in **3a**. In addition, two peripheral terminal oxygen ligands can engage in edge-sharing binding modes to $\{W_1\}$ bridges and thus result in the linking of the $\{W_{11}\}$ units into the trigonal ring-shaped $\{W_{36}\}$ cluster, see Figure 32.

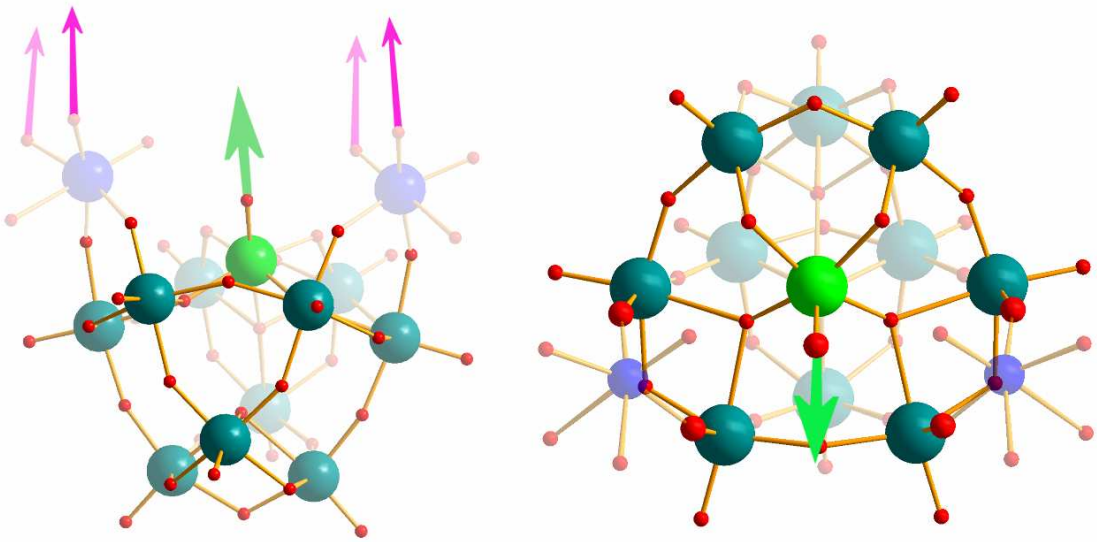

Figure 32: Illustration of the binding site and connectivity of the $\{W_{11}\}$ fragment ψ-metatungstate $[H_2W_{11}O_{38}]^{8-}$. The side view (left) illustrates the presence of one central coordination site (green) and two framework growth sites which are linked to two $\{W_1\}$ bridging units. These allow connection to adjacent $\{W_{11}\}$ fragments, emphasised by magenta arrows. The front-view (right) highlights the location of the potassium coordination site (green) in the center of the cluster with two peripheral sets of framework growth sites connecting to $\{W_1\}$ units (blue). W: teal, O: red.

The $\{W_{36}\}$ cluster incorporates 12 protons which are distributed over the $\{W_{11}\}$ and $\{W_1\}$ units. Detailed investigation of the W-O bond lengths in combination with bond valence sum (BVS) calculations can provide insight as to where the protons are located. Each $\{W_1\}$ linking octahedron features three distinct sets of W-O bonds. The shortest bond is the inward-pointing $W{=}O_t$ double bond which acts as binding site for the central guest cation. In comparison with typical non-coordination $W{=}O_t$ bonds (~ 1.70 Å), the coordinative interaction with the potassium centre is reflected by a slight elongation of the W-O distance and results in an average bond length of $d_{W\text{-}O}$ = 1.73 Å owing to attractive interactions with the K^+ cation. The four bridging μ_2-oxygen ligands which act as connecting nodes with two adjacent $\{W_{11}\}$ subunits feature longer tungsten-oxo bond lengths of 1.86 – 1.97 Å which reflects their bridging character. The terminal W-O bond which points away from the central cavity is distinctly elongated ($d_{W\text{-}O}$ = 2.29 – 2.35 Å) and bond valence sum (BVS) calculations clearly indicate that these positions are occupied by water ligands. In addition, analogous calculations show the presence of two protons in the internal cavity of every $\{W_{11}\}$ unit (see section 1.4.4.2). With regards to the 12-fold protonation, the cluster can thus be formulated as $(H_2O)_4K{\subset}\{H_2W_{11}\}_3\{H_2W_1\}_3$ .The supramolecular hydrogen-bonding effects of the protonated TEAH counter ions can be illustrated by detailed analysis of the crystal lattice of **3**. The cluster anions adopt an

ABAB-type layered structure in which the planes of the cluster ions are tilted at an angle of 79.2 °. The cluster anions are linked by TEAH cations which stabilise the lattice by a combination of attractive Coulomb electrostatic interactions and by an extensive network of hydrogen-bonds. It is this combination of attractive forces which allows the TEAH molecules to assemble the cluster anions into a supramolecular framework which is further supported by a multitude of hydrogen-bond interactions between cluster anions, TEAH cations and solvent water molecules.

An additional linking motif is based on the coordination of a sodium cation to the cluster surface. The sodium establishes one coordinative W-O-Na bond to a terminal oxygen ligand of a $\{W_{11}\}$ unit ($d_{Na\text{-}O}$ = 2.433 Å) and is further coordinated by two TEAH ligands; one TEAH cation binds through one pendant hydroxyl group whereas the second organic ligand acts as a chelating agent and forms two *cis*-bonds to the sodium centre *via* two hydroxyl groups, see Figure 33, right. The Na-O bond lengths vary between 2.34 and 2.49 Å, most likely due to steric demands based on the ligand geometry. The octahedral coordination shell of the sodium centre is completed by two water ligands with Na-O distances of 2.359 Å and 2.432 Å which undergo further hydrogen bonding to stabilise the molecular assembly.

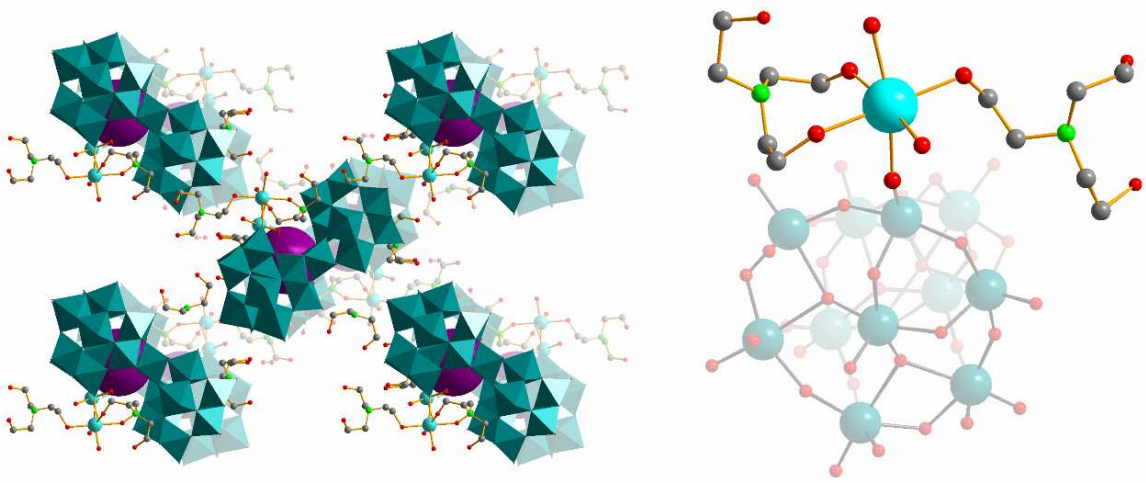

Figure 33: Illustration of the crystal lattice of **3** along the crystallographic *b*-axis (left) and illustration of the sodium coordination environment (right). The crystal lattice features an ABAB-type packing mode and shows the sodium cations (light blue spheres) which coordinate two TEAH ligands and act as hydrogen bonded linkers to adjacent cluster anions (teal polyhedral representation). The detailed view (right) highlights the diverse coordination environment around the sodium centre which binds to the cluster anion through one Na-O-W bond. In addition, two TEAH ligands are coordinated through one or two pendant hydroxyl groups respectively. The octahedral coordination sphere is filled by two water molecules. Colour scheme: $\{W_{36}\}$: teal, C: grey, O: red, N: green, K: purple.

The importance of the central potassium ion in the formation of the cluster anion can be illustrated on the basis of the synthesis of compound **3**. The material was initially obtained as a crystalline reaction product from an acidified solution of sodium tungstate under "potassium-free" conditions. A very low yield and the long crystallisation period of several weeks suggested a low solution concentration of the cluster. However, deliberate addition of potassium chloride under otherwise similar synthetic conditions resulted in the crystallisation of pure product **3** in high yield within 48 h.

These results in combination with the observation that the guest-free host complex could not be isolated led to the hypothesis that the potassium ion acts as a template which "pre-assembles" the cluster in solution and thus allows isolation of this material. The observation of this templating effect of potassium cations sparked further research to investigate whether other alkali or earth alkali metals can act as templates and central guest ions and thus allow the modification and design of a whole family of related cluster compounds.

3.3.2 Host-guest chemistry of $\{W_{36}\}$: The inorganic approach

The initial results discussed above strongly suggested that the $\{W_{36}\}$ cluster shows similar properties to a well-known family of organic host compounds, the crown-ethers or coronands.[1] This class of materials has been extensively studied because they strongly coordinate cations and thus can act as cation receptors. Crown ethers in particular are an extremely versatile family of materials owing to their selective binding of metal cations in a cavity that can be tailored to match the ionic radius of the prospective guest. As already discussed, the $\{W_{36}\}$ isopolytungstate features a similar oxygen environment as the 18-crown-6 coronand (= 18-C-6) and also shows the ability to capture potassium ions from aqueous solution, even though the oxygen atoms that form the central cavity are terminal oxo ligands rather than the ether moieties found in organic crown ethers.

Extension of this work was based on the fact that the formation of the $\{W_{36}\}$ cluster crucially depends on the presence of metal cations which can template its formation as discussed above. It is interesting to note that the $\{W_{36}\}$ cluster could not be isolated under strictly potassium free conditions in the presence of Na^+, even if the concentration of Na^+ in the reaction mixture was increased considerably. As a result, all further experiments

were conducted in plastic vessels to avoid sequestration of potassium from the glassware and a range of alkali and alkali earth metal salts were employed as potential templates. The cluster formation was studied as a function of pH, concentration of tungstate and TEAH and total ionic strength. The synthetic procedure involved adjusting an aqueous solution of sodium tungstate and triethanolamine hydrochloride to a certain pH with HCl, followed by a short period of heating, addition of the metal salts to the reaction mixture and setup for crystallisation. In addition to the use of plastic vessels, special attention was focussed on preventing possible contamination of the reactions with potassium sources (e.g. from the reagents, pH-probe *etc.*). As a further internal control, samples of the reaction mixture without added metal salt were retained but never led to the formation of the $\{W_{36}\}$ cluster, thus indicating the effective exclustion of potassium sources and the resulting inhibition of the $\{W_{36}\}$ formation. Complexation experiments on the $\{W_{36}\}$ reaction systems using alkali and alkali earth cations yielded colourless needle crystals of compounds **4 - 7,** see Table 3. For Rb^+, Cs^+ and Sr^{2+}, the reaction condition with a pH of 2.2 seems to be optimal for the formation and crystallisation of the $\{W_{36}\}$ cluster. For Ba^{2+} no crystals could be obtained. However, a white dense material quickly precipitates at this pH. A different synthetic approach which involved adding the barium source to the tungstate solution at pH 1.3 and subsequent adjustment of the pH to 2.2 yielded diffraction quality crystals of the Ba^{2+} compound **7**. This suggests that a lower pH is necessary to prevent the polyoxotungstate from forming barium oxo tungstate precipitates, whereas a higher pH is required to allow crystallisation of the final product. The structures of all cluster compounds **4 – 7** were determined by single-crystal X-ray diffraction and feature isostructural cluster anions which can be rationalised as $M\subset\{W_{36}\}$ with M = Rb^+, Cs^+, Sr^{2+}, Ba^{2+}; their detailed composition is summarised in Table 3.

Table 3: Composition of the $\{W_{36}\}$ family of host-guest complexes

Compound	**Guest ion**	**Formula**
3	K^+	$(TEAH)_9Na_2[(H_2O)_4K\subset[H_{12}W_{36}O_{120}]]\cdot 17H_2O$
4	Rb^+	$(TEAH)_9Na_2[(H_2O)_4Rb\subset[H_{12}W_{36}O_{120}]]\cdot 17H_2O$
5	Cs^+	$(TEAH)_9Na_2[(H_2O)_4Cs\subset[H_{12}W_{36}O_{120}]]\cdot 15H_2O$
6	Sr^{2+}	$(TEA)(TEAH)_8Na_2[(H_2O)_4Sr\subset[H_{12}W_{36}O_{120}]]\cdot 17H_2O$
7	Ba^{2+}	$(TEA)(TEAH)_8Na_1Ba_{0.5}[(H_2O)_4Ba\subset[H_{12}W_{36}O_{120}]]\cdot 17H_2O$

All four compounds **4 - 7** are essentially isomorphous and crystallise in the same orthorhombic crystal system with space group *P*nma. The asymmetric unit contains half a $\{W_{36}\}$ cluster with a crystallographic mirror plane passing through the cluster and the central coordinated metal ions (Rb^+ to Ba^{2+}). Despite the highly disordered nature of the TEAH and sodium cations and solvent water molecules, the main structures, i.e. the cluster anion $[H_{12}W_{36}O_{120}]^{12-}$ together with the coordinated metal ions (Rb^+, Cs^+, Sr^{2+} and Ba^{2+}) are well defined, see Figure 34.

Compounds **4** Rb⊂$\{W_{36}\}$ and **6** Sr⊂$\{W_{36}\}$ incorporate Rb^+ and Sr^{2+} in the centre of the $\{W_{36}\}$ cavity at full occupancy as determined by crystallographic analysis and flame atomic absorption spectroscopy, similar to the coordination situation reported for compound **3,** see above. The cations are coordinated by a set of six terminal oxygen ligands which can be separated into two distinct groups.Three terminal oxo ligands are located on the apex of a $\{W_{11}\}$ unit so that this set of three oxygens forms a triangular arrangement resembling an equilateral triangle. A similar arrangement is exhibited by the second group of three terminal W=O coordination sites which are located on the $\{W_1\}$ bridging units and point towards the centre of the cluster cavity, see Figure 34.

However, detailed crystallographic studies suggested a different situation in compound **5**, Cs⊂$\{W_{36}\}$. Refinement of the occupancy factors strongly suggest that the Cs^+ site at the centre of the $\{W_{36}\}$ cavity is not fully occupied and additional electron density that can be assigned as partially occupied Cs^+ ion positions was found between two $\{W_{11}\}$ cluster subunits, see Figure 34. These positions can only be assigned to partially occupied Cs centres according to the bond distances to neighbouring oxygen atoms. Further evidence is provided by flame atomic absorption spectroscopy which suggests the presence of one Cs ion per cluster formula unit.

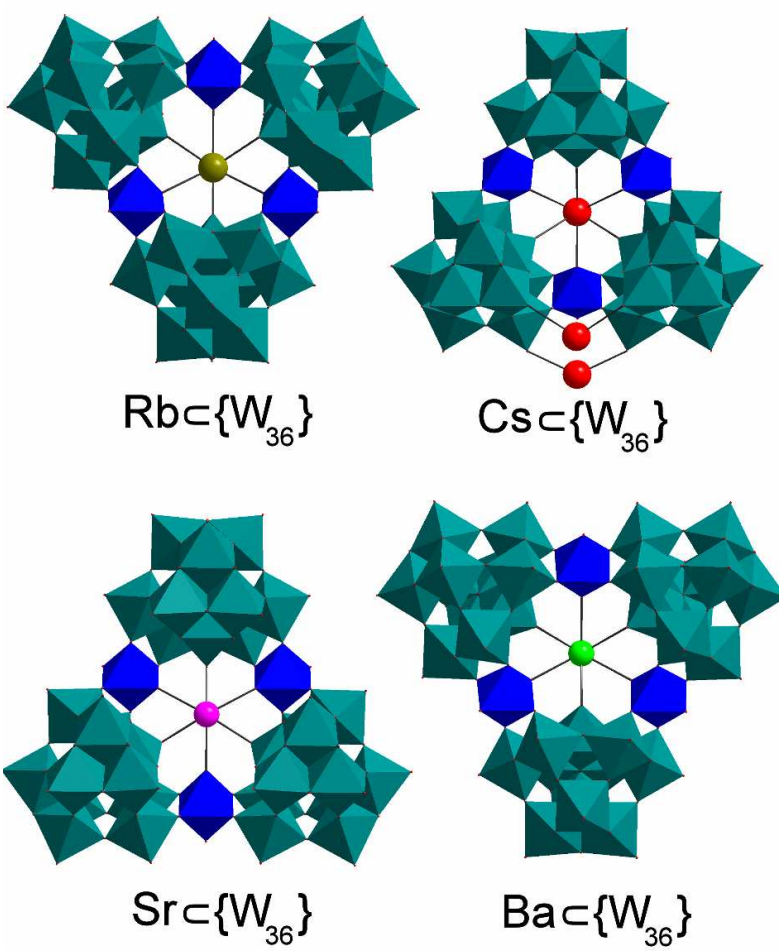

Figure 34: Polyhedral representation of the cluster anions Rb⊂{W_{36}} **4a** (top left), Cs⊂{W_{36}} **5a** (top right), Sr⊂{W_{36}} **6a**, and Ba⊂{W_{36}} **7a**. Structural comparison shows that the polyoxometalate frameworks are virtually identical and that the cations occupy the same positions within each structure. Notably, in **5a** additional Cs^+ sites can be detected in two peripheral positions between two adjacent {W_{11}} subunits. The {W_{11}} subunits are illustrated as teal polyhedra, the linking {W_1} units as blue octahedra.

The arrangement of the molecular {W_{36}} cluster units in the crystal lattice of compounds **4**, **5** and **6** is virtually identical to the arrangement of the archetypal compound **3**. An ABAB layer arrangement is formed with additional sodium ions coordinating to the cluster periphery and subsequently linking the structure into a hydrogen-bonded ionic crystalline network of non-connected discrete {W_{36}} cluster units.

The detailed structural analysis of the single-crystal XRD data of compound **7**, Ba⊂{W_{36}} reveals an intriguing framework feature. In addition to the central Ba^{2+} cation which acts as a guest in the {W_{36}} cavity, another Ba^{2+} site can be located on the periphery of the {W_{36}} cluster. The cation acts as a linker between two adjacent {W_{36}} units by coordinating to two terminal oxygen ligands, one on each of the clusters, through W-O-Ba bonds with

barium-oxo bond lengths of *ca.* 2.90 Å. In addition, the metal cation coordinates a TEAH ligand through one pendant hydroxyl group with a Ba-O distance of 2.83 Å. As a result of this coordination mode, the additional barium cation links the $\{W_{36}\}$ clusters into an infinite 3D framework in the solid state, see Figure 35. The 3D framework nature of compound **7** is reflected by the physical properties of the material which differ from the remaining compounds in the $\{W_{36}\}$ family. In contrast to compounds **3, 4, 5** and **6**, the infinite framework **7** is poorly soluble in water. This discrepancy is most evident by comparison with **5**, $Cs\subset\{W_{36}\}$ which is the most soluble of the set of host guest complexes. The barium-linked 3D framework **7** shows only half the solubility in aqueous solutions. The formation of this framework might also be the reason for the altered synthesis behaviour discussed above, as the precipitation at the original pH of 2.2 is most likely due to the formation of an infinite polymeric barium tungsten oxide.

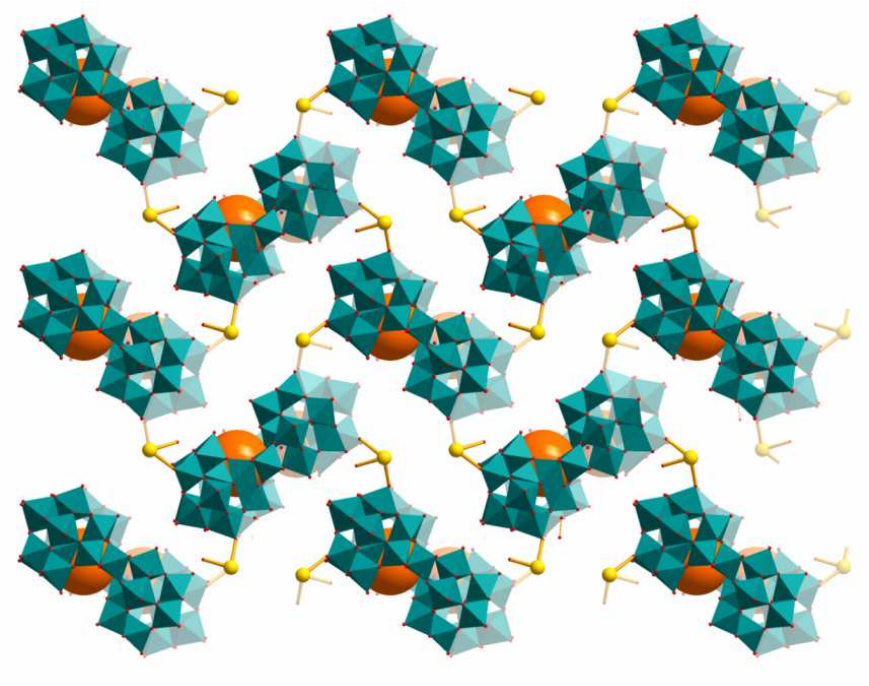

Figure 35: Illustration of the 3D infinite framework structure of compound **7**, $Ba\subset\{W_{36}\}$ along the crystallographic *b*-axis. The $\{W_{36}\}$ clusters are illustrated as teal polyhedra, the central Ba^{2+} cations are highlighted as large orange spheres. The linking Ba^{2+} cations are illustrated as yellow spheres and demonstrate the connectivity between the polytungstate clusters which results in the formation of an infinite 3D network. Comparison with Figure 33 highlights that the arrangement of the $\{W_{36}\}$ cluster units relative to each other has not changed. The inter-network spaces are filled with hydrogen-bonded TEAH cations and solvent water molecules which have been omitted for clarity.

The comparison of this 3D framework in **7** with compounds **3**, **4**, **5** and **6** reveals that the overall arrangement of the $\{W_{36}\}$ clusters is almost identical. In **7** the ABAB-type arrangement of $\{W_{36}\}$ units is retained and the additional Ba^{2+} cations are large enough to fit exactly in between the cluster layers and can thus act not only as guest molecules in the central cluster cavity but also as linkers between neighbouring clusters *via* the formation of two Ba-O coordination. It is therefore not unexpected that the angle between the cluster layers remains almost unchanged and is found to be 78.8 ° in the 3D framework **7**, $Ba\subset\{W_{36}\}$compared with 79.2 ° in the archetypal compound **3**, $K\subset\{W_{36}\}$ which consists of discrete $\{W_{36}\}$ units, see Figure 35.

The displacement of the guest cations within the central binding cavity was investigated as a function of their ionic radii. The equatorial plane defined by the six coordinating terminal oxo ligands was used as a reference point. These displacements were elucidated by detailed structural analysis of the crystallographic data using the distances between the corresponding central ions and the six surrounding oxygen atoms from the W=O ligands of the $\{W_{36}\}$ unit. These distances are summarised in Table 4 and compared with the average displacement values for the most similar crown ether, 18-C-6. It was observed that the degree of displacement above or below the equatorial plane reflects the increasing steric restraints caused by increasing ionic radii of the cations.

Table 4: Metal-oxygen distances of the central cations M in the binding pocket of $\{W_{36}\}$

M^{n+}	r_{ionic} / Å	$d_{M-O,\min}$ / Å	$d_{M-O,\max}$ / Å	$\bar{d}_{M-O}$ / Å	$d_{M-Centre}$ / Å ($\{W_{36}\}$)	$d_{M-Centre}$ / Å (18-C-6)
K^+(**3**)	1.59	2.748	2.801	2.795	0.70	0.00
Rb^+(**4**)	1.61	2.798	2.938	2.876	0.84	0.93
Cs^+(**5**)	1.74	2.839	3.436	3.150	1.61	1.47
Sr^{2+}(**6**)	1.31	2.614	2.788	2.703	0.53	0.00
Ba^{2+}(**7**)	1.47	2.716	2.863	2.809	0.73	0.00

Table 4 illustrates that the metal-oxygen distances d_{M-O} between the respective central guest cation and the oxygen coordination sites of the $\{W_{36}\}$ host complex increase with increasing ionic radii. This is not unexpected and indeed similar effects have been

observed and reported for the 18-C-6 crown ether. However, whilst the difference between the minimum and maximum metal-oxygen distances is relatively small in compounds **3**, **4**, **6** and **7**, the situation for compound **5**, Cs⊂{W_{36}} requires further analysis. Comparison of the coordination environment around the Cs^+ centre with the situation found for K^+, Rb^+, Sr^{2+} and Ba^{2+} illustrates the different binding mode adopted by the large caesium ion.

The Cs^+ cation forms three short coordinative bonds to the W=O sites located on the {W_{11}} subunits (*ca.* 2.84 Å) whereas the interactions to the remaining three terminal oxygen ligands on the {W_1} bridges are considerably elongated, with Cs-O distances of *ca.* 3.44 Å. As a result, the Cs^+ cation is displaced from the center of the {W_{36}} complexation plane by $d_{Cs\text{-}centre}$ = 1.61 Å which is noticeably larger than any other cation displacement distance, see Table 4.

A similar trend is also observed in the organic counterpart, the 18-C-6 crown ether, which shows comparable displacement in the case of Cs^+. As a result, these comparisons show that the large Cs^+ cation is too bulky to be accommodated in the centre of the {W_{36}} coordination pocket and thus has to adopt a sterically preferred coordination on one side of the cluster which results in the formation of two sets of coordination bonds.

As illustrated in Table 4, the observed average metal–oxygen distances in the {W_{36}} host–guest complexes $\bar{d}_{M-O}$ are comparable to the values obtained for the corresponding 18-crown-6 complexes. The metal cations in the {W_{36}}-based materials show different distances from the equatorial plane of the cluster framework which reflect the increasing ionic radii and thus the less optimal fit, see Figure 36. Although there are some striking similarities between the {W_{36}} system and 18-C-6, there are some features which are unique to each host-guest system and reflect the observed discrepancies in coordination behaviour. The main functional difference between the oxygen sites is the fact that the oxygens in the inorganic {W_{36}} system are terminal W=O ligands whereas in the organic 18-crown-6, the oxygens are bivalent ether functionalities. The obvious structural difference is that the six coordinating oxo ligands in the {W_{36}} cluster are not arranged in a planar fashion but form a six-membered ring in chair configuration thus creating two parallel planes of three oxygens with an inter-planar distance of *ca.* 0.5 Å. In the 18-C-6 crown ether, the oxygen coordination sites can adopt a planar conformation.

The resulting diameters of the six-membered coordination pockets are, however comparable in both the inorganic and the organic host compound. Further, the six W=O donor groups of the $\{W_{36}\}$ anion are considerably more rigid due to the robust tungsten-oxide framework unlike 18-C-6, which is much more flexible. As a result, the 18-crown-6 unit can bend to form metal complexes with small ions like Na^+, Ca^{2+}, lanthanide ions and transition metal ions. This is caused by the ability of crown ethers to distort and fold themselves around these smaller metal cations in an attempt to maximise the attractive electrostatic interactions. However, this deformation increases the geometric strain of the ligand, which makes these complexes less stable than these with metal cations of optimal spatial fit.

In contrast, the $\{W_{36}\}$ framework, due to its high rigidity, cannot adopt its structure in such a way to bind these metal cations. This is further supported by the observation that the diameter of the central cavity in the family of $\{W_{36}\}$ clusters presented here is very well defined and shows no significant differences in all compounds structurally characterised thus far. In fact, overlaying the anion structures observed in all $\{W_{36}\}$ compounds shows that the whole framework is structurally virtually unaffected by the coordination of the central cations, see Figure 36. In addition, further complexation studies also confirmed that small ions cannot be coordinated by the $\{W_{36}\}$ cluster.

Attempts to synthesise the $\{W_{36}\}$ cluster in the presence of Ca^{2+}, lanthanide ions, and first row transition metal ions were without success. In the case of lanthanide ions, the electrophilic nature of these cations appeared to result in rapid complexation with tungstate-based species leading to the formation of insoluble compounds which precipitated almost immediately.

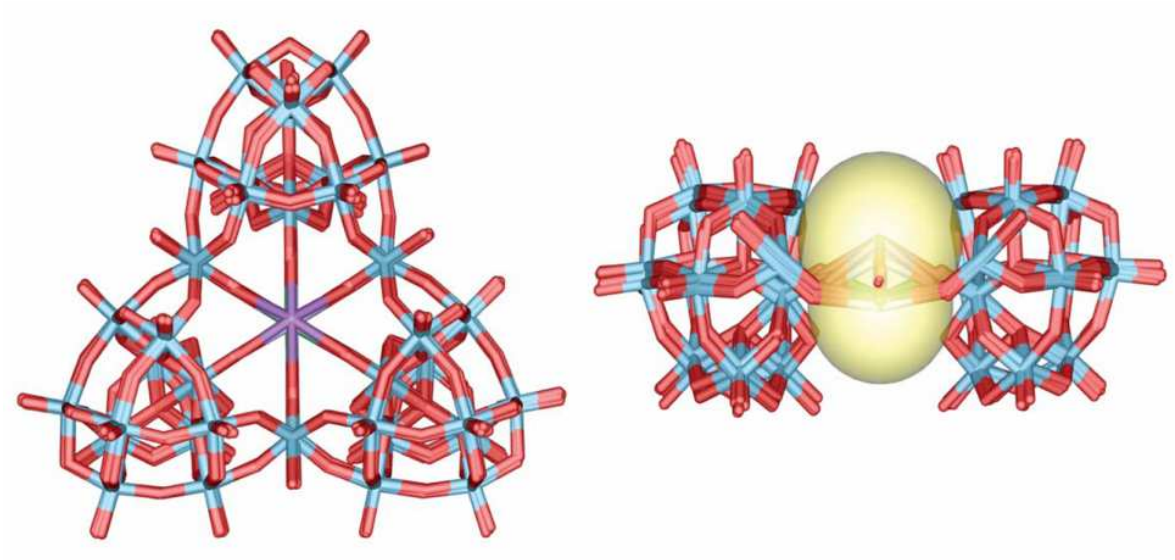

Figure 36: Overlay of the wireframe representations of the cluster anions **3a**, **4a**, **5a**, **6a** and **7a**. The top view (left) illustrates that the tungsten oxide framework structures are virtually identical in all compounds. Further it is shown that the guest cations are all horizontally centered within the coordination cavity of the $\{W_{36}\}$ cluster. The side view (right) illustrates the vertical displacement of the guest cations which are illustrated as yellow spheres. Maximum displacements are observed for Cs^+ (1.61 Å above the cluster plane) and Rb^+ (0.84 Å below the cluster plane), respectively, showing the increasing steric bulk introduced by large cations.

However, owing to the restricted number of potential alkali and alkali earth metal cations and the negative results with lanthanide and transition metals, the focus of the host-guest behaviour study of the $\{W_{36}\}$ framework was shifted towards other potential candidates, specifically small positively charged hydrogen-bond donors such as ammonium cations. This approach would allow maximum exploitation of the binding modes of the $\{W_{36}\}$ framework by combining electrostatic Coulomb attraction with hydrogen-bonding to reinforce the host-guest compound.

3.3.3 Towards organic guests: Complexation of ammonium in $NH_4\subset\{W_{36}\}$

The complexation behaviour thus far indicated that the $\{W_{36}\}$ framework can selectively bind a range of inorganic alkali and alkali earth metal cations. It is in fact well known that the ammonium cation, NH_4^+, is very similar in chemical behaviour to the potassium cation K^+ which has been successfully employed in the synthesis of the first $\{W_{36}\}$ cluster, compound **3**. Further, both cations feature very similar ionic radii which made the ammonium cation a promising candidate for complexation experiments.

Indeed, under synthetic conditions similar to those employed in previous syntheses, compound **8** was obtained with the formula $(TEAH)_9Na_2[NH_4\subset[H_{12}W_{36}O_{12}O]]\cdot 17H_2O$. The cluster anion $\{W_{36}\}$ is virtually identical to the structures discussed previously; it is made up from three $\{W_{11}\}$ subunits and three $\{W_1\}$ linkers. The cluster binds to one ammonium cation within its central cavity, however, detailed structural analysis shows that the ammonium centre is disordered over two positions so that it is located slightly above or below the main cluster plane with displacement distances of 0.97 and 0.66 Å respectively.

This distinct arrangement of the ammonium guest ions over two positions results in two different binding situations. The ammonium ion which resides 0.97 Å above the cluster plane forms two sets of N-O interactions. Three short N-O contacts ($d_{N\text{-}O}$ ~ 2.6 – 2.8 Å) are established to the triangular binding motif based on the W=O binding sites of the $\{W_{11}\}$ sub-units. The N-O distances to the $\{W_1\}$ linker oxygen donors however, are elongated to $d_{N\text{-}O}$ ~ 3.0 – 3.2 Å.

Interestingly the ammonium ion which is located 0.66 Å below the coordination plane of the $\{W_{36}\}$ anion shows a different binding behaviour where more uniform N-O distances of $d_{N\text{-}O}$ ~ 2.8 Å for the $\{W_{11}\}$-based oxygen donors and $d_{N\text{-}O}$ ~ 2.9 Å for the $\{W_1\}$ linker sites are observed.

It is most likely that this distinct complexation behaviour is a combination of attractive electrostatic interactions and the intrinsic hydrogen-bonding ability of the ammonium cations which allows them to adopt two different positions in the $\{W_{36}\}$ central cavity, both of which allow strong hydrogen-bonding interactions, see Figure 37.

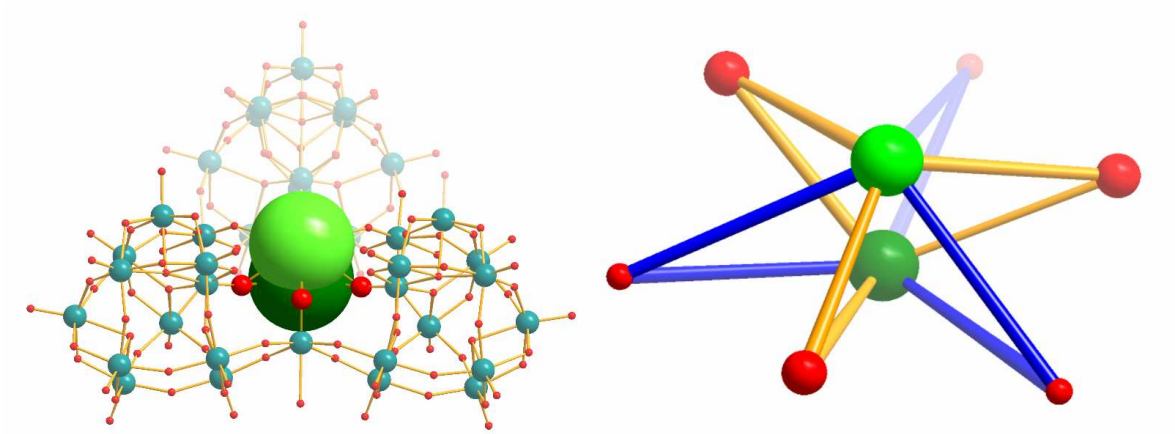

Figure 37: Illustration of the cluster anion **8a**, $NH_4 \subset \{W_{36}\}$ (left) and detailed view of the environment around the two disordered NH_4^+ positions (right). The two different locations of the ammonium cation within the cluster framework are highlighted by a light green sphere (0.97 Å above the mean binding plane made up by the six binding oxygen ligands) and a dark green sphere (0.66 Å below the mean binding plane). The detailed view on the right illustrates the two sets of N-O distances observed for both nitrogen centres (light green and dark green spheres). Long-range interactions with the $\{W_1\}$ oxygens (small red spheres) are highlighted by blue bonds, short interactions with the $\{W_{11}\}$ oxygen donors (large red spheres) are highlighted by orange bonds. NB: Each ammonium cation can establish a maximum of four hydrogen bonds. However, due to thermal activation, an average distribution over all potential sites is assumed.

The crystal lattice packing of compound **8** features the well-known ABAB-type arrangement of $\{W_{36}\}$ complexes that has already been observed for compounds **3** - **7**. The cluster anions in the lattice feature a torsion angle between the central cluster planes of *ca.* 79 ° and are supported by an extensive network of TEAH ligands and water molecules. As illustrated before, two sodium cations bind to the periphery of each cluster anion and reinforce the supramolecular framework by interacting with TEAH cations *via* hydroxyl group coordination. Comparison of all $\{W_{36}\}$-based crystal structures reveals that the influence of the guest cations on the overall arrangement is negligible. In fact compounds **3** - **8** all feature the same monoclinic crystal system with a space group of *P*nma and thus demonstrate that this arrangement is not influenced by size or charge of the guest cation.

Synthetic considerations based on the binding of ammonium ions suggested that primary organic amines might be successfully employed in an attempt to create organic-inorganic host-guest complexes based on the $\{W_{36}\}$ system.

3.3.4 Host-guest chemistry of {W_{36}}: The organic approach

The discovery that the {W_{36}} host anion can bind ammonium cations *via* electrostatic interactions and hydrogen-bonding opened the door for a new approach which would eventually allow the isolation of hybrid organic inorganic host-guest systems. The use of protonated primary amines was key to this approach as they structurally resemble the ammonium group and can thus replace this small cation in the binding pocket of the {W_{36}} cluster anion. In an attempt to accomplish this aim, protonated phenethyl amine, C_6H_5-$(CH_2)_2$-NH_3^+, (hereafter referred to as PHEN) was added to an acidified solution of sodium tungstate at pH 2.2 following the most typical preparation of the {W_{36}} system.

As discussed above, strictly potassium-free reaction conditions had to be followed to avoid any cross-contamination from glassware or other sources. Within one week, large rhombohedral crystals of compound **9** were obtained and examined using single crystal diffractometry. Structural analysis confirmed that the compound of the formula $(TEAH)_{11}[PHEN\subset[H_{12}W_{36}O_{120}]]\cdot 17H_2O$ (=$(TEAH)_{11}$**9a**$\cdot 17H_2O$) contained the {W_{36}}-type cluster anion with the PHEN ligand bound to the central recognition site made up by six terminal oxygens, see Figure 38.

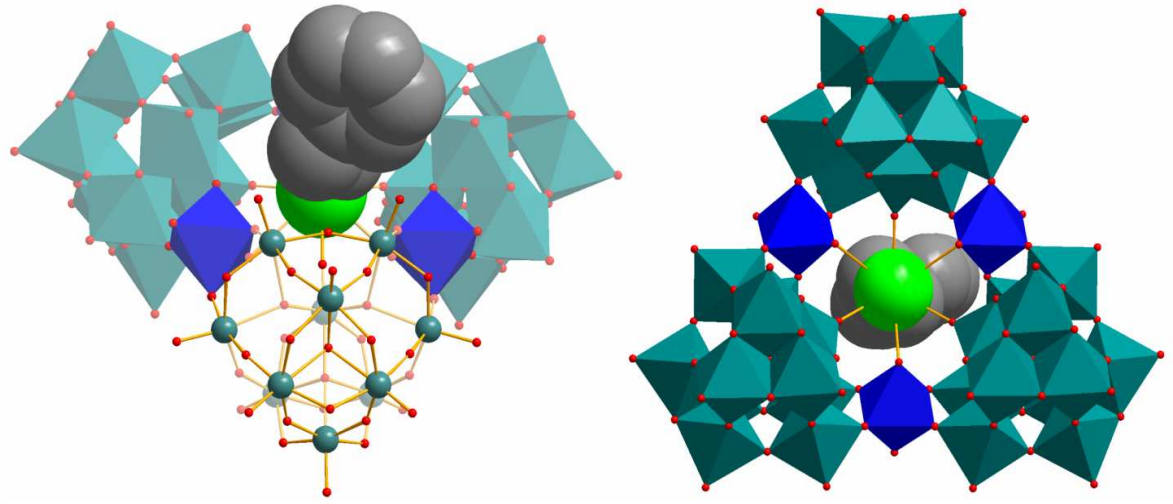

Figure 38: Side view (left) and top view (right) of the host guest complex **9a**. The side view illustrates the binding mode of the primary amine of the PHEN ligand C_6H_5-$(CH_2)_2$-NH_3^+ which interacts with the central ring of six W=O terminal oxygen sites. The top view illustrates the protruding organic substituent which includes an electron-rich phenyl ring. Colour scheme: {W_{11}}: teal, {W_1} linkers: blue, O: red, N: green, C: grey.

In contrast to the cations discussed thus far, the PHEN ligand in compound **9a** can, for steric reasons, not occupy the centre of the binding site and has to be located in one hemisphere of the cluster shell. The ligand nonetheless follows the general trend observed for bulky (Cs^+, **5a**) and hydrogen-bonding cations (NH_4^+, **8**) by forming short contacts with the three oxygen ligands located on the $\{W_{11}\}$ subunit and uniform N-O distances of *ca.* 2.77 Å are observed. In contrast, the N-O interactions to the oxygen ligands on the far side of the binding pocket which belong to the $\{W_1\}$ linking units are elongated to *ca.* 3.25 Å. This binding motif is comparable with the situation observed in compound **8a** where an ammonium centre is located in a very similar position with marginally increased N-O distances, see Figure 37.

The effect of the bulky organic substituent becomes evident when the distance between the nitrogen centre of the PHEN ligand and the mean plane formed by all six oxygen atoms is investigated. Due to the steric bulk introduced by the phenyl ring, the nitrogen atom is displaced to a larger degree from the mean complexation plane ($d_{N\text{-centre}}$ = 1.22 Å) as compared with the non-substituted ammonium ion in **8a** which featured a distance to the centre of $d_{N\text{-centre}}$ = 0.97 Å.

The supramolecular framework arrangement found in compounds **3 - 8** where the cluster anions were tilted in a layered arrangement cannot be established in compound **9** due to the bulky PHEN substituent which protrudes from the central binding pocket. Instead the clusters in compound **9** are arranged in an ABAB-type layered fashion so that the PHEN ligands of neighbouring cluster anions protrude alternatively to opposite sides, see Figure 39. This framework assembly results in an antiparallel arrangement of $\{W_{36}\}$ groups where the inter-cluster voids are filled by protonated TEAH ligands which reinforce the structure by hydrogen-bonding interactions. Further, compound **9** contains a complex network of hydrogen-bonded water molecules which interact with both the cluster anions and the TEAH ligands. Another difference from the structures discussed above is the absence of any sodium cations in compound **9** which were previously observed to interact with the peripheral oxygen environment of the $\{W_{36}\}$ shell and the TEAH ligands, thus providing additional structural stability.

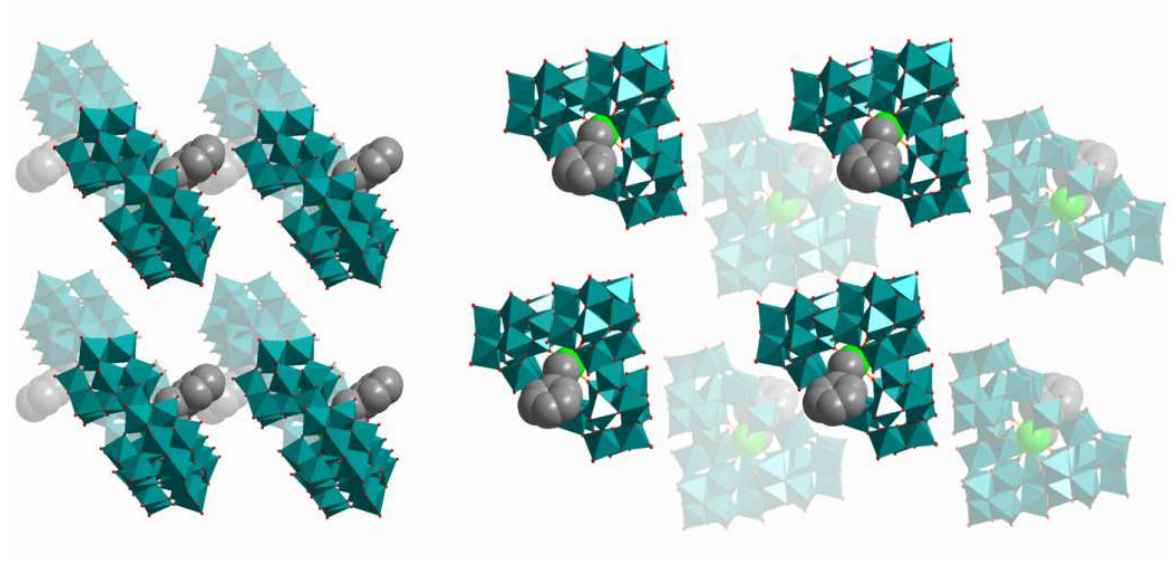

Figure 39: Illustration of the framework arrangement of **9**. The side-view (left) illustrates the protruding PHEN ligands which act as spacers between the {W_{36}} layers. The top view (right) highlights the antiparallel arrangement of the cluster units with PHEN ligands protruding in opposite directions. {W_{36}}: teal, C: grey, N: green. Water molecules and TEAH counterions are omitted for clarity.

Encouraged by the initial results obtained with the PHEN ligand in compound **9** a supramolecular design approach was chosen to investigate the feasibility of replacing the phenethyl ammonium groups with longer alkyl-chain homologues such as protonated 4-phenylbutyl amine (C_6H_5-$(CH_2)_4$-NH_3^+, hereafter referred to as 4PBA). The addition of 4PBA to the {W_{36}} reaction mixture under strictly potassium-free conditions led to the isolation of compound **10**, $(TEAH)_{11}[4PBA\subset[H_{12}W_{36}O_{120}]]\cdot 17H_2O$. Structural analysis reveals striking similarities between the host-guest anion **10a**, $[4PBA\subset[H_{12}W_{36}O_{120}]]$, and the cluster anion **9a**. The 4PBA ligand is located in the binding site of the {W_{36}} framework and is displaced towards one side of the cluster. It thus forms two sets of N-O distances and attractive interactions are established to the {W_{11}} terminal oxygen sites with average N-O distances of *ca.* 2.80 Å. In opposite, the distance between the nitrogen centre and the {W_1}-based oxygen atoms ($d_{N\text{-}O}$ ~ 3.3 Å) is larger than the sum of the van der Waals radii of N (r_{vdw} = 1.55 Å) and O (r_{vdw} = 1.52 Å) and therefore no attractive interactions are established. The displacement of the 4PBA ligand from the cluster centre is even more pronounced in **10a**, with a spatial separation of $d_{N\text{-centre}}$ = 1.32 Å (compared to 1.22 Å for PHEN and 0.97 Å for NH_4^+) which is most likely related to the higher steric bulk of the 4PBA ligand, see Figure 40.

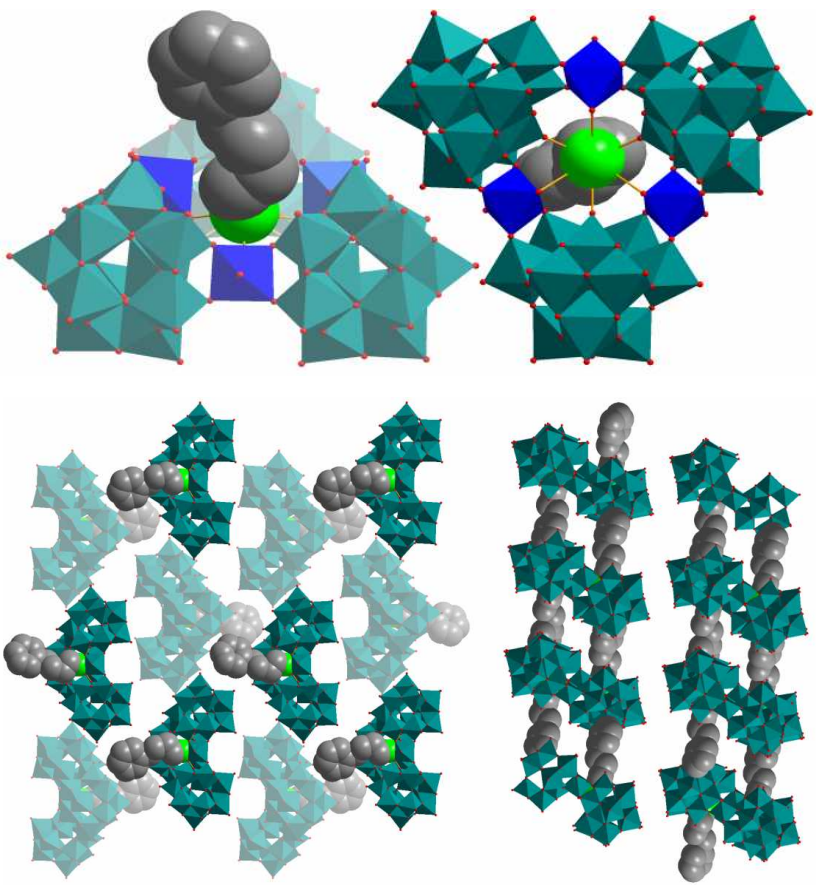

Figure 40: Side view (top left) and top view (top right) of the $\{W_{36}\}$-based cluster anion **10a**. The location of the organic ligand 4-phenylbutyl amine (4PBA) in the centre of the binding pocket is illustrated. Detailed structural analysis shows that the ligand is displaced so that the nitrogen centre is located above the mean binding plane of the $\{W_{36}\}$ host. The top view shows that the amino group is located centrally within the equatorial binding plane and forms hydrogen-bonds to the oxygen-donors. View of the crystal lattice of **10** along the crystallographic *a*-axis (bottom left) and *b*-axis (bottom right). The protruding 4PBA ligands are highlighted by a space-filling representation to emphasise their supramolecular effect on the crystal packing. By alternatively pointing towards the same inter-cluster voids, the ligands create a layered arrangement which is pillared by TEAH counterions and water molecules (omitted for clarity). $\{W_{36}\}$: teal polyhedra, C: grey, N: green, O: red.

The supramolecular framework arrangement of compound **10** is comparable to the structural situation observed in compound **9** where the cluster anions are arranged in an antiparallel fashion. This pattern is governed by the protruding organic ligands which are pairwise aligned so that one set of two $\{W_{36}\}$ cluster ligands point to the same void. These inter-cluster voids are filled with TEAH counter ions which form hydrogen-bonds between the clusters and the additional solvent water molecules, thus reinforcing the structural stability of the assembly.

The phenyl rings which protrude from the binding sites are aligned in an almost parallel fashion, however, adjacent rings are too far apart to interact via π–π stacking. This structural feature does therefore not contribute to the stability of the framework assembly, see Figure 40.

Due to these promising initial results it was subsequently decided to introduce an additional functionality to examine the compatibility of bifunctional molecules with the $\{W_{36}\}$ host anion. The diamino-functionalised compound *para*-xylylene diamine $[H_3N\text{-}CH_2\text{-}C_6H_5\text{-}CH_2\text{-}NH_3]^{2+}$ (= *p*XDA) was chosen for several structural and chemical reasons. A primary amine is required as the binding motif of the guest cation to act as a recognition site which interacts with the cluster anion. It was further considered necessary to maintain the phenyl ring which adds structural stability and introduces less crystallographic disorder compared to alkyl chains. In addition, the increased electron density allows precise location of the ligand by X-ray crystallographic studies. Finally it was decided that the second functionality should also be a primary amine structurally equivalent to the first unit in order to minimise competitive binding and interference effects. To limit the steric bulk of the guest molecule, a *para*-substitution of the two amino-substituents on the phenyl ring was considered most favourable.

The reaction of *p*XDA with an acidified sodium tungstate solution at pH 2.2 under the standard $\{W_{36}\}$ reaction conditions yielded a crystalline product, compound **11**. The material was characterised by single-crystal X-ray diffraction and structural analysis revealed the formula $TEAH_9Na_1[pXDA\subset[H_{12}W_{36}O_{120}]]\cdot 17H_2O$ (= $TEAH_9Na_1$**11a**$\cdot 17H_2O$). The compound contains the well-known $\{W_{36}\}$ cluster anion with W-O bond lengths and angles virtually identical to the structures discussed above. The binding pocket in the cluster centre interacts with a diprotonated *p*XDA ligand which protrudes from the cluster cavity and thus is displaced from the cluster equatorial plane by 1.30 Å. As a consequence, the amine nitrogen centre in the cavity forms a set of distinct interactions with the oxygen oxygen sites, depending on their location within the $\{W_{36}\}$ framework. As already observed for the other organo-substituted cluster anions **9a** and **10a**, the $\{W_{11}\}$-based oxygens in **11a** are engaged in attractive interactions with the *p*XDA nitrogen centre ($d_{N\text{-}O}$ ~ 2.78 Å) whereas the oxygen centres located on the $\{W_1\}$ linking units are separated by long N-O distances of $d_{N\text{-}O}$ ~ 3.29 Å which do not contribute to the attractive interactions.

This effect is caused by the non-planar arrangement of the six oxygen donors where the set of $\{W_{11}\}$ oxygens is located slightly above the mean plane (and thus on the side of where the *p*XDA ligand is located) whereas the $\{W_1\}$ oxygen set sits slightly below the equatorial plane, see Figure 41.

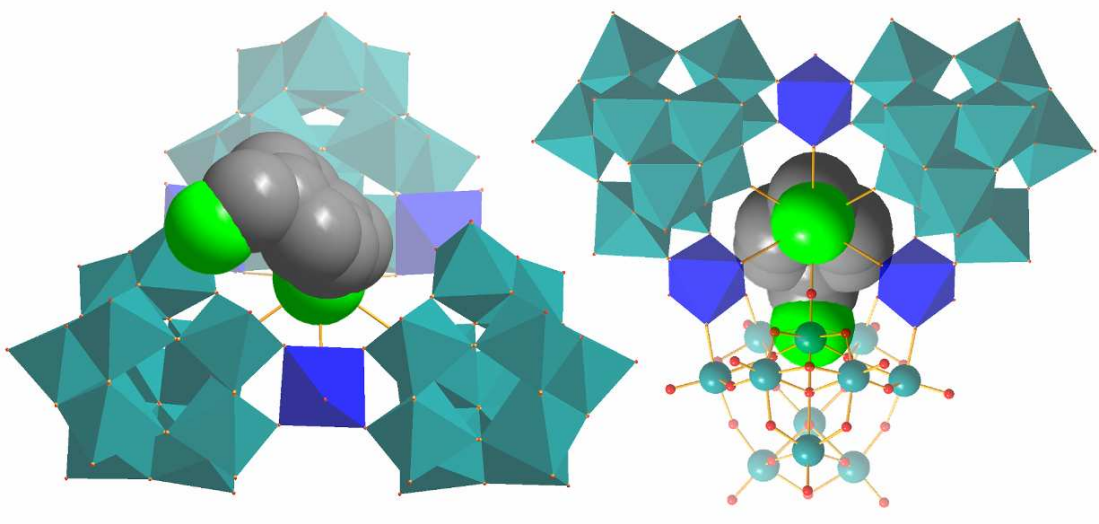

Figure 41: Polyhedral representation of host guest complex **11a**, *p*XDA⊂$\{W_{36}\}$. The side view (left) illustrates the protruding *para*-xylylene diamine ligand in space-filling representation with the peripheral amino group which can engage in further supramolecular interactions. The top view (right) highlights the location of the organic ligand within the binding pocket of the $\{W_{36}\}$ host anion. $\{W_{11}\}$ subunits: teal, $\{W_1\}$ linkers: blue, C: grey, N: green.

With regard to the supramolecular structural arrangement of the anions in the crystal lattice of **11**, a fascinating effect of the *p*XDA ligand can be observed. The $\{W_{36}\}$ cluster anions in compound **11** do not arrange in an antiparallel fashion as the organo-derivatives **9** and **10,** but feature a spatial orientation which resembles the crystal lattices found in the purely inorganic compounds **3 - 8.** The clusters adopt an ABAB-type pattern resulting in two layers of $\{W_{36}\}$ anions in which the clusters are tilted by 76.2 °. This arrangement is almost identical to the inorganic structures discussed previously (see section 3.2.2.2); the archetypal compound **3**, K⊂$\{W_{36}\}$, for example features a similar inter-layer torsion angle of 79.2 °. Intriguingly, it seems that this arrangement is structurally supported by the protruding *p*XDA ligands which form strong hydrogen-bonds to adjacent $\{W_{36}\}$ units *via* the peripheral protonated ammonium group. In detail, the pendant NH_3^+ group interacts with three terminal oxo ligands located on the cluster shell of a neighbouring $\{W_{36}\}$ unit. The shortest N-O bond is observed between the protonated amine and the coordinating water ligand on the outside of the $\{W_1\}$ linking unit ($d_{N\text{-}O}$ = 2.786 Å). This suggests strong,

probably multiple hydrogen-bonding interactions since both the amine and the water ligand can act as hydrogen-bond donors. Furthermore two hydrogen-bonds to the $\{W_{11}\}$ subunits on either side of the $\{W_1\}$ linker are observed which feature slightly elongated N-O distances of $d_{N\text{-}O}$ = 2.979 Å.

Remarkably, this spatial arrangement allows for close contacts between the *alpha*-methylene group of the *p*XDA ligand and the $\{W_{11}\}$ terminal oxygen atoms so the formation of CH···O hydrogen bridges is highly likely ($d_{C\text{-}O}$ = 2.986 Å). The result of this sophisticated arrangement is a supramolecular interaction between the *p*XDA group and two adjacent $\{W_{36}\}$ anions *via* interactions with the binding pocket and by hydrogen-bonding of the pendant amine arm. This set of directed interactions results in the stabilisation of the tilted spatial arrangement observed in **11**, see Figure 42. Further framework stabilisation is provided by the presence of a coordinating sodium cation which is located on the periphery of each $\{W_{36}\}$ anion and which interacts with TEAH cations *via* hydroxyl coordination bonds. This motif in combination with further non-coordinating TEAH ligands and water molecules, results in the formation of a vast hydrogen-bonded network and reinforces the structural stability of compound **11**.

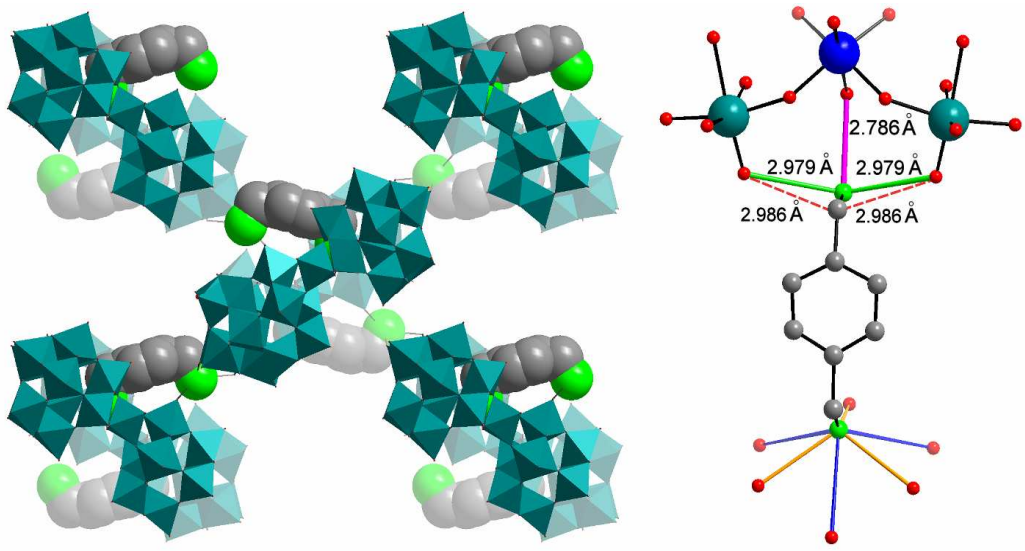

Figure 42: View along the crystallographic *b*-axis of **11** *p*XDA⊂$\{W_{36}\}$ (left), illustrating the twofold interactions between the bifunctional organic amine *p*XDA and two adjacent $\{W_{36}\}$ cluster anions. The organic cation binds to the central cavity of one $\{W_{36}\}$ host and establishes hydrogen-bonding interactions to an adjacent cluster "locking" the two clusters in a tilted arrangement. The detailed view of the interactions of the *p*XDA ligand (right) illustrates the binding of one amine to the central $\{W_{36}\}$ binding pocket (bottom) *via* long (blue) and short (orange) hydrogen-bonded N-O interactions. The supramolecular interactions of the pendant amine arm (top) highlight the two hydrogen-bonded N-O

interactions (magenta and green) and the CH···O interactions (red dashed line). {W_{11}}-fragment: teal, {W_1}-linker: blue, O: red, N: green, C: grey.

The use of bifunctional amine ligands can obviously provide a certain degree of control over the supramolecular framework assembly and thus allow facile access to a more directed approach in synthesising hybrid organic-inorganic frameworks. Thus far, all guest cations were supported by a rigid aromatic backbone and were, therefore, restricted in their ability to interact with neighbouring groups (although this rigidity was introduced deliberately). In order to study the feasibility of binding aliphatic amine systems to the cluster cavity in the {W_{36}} system a bifunctional, non-branched primary amine, 1,6-diaminohexane (DAH), was employed.

The reaction of 1,6-diaminohexane with sodium tungstate in aqueous solution at pH 2.2 resulted in the isolation of a crystalline product, compound **12**. Structural analysis was accomplished by single-crystal XRD and revealed the composition $(TEAH)_{10}[DAH\subset[H_{12}W_{36}O_{120}]]\cdot 17H_2O$ (= $(TEAH)_{10}$**12a**$\cdot 17H_2O$). Investigation of the crystal structure showed that the tungsten oxide cluster observed in compound **12** was the expected {W_{36}} cluster anion and further revealed that a diprotonated 1,6-diaminohexane molecule was located in the centre of the coordination cavity, see Figure 43.

Structurally, the aliphatic ligand behaves similarly to the organic groups discussed above in that it forms two distinct N-O interactions with the two sets of oxygen donors on the {W_{36}} framework. Short N-O distances (*ca.* 2.80 Å) are observed for interactions with the oxygen atoms based on the {W_{11}} subunits whereas elongated hydrogen-bonded distances were found for the {W_1}-based terminal oxo ligands ($d_{N\text{-}O}$ ~ 3.33 Å). As a result of these interactions, the DAH cation is displaced from the cavity centre by 1.33 Å which is in line with the observations previously made and suggests that the steric strain introduced by the bulky phenyl rings in the compounds discussed earlier (**9, 10** and **11**) is negligible.

Further it should be noted that in the crystal structure of **12**, the flexible DAH group is disordered over two sites. As a result, the C_6 chain adopts two different positions which result in a very similar overall arrangement within the C_3-symmetric central cavity of the {W_{36}} cluster framework.

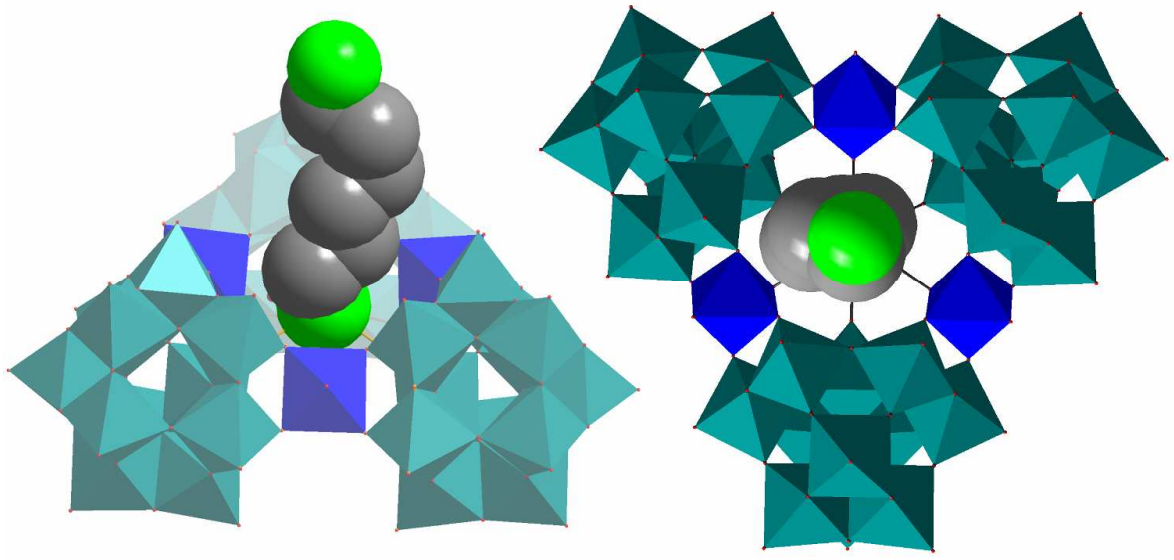

Figure 43: Side view (left) and top view (right) of the cluster anion **12a**, DAH⊂{W_{36}}. The side view illustrates the structural arrangement of the aliphatic diamine 1,6-diaminohexane and the conformation of the C_6 chain. The top view highlights the positioning of the protonated amine in the centre of the cluster, but displaced above the equatorial plane through the interactions with the {W_{11}}-based oxo ligands. {W_{11}}: teal, {W_1} linkers: blue, N: green, C: grey.

In the crystal lattice, the {W_{36}} cluster units are positioned in an ABAB fashion similar to the situation discussed above for compound **11** and for the inorganic derivatives **3-8**. The clusters form two distinct layers and are tilted by 76.9 ° based on their equatorial planes. The organic DAH ligand supports this arrangement by docking on to the adjacent cluster anion with a pendant protonated amino function, thus acting as a supramolecular linking unit. In detail, the protruding amino group establishes four short N-O interactions, see Figure 44. The shortest N-O distance is formed between the pendant nitrogen centre and two μ_2-bridging oxygen ligands which connect the {W_1} linker unit with the {W_{11}} fragment (d_{N-O} = 3.026 Å, highlighted by green bonds in Figure 44). This close contact results in the formation of two symmetry-related supramolecular interactions. Slightly longer N-O distances are observed between the nitrogen atoms and two terminal oxygen ligands located on the {W_{11}} subunit, see Figure 44, magenta bonds. As a result, the DAH ligand connects two {W_{36}} units in very much the same way as discussed previously for the *p*XDA ligand in compound **11**, i.e. by the combination of binding to the central {W_{36}} cavity and additional hydrogen-bonding interactions with an neighbouring cluster unit, see Figure 44, left.

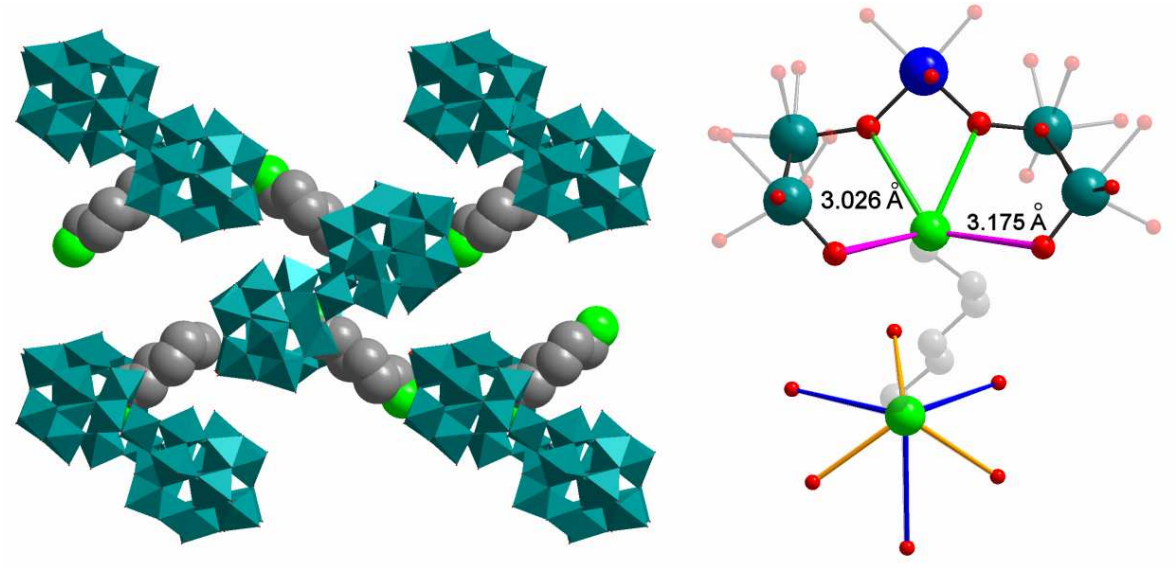

Figure 44: View along the crystallographic *b*-axis of **12**, DAH⊂{W_{36}} (left), illustrating the interactions between the diprotonated 1,6-diaminohexane cation and two neighbouring {W_{36}} cluster anions. The organic cation binds to the central cavity of one {W_{36}} host and furthermore forms hydrogen-bonding interactions to an adjacent cluster and resulting in the stabilisation of the tilted layer arrangement. The detailed view of the supramolecular effect of the DAH cation (right) illustrates the binding of one amine moiety to the central binding site (bottom) *via* long (blue) and short (orange) N-O interactions. The supramolecular interactions of the pendant amine arm (top) highlights the two N-O interactions (magenta and green). {W_{11}}-fragment: teal, {W_1}-linker: blue, O: red, N: green, C: grey.

In conclusion, thus far it has been shown that organic amines can be used as supramolecular linkers, which enable framework formation by a combination of electrostatic, coordinative and hydrogen-bonding interactions. The effects of TEAH have been exemplified in the {Mo_{36}} cluster formation where different coordination modes result in the formation of distinct framework arrangements (see compounds **1** and **2**, section 3.2). Within the {W_{36}} family the influence of TEAH has been discussed and it has been shown that the organic group acts not only as a "simple" counterion, but in addition supports framework formation as a coordinative ligand and can further establish hydrogen-bonds to stabilise the supramolecular assembly. It has further been elucidated that bifunctional organic molecules such as *para*-xylylene diamine (in compound **11**) and 1,6-diaminohexane (in compound **12**) can establish distinct interactions with two clusters and act as supramolecular linkers to encourage framework formation. However, further understanding of the effects of organic amines on the supramolecular assembly of polyoxometalates is necessary to lay the foundations for a crystal engineering approach by design.

3.4 Assembly of polyoxometalate-based frameworks

3.4.1 Supramolecular effects of organic amines on the assembly of $\{Mo_6\}_2$-based frameworks

It has been exemplified by the use of protonated triethanol amine (TEAH), that multifunctional organic amines can have tremendous effects on the structural arrangement of polyoxometalates in the solid state. A range of interactions allows these organic groups to interact with the anionic metal-oxo framework and thus create a set of unique binding modes which enable the formation of novel frameworks with synergistic properties. To understand the effects of different organic amines in the assembly of molecular frameworks, a systematic study was undertaken where three amines were investigated in detail under similar conditions, using an identical polyoxometalate building block as inorganic scaffolds to support the framework. The three organic molecules were chosen to cover a large range of structural properties, geometrical arrangements, rigidities and intermolecular interaction capabilities. In detail, the following amines were investigated:

- Ethylene diamine (EN, Figure 45, centre) is a flexible diamine which can be mono- or diprotonated and which offers two well-defined binding sites for supramolecular interactions. As already discussed above, ammonium groups can establish non-directed electrostatic interactions *via* Coulomb attraction, but can also form more specific hydrogen-bonding motifs with negatively polarised acceptor sites and thus provide the potential to act as "recognition sensors" which help to build specific frameworks. The flexibility of the carbon backbone allows the amine to adopt various conformations and in addition, does not impose any steric restraints on the cluster packing.
- Guanidinium (GUA, Figure 45 left) is a small, nitrogen-rich cation with three NH_2 groups bound to the central carbon atom. This specific trigonal planar arrangement allows for distinct hydrogen-bonding interactions in combination with the non-directed electrostatic attraction which results in two possible interaction modes with the anionic cluster molecules. The planar 2D structure of the molecules may allow the formation of close contacts to POM clusters without interference by bulky substituents.

- 2-aminopyrimidinium (APY, Figure 45, right) is a planar, aromatic heterocycle which features two distinct hydrogen-bonding sites. The first binding site is the ring-nitrogen atom which can be protonated and can act as a hydrogen-bond donor and thus interact with cluster anions. The second binding site is a primary amine substituent which, under the given reaction conditions, is not protonated. This site can act as both a hydrogen-bond donor and indeed an acceptor and thus allows for a range of potential interactions. In addition, the molecule features a second nitrogen atom in the ring which may act as a coordinating site since it cannot be protonated under the given reaction conditions. The presence of an aromatic ring system further introduces the potential for interactions with the electronic structure of the π–system.

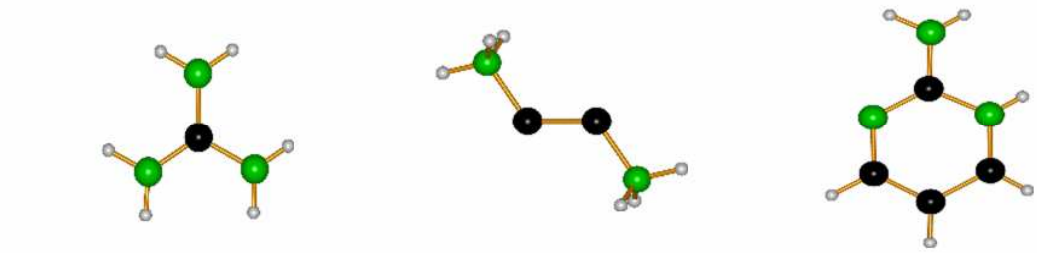

Figure 45: Illustration of the three organic amines which were chosen to study their ability to direct framework assembly using polyoxometalates as structural building blocks. Guanidinium (GUA, left) offers the potential to act as a triple hydrogen bond donor. Ethylene diamine (EN, centre) acts as a flexible ligand which features two well-separated cationic ammonium functions which can form electrostatic as well as hydrogen-bonding interactions. 2-aminopyrimidinium (APY, right) features a planar aromatic ring system and two potential hydrogen-bonding sites, one protonated nitrogen donor on the ring and one substituent amino group. C: black, N: green, H: white.

The conceptual approach to this study was to fully exploit all potential interactions between cluster anion and the amines under investigation. This was synthetically achieved by introducing the organic amine to the reaction mixture before the actual cluster self-assembly occurs. It was thus necessary to study a cluster system which was stable enough to form under a given set of reaction conditions and which would provide potential for developing frameworks by interacting with the organic amine groups.

The cluster of choice for this systematic study was a heteropolyoxomolybdate $[Mo_{12}O_{62}NaP_8]^{23-}$ anion which can be described as a dimeric unit $Na[Mo_6O_{31}P_4]_2$ (hereafter referred to as $\{Mo_6\}_2$). The cluster resembles a dumbbell made up of two six-membered

{Mo_6} rings which coordinate to a central sodium cation, see Figure 46. The {Mo_6} groups are formed by six edge-sharing [MoO_6] octahedra. All molybdenum centres in the cluster are reduced to oxidation state +V and consequently are able to form formal Mo-Mo single bonds by engaging their $4d^1$ valence electrons in bonding interactions.

It is interesting to note that the Mo-Mo single bond is vital for the formation of this cluster and for its stabilisation since no fully oxidised equivalent has been observed thus far. These bonding interactions are also evident in the structure of the {Mo_6} rings by the formation of two distinct sets of Mo-Mo distances. The six-membered rings are formally assembled from three dimeric {Mo^V_2} units in which two molybdenum centres are connected by a single bond characterised by a short metal-to-metal distance of *ca.* 2.6 Å. This arrangement is further stabilised by two μ_2-bridging oxygen ligands which are located between the Mo centres with typical Mo-O distances of *ca.* 1.95 Å. Characteristically for reduced Mo^V species, each [MoO_6] octahedron features one terminal oxygen apex with short Mo-O distances of *ca.* 1.7 Å. Three {Mo^V_2} fragments are formally assembled around a central phosphate which templates the structure formation *via* coordination of three oxygen ligands to two neighbouring but non-bonded Mo(V) centres. The resulting μ_3-oxo bridge features long Mo-O distances of approximately 2.3 Å. The structure is further stabilised by coordination of three peripheral phosphate bridges which connect the non-bonded molybdenum centres and thus further reinforce the structure and contribute to its stability. As a result, the non-bonded Mo centres are separated by the bridging phosphate ligands and feature Mo-Mo distances of *ca.* 3.5 Å. All four phosphate ligands are located in one hemisphere of the cluster anion and consequently this arrangement creates an ideal coordination environment on the opposite side of the ring as it leaves three bridging oxygens in a trigonal geometry with oxygen-oxygen distances of *ca.* 3.4 Å (highlighted in Figure 46, magenta arrow).

This structural feature provides a distinct coordination environment which features three oxygen ligating sites in a *fac*-arrangement and thus enables each {Mo_6} unit to occupy one half of an octahedral coordination sphere. Indeed the effectiveness of this coordination site is demonstrated by the fact that these {Mo_6} rings cannot be isolated as monomeric units but always form a dimeric coordination compound by complexing a central metal cation in an

octahedral fashion. In the present study, sodium was used as an "innocent" central cation so as not to introduce any additional effects on the framework assembly through the use of highly coordinating transition metals which might interact with the organic amines.

It is well-known in the literature that these $\{Mo_6\}$ units can be employed as sterically demanding inorganic tridentate ligands in the complexation and binding of various transition metals such as Fe, Co, Ni and Zn.[168-171] The resulting $\{Mo_6\}_2$ dimer is sterically arranged in a staggered fashion where one ring is rotated by 60 ° in comparison to the other in order to minimise repulsive interactions and to provide the optimum octahedral coordination environment for the central sodium cation, see Figure 46. The $\{Mo_6\}_2$ dimers feature acidic properties as they can be protonated both on the metal-oxo framework and on the acidic phosphate groups. This in turn enables further hydrogen-bonding interactions and provides a versatile route for the assembly of supramolecular frameworks.

The first challenge however, was to elaborate a route to form these clusters under ambient conditions since the typical approach thus far has been a hydrothermal route which involves reaction of elemental molybdenum(0) with a molybdate(VI) source to generate the reduced species *in situ*. However, this high-temperature, high-pressure approach was not feasible for this project as it does not allow the high degree of reaction control that is necessary to engineer sophisticated polyoxometalate frameworks.

Detailed studies of the reaction system eventually showed that the complex anions can be synthesised by reducing an aqueous acidic molybdate solution with sodium dithionite ($Na_2S_2O_4$) and thus generate the clusters in the presence of the amine under ambient conditions, see Figure 46. This in turn gives vital control of pH and ionic strength and further allows changing the reaction parameters as the self-assembly proceeds. The development of this synthetic route proved advantageous over the standard hydrothermal approach and allowed the isolation of four novel framework compounds.

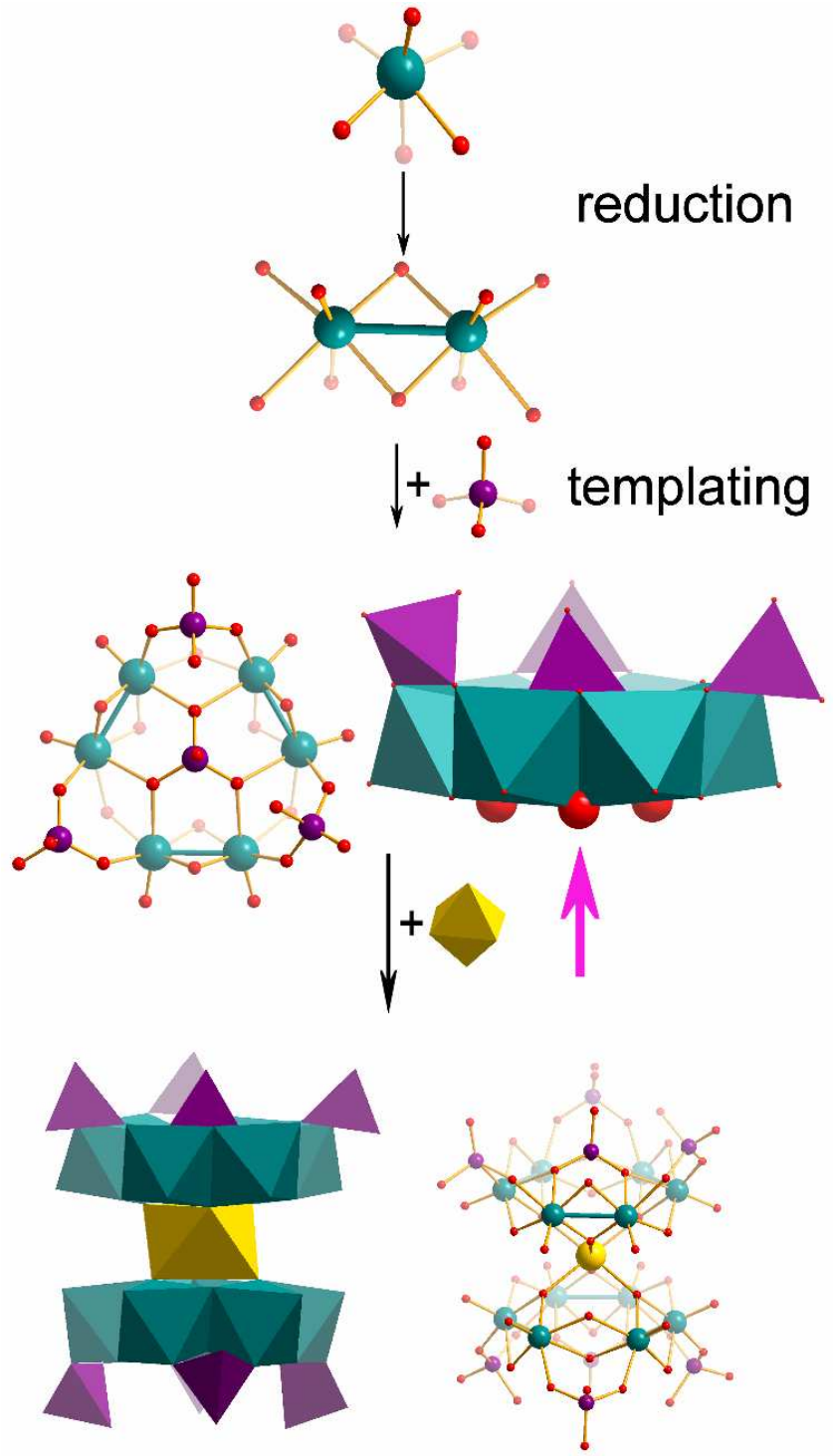

Figure 46: Self-assembly of the $\{Mo_6\}_2$ dimer. A molybdate solution is reduced in the presence of phosphate anions and formally proceeds *via* the formation of $\{Mo^{V}_2\}$ dimers (top) which are subsequently assembled into six-membered $\{Mo_6\}$ rings (centre) by a phosphate-induced templating mechanism. Three additional phosphate ligands act as peripheral stabilisers to support the structure. Two $\{Mo_6\}$ rings coordinate one central sodium centre in an octahedral fashion and form the stable structure $[Mo_{12}O_{62}NaP_8]^{23-}$ (bottom). Mo: teal, P: purple, O: red, Na: yellow.

3.4.1.1 Formation of $(GUA)_{12}[Mo_{12}O_{62}H_{11}Na_1P_8]\cdot 11H_2O$ (**13**)

The reaction of the organic cation guanidinium ($CH_6N_3^+$) with a reduced molybdate solution in the presence of phosphate anions resulted in the isolation of dark red crystals. Single crystal XRD analysis of compound **13** gave the structural composition $(GUA)_{12}[Mo_{12}O_{62}H_{11}Na_1P_8]\cdot 11H_2O$. The main structural feature is the dimeric $\{Mo_6\}_2$ heteropolymolybdate which acts as an inorganic building block and is arranged in two layers following an ABAB pattern within the crystallographic *bc* plane. The cluster anions are aligned in a co-linear fashion so that they run almost parallel to the crystallographic *c*-axis, see Figure 47.

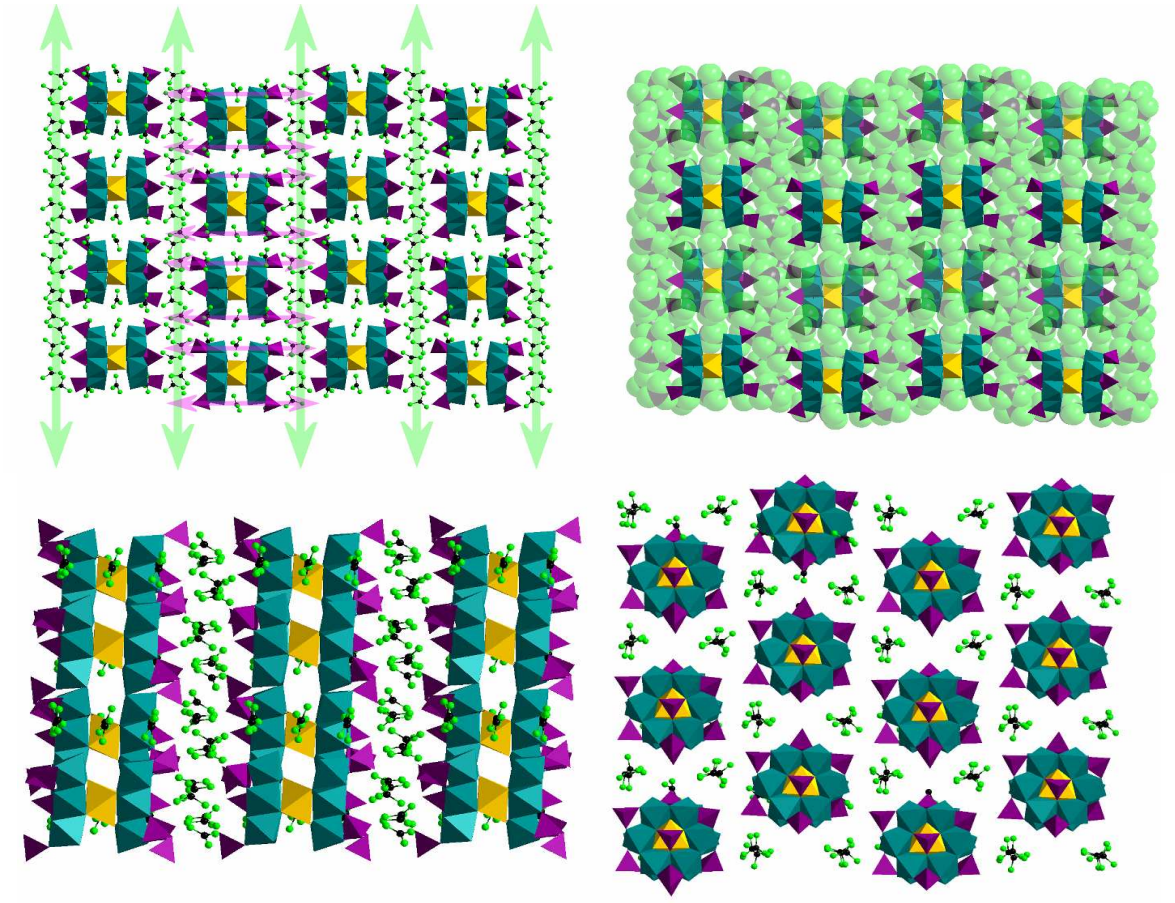

Figure 47: Illustration of the supramolecular crystal lattice of compound **13.** View along the crystallographic *a*-axis (top) illustrates the distinct arrangement of two types of guanidinium cations (top left); one set is located inside the inter-layer voids (green arrows) the second set fills the intra-layer spaces (magenta arrows). The space-filling representation (top right) highlights how the organic cations "encapsulate" the $\{Mo_6\}_2$ cluster anions. Bottom left: View along the crystallographic *b*-axis highlighting the layered arrangement and the two groups of guanidinium cations. Bottom right: View along the crystallographic *c*-axis showing the hexagonal packing of the $\{Mo_6\}_2$ anions. $[MoO_6]$ octahedra: teal; $[PO_4]$ tetrahedra: purple, $[NaO_6]$ octahedra: yellow, C: black, N: green

This distinct arrangement results in the creation of inter- and intra-layer voids which are accessible for the small planar guanidinium cations. The detailed analysis of the supramolecular framework reveals two types of guanidinium cations which feature different interactions depending on their location within the framework. The first set of guanidinium cations is located in the inter-layer voids between two AB-type layers of $\{Mo_6\}_2$ clusters (cluster spacing *ca.* 3.4 Å). The molecular plane of the guanidinium cations is oriented perpendicular to the cluster layers so that the hydrogen-bonding interactions between the ammonium donors and the cluster oxygens can be maximised. As a result, the structure displays a multitude of hydrogen-bonding interactions with minimum N-O distances of 2.810 Å. The clear function of this arrangement of guanidinium cations is to link the cluster layers into a supramolecular framework by a combination of electrostatic and hydrogen-bonding interactions, see Figure 47.

The second set of guanidinium cations is located in the intra-layer voids and is revealed by projection of the lattice along the crystallographic *c*-axis. In contrast to the inter-layer guanidiniums, this second set is arranged so that the molecular plane lies parallel to the $\{Mo_6\}$ rings. This enables the formation of hydrogen-bonds to the cluster ions *via* a range of close N-O contacts. Intriguingly, it seems that the trigonal shape of the organic cations in combination with the potential for hydrogen-bonding along a 120 ° angle is reflected in the supramolecular lattice. The organo-cations adopt a distinctive arrangement around each $\{Mo_6\}_2$ dimer: 18 guanidinium cations form a hexagonal cell where each hexagon corner is occupied by a set of three organic cations which are aligned along the crystallographic *c*-axis, see Figure 48.

Each set of three guanidinium cations on this hexagon forms a recognition motif which allows the arrangement of three $\{Mo_6\}_2$ clusters in a trigonal fashion through a range of hydrogen-bonding interactions, see Figure 48. As a result, the $\{Mo_6\}_2$ dimers are arranged in a hexagonal cell so that each cluster has six equidistant neighbours with inter-cluster distances (measured between the central Na^+ cations) of *ca.* 13.08 Å.

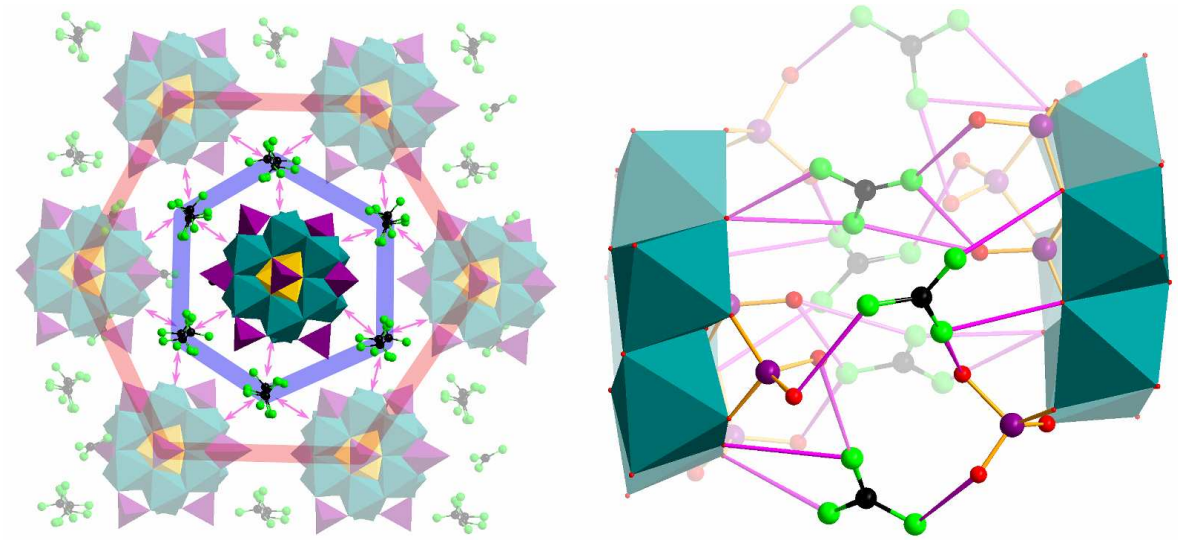

Figure 48: Illustration of the interactions of the two types of guanidinium cations. The intra-layer guanidinium ions (left) are arranged in a hexagonal fashion around the $\{Mo_6\}_2$ cluster anion (blue hexagon) and can form hydrogen bonds to the central cluster as well as to two additional clusters. Thus three clusters are arranged around each set of guanidinium cations in a trigonal fashion. As a result, the $\{Mo_6\}_2$ cluster anions are packed in a hexagonal superstructure (red hexagon). Magenta arrows indicate hydrogen-bonding interactions. The inter-layer guanidiniums (right) are arranged perpendicular to the $\{Mo_6\}$ ring plane and form a vast hydrogen-bonded network (N-O interactions highlighted by magenta bonds) between oxo-ligands on the cluster and on the phosphate groups which then stabilises the supramolecular framework. $[MoO_6]$ octahedra: teal; $[PO_4]$ tetrahedra: purple, $[NaO_6]$ octahedra: yellow, C: black, N: green.

The hexagonal superstructure discussed above might also give some insight in the initial steps of crystal formation of compound **13**. It is conceivable that in solution the cluster establishes supramolecular interactions with a set of guanidinium cations *via* Coulomb- and hydrogen-bonding attraction. Subsequently the rigid arrangement of the hydrogen-bond donors of the guanidinium cations allows the establishment of further close contacts with two additional cluster units and thus initiates the layer assembly.

This observation might help to develop a more designed crystal engineering approach in the formation of hybrid organic-inorganic framework materials where the intrinsic geometric properties of the cation can be used to “direct” the assembly of larger anionic species in distinct spatial arrangements.

3.4.1.2 Formation of $(APY)_{14}[Mo_{12}O_{62}H_9NaP_8]\cdot 13H_2O$ (**14**)

After the initial success using guanidinium as a structure-influencing cation, the use of another planar, but structurally more demanding organic molecule in the $\{Mo_6\}_2$ reaction system was attempted. The reduction of sodium molybdate in the presence of 2-aminopyrimidinium (APY) resulted in the formation of compound **14** which was isolated as a crystalline product. Structural analysis of the single crystal X-ray diffraction data revealed the composition $(APY)_{14}[Mo_{12}O_{62}H_9NaP_8]\cdot 13H_2O$. As dictated by the reaction conditions, the cluster anion present in the crystal lattice is the familiar dimeric $\{Mo_6\}_2$ unit formed by a central sodium cation which is coordinated by two $\{Mo_6\}$ rings. The six-membered rings are each supported by three Mo-Mo single bonds ($d_{Mo\text{-}Mo}$ ~ 2.6 Å) and by four phosphate bridges located on one side of the ring. One central phosphate unit connects the three bonded $\{Mo^{V}_2\}$ dimers whereas three peripheral PO_4^{3-} ligands bridge the non-bonded Mo-Mo distances ($d_{Mo\text{-}Mo}$ ~ 3.5Å).

The crystal lattice of compound **14** shows similarities to the guanidinium-linked compound **13** in so far as the dimeric POM clusters are arranged in a layered ABAB-type fashion. However, in contrast to compound **13,** the layers discussed here do not feature a co-linear arrangement of $\{Mo_6\}_2$ units but show a cluster torsion angle of *ca.* 26.3 ° along the C_3 symmetry axis of the clusters. This distinct arrangement results in the formation of inter-layer voids of *ca.* 6.4 Å which are filled with 2-aminopyrimidinium cations. The molecular plane of the organic cations is aligned with the equatorial plane of the $\{Mo_6\}$ rings in order to enable the formation of hydrogen-bonding interactions, see Figure 49. The hydrogen bonds are characterised by typically short distances between the nitrogen donors on the aromatic ring and oxygen ligands on the cluster anion ($d_{N\text{-}O,min}$ = 2.83 Å). The APY cations form a supramolecular assembly within the crystal lattice by engaging in π- π stacking interactions with minimum centroid distances of 3.50 Å. As a result, columns of protonated APY molecules propagate along the crystallographic *b*-axis which guide the alignment of $\{Mo_6\}_2$ clusters in the lattice. Detailed structural investigation reveals that the APY cations are slightly offset from one another in the columnar structures so as to maximise orbital overlay and thus provide maximum support for the structural assembly.

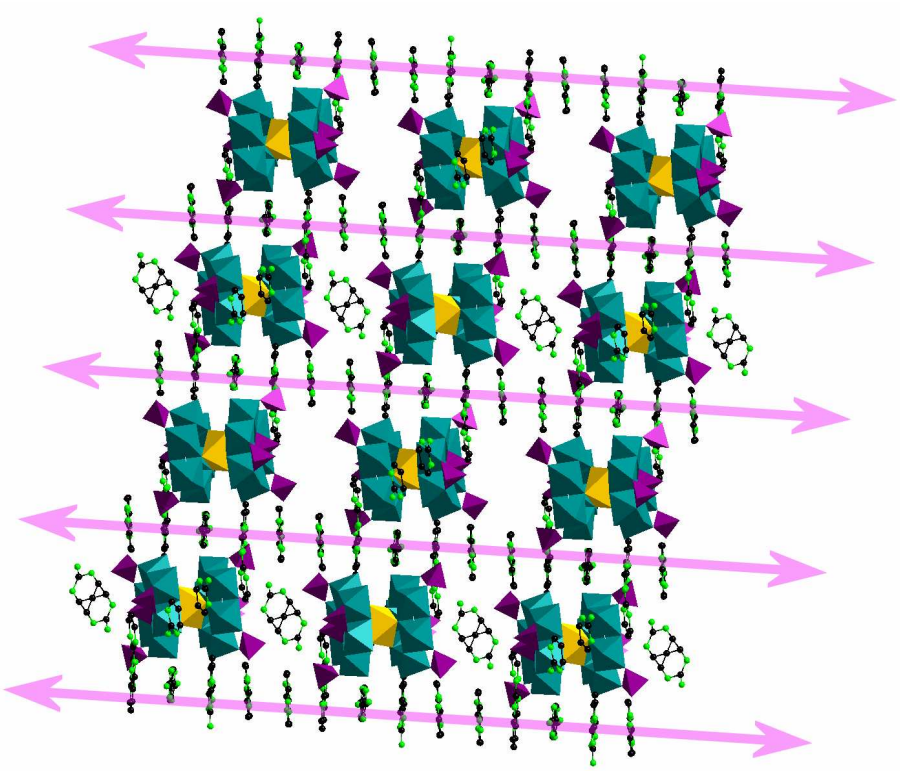

Figure 49: View of compound **14** along the crystallographic *a*-axis, highlighting ABAB-layered arrangement of $\{Mo_6\}_2$ units in the crystal lattice. The supramolecular π–π-stacked arrangement of the 2-aminopyrimidinium cations and subsequent formation of the supramolecular columnar structures is emphasised by magenta arrows. The disordered intra-layer APY cations are visible within the layers. [MoO_6] octahedra: teal, [PO_4] tetrahedra: purple, [NaO_6] octahedra: yellow, C: black, N: green. Water molecules and hydrogen atoms omitted for clarity.

Detailed studies of the hydrogen-bonded interactions between the cluster anions and the 2-aminopyrimidinium cations reveal two distinct interaction modes. As expected the organic molecules are protonated on one ring-nitrogen and can thus act as hydrogen-bond donors which bind to negatively polarised oxo ligands on the cluster surface. An abundance of interactions between the nitrogen donors and the phosphate-based oxygen ligands are observed. This suggests that these oxygen atoms feature a higher negative polarisation are, therefore a stronger binding site, see Figure 50.

In addition, close N-O contacts (<3.0 Å) are observed to μ_2-bridging oxo ligands within the Mo-O framework which supports theoretical indications that these oxygen sites are more basic than the terminal Mo=O motifs. However, the primary amine substituent on the pyrimidinium ring also engages in hydrogen-bonding interactions with the cluster anion and thus allows effective docking of the cation to the cluster *via* two distinct binding

mechanisms. Close interatomic distances can be established as a result of these binding mechanisms, see Figure 50.

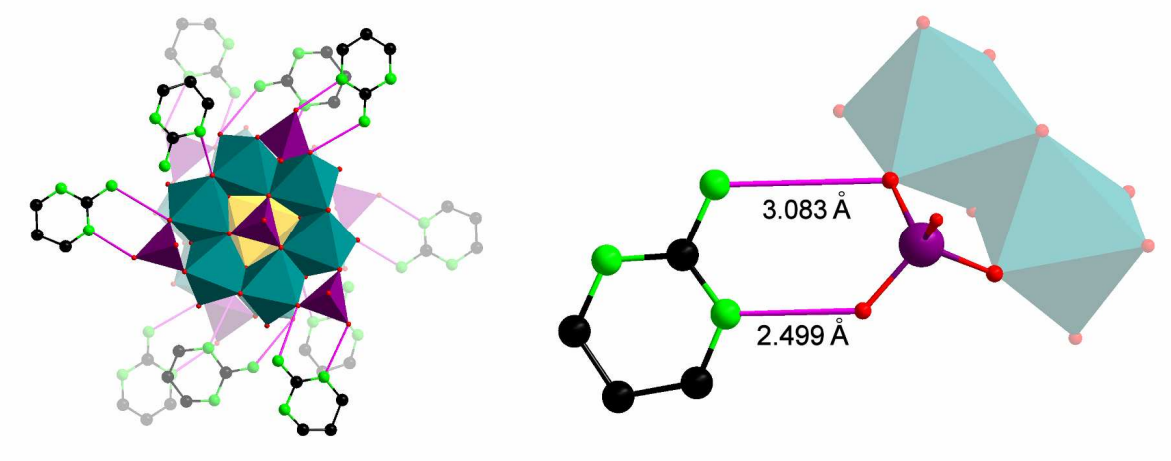

Figure 50: Interactions of APY with the cluster framework. Illustration of the docking sites of the 2-aminopyrimidinium cations on the cluster anion (left), highlighting the preference of phosphate groups and the distribution of cations around the anion. The co-planar arrangement of the {Mo_6} ring and the aromatic system of APY is highlighted. The detailed view (right) illustrates the hydrogen-bonding docking mechanism of the APY cations *via* the ring nitrogen atom and through the substituent primary amine. [MoO_6] octahedra: teal; [PO_4] tetrahedra: purple, [NaO_6] octahedra: yellow, C: black, N: green. Hydrogen atoms omitted for clarity.

In addition to the first group of inter-layer APY cations, which are assembled into columnar structures, a second group of 2-aminopyrimidinium cations are observed. These cations act as intra-layer stabilisers by forming hydrogen-bonding motifs with the cluster anions. It was noted that these cations are located exactly in the centre between two {Mo_6}$_2$ dimers so as to establish hydrogen-bonding interactions with the basal surfaces of both clusters. Consequently, the crystallographic studies show that the APY molecule is disordered over two positions so that, averaged over the whole structure, the molecule interacts with both cluster anions *via* a twofold hydrogen-bonding motif with minimum N-O distances of 2.49 Å, see Figure 51, right.

The result of this supramolecular arrangement is the formation of chain-motifs in the crystallographic *ab* plane. However, these chain-like motifs do not reinforce the framework because the disordered nature of the connecting APY ligands does not allow the linking the clusters into truly 1D hydrogen-bonded chains, see Figure 51, left.

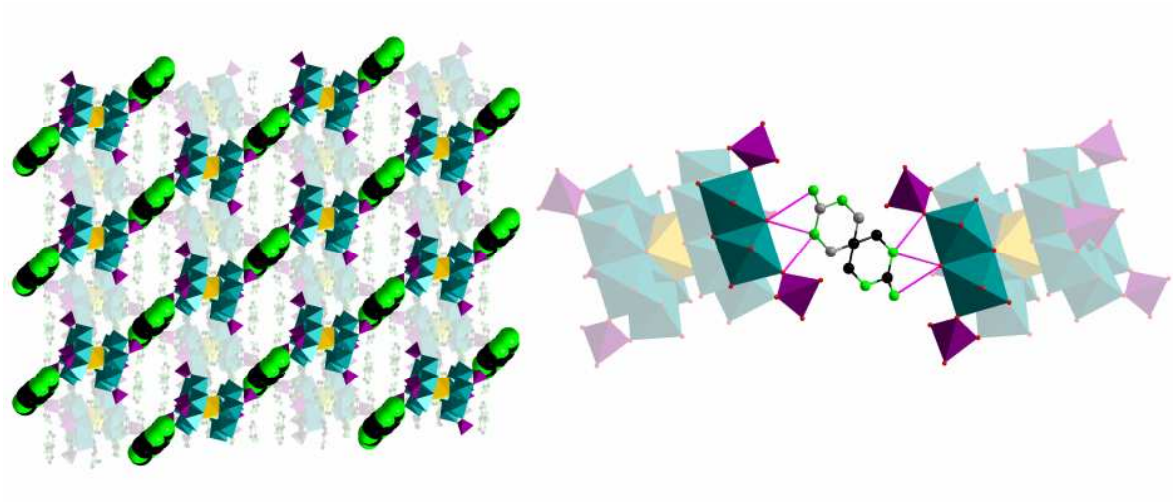

Figure 51: Illustration of the interaction mode of the intra-layer 2-aminopyrimidinium cations in compound **14**. The view along the crystallographic *c*-axis (left) highlights the formation of "pseudo" chain-like structures formed by hydrogen-bonding of the disordered APY ligand with the basal planes of two $\{Mo_6\}_2$ dimers. The detailed illustration (right) emphasises the hydrogen-bonding of the two nitrogen donor groups within the organic cation which preferably bind to bridging oxygen ligands on the cluster framework (N-O distances < 3.0 Å highlighted by magenta bonds). $[MoO_6]$ octahedra: teal; PO_4 tetrahedra: purple, $[NaO_6]$ octahedra: yellow, C: black, N: green. Hydrogen atoms omitted for clarity.

The results of this study so far suggest that the use of rigid amines with a planar geometry and the ability to support multiple hydrogen bonds allows a certain degree of control over the framework assembly. In compound **13**, guanidinium cations were able to "template" a supramolecular assembly in which three hydrogen-bonded interactions, in a distinct 120 ° trigonal arrangement, assembled a hexagonal array of $\{Mo_6\}_2$ cluster anions.

In compound **14** the use of 2-aminopyrimidinium cations allowed the assembly of a layered superstructure of cluster anions within a well-defined organic scaffold established by the columnar arrangement of the aromatic ring systems. These π- π interactions in combination with an extensive net of hydrogen-bonds allowed the formation of a sophisticated framework in which the $\{Mo_6\}_2$ dimers are connected *via* a range of distinct supramolecular interactions.

3.4.1.3 Formation of $(EN)_6[Mo_{12}O_{62}H_9Na_3P_8]\cdot 18H_2O$ (**15**)

Based on the encouraging results obtained with rigid amines in compounds **13** and **14** the effects of a flexible diamine, diprotonated ethylenediamine (H_3N-$(CH_2)_2$-NH_3^{2+}, EN) in the $\{Mo_6\}_2$ reaction system were studied. However, initial experiments indicated that protonated EN quickly forms insoluble precipitates with molybdenum-oxo species so a more sophisticated approach had to be developed which involves the slow release of EN into the reaction mixture.

A highly water-soluble precursor, N,N,N',N'-*tetrakis*-(hydroxyethyl)-ethylenediamine was introduced to the initial synthesis mixture. The four hydroxyethyl substituents on the central EN molecule can be considered to act as protecting groups which slowly hydrolyse under the reducing acidic reaction conditions and thus slowly release "deprotected" diprotonated ethylenediamine. This approach allows the reaction to equilibrate and to form crystalline materials rather than amorphous precipitates. Single-crystal X-ray diffraction analysis of the crystalline reaction product **15** revealed the composition $(EN)_6[Mo_{12}O_{62}H_9Na_3P_8]\cdot 18H_2O$.

The inorganic cluster component is the $\{Mo_6\}_2$ dimer which is structurally virtually identical to the cluster anions in **13** and **14**. Each $\{Mo_6\}$ ring contains six Mo(V) centres and features three bonding ($d_{Mo\text{-}Mo}$ ~ 2.6 Å) and three non-bonding ($d_{Mo\text{-}Mo}$ ~ 3.5 Å) Mo-Mo distances. Structural support is provided by one central and three peripheral phosphate groups which bridge between the Mo centres. Two$\{Mo_6\}$ rings combine into a dimeric unit by coordinating to a central sodium cation. In contrast to the previous structures, the clusters in compound **15** are not discrete molecules but form an infinite 1D chain by linking up *via* $[Na_2O_{10}]$ dioctahedral bridging units. These $\{Na_2\}$ bridges are connected to phosphate units on opposite sides of the cluster anion so that they are structurally related by a centre of inversion located at the position of the central sodium cation, see Figure 52, right.

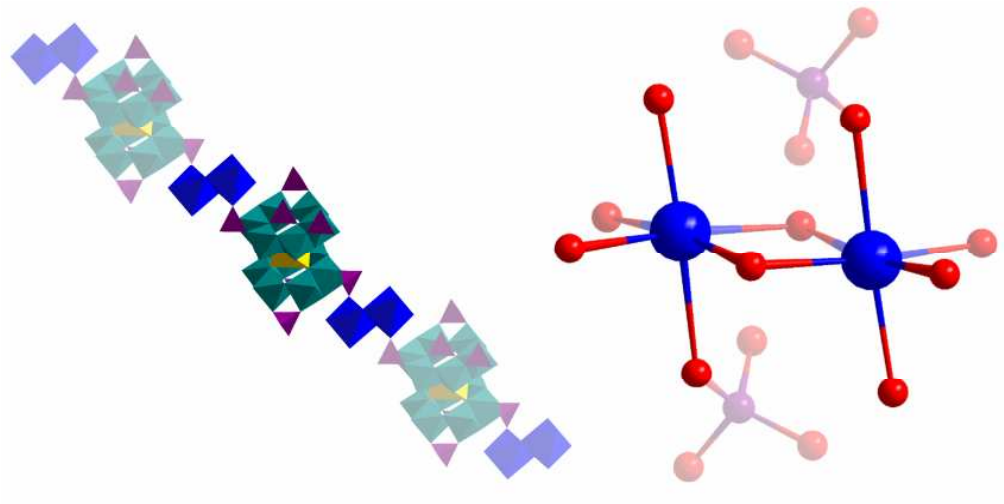

Figure 52: Illustration of the $\{Na_2\}$-linked $\{Mo_6\}_2$ chains in compound **15** (left). The linking mode of the dioctahedral $\{Na_2\}$ bridges *via* coordination to terminal phosphate oxygen centres allows the assembly of a polymeric 1D chain. The detailed view (right) of the Na^+ coordination environment illustrates the connectivity as well as the different types of oxygen ligands. $[MoO_6]$ octahedra: teal; $[PO_4]$ tetrahedra: purple, central $[NaO_6]$ octahedra: yellow, $\{Na_2\}$ units: blue, C: black, N: green. Hydrogen atoms omitted for clarity.

The $\{Na_2\}$ units feature a combination of terminal water ligands, bridging oxo units and phosphate-based oxygen bridges which are characterised by distinct Na-O distances. The terminal water ligands typically show metal-oxygen separations of $d_{Na\text{-}O}$ ~ 2.35 Å for equatorial positions and $d_{Na\text{-}O}$ ~ 2.40 Å for apical positions. The bridging oxygen donors located between the two sodium centres feature Na-O bond lengths of 2.37 and 2.45 Å respectively. The longest bonding distances are observed between the sodium cations and the phosphate-based oxo ligands which display separations of $d_{Na\text{-}O}$ ~ 2.62 Å.

In the supramolecular lattice, the $\{Na_2\}$-linked $\{Mo_6\}_2$ units form infinite polymeric chains which are separated by diprotonated ethylene diamine cations. These organic groups interact with the cluster anions primarily *via* electrostatic attractive forces. Further the two protonated amine groups enable the formation of hydrogen-bonding interactions. It is interesting to note however that compared with compounds **13** and **14**, these ethylene diamine cations do not appear to exert any supramolecular effects on the arrangement of the $\{Mo_6\}_2$ cluster ions. It is their pronounced flexibility which allows them to adopt several conformations by rotation around the C-C single bond. This feature puts these EN cations in stark contrast to the rigid guanidinium and 2-aminopyrimidinium cations discussed earlier which could dock on to a certain binding site in one given configuration

only. Consequently the crystallographic analysis of the structure of compound **15** shows an unusually high degree of disorder in the structure which is caused by these multiple steric arrangements of particular EN cations. An example thereof is the disordered EN unit illustrated in Figure 53, right. It is shown that the disorder introduced by a flexible molecule allows the formation of a multitude of binding modes and illustrates that the probability of forming cation-directed supramolecular polyoxometalate frameworks is maximised by employing rigid amines which can bind to the cluster anion in one distinct binding mode only.

The EN molecule is located between the basal planes of two adjacent cluster anions in an environment ideal for hydrogen-bonding. A multitude of potential acceptor sites including terminal and bridging Mo-O units, phosphate groups and solvent water molecules allow the EN molecule to adopt two spatial arrangements. As a result, the molecule can form six strong hydrogen bonds ($d_{N\text{-}O} < 3.0$ Å) to the two $\{Mo_6\}_2$ units and can bind two additional solvent water molecules. However, the lack of rigidity in the EN system does not favour the formation of distinct supramolecular interactions as observed with guanidinium (120 ° hydrogen-bonding angle) or 2-aminopyrimidinium (co-planar arrangement of the aromatic ring systems; two distinct hydrogen-bonding sites).

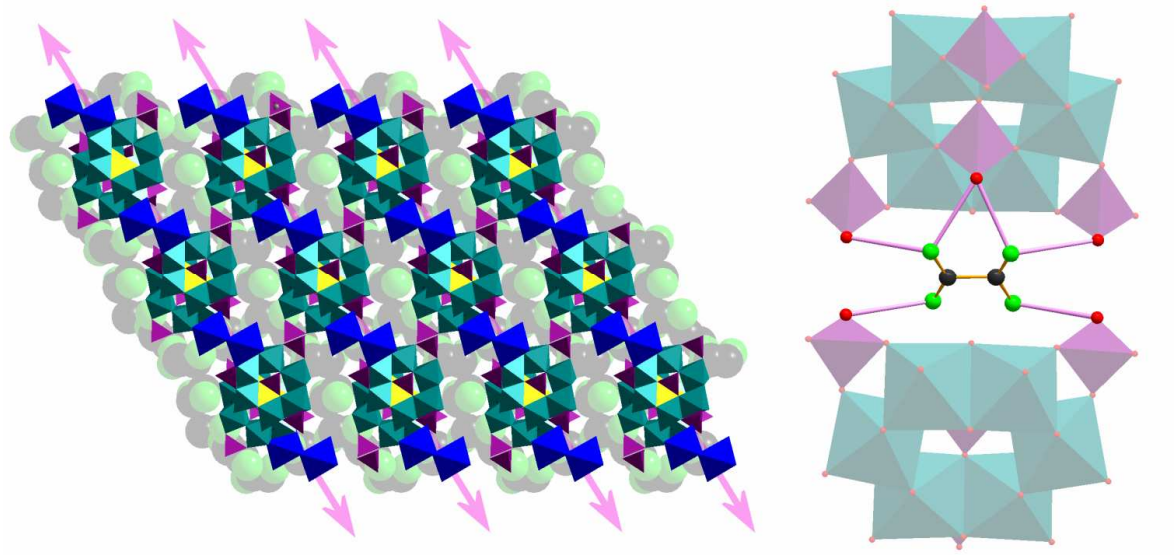

Figure 53: View along the crystallographic *c*-axis (left) of compound **15**, illustrating the arrangement of the inorganic chains $[\{Na_2\}\{Mo_6\}_2]_\infty$ in the crystal lattice (highlighted by magenta arrows). The detailed representation of the multiple, non-site-specific hydrogen-bonding of the ethylenediamine cations (right) illustrates how one disordered cation can form several hydrogen bonding motifs between adjacent cluster units. Short N-O distances (< 3.0 Å) are represented as magenta bonds. $[MoO_6]$ octahedra: teal; $[PO_4]$ tetrahedra: purple, central $[NaO_6]$ octahedra: yellow, $\{Na_2\}$ units: blue, C: black, N: green. Hydrogen atoms omitted for clarity.

In conclusion, the use of the rigid amines GUA and APY allowed the formation of supramolecular $\{Mo_6\}_2$-based networks which were cross-connected by hydrogen-bonding motifs formed between the protonated organic cations and the cluster anions. It was established that three key-factors can be used to direct the arrangement of the 2D-layered frameworks. The overall molecular shape of the organic cation affects supramolecular arrangement of the cluster anions and thus enables framework formation *via* the establishment of a range of supramolecular interactions. Further the precise geometry of hydrogen-bonding sites is vital in controlling the arrangement of cluster anions. It has been demonstrated that the intrinsic triangular arrangement of the hydrogen-bonding sites in guanidinium allows the formation of hexagonal superstructures and thus, control of the overall framework assembly. Additional interactions such as π- π–stacking as observed for 2-aminopyrimidinium can provide additional support for framework assembly. This is because the molecules do not only act as discrete isolated groups but can interact and form supramolecular columns, thus enhancing the attractive interactions with the cluster anions. Contrary to the results observed with these rigid cations, the very flexible ethylene diamine molecules do not seem to interact with the cluster anions in a way that allows the "directed" formation of a supramolecular assembly. It is notable however, that the EN cations do allow the formation of a crystal lattice based on infinite 1D chains of $\{Na_2\}$-linked $\{Mo_6\}_2$ clusters, where the EN cations are arranged between the chains as an organic "scaffold" without introducing the steric demands of rigid amines.

3.4.1.4 Assembly of a $\{Mo_5\}$-based hybrid framework (**16**)

The versatility of the reaction system was demonstrated when a second product, compound **16**, was isolated from a synthetic procedure virtually identical to the synthesis of compound **14**. Single-crystal XRD studies of compound **16** showed a framework composition of $(APY)_5[Mo_5O_{15}H(PO_4)_2]\cdot 5H_2O$ (= $(APY)_5$**16a**$\cdot H_2O$). In contrast to compounds **13 - 15**, the inorganic building blocks in **16** are not the dimeric $\{Mo_6\}_2$ units which were expected under the given reaction conditions. Instead a pentagonal ring structure $[Mo_5O_{15}H(PO_4)_2]$ was identified in which five Mo (VI) centres are linked by corner- and edge-sharing modes. The structure is reinforced by two phosphate units which are located centrally above and below the $\{Mo_5\}$ ring plane. The phosphate oxygen donors act as bridging ligands and connect two adjacent molybdenum centres. Typically, the Mo-

O distance of these bridging phosphate oxygens varies from 2.2 to 2.45 Å in order to accommodate the steric demands of the rigid phosphate groups. In addition, μ_2-bridging oxygen ligands stabilise the structure by interacting with two neighbouring Mo atoms (d_{Mo-O} ~1.9 Å). The octahedral coordination sphere of each metal ion is completed by two terminal oxo ligands with Mo-O distances of *ca.* 1.7 Å which is the characteristic Mo-O bond length for fully oxidised Mo(VI) centres.

This distinct arrangement of [MoO_6] octahedra results in the formation of four edge-sharing and one corner-sharing connection, and is characterised by two sets of non-bonded Mo-Mo separations. As expected, the edge-sharing octahedra feature shorter Mo-Mo distances of *ca.* 3.4 Å, whereas the corner-sharing octahedra feature Mo-Mo spacings of *ca.* 3.7 Å. This five-membered ring is capped top and bottom by phosphate tetrahedra resulting in the formation of a cluster anion with unusually low symmetry, see Figure 54, left. It is interesting to note that the supramolecular arrangement of the present compound **16** shows striking similarities to the other 2-aminopyrimidinium-based compound **14**.

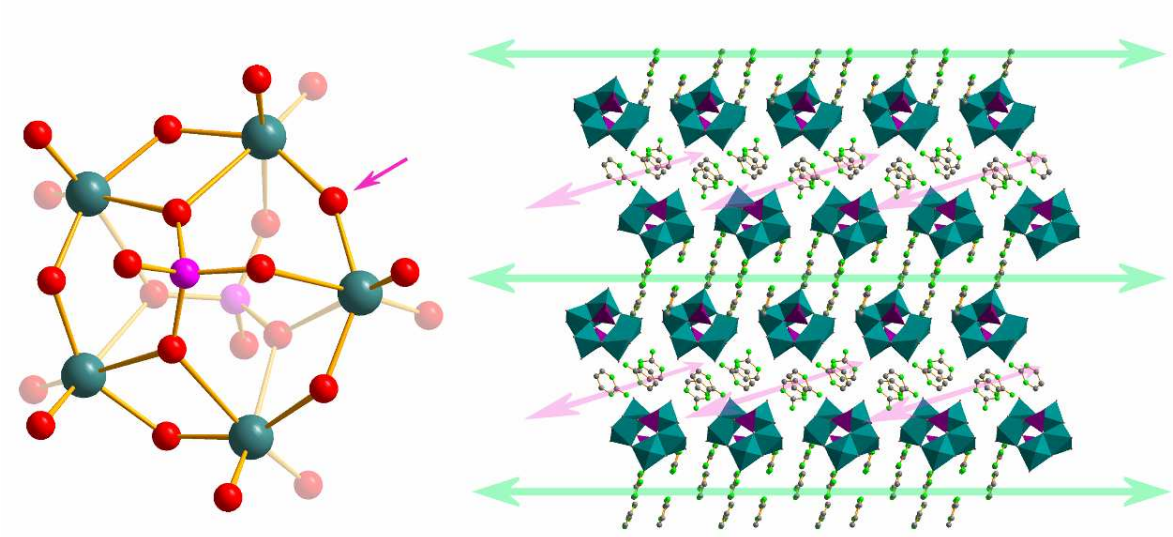

Figure 54: Illustration of the cluster anion **16a**, $[Mo_5O_{15}H(PO_4)_2]^{5-}$ (left) highlighting the four edge-sharing and one corner-sharing modes. The phosphate ligands are located above and below the cluster plane. The position of the corner-sharing oxygen ligand is highlighted by a magenta arrow. View along the crystallographic *a*-axis of **16** (right). The green and magenta arrows indicate the direction of propagation of the π-π-stacked 2-aminopyrimidinium columnar structures. [MoO_6] octahedra: teal, [PO_4] tetrahedra: purple, central C: grey, N: green. Hydrogen atoms omitted for clarity.

The {Mo_5} anions in **16** are arranged in an ABAB-fashion to form layers with an intra-layer spacing of 4.2 Å. The cluster ions within one layer are cross-linked by a hydrogen-bonded network of solvent water molecules which stabilise the supramolecular

arrangement. The inter-layer voids (6.6 Å) are filled by two sets of 2-aminopyrimidinium cations which assemble into distinctive π-π-stacked columnar structures similar to the arrangement discussed in compound **14**. However, in the present structure, these columns are not arranged in a co-linear fashion, but also form a layered ABAB-type arrangement which results in a complex supramolecular assembly (emphasised by green and magenta arrows in Figure 54). As expected the 2-aminopyrimidinium cations interact with the cluster anions *via* electrostatic and hydrogen-bonding motifs and adopt the distinct twofold binding mode discussed earlier where the cations interact with the cluster oxygens through two hydrogen-bonds. This allows the formation of strong interactions between the organic columns and the cluster layers and results in the assembly of a robust crystalline structure.

3.4.1.5 Introducing functionality: Synthesis of $(SPA)_4(BTC)_1[H_{15}Mo_{12}NaO_{62}P_8]\cdot 10H_2O$ (**17**)

The effects of different amines on the framework formation of $\{Mo_6\}_2$-based systems has shown that strong supramolecular interactions can be introduced by rigid amines with multiple hydrogen-bonding sites. However, this approach can be further diversified by choosing an appropriate amine which does not only introduce the potential for hydrogen-bonding but is enantiomerically pure; in other words it can imprint a chiral motif on the framework assembly. Notably a co-operative effect has been observed when using aromatic systems where columnar structures consisting solely of aromatic cations have been observed in the crystal structures of compounds **14** and **16**, owing to the formation of π-π-stacking interactions. It has been shown that such a supramolecular motif can indeed be employed to act as a structure-directing feature which strongly interacts with polyoxometalate cluster systems. Based on these principles a three compound approach was chosen so that each compound would introduce a specific property into the framework.

- The well-established $\{Mo_6\}_2$ anion was used as an inorganic building block to provide framework stability and further encourage the formation of hydrogen-bonding interactions between the organic components and the negatively polarised surface of the cluster. This would allow stability and directed assembly of the supramolecular structure.

- (-)-Sparteine was chosen for this study as it is a chiral rigid amine with multiple hydrogen-bonding sites. The molecule is based on a rigid alkaloid bicyclic framework with two six-membered rings fused to either side of this scaffold. Two secondary amines can be protonated to act as electrostatic and hydrogen-bonding interaction sites (see Figure 55).
- It was further decided to employ a second organic molecule, 1,3,5-benezenetricarboxylic acid (BTC), which combines geometrically well-defined hydrogen-bonding sites with an aromatic phenyl ring system. The molecule is well-known for its use as a supramolecular linker in the assembly of metal-organic frameworks and was considered to be able to interact with the organic sparteine cations through Coulomb attraction as well as with the $\{Mo_6\}_2$ groups *via* coordination and hydrogen bonding. In addition, the planar geometric arrangement of the three carboxylate groups at an angle of 120 ° was considered advantageous for the directed assembly of supramolecular frameworks (see Figure 55).

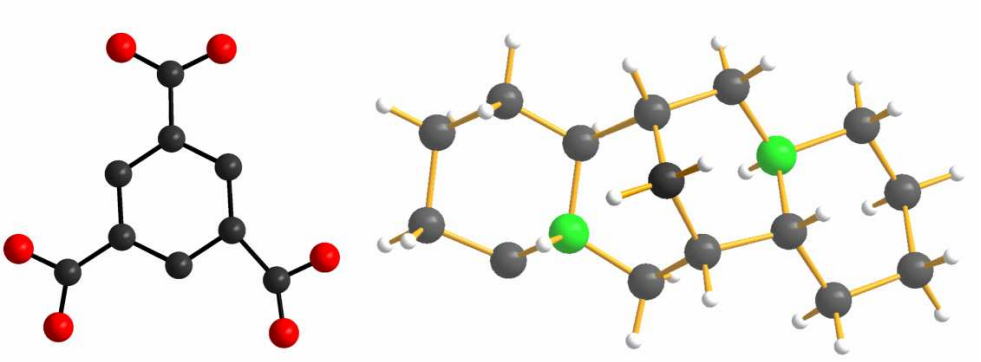

Figure 55: Illustration of the organic molecules used in the three-compound approach. 1,3,5-benzenetricarboxylate (left) is a planar molecule which features an aromatic system as well as three carboxylate groups arranged at a well-defined angle of 120 °. (-)-Sparteine (right) is a chiral rigid molecule which is made up of a central bicyclic functionality as well as two six-membered heterocycles fused to the periphery. Two protonated amine functions allow the formation of hydrogen bonding interactions. C: black, N: green, O: red.

The reduction of a sodium molybdate solution in the presence of BTC and (-)-sparteine resulted in the formation of a dark red crystalline material. Single crystal XRD studies of compound **17** gave the composition as $(SPA)_4(BTC)_1[H_{15}Mo_{12}NaO_{62}P_8]\cdot 10H_2O$ (=$(SPA)_4(BTC)_1$**17a**$\cdot 10H_2O$) and indicated the presence of a chiral structure with the orthorhombic space group $P2_12_12_1$. The synthetic procedure however, was all but straightforward and will therefore be discussed briefly at this stage: The key factor to the

successful formation of compound **17** was the ability to form the dimeric $\{Mo_6\}_2$ units at ambient conditions as opposed to the standard hydrothermal synthesis. This approach allowed precise reaction control and *in situ* alteration of the synthetic parameters. This is vital for the formation of **17** since the experimental procedure involved the precipitation and re-dissolving of a sparteine-molybdate precursor from an aqueous saturated BTC solution, followed by controlled acidification with phosphoric acid to pH 4.0. After reduction of the solution with $Na_2S_2O_4$, the pH was monitored and set to exactly 3.5 yielding a dark blue precipitate and a clear red-brown solution which produced crystals of **17** after *ca.* one week, see Figure 56.

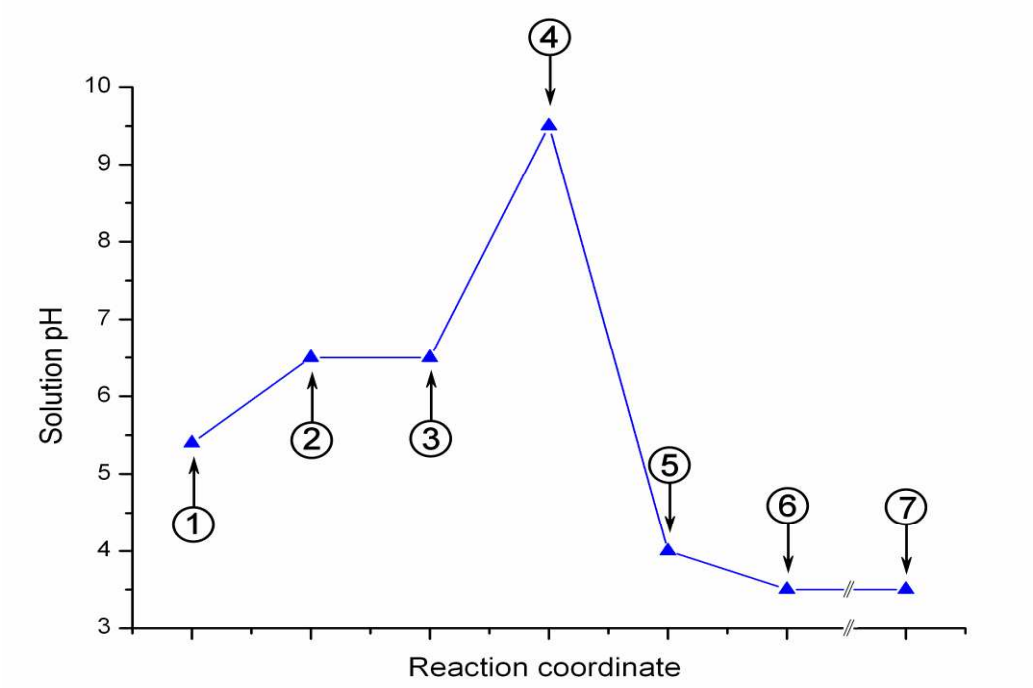

Figure 56: Change of the solution pH over the course of the synthesis of **17**. The diagram illustrates the demanding reaction control necessary to form compound **17** which cannot be established under hydrothermal conditions in an autoclave. Step 1: Saturated aqueous solution (25 ° C) of BTC. Step 2: Addition of sodium molybdate. Step 3: Addition of (-)-(-)-sparteine, resulting in immediate precipitation of a white amorphous material. Step 4: Addition of aqueous sodium hydroxide solution re-dissolves the precipitate. Step 5: Acidification to pH 4.0 using dilute phosphoric acid. Step 6: Reduction of the molybdate solution with sodium dithionite and pH control to pH = 3.5 with dilute phosphoric acid. Step 7: Crystallisation of compound **17**.

Structural analysis of the single crystal XRD data showed the presence of the anticipated inorganic building block $\{Mo_6\}_2$ which had been formed *in* situ under acidic reducing conditions in the presence of phosphoric acid and sodium dithionite as a reducing agent. The cluster features the typical structural assembly which has been discussed in detail above. The heteropolyoxomolybdate anion **17a** is made up of two planar hexanuclear

rings, each formed by six edge-sharing [MoO_6] octahedra with alternating bonding (~ 2.6 Å) and non-bonding (~ 3.6 Å) Mo-Mo distances. Three peripheral and one central phosphate tetrahedra are located in the outer coordination sphere of each {Mo_6} monomer. These four phosphates bridge the non-bonded Mo-Mo groups and thereby provide structural stability for the cluster. The dimer is formed by linking two {Mo_6}-rings *via* one central sodium ion which is coordinated octahedrally by three oxygen atoms of each {Mo_6} group, hence the two Mo_6 rings are arranged in a staggered fashion. Characteristically for the reduced Mo^V species, every [MoO_6] octahedron features one free apex with short Mo-O distances of *ca.* 1.7 Å. Larger Mo-O distances (*ca.* 1.95 Å) are found for the μ_2-oxygen bridges between two bonded Mo centres. The longest Mo-O distances were observed for the oxygen bridges between the non-bonded Mo-Mo central ions with Mo-μ_2O distances of ca. 2.1 Å and Mo-μ_3-O (connecting to the central phosphate unit) with bond lengths of *ca.* 2.3 Å.

The framework assembly is dominated by close intermolecular interactions between the diprotonated SPA cations with the {Mo_6}$_2$ cluster anions. Detailed structural analysis showed that two types of (-)-sparteine cations can be observed which both interact with the cluster anions *via* hydrogen bonding. The first type of SPA cations is characterised by strong hydrogen-bonded interactions with between the protonated nitrogen centres on the organic molecule and only one terminal P-O oxo ligand (d_{N-O} ~ 2.67 Å). This type of (-)-sparteine cation cannot act as a supramolecular linker unit as it engages both hydrogen bonding sites in interactions with only one cluster anion, see Figure 57. In effect, the organic cation acts as a rigid cap which shields the acidic phosphate group from further interactions. However, between the basal planes of two {Mo_6}$_2$ units, a second type of SPA molecules can be found which establishes hydrogen-bonds to two adjacent clusters and thus does act as a supramolecular linker *via* attractive electrostatic and hydrogen-bonding interactions . The SPA cation forms two hydrogen bonds to bridging μ_2-oxo ligands with N-O distances of 2.73 and 2.89 Å respectively. This distinctive arrangement results in the connection of two cluster molecules and eventually in the assembly of a supramolecular (-)-sparteine-linked {Mo_6}$_2$ framework.

The two distinct binding modes of the SPA molecules are not merely caused by different arrangements or orientations of the (-)-sparteine molecules in the crystal lattice but rather

by the presence of two diastereoisomers of the (-)-sparteine structure. These diastereoisomers can be distinguished by the configuration of the central 3,7-diazabicyclo[3.3.1]nonane unit which forms the backbone of the (-)-sparteine structure. In case of the capping (-)-sparteine units, the two nitrogen centres in this bicyclus are arranged in a *syn*-fashion so that they both face in the same direction. In other words, both nitrogens can form hydrogen bonds to the same oxygen acceptor. However, in case of the linking (-)-sparteine molecule, the nitrogen atoms adopt an *anti* conformation. This enables the formation of hydrogen-bonds with multiple donor sites and thus the formation of a supramolecular linking mode, see Figure 57, right.

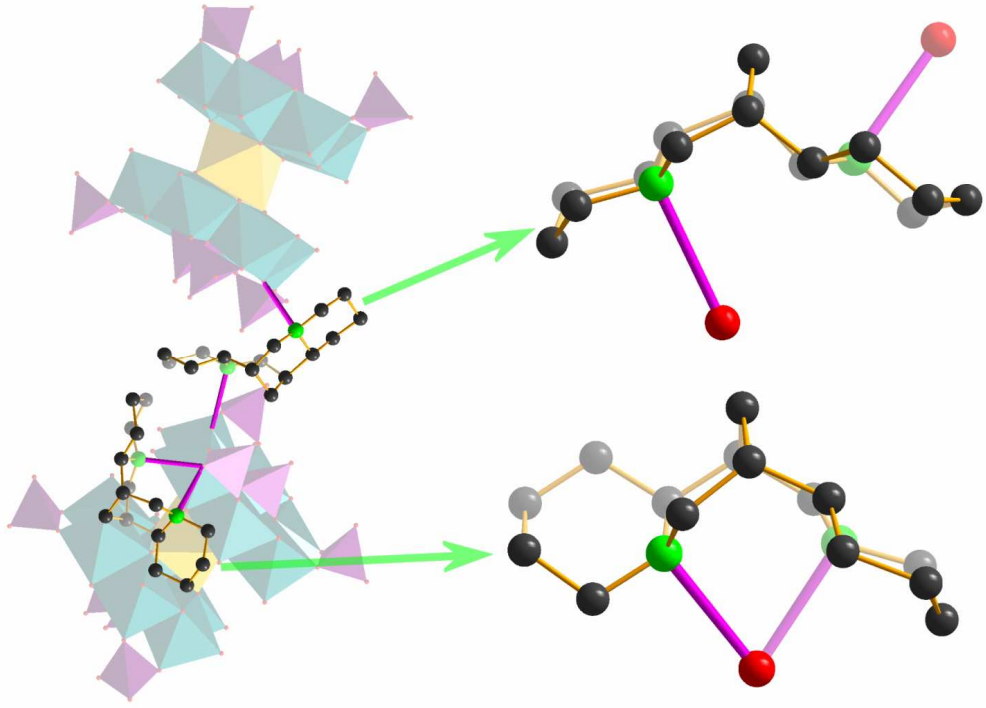

Figure 57: Illustration of the two distinct binding modes of the (-)-sparteine cations in **17** (left). In the "capping" mode one (-)-sparteine molecule interacts with only one cluster anion. In the "linking" mode, the SPA cation hydrogen-bonds with two adjacent clusters and links these into a 3D framework. The detailed illustration of the (-)-sparteine cations (right) shows how the two binding modes are established by adopting distinct configurations on the central bicyclus. The capping ligand (bottom right) feature two nitrogen centres pointing in the same direction whereas the linking SPA molecule features two nitrogen centres which point in opposite directions (top right). C: black, N: green, O: red.

Thus far, the strong and diverse interactions of the (-)-sparteine cations with the inorganic $\{Mo_6\}_2$ building blocks have been discussed and it has been established that one type of SPA diastereoisomeric cations can link the clusters into a 3D hydrogen-bonded framework. In this supramolecular framework, the clusters adopt a hexagonal arrangement which results in the formation of a internal void propagating along the crystallographic *a*-axis

with internal dimensions of *ca.* 19 x 9 Å, see Figure 58. The walls of these channels are composed of $\{Mo_6\}_2$ anions and (-)-sparteine cations which create a rigid supramolecular assembly around the central cavity. However, this void is not empty but filled with BTC molecules which are arranged in a co-parallel fashion so as to engage their aromatic systems in π- π-stacking interactions. As a result, columns of 1,3,5-benzenetricarboxylic

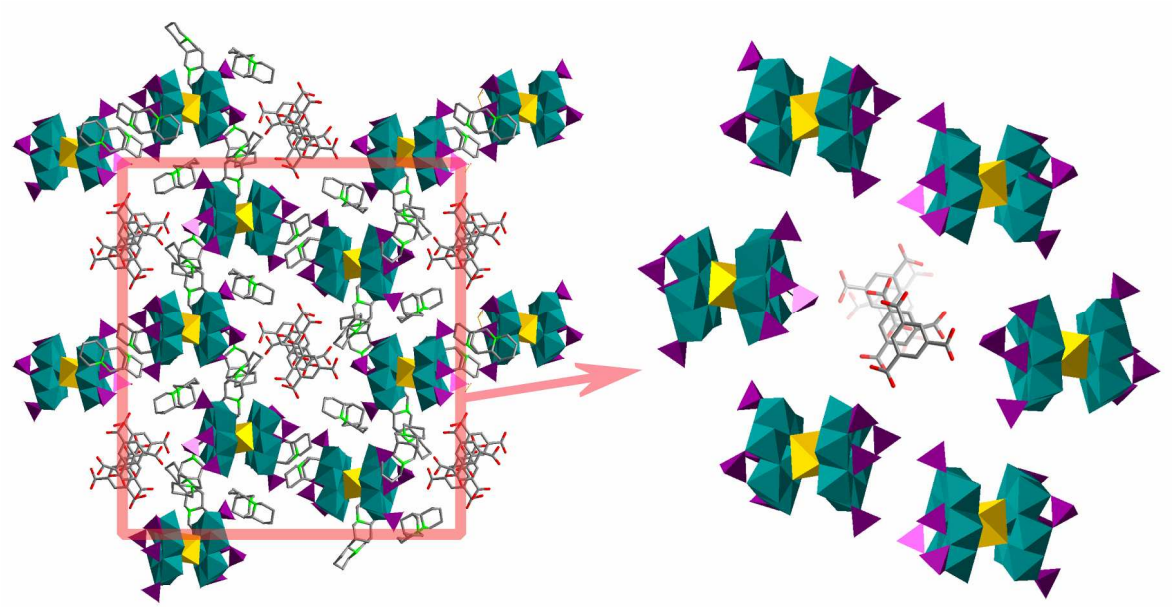

acid molecules are formed which run parallel to the crystallographic *a*-axis, see Figure 58.

Figure 58: View of the crystal lattice of **17** along the crystallographic *a*-axis. Left: The hexagonal arrangement of $\{Mo_6\}_2$ cluster anions and of the (-)-sparteine cations results in the formation a supramolecular lattice which creates a central void (dimensions ca. 19 x 9 Å). These voids are filled with organic BTC molecules. Right: The detailed view of the hexagonal arrangement of cluster anions illustrates the assembly of the framework and the internal channel which is filled by a set of BTC molecules arranged in a parallel fashion so as to maximise π- π-interactions. $[MoO_6]$ octahedra: teal, $[PO_4]$ tetrahedra: purple, $[NaO_6]$ octahedra: yellow, C: black, N: green. (-)-Sparteine molecules omitted for clarity (right).

It is intriguing to notice that the supramolecular packing of the BTC molecules into columnar structures further allows the formation of hydrogen bonding interactions between the carboxylate moieties of the BTC molecules and adjacent phosphate-based terminal oxygen sites on the$\{Mo_6\}_2$ clusters. This strongly suggests that the interactions between the aromatic rings are strong enough to form these columnar structures rather than occupying the lattice as discrete, non-connected molecules. In line with these observations is the distance between adjacent BTC rings observed in compound **17**, with minimum centroid separations of 3.48 Å. It is furthermore noteworthy that these BTC columns seem

to "template" the framework formation *via* non-coordinative, supramolecular interactions. It can be speculated that the assembly of the present framework proceeds by the formation of the BTC columns which in turn enable multiple interactions of this supramolecular entity with the discrete $\{Mo_6\}_2$ cluster anions and the (-)-sparteine cations and eventually allow the precise structural arrangement to be established.

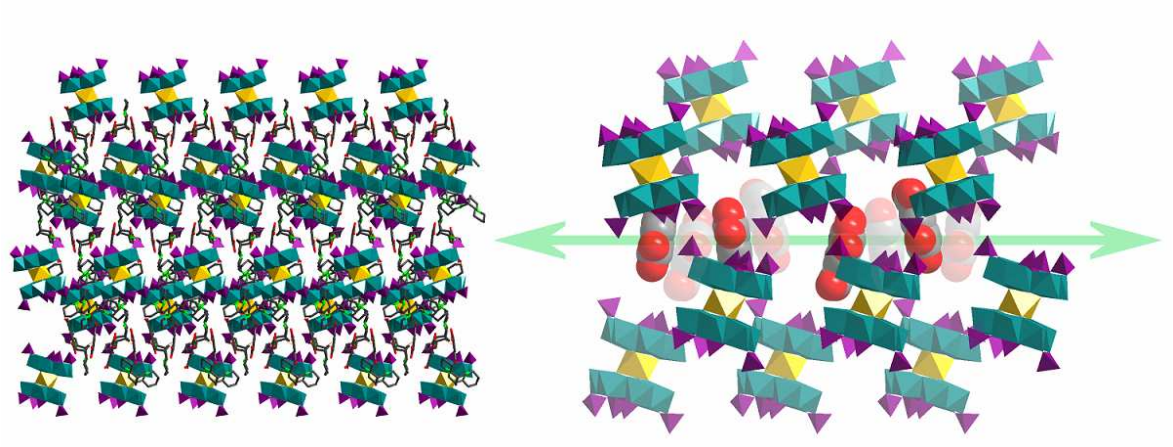

Figure 59: Representation of the BTC columns propagating along the channels in compound **17**. View along the crystallographic *b*-axis (left), illustrating the complex arrangement of the three building blocks, (-)-sparteine, 1,3,5-benzenetricarboxylic acid and $\{Mo_6\}_2$ cluster anions. The detailed illustration (right) highlights the arrangement of BTC molecules (space-filling representation) in the pores within the framework. The green arrow emphasises the propagation of the columnar structure along the crystallographic *a*-axis. $[MoO_6]$ octahedra: teal; $[PO_4]$ tetrahedra: purple, $[NaO_6]$ octahedra: yellow, C: black, N: green. (-)-Sparteine omitted for clarity (right).

Of further interest for the supramolecular arrangement of compound **17** is the actual protonation state of the BTC molecules. Although it is not possible to unambiguously assign one precise protonation state to the BTC molecule, the structural evidence and the infra-red data would suggest that the organic triacid molecules in compound **17** co-exist in a range of protonation states. This is indicated by a detailed structural study of the C-O bond lengths in combination with examination of the chemical environment of the carboxylate functions which allow for hydrogen-bonding or complete proton transfer to the basic oxo ligands on the cluster anion. Further evidence for the presence of protonated and deprotonated carboxylic acid functions is provided by FT-IR studies which show peaks at 1715 and 1635 cm^{-1}. These two peak positions are indicative of protonated carboxylic acid functions and of deprotonated carboxylates, respectively. The proton transfer mechanism involved in this process is further supported by the observation of close hydrogen-bonding interactions between BTC carboxylate groups and cluster-based phosphate groups ($d_{O\text{-}O}$ ~ 2.55 – 2.78 Å) which facilitate proton transfer from the BTC to the cluster anion. Detailed

structural analysis of the hydrogen-bonding around the BTC molecules suggests an additional proton transfer mechanism: The BTC molecules not only interact directly with the cluster anion through C-O···H···O-P interactions but can also interact with the cluster through an additional solvent water bridge which connects the organic molecule in the channel to the framework wall, see Figure 60. These hydrogen-bonds between carboxylic acid groups and water ligands (minimum $d_{O\text{-}O}$ ~ 2.67 Å) allow the formation of a vast hydrogen-bonded network which stabilises the BTC positions within the channels and further allows the precise spatial arrangement of clusters and (-)-sparteine cations.

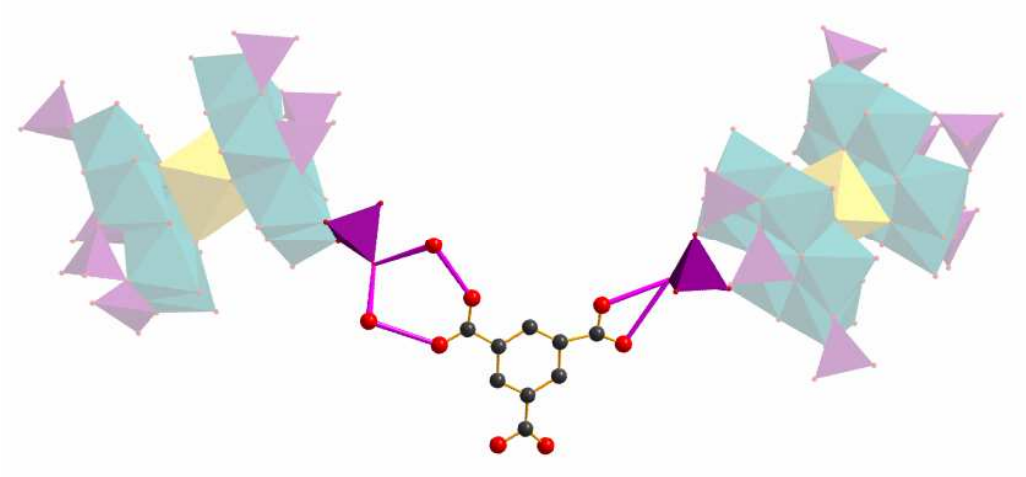

Figure 60: Illustration of a typical binding mode adopted by the BTC molecules in **17**. Emphasised by magenta bonds are the hydrogen-bonded interactions between carboxylate moieties on the BTC groups and the phosphate-based oxo ligands (right) as well as the solvent-water-bridged hydrogen-bonding interactions with an adjacent cluster phosphate group (left). [MoO_6] octahedra: teal, [PO_4] tetrahedra: purple, [NaO_6] octahedra: yellow, C: black, N: green.

Thermogravimetric analysis was performed on compound **17** to verify the amount of solvent water. It was observed that the material typically contained *ca.* 7.5 wt.-% of solvent water which was released by thermal treatment between 20-120 °C. This value corresponds to *ca.* 15 water molecules per unit cell. However, crystallographic studies indicated the presence of ten molecules of solvent water per formula unit which corresponds to 4.8 wt.-% of water. These water molecules are exclusively accommodated in the channels templated by the BTC molecules. Detailed analysis of the crystallographic data showed that each BTC position features occupancy factors of only 50 % so that on average each BTC molecule is disordered over two distinct positions. This in turn creates internal vacancies within the channels which can accommodate the additional solvent water molecules.

Further TGA studies confirmed that compound **17** can release up to 7.5 wt.-% of water when heated to 120 ° C. It was observed that the dehydrated material re-gains its original weight when exposed to ambient atmosphere for 24 h by re-absorbing the solvent water. A series of sorption and desorption cycles showed that the material can reversibly adsorb and desorb *ca.* 7.5 wt.-% of water by dehydrating at 150 ° C and subsequently re-exposing the material to the ambient atmosphere, see Figure 61.

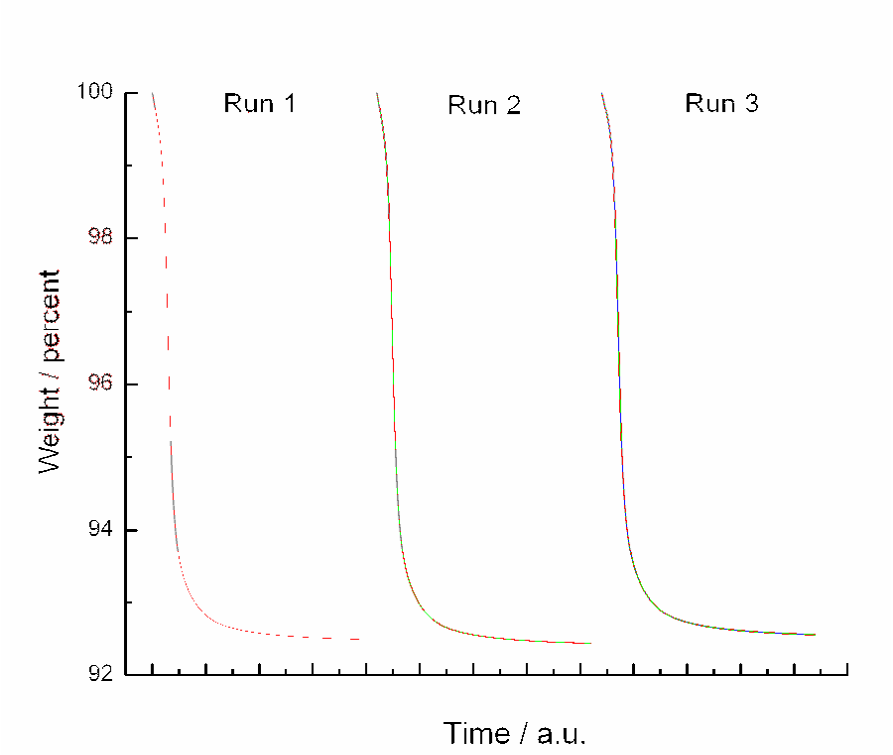

Figure 61: The thermogravimetric analysis of the sorption process of compound **17** shows three consecutive runs on the same sample demonstrating the reversible adsorption and desorption of *ca.* 7.5 wt.-% of solvent water. In the desorption step, the sample was heated in the TGA apparatus to 150 ° C under a flow of nitrogen until no further weight loss was observed. The sample was then cooled to room temperature and exposed to the ambient atmosphere for 24 h to allow for re-adsorption of the solvent water. The desorption process was subsequently repeated to demonstrate full reversibility.

The framework stability was monitored during the sorption and desorption cycles using powder XRD methods to confirm that the structural integrity was retained throughout the process. Initially it was shown that the bulk microcrystalline sample used for the sorption studies was structurally identical to the single crystal data obtained for compound **17**. In the next step the powder XRD pattern of a dehydrated sample was compared with the native material. The peak positions and relative intensities were comparable to the native material; however, the thermal treatment caused a general line broadening which suggested a decreased degree of crystallinity as compared with the native compound **17**. Finally, a

sample of the re-hydrated material was investigated and was virtually identical to the dehydrated sample which further supports the findings and suggests that the decreased long-range order is caused by the thermal treatment at 150 ° C, see Figure 62.

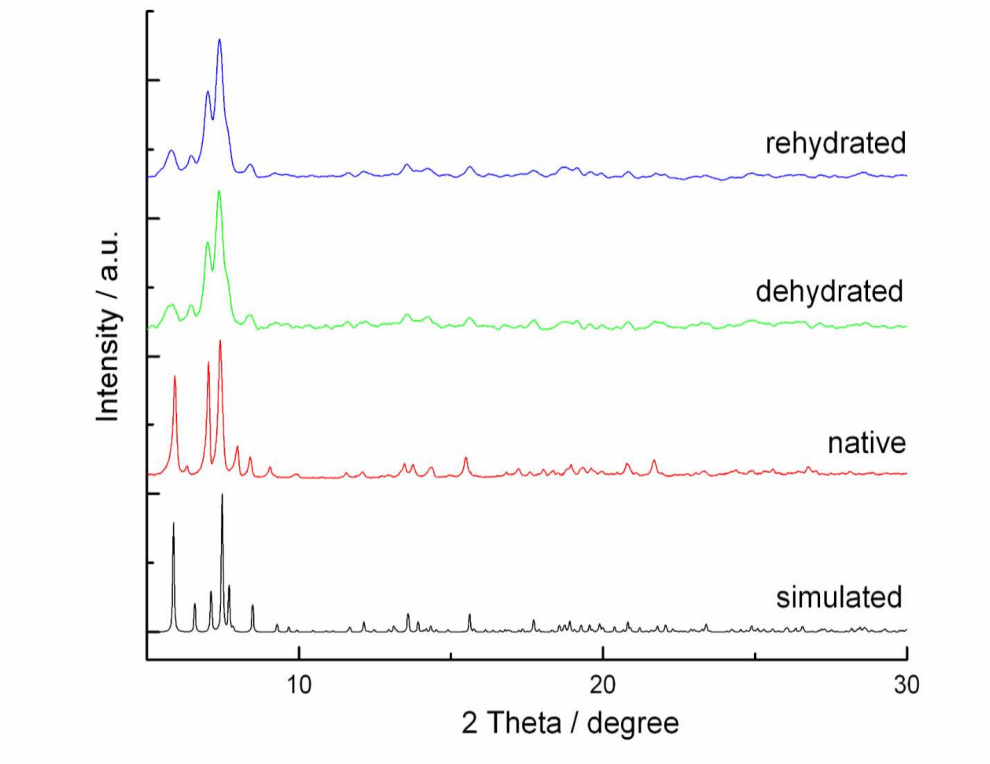

Figure 62: Powder X-ray diffraction patterns of compound **17**. The native material is virtually identical to the simulated pattern calculated from single-crystal XRD data. The dehydrated material features line broadening effects which are most likely due to the thermal treatment during the desorption process. The re-hydrated and dehydrated samples are virtually identical.

In summary it has been shown that the framework formation principles elaborated in the early $\{Mo_6\}_2$ systems can be applied more broadly and in more sophisticated systems. Rigid amines can be used to direct the steric arrangement of cluster anions and in addition can be employed to introduce further functionality such as chirality. It has been established that "weak" supramolecular interactions such as π- π-stacking can affect the overall framework arrangement and can even be used to create open-pore systems which show permanent porosity.

It is interesting to note however, that the ability to form vast hydrogen-bonded networks is caused by the high number of hydrogen-bond acceptor sites located on the cluster surface. It is thus difficult to control or even predict the binding modes a cluster can adopt in combination with a given organic compound.

A more sophisticated approach might be the use of transition metals to target specific multiple binding sites such as chelating oxygen environments created by two adjacent terminal oxygen ligands. This approach might allow utilisation of suitable metal centres to interact with several clusters and thus act as linkers through coordinative covalent bonds.

However, if following this approach it would be vital to select transition metals which support a given binding mode by providing the correct coordination geometry or indeed those which would provide a range of coordination modes. A prime candidate for this study would, therefore, be silver (I) which supports ligand environments ranging from linear, trigonal planar and square planar to pentagonal and octahedral. The following section thus aims to exploit this potential by studying the interactions between silver cations and isopolyoxometalates in organic solvents. This approach involves formation of the cluster in aqueous solution and subsequent transfer in to organic solvents which allows the exclusive utilisation of one specific, pre-assembled cluster type. Further, the use of organic solvents eliminates a range of reaction parameters such as pH and hydrogen-bonding effects through solvent water molecules.

3.5 Silver-linked polyoxometalate assemblies: From chains to frameworks

3.5.1 Silver-linked assemblies of $[V_{10}O_{28}]^{6-}$

It has been demonstrated before that the assembly of polyoxometalate-based frameworks in aqueous solution can be influenced by a range of reaction parameters including the solution pH, the type of acid, ionic strength of the solution and the presence of non-innocent counter ions. Further the solvent water itself can interact with the cations and thus compete with the cluster anions to form coordinative interactions. It can, therefore, be advantageous to synthesise the cluster of choice in aqueous solution and subsequently transfer it into organic solvents *via* an ion-exchange process prior to carrying out the desired framework synthesis.

Typically, the transfer of polyoxometalates from aqueous to organic media is achieved by precipitation from aqueous solution using bulky organo-cations such as *n*-tetrabutyl ammonium (TBA) halides. A water-insoluble material is obtained which can be re-dissolved in polar coordinating solvents such as acetonitrile, DMSO or DMF. The advantage of using polyoxometalate clusters in organic solvents is the elimination of several reaction parameters such as pH and the presence of non-innocent counter ions such as Na^+, K^+ which interfere with the assembly of frameworks and the coordination of transition metals. This approach allows utilisation of the clusters in a more restricted reaction environment and gives increased control over the general reactivity towards transition metal linkers such as silver(I).

3.5.1.1 Formation of a 1D chain $([Ag_3(DMSO)_6][Ag_1(DMSO)_3][H_2V_{10}O_{28}])_\infty$ (**18**)

The first isopolyoxometalate system investigated in organic solution was the decavanadate cluster $[H_3V_{10}O_{28}]^{3-}$ which was discussed briefly in section 1.4.1.2. The TBA salt of the cluster, $(TBA)_3[H_3V_{10}O_{28}]$ was reacted with silver nitrate in DMSO and orange-red crystals could be isolated after several days. Structural analysis of the single crystal X-ray diffraction data gave the composition as $Ag_4(DMSO)_9[H_2V_{10}O_{28}]\cdot 1DMSO$ (**18**) and

indicated the presence of $\{V_{10}\}$ decavanadate units as inorganic building blocks. Bond valence sum calculations indicated that all vanadium centres are fully oxidised in oxidationstate +V. In addition, the presence of two protons per cluster unit was verified, located on oxygen O6 and O10, respectively.This indicates that during the reaction, the cluster anion is deprotonated so that the product contains diprotonated $\{V_{10}\}$ units whereas the starting material contained three protons per cluster unit.

The $\{V_{10}\}$ clusters are composed of octahedral $[VO_6]$ units which are connected exclusively by edge-sharing modes. The central building motif is the well-established $[V_6O_{19}]^{8-}$ cluster anion which is extended in one hemisphere by adding a $[V_2O_{10}]$ fragment to the central belt. The assembly is further stabilised by the addition of two $\{V_1\}$ fragments above and below the central plane which share edges with adjacent V-centered octahedra. As a consequence of this structural arrangement, three different oxygen types can be identified by their distinctive V-O interaction distance. Each vanadium (V) centre features a terminal V=O bond with characteristic V-O distances of *ca.* 1.6 Å. Bridging oxygen ligands which connect two or three V centres are found on the outside surface of the cluster and show typical coordination bond lengths of *ca.* 1.7 – 2.0 Å, depending on the exact coordination environment. The internal oxygen ligands which connect six V centres are characterised by elongated bonding V-O distances of *ca.* 2.05 – 2.40 Å owing to the demanding coordination environment and the multitude of coordinating V(V) centres, see Figure 63.

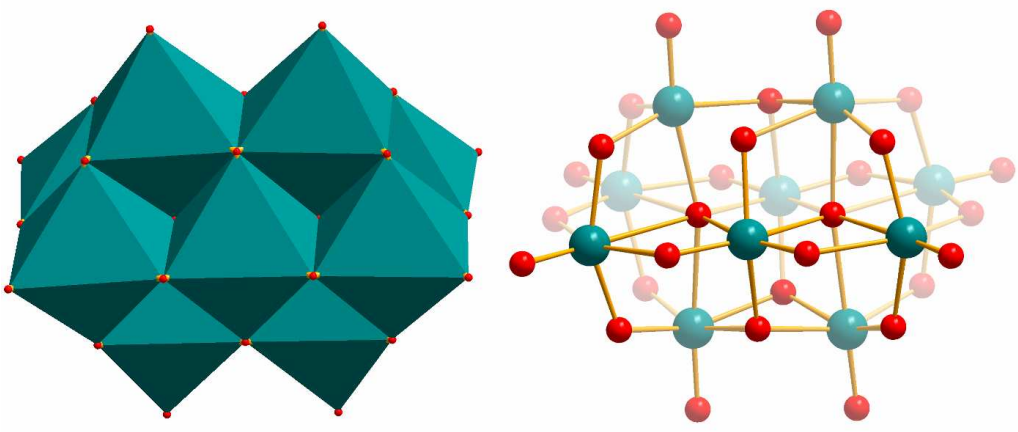

Figure 63: Illustration of the metal-oxide framework of the decavanadate cluster $[H_2V_{10}O_{28}]^{4-}$ in **18**. The polyhedral illustration (left) shows the connectivity of the $[VO_6]$ octahedra which are linked through edge-sharing modes only. The ball-and-stick representation (right) emphasises the oxygen binding modes which can be separated into terminal ligands ($d_{V\text{-}O}$ ~ 1.6 Å), bridging oxygen ligands on the outside of the cluster ($d_{V\text{-}O}$ ~ 1.7 – 2.0 Å) and internal bridging oxygens ($d_{V\text{-}O}$ ~ 2.05 -2.4 Å). $[VO_6]$ octahedra and V: teal, O: red. Hydrogen atoms omitted for clarity.

Structural analysis of the crystallographic data obtained for compound **18** reveals that the cluster binds to three sets of silver ligands which results in the formation of supramolecular 1D zigzag-chains in the solid state. In these assemblies, each $\{V_{10}\}$ unit is connected to two adjacent cluster units *via* two trinuclear silver(I) DMSO assemblies, $[Ag_3(DMSO)_6]^{3+}$, which act as bridges to support the arrangement of the $\{V_{10}\}$ units, see Figure 64. In addition, the non-connected hemisphere of the cluster is capped by a monomeric $[Ag(DMSO)_3]$ unit which shields the cluster from further supramolecular interactions and allows the formation of 1D chains rather than supramolecular arrangements of higher dimensionality.

Detailed analysis of the interaction mode between the silver centres and the $\{V_{10}\}$ isovanadate reveals that as a common principle, all silver ions interact exclusively with bridging oxygen ligands. This effect illustrates the higher nucleophilicity of the bridging oxo ligands as compared with the less nucleophilic terminal oxygen centres. Although all silver centres share these common coordination sites, the exact coordination environment of every Ag(I) ion is unique and requires further discussion.

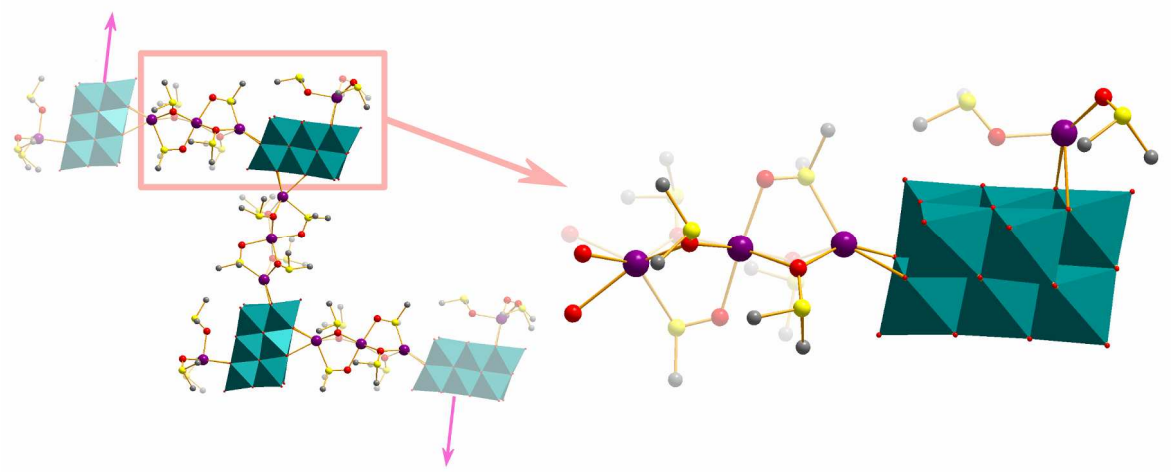

Figure 64: Illustration of the supramolecular zigzag-chains observed in compound **18**. The illustration of the connectivity between the $\{V_{10}\}$ cluster anions (teal) and the $\{Ag_2\}$ silver trimers (left) shows the distinct linkage where one $\{Ag_3\}$ unit connects two clusters by coordinating to one "side" face and one "front" face of the cluster anion, thus creating a angle of *ca.* 86.9 °. Further the capping mode of the additional $\{Ag_1\}$ unit illustrates the "shielding" character of this assembly which inhibits any further supramolecular interactions of the $\{V_{10}\}$ cluster and thus allows the isolation of a 1D chain. Magenta arrows indicate the direction of chain growth. The detailed illustration of the unique $\{Ag_3\}\{Ag_1\}\{V_{10}\}$ building unit (right) illustrates connectivity between silver linkers and cluster scaffold which allows the formation of the 1D chain motifs in the solid state. $\{V_{10}\}$: teal, Ag: purple, O: red, S: yellow, C: grey. Hydrogen atoms were omitted for clarity.

The $\{Ag_1\}$ capping unit $[Ag(DMSO)_3]^+$ forms two coordinative interactions with bridging oxygens to bind to the $\{V_{10}\}$ cluster anion with Ag-O coordination bond lengths of 2.57 Å and 2.67 Å, respectively. In addition, the coordination sphere of the silver centre is filled with three DMSO ligands which bind to the Ag ion by engaging their oxygen atoms in coordinative interactions. The resulting Ag-O coordination bonds are of comparable length between 2.30 and 2.40 Å. As a result, the Ag(I) atom is located within an all-oxygen, fivefold coordination motif which resembles a highly distorted trigonal bipyramid. Due to the sterically demanding coordination environment of the $\{V_{10}\}$ unit, the angle between the two apical oxygen positions and the central Ag ion is reduced from 180 ° to 159 °. In addition, the angles between the equatorial oxo positions and the silver(I) centre are irregular and diverge from the expected 120 ° in an ideal trigonal bipyramid to 93.8 °, 113.5 ° and 150.6 °, see Figure 65. In effect, this coordination arrangement creates an $[Ag(DMSO)_3]^+$ cap which shields one face of the $\{V_{10}\}$ cluster from any further interaction through coordination or hydrogen bonding and thus allows growth only through the two additional $\{Ag_3\}$ linkers.

Structural analysis of the $\{Ag_3\}$ linking units shows an almost linear arrangement between the three adjacent silver centres with an Ag-Ag-Ag angle of *ca.* 171 °. This structure is reinforced by six DMSO ligands which act as bridges between the silver centres, see Figure 65. Four DMSO ligands act as μ_2-bridges between adjacent silver centres *via* their oxygen donor atoms and are engaged in Ag-O coordination bonds with $d_{Ag\text{-}O}$ ~2.36 – 2.51 Å. Two additional DMSO ligands act as η^2-bridges between the central and the peripheral silver centres. These η^2-bridging DMSO molecules coordinate to the peripheral Ag centres *via* Ag-S coordinative interactions ($d_{Ag\text{-}S}$ ~2.59 Å and 2.67 Å). In addition, the two η^2-DMSO units form Ag-O coordination bonds to the central silver(I) ion ($d_{Ag\text{-}O}$ ~2.41 Å and 2.45 Å) so that this transition metal centre is coordinated exclusively by oxygen ligands in an octahedral coordination environment. It is interesting to note that the arrangement of the DMSO ligands around the Ag(I) centre is such that the equatorial positions are occupied by μ_2-bridging oxo ligands whereas at the apical positions the η^2-bridging DMSO molecules bind *via* their terminal oxygen centre, see Figure 65, right. This precise coordination environment around the central silver ion results in Ag-Ag distances of 3.51Å and 3.59 Å respectively. This small but significant discrepancy observed for the silver-silver separation is a direct result of the interactions of the peripheral Ag(I) centres with the $\{V_{10}\}$ cluster anions. One Ag(I) linker forms three Ag-O bonds with bridging oxo ligands

on the $\{V_{10}\}$ surface. Three different Ag-O bonding distances are observed (2.38 Å, 2.62 Å and 2.71 Å, respectively) which reflect the difference in strength of the three coordinative bonds. As a direct result of this threefold interaction, the silver centre is displaced further from the central silver and results in a Ag-Ag-distance of 3.59 Å. The resulting coordination environment created by five oxo and one sulphur ligand is best described as a distorted trigonal prism with the silver(I) atom located in the centre. The Ag ion located on the opposite side of the $\{Ag_3\}$ linker interacts with the adjacent $\{V_{10}\}$ cluster *via* two Ag-O coordination bonds only ($d_{Ag\text{-}O}$ = 2.43 Å and 2.49 Å respectively) and therefore is located closer to the central silver ($d_{Ag\text{-}Ag}$ = 3.51 Å). The coordination geometry of this transition metal centre can be described as a distorted square pyramid where four oxo-ligands form the base and the sulphur-ligand is positioned at the apex, see Figure 65, right.

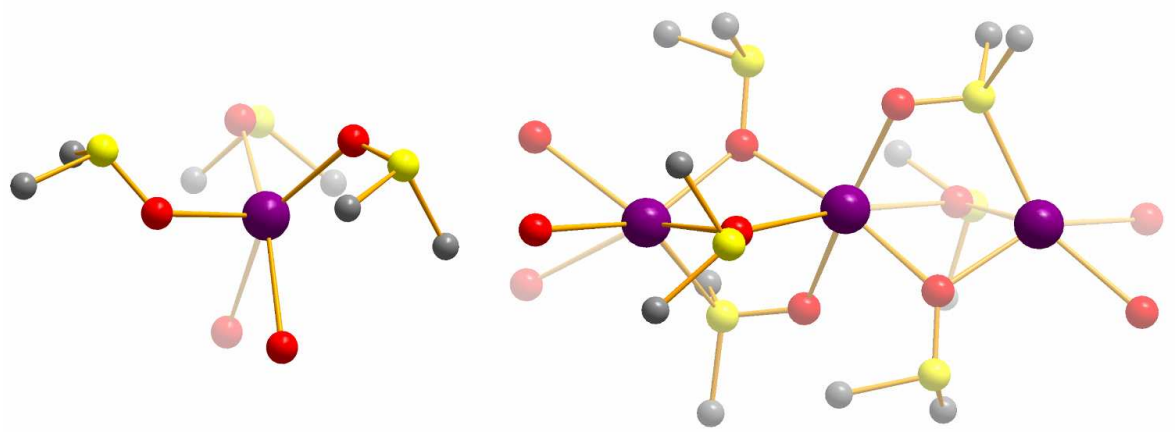

Figure 65: Illustration of the capping $\{Ag_1\}$ unit (left) and of the linking $\{Ag_3\}$ unit (right) which are observed in compound **18**. The capping unit $[Ag(DMSO)_3]^+$ features three DMSO ligands on one side of the silver(I) centre which bind through terminal oxygen ligands. In the other coordination hemisphere of the silver centre, two bridging oxygen ligands of the $\{V_{10}\}$ cluster anion are engaged in Ag-O interactions. The $\{Ag_3\}$ motif (right) features three Ag(I) centres in trigonal prismatic (left), octahedral (centre) and square pyramidal (right) coordination environments. The two coordination modes of the DMSO molecules should be noted, where these ligands act as either μ_2-bridges through a connecting oxygen site, or as η^2-ligands by coordination through the oxygen and sulphur centre. Colour scheme: Ag: purple, O: red, S: yellow, C: grey.

In the lattice, every $\{V_{10}\}$ unit binds two $\{Ag_3\}$ linking units on two adjacent faces of the cluster so, in effect, a dihedral angle of 86.9 ° is established. As a result, infinite chains of the composition $(\{Ag_3\}[\{V_{10}\}\{Ag_1\}])_\infty$ are formed which run along the crystallographic *b*-axis, see Figure 66. It is interesting to note that the positive and negative charges within one chain cancel each other out and thus the supramolecular chains are neutral. As a consequence, no additional counterions have to be incorporated in the crystal structure and

the result is a dense packing of the chains in the crystallographic *ac*-plane. The angular shape of the chains allows the formation of layers where the apex of one chain slots into a void space of the adjacent chain, see Figure 66, left. The non-charged character of the chains is furthermore exemplified by the lack of inter-chain interactions, with the absence of any attractive electrostatic or hydrogen-bonding interactions. Thus an intra-layer spacing of *ca.* 7.6 Å between neighbouring $\{V_{10}\}$ cluster units is achieved. The spacing between layers (*ca.* 7.9 Å) is only marginally larger. As discussed above, this phenomenon is due to the absence of any "pillaring" counterions, see Figure 66, right.

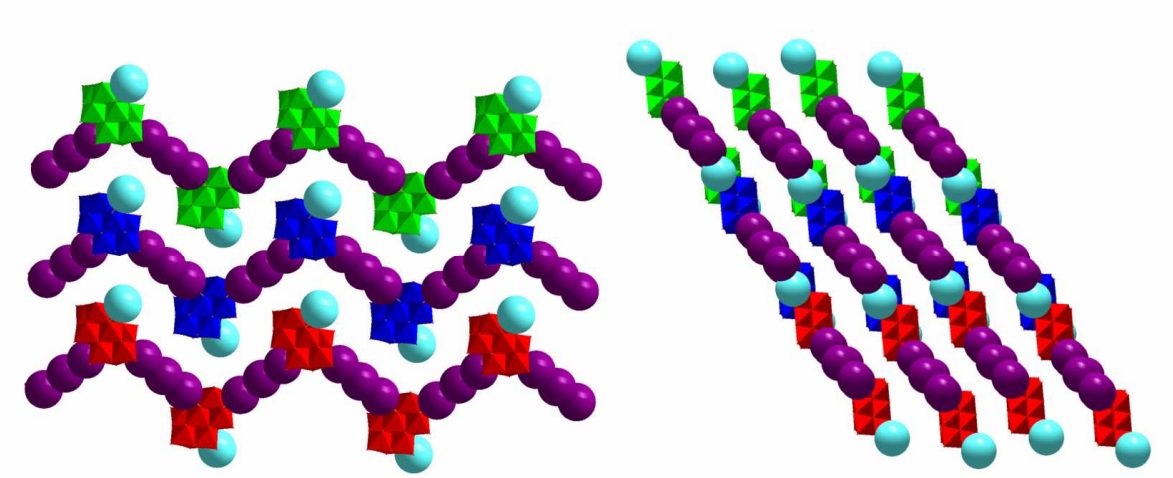

Figure 66: Illustration of the supramolecular $[\{Ag_3\}\{V_{10}\}\{Ag_1\}]$ chains in compound **18**. The view along the crystallographic *a*-axis (left) illustrates the chains formed by the connection of $\{V_{10}\}$ decavanadate clusters (green, blue and red polyhedra) *via* $\{Ag_3\}$ linkers (purple spheres). The non-linked hemispheres of the clusters are "shielded" by monomeric $\{Ag_1\}$ groups (light blue spheres). The intra-chain spacing between adjacent $\{V_{10}\}$ clusters is *ca.* 7.6 Å. The view along the crystallographic *b*-axis (right) illustrates the arrangement of the polymeric neutral chains into layers with an inter-layer spacing of *ca.* 7.9 Å.

In conclusion it has been demonstrated that supramolecular assemblies can be designed based on silver-coordination to isopolyoxovanadate clusters. It has been shown that the silver centres can adopt various coordination modes and can thus act as versatile linkers or act as capping sites which prevent growth in a given direction and allow the isolation of 1D chains.

The diversity of the system was demonstrated by the discovery of a related structure of higher dimensionality, where the $\{V_{10}\}$ cluster anions are cross-linked by silver ions into a 2D network structure. This structure will be discussed in detail in the following section.

3.5.1.2 Formation of a 2D net $([Ag_3(DMSO)_6][Ag_1(DMSO)_2][H_2V_{10}O_{28}])_\infty$ (**19**)

Exhaustive examination of the silver(I)-decavanadate reaction system showed that a second $\{V_{10}\}$-based compound can be isolated under conditions similar to the synthesis of compound **18**. The material was obtained as orange crystals and structural analysis of the single crystal X-ray diffraction data of compound **19** gave the formula $[Ag_3(DMSO)_6][Ag_1(DMSO)_2][H_2V_{10}O_{28}]\cdot 1DMSO$. Investigation of the structural composition indicated the presence of diprotonated decavanadate cluster units which were isostructural to the cluster anions observed in compound **18**. The cluster shell is assembled from ten $[VO_6]$ octahedral units which are exclusively linked through edge-sharing connections. Two protons were located by BVS calculations (bound to O6 and O6A, respectively) and all vanadium centres were found to be fully oxidised in oxidation state +V. The resulting V-O interactions can be separated into three distinct groups. Every V(V) centre establishes one short terminal V=O bond ($d_{V\text{-}O}$ ~ 1.6 Å) which points away from the cluster core. The bridging μ_2- and μ_3-oxygen ligands on the cluster surface feature typical V-O distances between 1.7 Å and 2.1 Å. This wide range is caused by the rigid metal-oxide framework and the varying strength of the V-O interactions so that some interactions are favoured over others. As a result, the bridging oxygen ligands are not always located symmetrically between the participating vanadium (V) centres but can be shifted in the direction of the most favoured orbital overlap. The third type of oxygen ligand ($d_{V\text{-}O}$ ~ 2.1 - 2.4 Å) is located in the centre of each cluster and connects six vanadium (V) metal ions which are arranged around the oxo ligand in an octahedral fashion.

Structurally, compound **19** is comparable to the 1D chain motifs in **18** in so far as the $\{V_{10}\}$ cluster anions are linked with $\{Ag_3\}$ connecting groups. However, in contrast to the previous chain structure, compound **19** does not feature capping $\{Ag_1\}$ groups. Instead monomeric $[Ag(DMSO)_2]$ bridges are observed which create additional linkages between neighbouring cluster anions so that a 2D network is formed, see Figure 67, left. The trinuclear $[Ag_3(DMSO)_6]^{3+}$ bridges coordinate to opposite faces of the $\{V_{10}\}$ clusters so that a linear linkage between the decavanadate ions is established.

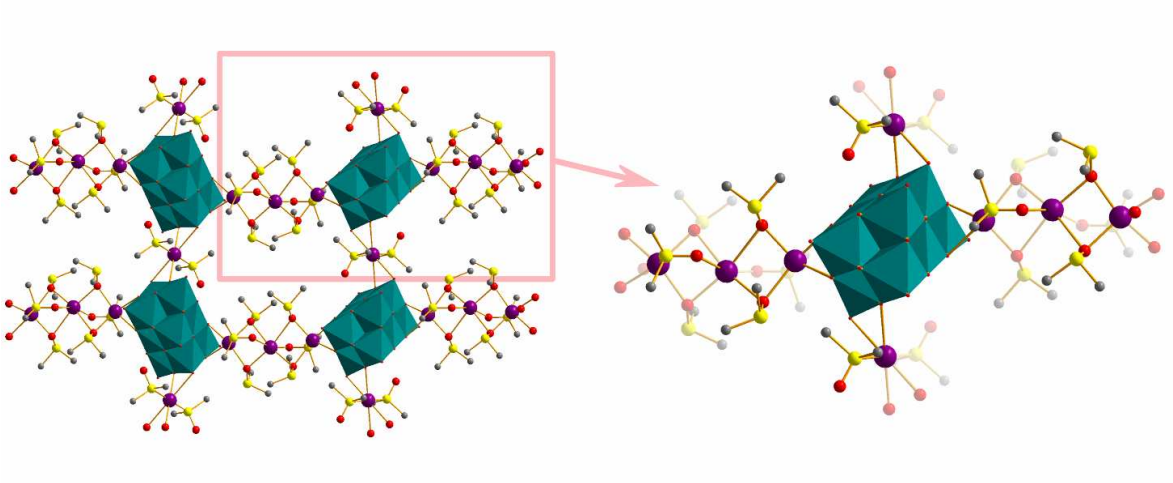

Figure 67: Illustration of the network structure of compound **19**. The connectivity between $\{V_{10}\}$ cluster ions is illustrated on the left: each decavanadate cluster is coordinated by two $\{Ag_3\}$ groups and two additional $\{Ag_1\}$ monomers thus creating a 2D network. The detailed view (right) illustrates the binding modes of the $[Ag_3(DMSO)_6]^{3+}$ bridges and the additional $[Ag_1(DMSO)_2]$ linking units on opposite faces of the cluster anions. The linear arrangement of clusters in the cross-linked network is a result of the perpendicular arrangement of the $\{Ag_1\}$ and $\{Ag_3\}$ linkers. $\{V_{10}\}$: teal polyhedra, Ag: purple, C: grey, O: red, S: yellow. Hydrogen atoms omitted for clarity.

Detailed analysis of the $\{Ag_3\}$ linkers in **19** shows a similar arrangement of silver centres and DMSO linkers to the supramolecular $\{Ag_3\}$ silver bridges in compound **18**. However, small but distinct differences in the structural arrangement and in the interactions of the silver centres with the cluster anions result in subtle discrepancies between the overall structures. The three silver(I) centres are arranged in an almost linear fashion with an Ag-Ag-Ag angle of *ca.* 165.7 °. The central silver(I) ion is connected to the two peripheral Ag(I) centres by six DMSO molecules. Four of the DMSO ligands act as μ_2-bridges by linking the silver centres through μ_2-oxygen interactions. The Ag-O_{DMSO} bond lengths observed are between 2.36 Å and 2.85 Å and thus range from strong to relatively weak coordinative bonds. In addition to the four oxygen-bridging DMSO molecules two additional η^2-DMSO molecules fill the silver coordination spheres and link the three silver ions. This binding motif is achieved by coordination of the DMSO-oxygen atom to the central silver ion ($d_{Ag\text{-}O}$ =2.31 Å) whereas the peripheral silver ion is connected by coordination of the sulphur atom with silver-sulphur coordination bond lengths of $d_{Ag\text{-}S}$ ~ 2.57 Å. As a result, the central silver atom is exclusively coordinated by oxygen ligands in an octahedral fashion. It is interesting to note that the $\{Ag_3\}$ linker in **19** is more symmetric than its counterpart in compound **18** where the different interactions of the peripheral silver with the cluster oxo ligands result in a decreased symmetry. In compound **19** both

peripheral silver centres feature similar interactions with the cluster anion and form two Ag-O coordination bonds with μ_2-bridging oxo ligands on the cluster surface. This arrangement results in Ag-O separations of 2.36 Å and 2.54 Å. In addition a third, long-range Ag-O interaction with a third μ_2-oxo centre ($d_{Ag\text{-}O}$ = 2.96 Å) is observed. Therefore, the coordination environment around both peripheral silver(I) groups can be described as a trigonal prismatic arrangement where one face of the prism is created by three cluster oxo ligands and the other face is formed by two DMSO oxygen atoms and one DMSO sulphur ligand, see Figure 68. Owing to the symmetric arrangement of the peripheral silver(I) centres around the central silver ion, identical Ag-Ag distances of 3.48 Å are formed. In summary, the $\{Ag_3\}$ linking units connect adjacent $\{V_{10}\}$ cluster anions into infinite 1D linear chains which run along the crystallographic *b*-axis.

The overall supramolecular architecture of compound **19** however, is not a 1D chain but a 2D network of cross-linked decavanadate units. Vital for the formation of this net is a second connection between adjacent cluster anions which is established by a monomeric $[Ag(DMSO)_2]^+$ bridge. This moiety forms four coordinative bonds with two neighbouring decavanadate units so that each cluster unit is engaged in two Ag-O interactions through one bridging μ_2-oxo and one terminal V=O ligand. The resulting Ag-O bridges are symmetry-related and thus feature a bond length of $d_{Ag\text{-}\mu2\text{-}O}$ = 2.64 Å and $d_{Ag\text{-}O\text{-}terminal}$ = 2.80 Å. Another consequence of this symmetry is the linear O-Ag-O arrangement between the silver centre and the two equivalent cluster oxygens with an angle of 180 °. The silver coordination sphere is filled by two additional DMSO ligands which are arranged perpendicular to the direction of network growth. As a result, the central silver ion is coordinated by six ligands in a distorted octahedral coordination shell. The DMSO ligands are disordered over two positions and adopt two coordination modes by binding to the silver centre through either the sulphur atom or through the oxygen donor, see Figure 68. Two distinct coordination environments are created with $Ag\text{-}S_{DMSO}$ bond lengths of 2.45 Å and $Ag\text{-}O_{DMSO}$ bonding distances of 2.31 Å, respectively. It is notable that both coordination modes result in a octahedral arrangement around the silver(I) centre which, under the given coordination restraints, seems to be most favoured.

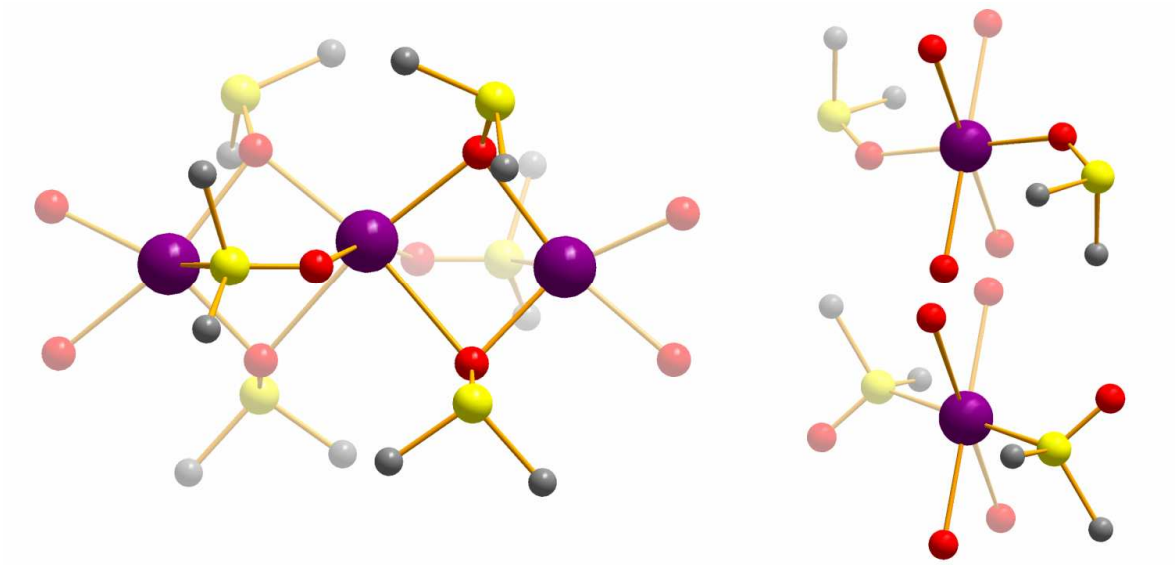

Figure 68: Detailed illustration of the trinuclear $\{Ag_3\}$ linker (left) and the mononuclear $\{Ag_1\}$ linkers (right) observed in compound **19**. The $\{Ag_3\}$ unit $[Ag_3(DMSO)_6]^{3+}$ features two distinct silver coordination environments. The central silver is coordinated octahedrally by an all-oxygen environment created by six DMSO ligands. Four DMSO ligands act as μ_2-oxo-bridging ligands between the peripheral and the central silver, whereas two additional η^2-DMSO ligands bind to the central silver *via* their oxygen atom and connect to the peripheral silver unit through the sulphur atom. The peripheral silver ions feature a trigonal prismatic coordination environment. The detailed view of the monomeric $\{Ag_1\}$ linker $[Ag(DMSO)_2]^+$ (right) illustrates the two different coordination modes adopted by the disordered DMSO ligands which coordinate either through the sulphur atoms (bottom) or through the oxygen atoms (top). The silver centre further coordinates to two oxo ligands from each of the two connected $\{V_{10}\}$ clusters, resulting in an octahedral coordination environment.

The arrangement of decavanadate ions in a 2D net results in distances between the cluster ions of *ca.* 11.0 Å along the $\{Ag_3\}$-bridged chains and of *ca.* 5.1 Å between the $\{Ag_1\}$-connected clusters. In the lattice the clusters are arranged in a parallel fashion along the $\{Ag_1\}$-linked direction of propagation, whereas a torsion angle of ca. 82.2 ° is observed between neighbouring clusters within the $\{Ag_3\}$-bridged chain assemblies. This tilted arrangement is a result of the coordination of four silver linkers per cluster anion which bind to four of the cluster faces, thus directing the supramolecular arrangement of the $\{V_{10}\}$ units, see Figure 69. Consequently, this coordination behaviour of the silver linkers results in the formation of a 2D network which extends along the crystallographic *ab*-plane. Topologically, the $\{V_{10}\}$ cluster anions represent four-connected nodes in the supramolecular coordination network which are linked in one direction by two-connected $\{Ag_3\}$ linkers and cross-linked into a second direction by two-connected $\{Ag_1\}$ monomers. The close packing of $\{Ag_1\}$ and $\{Ag_3\}$ linkers around the central cluster anion does not

allow the creation of internal voids and thus only one additional DMSO solvent molecule can be accommodated per unit cell. A layered arrangement of the 2D network structure along the crystallographic *a*-axis can be observed with a minimum spacing of *ca.* 4.8 Å. This close packing can be established since there are no repulsive electrostatic interactions as each layer is neutral. In addition, no further counterions have to be accommodated in the structure and thus a close-packing of the layers of 2D nets can be formed, see Figure 69.

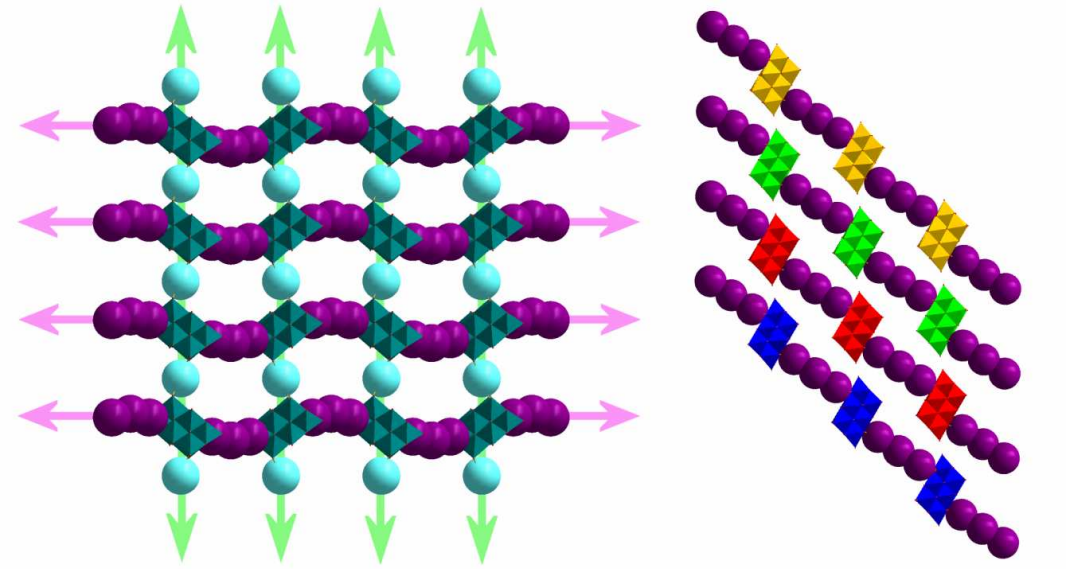

Figure 69: Illustration of the supramolecular network arrangement in compound **19**. The view along the crystallographic *b*-axis (left) shows the cross-linking of $\{V_{10}\}$ clusters (teal) by trinuclear $\{Ag_3\}$ units (purple spheres) and through $\{Ag_1\}$ linkers (light blue spheres). The parallel arrangement of the cluster anions along the $\{Ag_1\}$-linked chains is indicated by green arrows. The tilted arrangement along the $\{Ag_3\}$-connected chain is emphasised by magenta arrows. The view along the crystallographic *a*-axis (right) highlights the layered arrangement, the $\{V_{10}\}$ clusters within different layers are coloured in blue, red, green and yellow. DMSO ligands are omitted for clarity.

It is interesting to note that the formation of compounds **18** and **19** can only be achieved by an *in situ* deprotonation process which involves loss of one proton from the precursor $[H_3V_{10}O_{28}]^{3-}$ to create the final cluster composition $[H_2V_{10}O_{28}]^{4-}$. This process is facilitated by the addition of a small amount of water to the organic reaction mixture which might act as a proton acceptor or enable proton transfer to another cluster unit to form the well-known tetra-protonated species $[H_4V_{10}O_{28}]^{2-}$. This feature demonstrates the ability of the system to undergo a chemical re-arrangement before the framework self-assembly occurs so as to allow for the right charge-balance within the system. In addition, this observation provides vital insight into the formation mechanism of this type of complex systems and strongly suggests that similar processes can be achieved using similar protonated isopolyoxometalate systems in organic solvents.

In conclusion, it has been demonstrated that several supramolecular assemblies can be formed based on linking isopolyoxovanadate clusters with silver-based linking units. The clusters can interact with the transition metals *via* coordinative bonds which then allow cross-linking through DMSO-mediated silver linking modes. In addition it has been shown that monomeric silver units can either be employed as capping ligands which inhibit further growth in a given direction and thus allow isolation of 1D chain assemblies (**18**). On the other hand it has been demonstrated that under similar reaction conditions monomeric silver groups can act as linkers and interact with two neighbouring $\{V_{10}\}$ clusters to form a 2D network which underpins the versatility of silver as a prime candidate for linking discrete clusters into supramolecular framework materials. This feature further illustrates the ability of Ag(I) to interact with the cluster oxygen ligands by adopting various coordination geometries.

3.5.1.3 Formation of a metatungstate-based 3D porous network (**20**)

Previous studies and a thorough review of the current literature strongly suggested that silver(I) centres favour interactions with isopolyoxometalates over binding to heteropolyoxometalate clusters. In particular the formation of a range of silver-linked $[Mo_8O_{24}]^{4-}$ assemblies[86] and the isolation of two silver-$\{V_{10}\}$ architectures (see section 3.4.1) supported these findings and inspired further research into the self-assembly of silver(I)-linked isopolyoxometalate frameworks. Geometric considerations furthermore suggested that a highly symmetrical cluster unit might facilitate the formation of high-dimensionality frameworks as it does not feature any preferential spatial orientation which would allow the transition metal to establish connections in one favoured direction only. The use of a cluster anion with the ability to reversibly bind protons would allow the system to "self-adjust" the cluster charge so as to create the preferred protonation state under the given self-assembly conditions similar to the procedure employed in the synthesis of the $\{V_{10}\}$-based compounds. Furthermore, the use of a tungsten-based polyoxometalate cluster as the inorganic building blocks was thought to provide a structurally stable framework backbone since polyoxotungstates are amongst the most stable POM structures, due to the strong tungsten-oxo coordination bonds which result in the formation of a rigid cluster shell. In addition, the cluster surface typically features a multitude of oxo-ligands which provide an excellent oxygen coordination environment for

silver ions and thus facilitate cross-linking of the cluster units. Based on these considerations, α-metatungstate $[H_2W_{12}O_{40}]^{6-}$ was identified as a promising candidate which features all the attributes described above. In detail, the cluster is constructed from twelve $[WO_6]$ octahedra which utilise strong W-O coordination bonds in the assembly of the cluster shell. Further, the anion can be protonated so that between two and five protons are located on the metal-oxo framework. The cluster is highly symmetrical and resembles the Keggin cluster with its tetrahedral symmetry making it an ideal candidate for the coordination of a set of transition metals, see Figure 70.

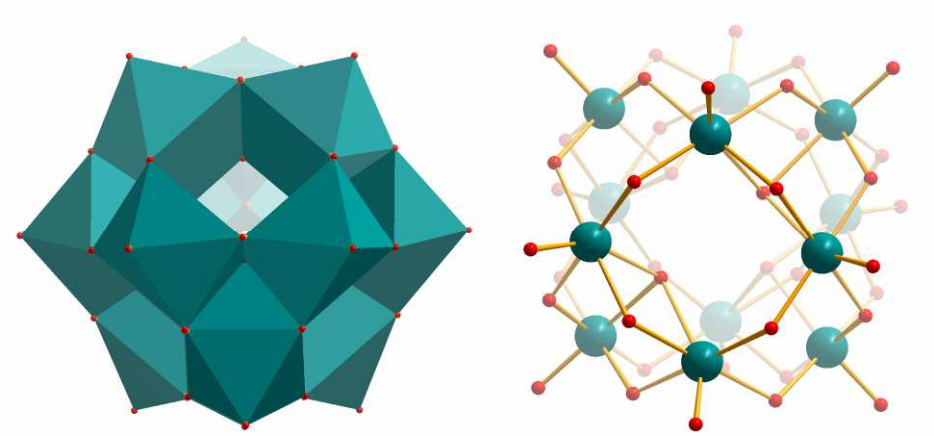

Figure 70: Illustration of the α-metatungstate cluster $[H_2W_{12}O_{40}]^{6-}$. The polyhedral representation (left) illustrates the connectivity between the $[WO_6]$ units which are connected exclusively through edge-sharing modes. Each tungsten centre features one W=O terminal oxo ligand. The ball-and-stick representation (right) illustrates the oxygen coordination environments as well as the central cavity which contains two protons in a tetrahedral oxygen environment. Furthermore, the cluster can bind up to three additional protons to the cluster surface and thus allows selective protonation depending on the reaction conditions. Colour scheme: $[WO_6]$ polyhedra and W: teal, O: red.

In order to study the interactions of α-metatungstate with silver(I) ions, the alkylammonium salt $(TBA)_4[H_4W_{12}O_{40}]$ was synthesised by precipitation of the cluster anion from aqueous solution. The reaction of $(TBA)_4[H_4W_{12}O_{40}]$ with silver(I) nitrate in acetonitrile in the presence of aqueous nitric acid resulted in the formation of colourless, hexagonal crystals which were analysed using single crystal X-ray diffractometry. Structural analysis gave the composition $[Ag(CH_3CN)_4][Ag_2(CH_3CN)_4][H_3W_{12}O_{40}]$ (**20**). Detailed investigation of the inorganic building block confirmed that the structural integrity of the α-metatungstate unit was retained. The cluster can be rationalised based on the assembly of four $[W_3O_{13}]$ triads which are arranged in a tetrahedral fashion so that each metal centre is located on the corner of a truncated tetrahedron, see Figure 70.

All tungsten centres are in oxidation state +VI and are thus fully oxidised. In addition, the addenda atoms are coordinated by six oxygen ligands in an octahedral fashion so that each W(VI) centre features one short W=O bond which points away from the cluster core and which is characterised by typical W-O bond lengths of *ca.* 1.7 Å. In addition, each of the twelve transition metal centres features four equatorial μ_2-oxygen ligands which bridge between adjacent W-centres and, therefore, show elongated W-O coordination bonds of 1.8 – 2.0 Å. This spatial arrangement of the μ_2-bridging oxygen ligands results in the exclusive formation of edge-sharing linkages between the particular $[WO_6]$ octahedra. The sixth coordination position of each $[WO_6]$ octahedron is occupied by internal μ_3-oxo ligands which point into the central cavity of the cluster. The resulting W-O separations are noticeably elongated due to steric demands of the interaction of one oxo site with three tungsten centres. The W-μ_3O distances range from 2.28 Å to 2.37 Å. These internal oxo ligands create a tetrahedral "cage" inside the cluster where two internal protons are located, forming an integral part of the $\{W_{12}\}$ cluster assembly.

In the crystal lattice of **20**, the clusters are not observed as discrete anions but are linked by $[Ag_2(CH_3CN)_4]^{2+}$ units to form an infinite 3D framework. Structurally, this $\{Ag_2\}$ linker can be described as a dinuclear silver-centered unit which is formed by close association of two Ag(I) cations, see Figure 71. Each silver ion coordinates to two $\{W_{12}\}$ cluster units by engaging in coordinative interactions with terminal W=O ligands. In the resulting W-O-Ag bonds, Ag-O distances of 2.41 Å are observed. An almost perpendicular arrangement of the two $\{W_{12}\}$ substituents in relation to the central silver linker is formed with an O-Ag-O angle of *ca.* 88.9 °. This phenomenon is most likely due to the steric bulk introduced by the large cluster anions which can be minimised by this arrangement. In addition, the silver ions each feature two acetonitrile ligands which coordinate to the transition metal *via* the nitrogen donor of the organic molecule.

Detailed investigation reveals Ag-N bond lengths of $d_{Ag\text{-}N}$ = 2.23 Å and an angle of *ca.* 174.9 ° between the two organic ligands. This slight deviation from the ideal arrangement of 180 ° is caused by the steric constraints introduced by the bulky $\{W_{12}\}$ units which result in torsion of the organic acetonitrile ligands away from the inorganic clusters. The oxygen coordination environment around the two silver centres can be described as an

elongated tetrahedron with four oxo-ligands located on the corners, see Figure 71, right. The distortion of the tetrahedron becomes evident when comparing the O-O distance along the shortest edge (3.41 Å) with that along the longest edge (6.97 Å). In effect, the length of this tetrahedral arrangement along the silver-silver bond is approximately twice its width.

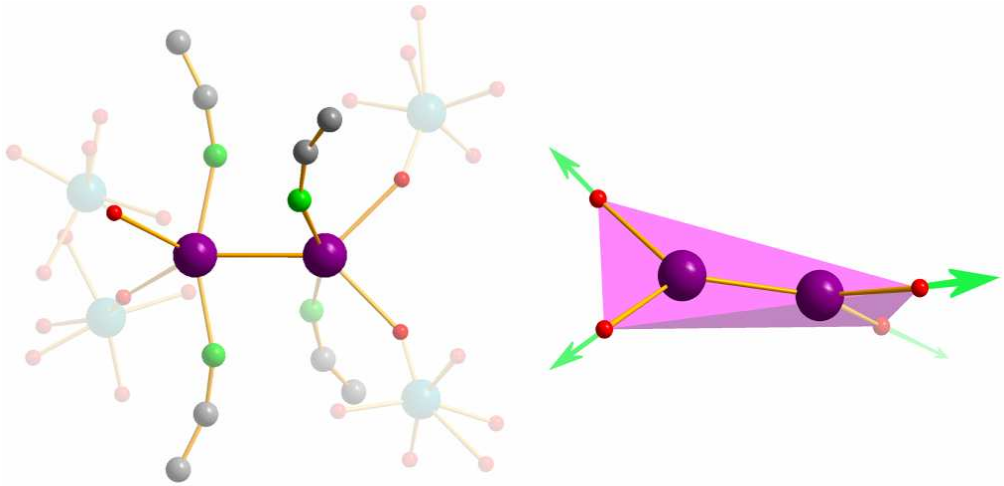

Figure 71: Illustration of the dinuclear silver(I) unit $[Ag_2(CH_3CN)_4]^{2+}$ which acts as a tetrahedral node in compound **20**. The ball-and-stick representation (left) illustrates the connectivity between the four cluster units and the silver centres with the additional acetonitrile ligands coordinating to the Ag(I) units. The short distance between two adjacent silver(I) centres (2.908 Å) is caused by argentophilic interactions based on electron correlation between the d-shell electrons of the silver ions. The polyhedral view (right) emphasises the tetrahedral character of the linking unit which connects the four $\{W_{12}\}$ clusters along the directions indicated by green arrows. Colour scheme: W: teal, Ag: purple, O: red, C: grey, N: green.

Also of interest in these $\{Ag_2\}$ linkers is that the distance between the silver centres (2.908 Å) is decisively shorter than the sum of the van der Waals radii of two silver (I) ions ($r_{vdw, Ag}$ = 1.72 Å[31]), therefore implying the presence of attractive interactions between the closed-shell d^{10} transition metals. This phenomenon on first sight appears to be counter-intuitive since it implies a close arrangement of two positively charged cations which based on their Coulomb interactions, should repel one another. However, this attractive interaction is a well-established phenomenon and is referred to as *metallophilic* or, in the case of silver centres, *argentophilic* interactions. Theoretical studies suggest that this type of attractive interaction is caused by electron correlation effects between the d shell electrons of the silver(I) centres. In addition, theoretical calculations which explicitly integrate relativistic effects caused by the heavy metal centres further support the presence of these attractive forces and suggest bond strengths comparable to hydrogen-bonding

interactions.[172] The silver-silver interaction in compound **20** was observed spectroscopically by a characteristic peak in the UV region at λ_{max} = 270 nm.

The arrangement of the $[Ag_2(CH_3CN)_4]^{2+}$ units in relation to the $\{W_{12}\}$ cluster anions in compound **20** reveals several intriguing steric features. Each cluster anion forms coordinative bonds to eight silver(I) ions *via* W-O-Ag coordinative interactions. Detailed structural elucidation reveals uniform Ag-O bonding distances of *ca.* 2.41 Å, suggesting that all interactions between silver(I) ions and $\{W_{12}\}$ cluster anions are of the same strength. Interestingly, the silver centres are assembled around the central $[H_3W_{12}O_{40}]^{5-}$ unit in a cubic fashion so that each silver centre occupies one corner of a supramolecular cube which circumscribes the tungstate cluster anion, see Figure 72.

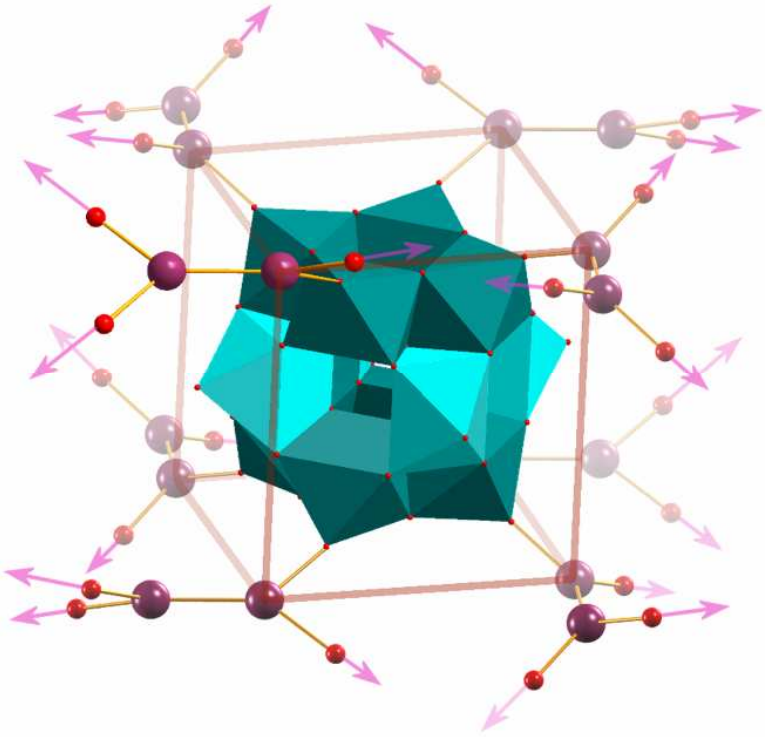

Figure 72: Illustration of the cubic arrangement of eight $\{Ag_2\}$ units around a central $\{W_{12}\}$ cluster anion. The silver(I) ions of the $\{Ag_2\}$ linkers coordinate to terminal W=O bonds *via* Ag-O-W interactions. The central cluster unit is connected to 24 other cluster units by virtue of the 4-connected linking mode of the $\{Ag_2\}$ bridges (highlighted by magenta arrows). The short Ag-Ag distances of *ca.* 2.9 Å are vital for the structural integrity. The arrangement of the silver linkers can be rationalised as two sets of four $\{Ag_2\}$ ligands coordinating to the top and bottom of the cluster unit (teal polyhedra), whereas the four central W=O sites remain non-coordinated (light blue polyhedra).

This supramolecular cubic arrangement of eight silver(I) ions is distorted so that in effect, two Ag-Ag distances of 8.2 and 9.1 Å are observed. This reduced structural symmetry is caused by the geometric relationship between the $\{W_{12}\}$-based oxo ligands. Structural analysis shows that the silver centres in compound **20** are exclusively bound to terminal W=O oxygen sites and detailed analysis illustrates that two types of terminal oxo-ligands can be distinguished on the cluster anion: eight of these ligands coordinate to silver(I) ions, whereas four remain non-coordinated. Structurally, this results in the formation of two sets of $\{W_4\}$ rings at the top and bottom of the cluster shell. Each tetranuclear ring features four W=O bonds which point away from the cluster surface and form coordinative bonds to the silver ligands (highlighted by teal polyhedra, Figure 72). In addition, a central belt of four W=O units remains non-coordinated (light blue polyhedra, Figure 72).

It is this spatial separation of coordinating and non-coordinating terminal oxo ligands which determines the distorted cubic arrangement of the silver linkers: the four $\{Ag_2\}$ bridges bound to one $\{W_4\}$ ring feature distances of $d_{Ag\text{-}Ag}$ = 8.21 Å, whereas the silver-silver distances between the top and bottom of the cluster are slightly elongated to 9.10 Å due to the set of non-coordinating W=O units in between. This unique coordination mode of eight silver(I) centres to the cluster in effect allows the formation of an infinite framework linked in three dimension by virtue of the $\{Ag_2\}$ linkers.

The structural consequences of this unique supramolecular arrangement of $\{Ag_2\}$-linked $\{W_{12}\}$ cluster ions become evident by examining the crystal lattice of compound **20**. The arrangement of the cluster anions results in the formation of structural voids so that two sets of perpendicular channels propagate along the crystallographic *a* and *b* axes, see Figure 73. The channel walls are created by connecting four cluster anions with two $\{Ag_2\}$ bridges so that 18-membered rings of the formula $\{W_6Ag_4O_8\}$ are formed, see Figure 73. This precise spatial arrangement means that the overall pore shape is not circular, but ellipsoidal with approximate dimensions of *ca.* 6.1 x 9.1 Å. It is interesting to note that two terminal W=O oxygen ligands point into the cavity and might act as binding sites for the uptake of oxophilic guest molecules.

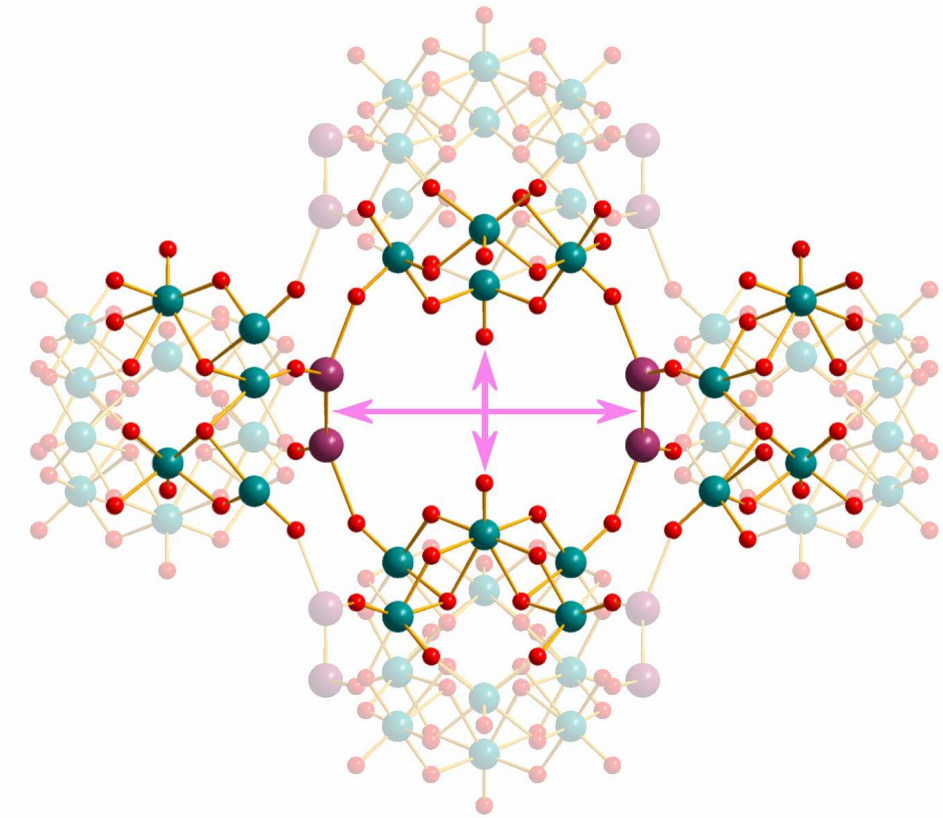

Figure 73: Illustration of the channels in compound **20** formed by the rectangular arrangement of four $\{W_{12}\}$ cluster units linked by two $\{Ag_2\}$ linkers. The maximum and minimum pore sizes are highlighted by magenta arrows (*ca.* 6.1 x 9.1 Å). The pore walls are formed by 18-membered rings so that two terminal cluster oxygen ligands point towards the cavity. NB: this vacancy is templated by a $[Ag(CH_3CN)_4]^+$cation which has been removed for clarity. Colour scheme: W: teal, O: red, Ag: purple. Organic ligands omitted for clarity.

The pores in compound **20** are not vacant but templated by a complex tetrahedral $[Ag(CH_3CN)_4]^+$ cation which resides in the centre of the structural void with four acetonitrile ligands extending along the four channel openings, see Figure 74. The supramolecular template features characteristic Ag-N bond lengths of *ca.* 2.25 Å which render the complex rigid enough to structurally direct the framework assembly.

Intriguingly the $[Ag(CH_3CN)_4]^+$ ion is structurally remarkably similar to tetra-alkyl ammonium cations such as tetra-*n*-propylammonium which are commonly used as structure directing agents in the synthesis of zeolitic frameworks.

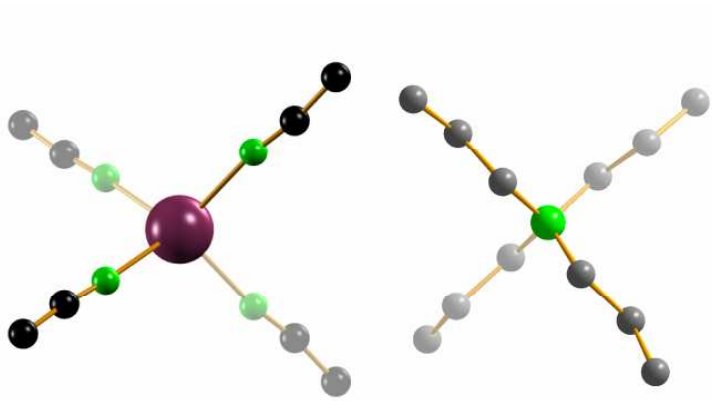

Figure 74: Illustration of the templating cation $[Ag(CH_3CN)_4]^+$ (left) and comparison with the structurally similar tetra-*n*-propylammonium cation (right) which is often used as a structure directing agent in the synthesis of zeolite frameworks. NB: The structures are displayed at the same scale. Colour scheme: Ag: purple, C: grey, N: green.

The structure features two equivalent sets of elliptical channels which propagate along the crystallographic *a*- and *b*-axes so that a $[Ag(CH_3CN)_4]^+$ cation is located at every intersection. In the resulting framework the $\{W_{12}\}$ clusters are arranged in a stacked fashion so that ABAB-type layers are formed. Within the layers the discrete $\{W_{12}\}$ cluster anions are arranged in a co-parallel fashion so that each cluster is separated from the adjacent anion unit by *ca.* 6.5 Å. Between the layers the clusters feature torsion angles of *ca.* 52.2 ° and are separated by *ca.* 8.4 Å. As a result of this layered assembly, the channels which propagate along the crystallographic *a*-axis are also stacked so that an ABAB pattern can be observed, see Figure 75. An intriguing structural detail is the distinct arrangement of $\{W_{12}\}$ anions and $\{Ag_2\}$ cations around the central cavity of each channel so that the top and bottom of the pores are delimited by $[Ag_2(CH_3CN)_4]^{2+}$ bridges whereas the two side walls are formed by a tungsten oxide environment. Two distinct chemical environments are created, which might interact very differently with guest molecules depending on their chemical nature. As described above, a porous structure is observed along the crystallographic *a*- and *b*-axes so that microporous, ellipsoidal channels with dimensions of 6.1 x 9.1 Å are established.

Along the crystallographic *c*-axis no porosity is observed due to the close packing of the cluster anions which allows no structural voids to be formed, see Figure 75. This structural feature does however, allow strong interactions between $\{Ag_2\}$ linkers and $\{W_{12}\}$ cluster ions so that a stable and rigid supramolecular 3D framework can be established.

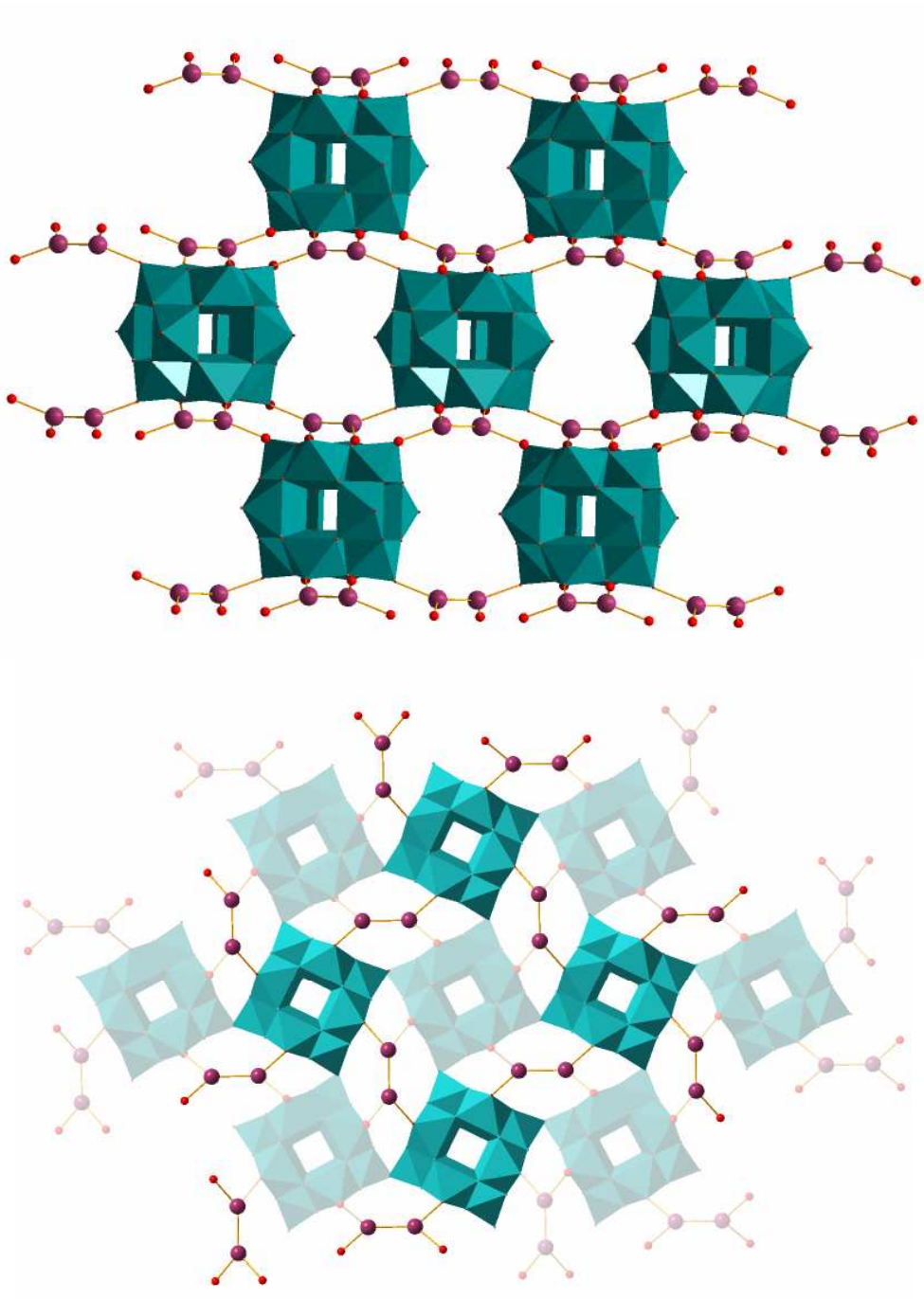

Figure 75: View of the framework arrangement of compound **20**. Top: View along the crystallographic *a*-axis. The $\{W_{12}\}$ cluster anions are arranged in ABAB-type layers and are interconnected by $\{Ag_2\}$ linking units Within the layers the clusters feature a parallel arrangement whereas between the layers, a torsion angle of *ca.* 52.2 ° is observed. Clearly visible is the arrangement of the channels which propagate along the crystallographic *a*-axis. Bottom: View of compound **20** along the crystallographic *c*-axis, illustrating the close packing of cluster anions which inhibits the formation of pores in this direction. The linking mode of the $\{Ag_2\}$ groups is illustrated and highlights the distorted tetrahedral arrangement of four clusters around one central $\{Ag_2\}$ unit. The templating $[Ag(CH_3CN)_4]^+$ cations were removed for clarity. Colour scheme: $\{W_{12}\}$ clusters: teal, Ag: purple, O: red. Organic ligands were removed for clarity.

The supramolecular structure of compound **20** was subsequently rationalised by a topological analysis of the framework arrangement. As discussed before, each $\{Ag_2\}$ unit acts as a 4-connected node which links a set of four clusters in a tetrahedral fashion. In addition, each $\{W_{12}\}$ unit features eight coordinated silver units which are arranged in a cubic fashion so that as a result each metatungstate cluster acts as an 8-connected node. Therefore, the framework in compound **20** can topologically be described as a 4,8-connected net, see Figure 76. This topological representation allows clear visualisation of the complex assembly which leads to the formation of the 2D channels where two cluster anions and two $\{Ag_2\}$ linkers enclose a central $[Ag(CH_3CN)_4]^+$ template.

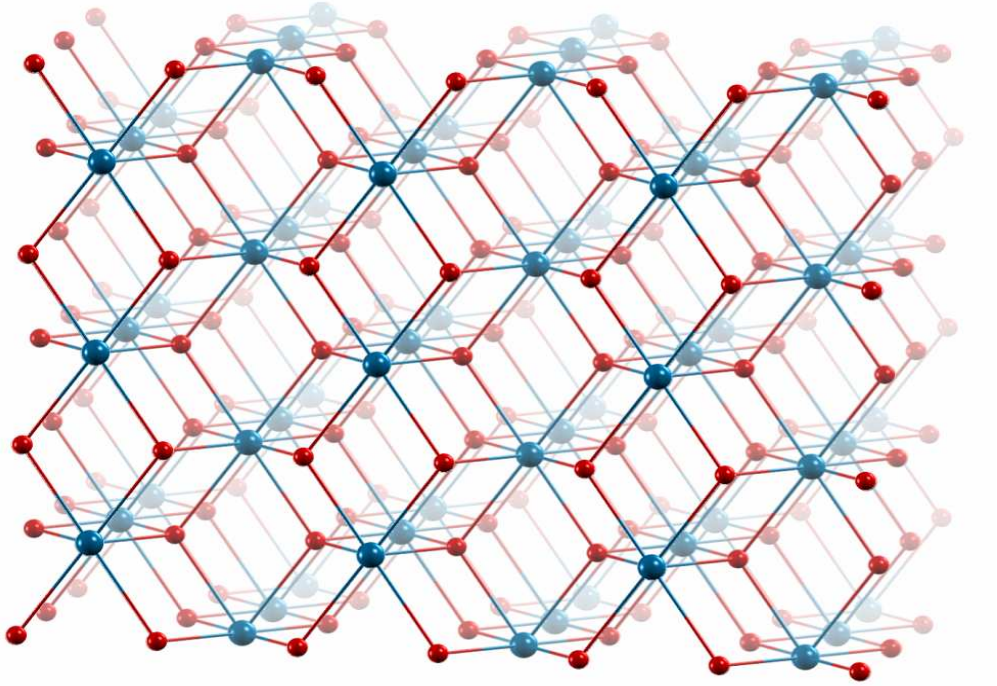

Figure 76: Illustration of the framework topology of compound **20**. The tetrahedral arrangement of $\{W_{12}\}$ units (blue) and $\{Ag_2\}$ linkers (red) results in the formation of a 4,8-connected net. The central templating ions, $[Ag(CH_3CN)_4]^+$ are omitted for clarity.

The structural stability of compound **20** was investigated using thermogravimetric analysis supported by dynamic scanning calorimetry in order to explore the possibility of removing the solvent molecules from the inorganic framework whilst retaining framework stability. It was demonstrated that heating the material to 150 ° C results in the loss of all solvent molecules so that a purely inorganic framework structure can be obtained. It was further observed that exposure of the desolvated compound to acetonitrile vapour results in the re-uptake of organic molecules so that the original weight of the material is regained. This sorption process demonstrates the accessibility of the porous system which allows

controlled release and re-adsorption of the organic nitrile compound within the framework structure. A series of five sorption cycles on the same sample was undertaken to demonstrate the full reversibility of the process and to provide further information on the framework stability, see Figure 77. It is interesting to note that a linear decrease in sorption capability from 10.9 wt.-% (run 1) to 8.7 wt.-% (run 5) was observed. This loss in solvent uptake capacity is most probably associated with a partial blockage of the pores due to the repeated thermal treatment at 150 ° C. In more detail, is likely that the complex template cations, $[Ag(CH_3CN)_4]^+$, are chemically reduced and result in the formation of larger Ag^0 particles so that this sintering process results in a partial blockage of the accessible pore volume. As a result, the amount of solvent uptake is decreased.

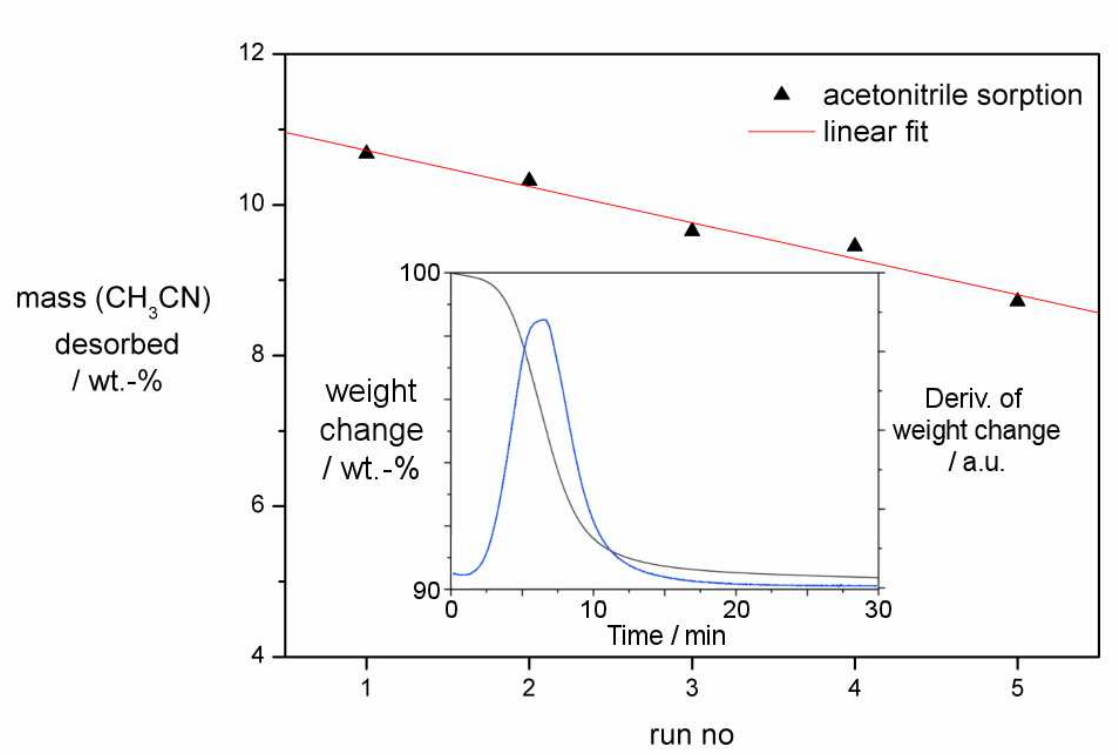

Figure 77: Graphical representation of the sorption cycling of compound **20**. The material was desolvated at 150 ° C to a constant weight to remove all solvent molecules. Subsequently the material was exposed to acetonitrile vapour for a 24 h to allow for equilibration and re-adsorption. The thermogravimetric desorption was then repeated. Interestingly a linear decrease in sorption capability was observed where the acetonitrile uptake dropped from 10.9 wt.-% (run 1) to 8.7 wt.-% (run 5). This is most likely due to partial pore blockage by a sintering process involving the central $[Ag(CH_3CN)_4]^+$ cations. The inset illustrates a typical thermogravimetric desorption process (black line: weight change, blue line: derivative of weight change).

Thus far it has been shown that compound **20** can be fully desolvated so that a purely inorganic material is obtained. In addition, exposure of the porous compound to acetonitrile allows re-adsorption of the solvent and suggests that the original framework is restored. However, these findings need further validation by detailed structural investigations. For these reasons, and in order to confirm the structural stability of compound **20**, powder-XRD studies were undertaken. These studies also allowed verification of the purity of the microcrystalline bulk sample used for the sorption studies and gave vital information of the structural integrity after the sorption cycles.

Initially, the powder pattern of the native compound **20** was compared with the simulated XRD pattern calculated from the single crystal X-ray diffraction data. It was shown that the native material used in the sorption studies was structurally identical to the single-crystals of **20** so that all structural properties deduced from the crystal structure were fully applicable to the bulk microcrystalline sample.

However, powder XRD studies showed that after thermal treatment the desolvated material shows a dramatic loss of crystallinity. This effect is due to the loss of all solvent molecules and the concurrent decrease in long-range order within the material. Intriguingly, re-solvation of compound **20** completely restores the crystallinity so that the powder XRD pattern of the resolvated material is identical to the XRD pattern of the native sample. At higher 2θ angles a marginal line broadening of the resolvated sample is observed which is most likely caused by the repeated thermal treatment at 150 ° C which might induce strain-dependant line width broadening, see Figure 78. The process of desolvation and resolvation could however also be interpreted as a destruction of the porous framework after the desolvation step and a full re-crystallisation of the material as the amorphous powder is exposed to acetonitrile vapour during re-adsorption of the solvent.

In conclusion, this study illustrates that compound **20** can be subjected to desorption and re-adsorption cycles of the solvent molecules whilst retaining its overall structural features and its porous character. Repeated thermal treatment of the material resulted in partial pore blockage most likely caused by a sintering process involving the templating silver(I) cations.

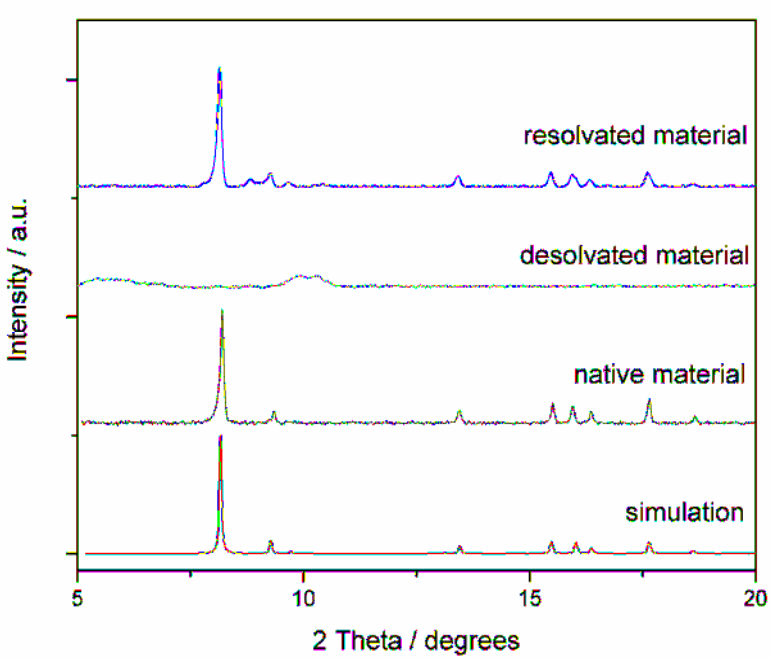

Figure 78: Powder X-ray diffraction patterns of compound **20**. Comparison of the native material with the simulated pattern obtained from single-crystal XRD data confirm the purity of the microcrystalline phase used in the sorption studies. The desolvated material shows a dramatic loss in crystallinity due to the large number of solvent molecules desorbed upon thermal treatment. The resolvated material features all peaks specific to the native compound and shows only a marginal line broadening which is most likely caused by the repeated thermal treatment at 150 ° C.

The initial sorption experiments suggested that compound **20** could be utilised as a sorbate for a range of small molecules. In addition, further sorption experiments were conducted to provide vital information on the binding affinities of compound **20** towards various organic functionalities. In particular methanol, acetone and water were used as sorbent molecules to investigate the adsorption of low molecular-mass organic and inorganic compounds and to compare the results with the acetonitrile sorption studies. A similar experimental procedure was employed which involved desolvation of compound **20** at 150 ° C and subsequent storage in an atmosphere of the respective sorbent for a period of 48 h to allow for equilibration. It was shown that compound **20** adsorbs all three compounds tested, however, the affinities observed were substantially lower than the original results obtained with acetonitrile. In detail it was observed that **20** adsorbs *ca.* 1.99 wt.-% of water, 2.70 wt.-% of methanol and 3.21 wt.-% of acetone, see Figure 79. Comparing these results with *ca.* 10.9 wt.-% uptake observed for acetonitrile this clearly demonstrates the specific interactions between the organic nitrile and the inorganic framework of compound **20** which facilitate the adsorption of this large amount of guest molecules. However, powder

XRD analysis of the materials after exposure to the respective sorbent indicated that the material did not regain its crystallinity and suggests that the sorption might occur *via* a surface-sorption process rather then by uptake of the molecules into the porous system.

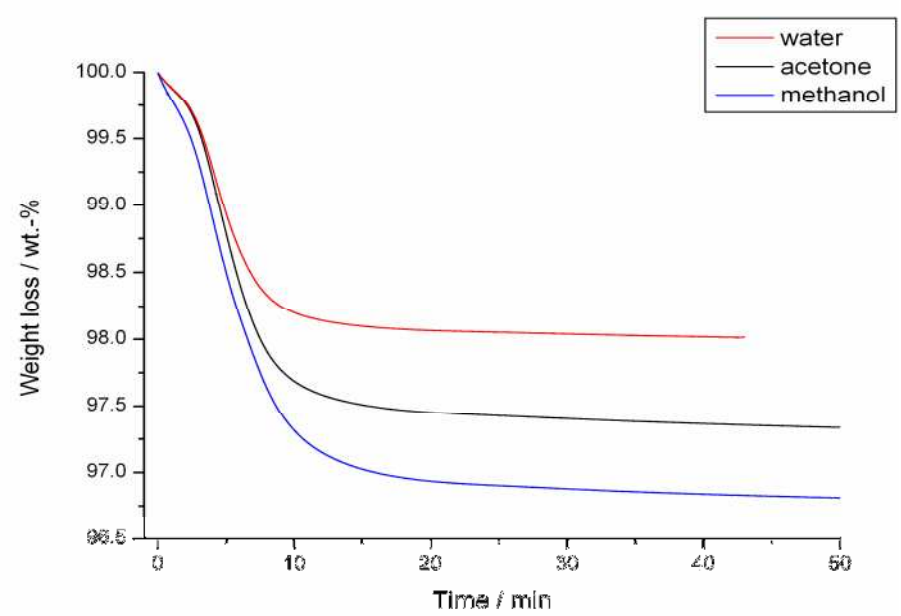

Figure 79: Thermogravimetric sorption study of compound **20** illustrating the thermal desorption of water (*ca.* 1.99 wt.-%), acetone (*ca.* 2.70 wt.-%) and methanol (*ca.* 3.21 wt.-%). The results demonstrate the different binding affinities of these small molecules and further demonstrate the high selectivity which compound **20** shows for the uptake of acetonitrile (10.9 wt.-%).

In conclusion, the sorption studies illustrate that compound **20** can be used to adsorb small organic molecules. The highest uptake was found for the original solvent, acetonitrile, indicating that the material features binding sites which are specifically tailored to form strong interactions with this organic molecule.

In order to obtain vital structural information on the porous nature of the material, crystallographic calculations based on the desolvated crystal structure were conducted using the crystallography tool PLATON.[173,174] The desolvated crystal structure was simulated by removing all solvent molecules were removed whilst retaining the crystallographic positions of the remaining framework atoms. Based on the pore size and pore geometry, this procedure allowed the approximation of the specific internal surface area as equal to *ca.* 1006 m^2 g^{-1}. In addition the solvent-accessible pore volume was calculated using a probe radius of 1.2 Å, see Figure 80. The results indicate that *ca.* 39.9 vol.-% of the desolvated structure is accessible for small molecules which is further underpinned by the uptake of acetonitrile and other small organic molecules as discussed

above. These results thus suggest that the 2D pore system is fully accessible for suitably sized molecules and can be used for the selective sorption of these compounds.

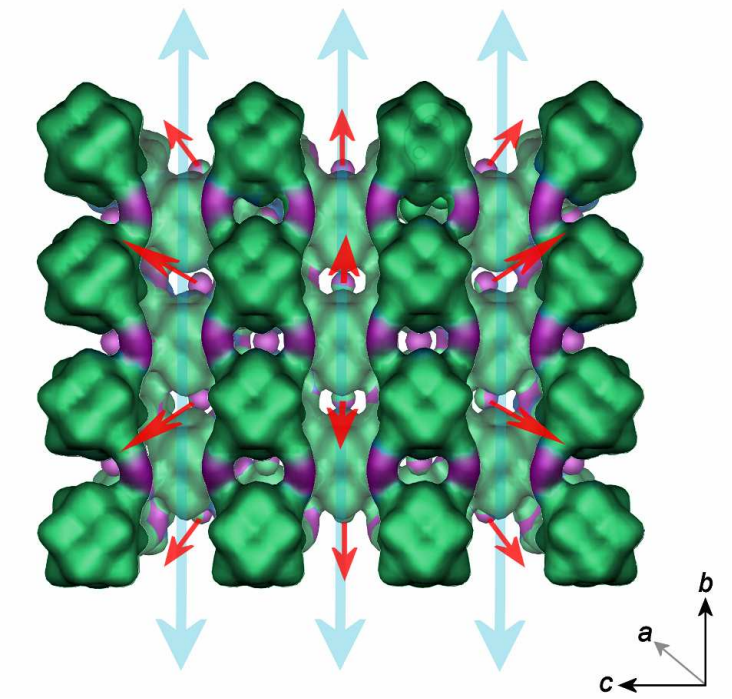

Figure 80: Illustration of the desolvated structure of compound **20** in which the positions of all framework atoms were retained whilst all organic molecules were removed. This structure was subsequently used to study the porosity of the system using the crystallography tool PLATON. The $\{W_{12}\}$ and $\{Ag_2\}$ units are represented using their van der Waals surface. The red and blue arrows highlight the directions of the 2D pores in compound **20**. Colour scheme: $\{W_{12}\}$: teal, Ag: purple.

Further investigations of the porosity of compound **20** were conducted to study the uptake of transition metal cations. This would allow the fine-tuning of the material properties by inclusion of a transition metal of choice into the pores of **20**. For an initial study, Cu^{2+} was used as an inorganic cationic probe. The cation combines stability in organic solvents with a negligible redox activity under the given sorption conditions and indeed allowed facile detection by UV-Vis spectroscopic measurements.

A series of sorption experiments was conducted and showed that compound **20** adsorbs Cu^{2+} into the porous system, see Figure 81. The stability of the framework structure was confirmed by powder XRD analysis fo the material after the sorption process. This preliminary data was fitted using a Langmuir model isotherm which introduces some theoretical restrictions such as the exclusive formation of monolayers of Cu^{2+} ions within the porous system. Analysis of the experimental data and the theoretical fit suggest a

saturation uptake of *ca.* 580 µmol of Cu^{2+} ions per gram of **20**, which can alternatively, be expressed as an uptake of *ca.* 3.5 wt.-%.

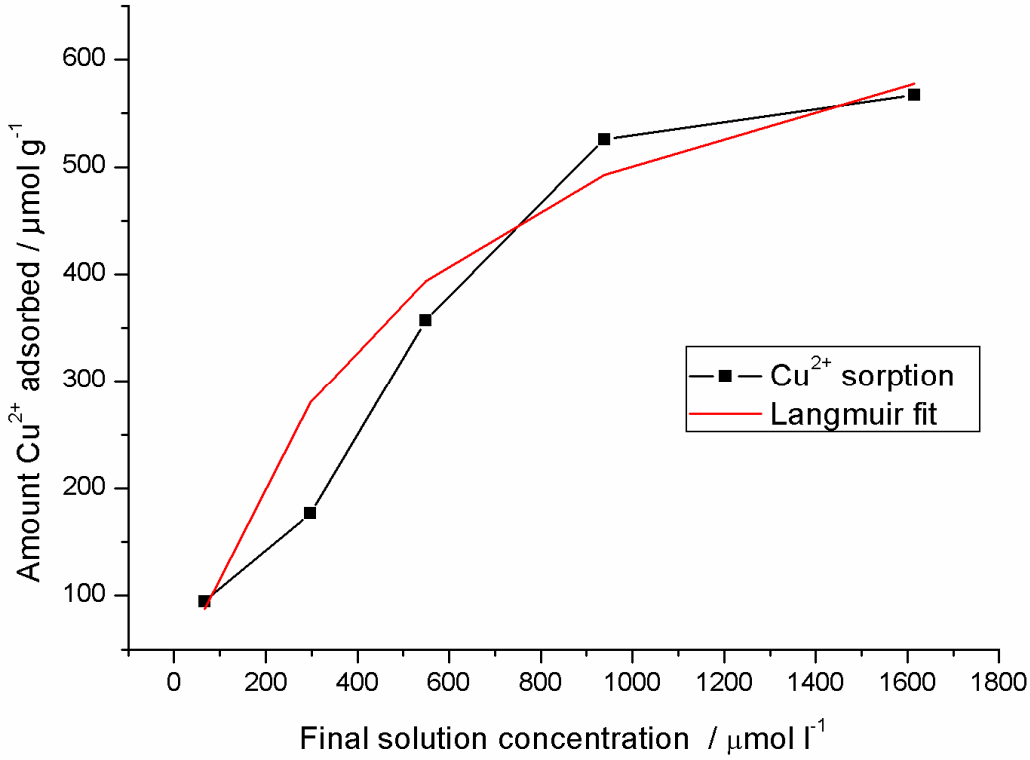

Figure 81: Adsorption isotherm illustrating the uptake of Cu^{2+} by compound **20**. The data was fitted using a Langmuir isotherm (red line) which suggests a saturation uptake of *ca.* 580 µmol Cu^{2+} per gram of sorbate. NB: The black line acts as a guide for the eye.

Theoretical considerations of the uptake process of Cu^{2+} suggest two feasible sorption mechanisms or a combination thereof:

- Ion exchange - This potential sorption mechanism proceeds *via* an ion-exchange process where the central $[Ag(CH_3CN)_4]^+$ cation is desorbed and released into the solvent so that the copper (II) ions replace the silver(I) centres.
- Ion uptake - This process involves the release of acetonitrile molecules into the solvent; the structural vacancies can subsequently be filled by Cu(II) cations and additional acetate anions for charge balance reasons.

Experimental results thus far indicate the occurrence of both processes. Sorption experiments in deuterated solvents indicate that during the sorption process, acetonitrile molecules are released from compound **20** into the liquid phase. This spectroscopic

observation supports both sorption mechanisms discussed above. However, no further information about the exact mechanism can be elucidated from this NMR study alone since both mechanisms involve the release of acetonitrile, either on its own or as ligand for the complex cation $[Ag(CH_3CN)_4]^+$.

Additional support for the ion exchange mechanism is provided by a flame atomic absorption spectroscopy study of the solvent used in the sorption experiments. After equilibration, low levels of silver were detected which suggests that at least a partial release of silver into the solvent system occurs. However, no direct correlation between silver release and copper uptake could be established which suggests that no quantitative exchange takes place. FT-IR studies were conducted on compound **20** after the copper sorption and indicated the presence of acetate bands which suggests uptake of additional acetate anions for charge-balance reasons. In conclusion, these preliminary findings suggest that a partial release of silver and concurrent uptake of acetate anions facilitates the sorption of Cu^{2+} cations up to a maximum saturation concentration of *ca.* 580 μmol g^{-1} of compound **20**.

It should be noted that the self-assembly process of compound **20** involves a deprotonation step where the starting material $(TBA)_4[H_4W_{12}O_{40}]$ (**21**) loses one proton and is isolated in the product as the triprotonated species $[H_3W_{12}O_{40}]^{5-}$. Whilst characterising compound **21**, the material was isolated as single crystals which visually appeared to be of diffraction quality. Single-crystal XRD analysis allowed full anisotropic refinement of the $[W_{12}O_{40}]^{8-}$ cluster framework, but all attempts to refine the positions of the organic TBA counter ions failed due to an exceptionally high degree of disorder. Further investigation of **21** by means of thermogravimetric analysis and elemental analysis however supported the presence of four TBA counterions and a tetraprotonated cluster core $[H_4W_{12}O_{40}]^{4-}$. In order to establish the true composition of the material, electrospray-ionisation mass-spectrometric studies (ESI-MS) were conducted to identify the true composition and the presence of any impurities in a bulk crystalline sample of compound **21**.

The mass-spectrometric analysis of a solution of **21** in acetonitrile demonstrated the presence of the cluster anion $[H_nW_{12}O_{40}]^{(8-n)-}$ in three distinct protonation states (n = 3, 4, 5), where the tetraprotonated cluster anion $[H_4W_{12}O_{40}]^{4-}$ was observed as the most

abundant species with signals at m/z = 1030.55 ($\{(TBA)_1[H_4W_{12}O_{40}]\}^{3-}$), 1667.69 ($\{(TBA)_2[H_4W_{12}O_{40}]\}^{2-}$) and 3578.21 ($\{(TBA)_3[H_4W_{12}O_{40}]\}^{1-}$). Further, the triprotonated cluster anion was identified by the signals at m/z = 1110.98 ($\{(TBA)_2[H_3W_{12}O_{40}]^{3-}\}$), 1788.06 ($\{(TBA)_3[H_3W_{12}O_{40}]^{2-}\}$) and 3819.49 ($\{(TBA)_4[H_3W_{12}O_{40}]\}^{1-}$). The pentaprotonated cluster anion $[H_5W_{12}O_{40}]^{3-}$ was observed at m/z = 1547.32 ($\{(TBA)_1[H_5W_{12}O_{40}]\}^{2-}$), see Figure 82, top.

In order to investigate the acidity of the cluster protons, a sample of **21** in acetonitrile was stirred over solid K_2CO_3 to remove any acidic protons. The sample was subsequently subjected to ESI-MS analysis and it was shown that after a period of 24 h, the protonation equilibrium had shifted and the new main product was the triprotonated cluster anion $[H_3W_{12}O_{40}]^{5-}$ which was identified by signals observed at m/z = 1111.28 ($\{(TBA)_2[H_3W_{12}O_{40}]^{3-}\}$) and at 1788.06 ($\{(TBA)_3[H_3W_{12}O_{40}]^{2-}\}$), see Figure 82, bottom. For the tetra- and pentaprotonated species, only weak residual signals were observed. This suggests that in the acetonitrile solution, the cluster can be deprotonated and thus the protonation state of the main product changes from n = 4 in the native sample to n = 3 in the K_2CO_3-treated solution.

The observation of mixed protonation states of the cluster, therefore, explains the high disorder observed in the crystal structure analysis of compound **21**. The cluster shell $[W_{12}O_{40}]^{8-}$ exists as a tri-, tetra- and pentaprotonated species and can thus be fully refined whereas a variable number of organic TBA cations per cluster are present, depending on the protonation state: the tri-protonated species require five TBA counterions per cluster unit, whereas the tetra- and pentaprotonated species require only four and three TBA counter ions respectively. This mismatch is reflected by the high disorder in the crystal structure which represents the statistical mixture of these three species and can be described as an incommensurate crystal structure. Intriguingly, an acetonitrile solution of **21** which also contained tetra-*n*-propylammonium (TPA) as the organic counter ion in an otherwise unchanged reaction system resulted in the crystallisation of compound **22**, $(TPA)_4[H_4W_{12}O_{40}]$ where single-crystal XRD analysis allowed full refinement of all components including full anisotropic refinement of the organic counterions. This observation demonstrates that the cluster ions can, in principle, be isolated as pure compounds in one given protonation state.

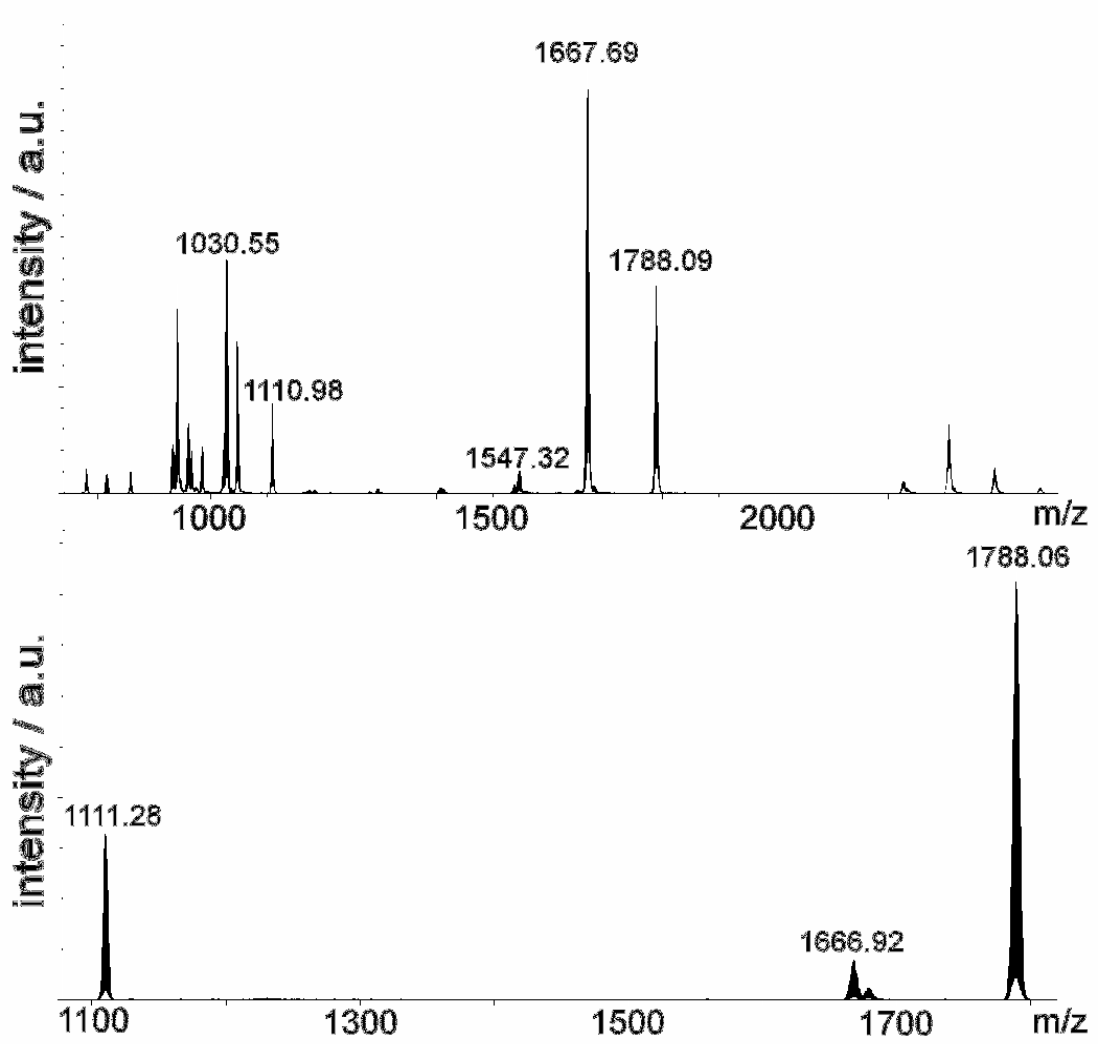

Figure 82: ESI-MS spectra of the native compound **21** in acetonitrile (top) and **21** after stirring over K_2CO_3 to remove acidic protons (bottom). Peak assignment (top): $[H_4W_{12}O_{40}]^{4-}$ at m/z = 1030.55 ($\{(TBA)_1[H_4W_{12}O_{40}]\}^{3-}$) and 1667.69 ($\{(TBA)_2[H_4W_{12}O_{40}]\}^{2-}$). $[H_3W_{12}O_{40}]^{5}$ at m/z = 1110.98 ($\{(TBA)_2[H_3W_{12}O_{40}]^{3-}\}$) and 1788.09 ($\{(TBA)_3[H_3W_{12}O_{40}]^{2-}\}$) $[H_5W_{12}O_{40}]$ at m/z = 1547.32 ($\{(TBA)_1[H_5W_{12}O_{40}]\}^{2-}$). Peak assignment (bottom): $[H_3W_2O_{40}]^{5-}$ at m/z = 1111.28 ($\{(TBA)_2[H_3W_{12}O_{40}]^{3-}\}$) and 1788.06 ($\{(TBA)_3[H_3W_{12}O_{40}]^{2-}\}$).

In summary, this study shows that a combination of crystallography and mass-spectrometry can provide vital complementary information on the solid-state and liquid-phase structure of polyoxometalate compounds. Whilst the XRD studies provide unrivalled structural information, ESI-MS studies can provide unique insight into the equilibrium processes and proton-transfer interactions between polyoxometalate clusters in organic solvents. The combination of these observations can subsequently be employed in the assembly of new architectures by a chemically directed approach.

4 Conclusions and Outlook

4.1 Host-guest complexes of isopolyoxometalates

The host-guest chemistry of two isopolyoxometalate cluster types was studied to investigate the interactions of various cations with the binding sites of the anionic cluster frameworks. Two families of related cluster anions were isolated which both featured the ability to strongly bind organic moieties so that in effect hybrid organic-inorganic compounds were produced. In addition, crystal engineering allowed the formation of supramolecular 1D chains and 3D-linked frameworks using appropriate cations as linking groups.

4.1.1 Host-guest chemistry of isopolyoxomolybdates: {Mo_{36}}

In the case of the {Mo_{36}} open-shell cluster **1**, $(TEAH)_6[Mo_{36}O_{112}(H_2O)_{14}(TEAH)_2]\cdot 10H_2O$ it was observed that an "empty" cluster anion without any guest cation could be isolated when using sodium-free precursors. In addition, it was shown that two organic cations can replace terminal water ligands and therefore, allow the introduction of organic functionality to the {Mo_{36}} framework. It was observed that these organic ligands act as supramolecular "connectors" which establish attractive hydrogen-bonded interactions between neighbouring clusters and thus enable a close supramolecular arrangement. The presence of these organic groups further allows facile modification of the cluster surface and results in the formation of a hybrid organic-inorganic cluster anion. Future work will build on these initial results and will aim to further exploit the formation of these hybrid clusters by engaging the coordinated cations in organic functionalisation reactions so that the organic moieties can be fine-tuned as desired.

The presence of sodium cations in the reaction mixture allowed the isolation of the host-guest compound **2,** $(TEAH)_4Na_2[Mo_{36}O_{112}(H_2O)_{14}(TEAH)_2]\cdot 28H_2O$, which features two Na^+ cations embedded within the two independent binding sites of the {Mo_{36}} cluster anion. In addition, compound **2** also coordinates two organic ligands and thus allows facile modification of the cluster properties. It is also of interest that the cluster anions in **2** are arranged in 1D supramolecular chains where the organic groups on the cluster periphery act as spacing units which inhibit any further growth into structures of higher dimensionality.

4.1.2 Host-guest chemistry of isopolyoxotungstates: {W_{36}}

A family of host-guest complexes based on the triangular cluster anion {W_{36}} was isolated using two approaches. First, inorganic alkali and alkali earth cations were used to study the self-assembly of the cluster anion in aqueous solution and it was observed that isostructural compounds can be isolated using potassium, rubidium, caesium, strontium and barium cations (compounds **3**-**7**, see Table 5). It was observed that in all cases the cations are located at the central binding site of the cluster ions where six terminal W=O coordination sites provide an ideal coordination environment. Structural analysis further showed that the ionic radii of the cations influenced the exact location of the metal centres so that larger cations were more dislocated from the central binding plane, due to a less optimal steric fit. Comparison with similar organic host-guest complexes showed that crown ethers feature almost identical binding modes and in addition allowed comparison of the structural features of these molecular receptors. It was observed that the largest cations, caesium and barium occupy additional coordination sites within the {W_{36}} framework. It was shown that additional caesium coordination sites can be located at the periphery of the tungstate clusters which results in a decreased occupancy of the central coordination site. However, the barium centres adopt a different binding mode. In addition to the central barium guest cation, additional barium sites are located between neighbouring cluster anions and result in a cross-linking of the {W_{36}} groups into a 3D supramolecular framework. This binding mode was furthermore reflected by the physical properties of the material where a drastically reduced solubility in aqueous media was observed, compared with the non-linked cluster units.

The complexation of ammonium, NH_4^+, within the binding pocket of a {W_{36}} unit was subsequently achieved and resulted in the isolation of compound **8**. This result provided further inspiration for the introduction of other organic groups by using protonated primary amines as guest molecules and thus mimicking the binding mode of the inorganic ammonium group which interacted with the cluster *via* electrostatic- and hydrogen-bonding interactions.

Four organic-inorganic hybrid materials were isolated and thus demonstrated the versatility of this organic approach for the formation of hybrid host-guest systems, see Table 5. It was observed that the central binding pocket was accessible even for bulky molecules such as

phenethyl amine, suggesting that in principle this coordination environment allows the binding of a vast range of different molecules and functionalitites.

It was demonstrated that not only rigid molecules with an aromatic backbone could be employed as guest cations but also flexible alkyl chain groups with two amino functions situated at either end of the carbon chain. This feature allows the formation of additional supramolecular interactions where the peripheral amine group which protrudes from the cluster cavity interacts with neighbouring clusters *via* strong hydrogen-bonding interactions. It was shown that these supramolecular interactions allow the modification of the $\{W_{36}\}$ arrangement in the crystal lattice so that a well-defined, layered structure is formed as a result. This approach might thus allow tailoring of the cluster anion arrangement by virtue of the guest molecules so that an intricate change in the guest could result in a new arrangement of the host complexes. This approach might eventually allow the precise arrangement of clusters on the molecular scale.

Table 5: Summary of the $\{W_{36}\}$ host-guest compounds

Compound	Guest	Formula
3	K^+	$(TEAH)_9Na_2[(H_2O)_4K\subset[H_{12}W_{36}O_{120}]]\cdot 17H_2O$
4	Rb^+	$(TEAH)_9Na_2[(H_2O)_4Rb\subset[H_{12}W_{36}O_{120}]]\cdot 17H_2O$
5	Cs^+	$(TEAH)_9Na_2[(H_2O)_4Cs\subset[H_{12}W_{36}O_{120}]]\cdot 15H_2O$
6	Sr^{2+}	$(TEA)(TEAH)_8Na_2[(H_2O)_4Sr\subset[H_{12}W_{36}O_{120}]]\cdot 17H_2O$
7	Ba^{2+}	$(TEA)(TEAH)_8Na_1Ba_{0.5}[(H_2O)_4Ba\subset[H_{12}W_{36}O_{120}]]\cdot 17H_2O$
8	NH_4^+	$(TEAH)_9Na_2[NH_4\subset[H_{12}W_{36}O_{120}]]\cdot 17H_2O$
9	PHEN	$(TEAH)_{11}[PHEN\subset[H_{12}W_{36}O_{120}]]\cdot 17H_2O$
10	4PBA	$(TEAH)_{11}[4PBA\subset[H_{12}W_{36}O_{120}]]\cdot 17H_2O$
11	*p*XDA	$(TEAH)_9Na_1[p XDA\subset[H_{12}W_{36}O_{120}]]\cdot 17H_2O$
12	DAH	$(TEAH)_{10}[DAH\subset[H_{12}W_{36}O_{120}]]\cdot 17H_2O$

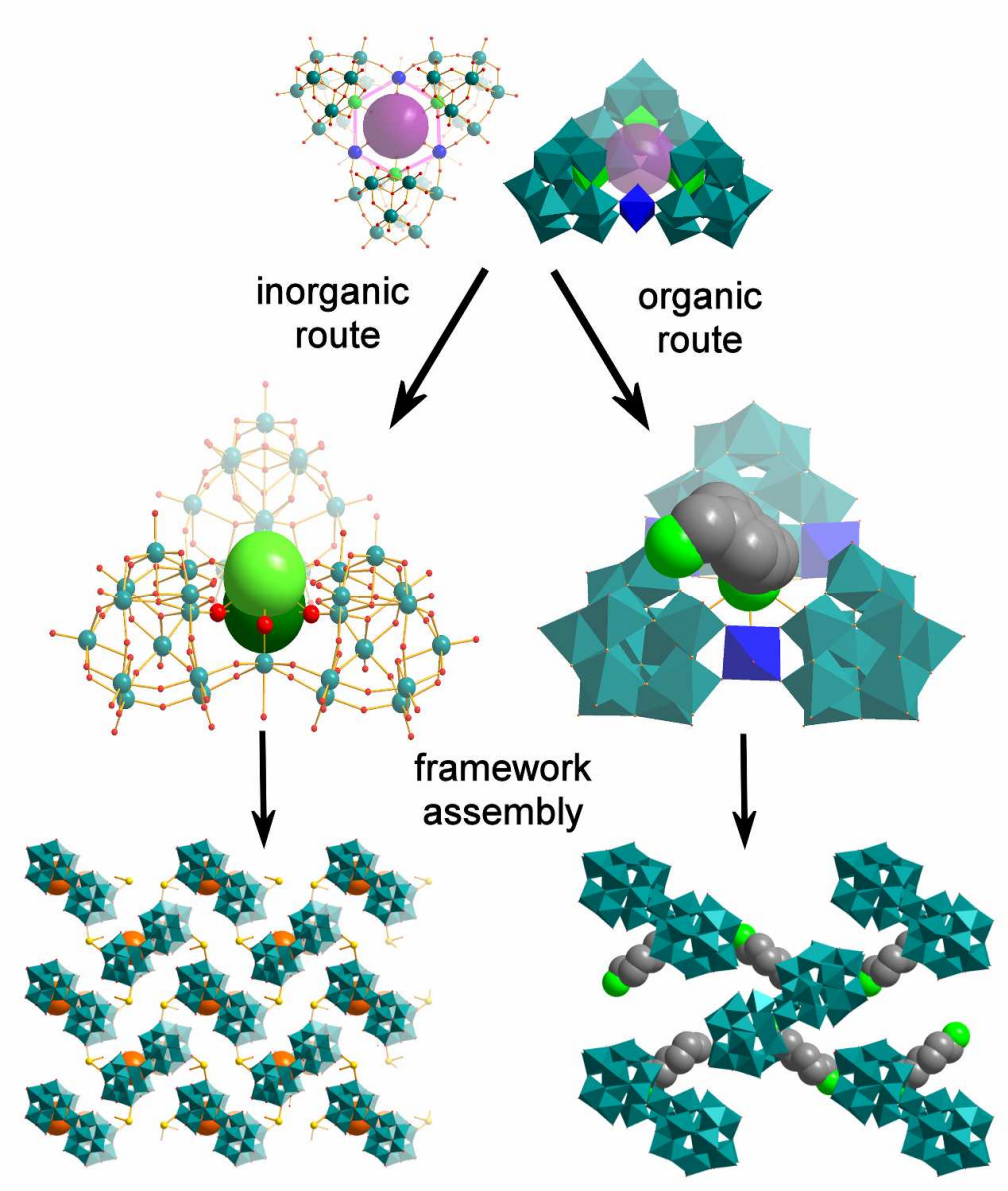

Figure 83: Illustration of the inorganic and organic routes which lead to the assembly of virtually isostructural framework arrangements of the $\{W_{36}\}$ units. The cluster assemblies are "locked" in a tilted superstructure by virtue of the inorganic or organic linking cations.

In conclusion, a family of host-guest complexes has been developed which allow binding of organic and inorganic cations to a purely inorganic polyoxotungstate core. It is this feature which makes these compounds interesting candidates for applications such as the formation of self-assembled monolayers and high-temperature inorganic sensor-arrays, for which their organic counterpart, the crown-ethers might be too labile. In addition it has been shown that these materials can be assembled into infinite frameworks which might allow the formation of solid-state materials with molecular recognition sites.

4.2 Assembly of polyoxometalate-based frameworks

4.2.1 Structural effects of amine counterions

A more detailed study of the structural effects of protonated organic amines was undertaken to support the initial observations made while investigating the host-guest systems described above. The investigation was focused on the supramolecular interactions of three amines whilst maintaining one type of polyoxometalate building block. This approach allowed a comparative study of the supramolecular effects of the amine cations on the solid-state structure. In detail, two distinct supramolecular arrangements were observed based on the type of amine used.

It was shown that planar rigid amines support the formation of a layered arrangement of $\{Mo_6\}_2$ cluster anions where the hydrogen-bonding ability of the organic amines allows a cross-linking between the layers so that the overall framework is structurally reinforced. The planar amine cations adopt two distinct functions within the structures. One type of organic cations acts as intra-layer cross-linking units which reinforce the supramolecular arrangement. A second type of amine linker is observed which act as "pillaring" agents between the $\{Mo_6\}_2$ layers and thus provide additional structural support. Furthermore the use of aromatic amines resulted in the formation of π-π-stacked supramolecular columns which were established between two cluster layers. These superstructures might have a structure-directing role by engaging in interactions with the cluster anions both *via* electrostatic and hydrogen-bonding interactions. It was further observed that the use of highly rigid amine molecules with a distinct 120 ° hydrogen-bonding angle seems to affect the overall arrangement of the $\{Mo_6\}_2$ cluster units. This is because the cations are engaged in a set of three hydrogen-bonds which "lock" the cluster anions into a hexagonal packing pattern.

In contrast, the use of a highly flexible amine resulted in the formation of 1D linear chains where the clusters are linked *via* $\{Na_2\}$ units so that a purely inorganic polymeric chain is created. It was shown that the flexible amine does not bind to the cluster anions in one distinct mode, but rather adopts a multitude of different conformations and therefore does not feature a pronounced supramolecular directing effect. However, due to its flexibility it

can be arranged in between the 1D chains and so supports the co-linear arrangement of the polymeric chains in the crystal lattice.

The introduction of framework functionality was achieved by a three component approach where $\{Mo_6\}_2$ anions were employed as inorganic structural backbones together with planar aromatic triacid molecules which acted as a supramolecular template by forming π-π-stacked columnar assemblies. In addition, the clusters were linked by rigid chiral amine groups which resulted in the formation of a chiral, porous framework with high thermal stability and reversible sorption capabilities.

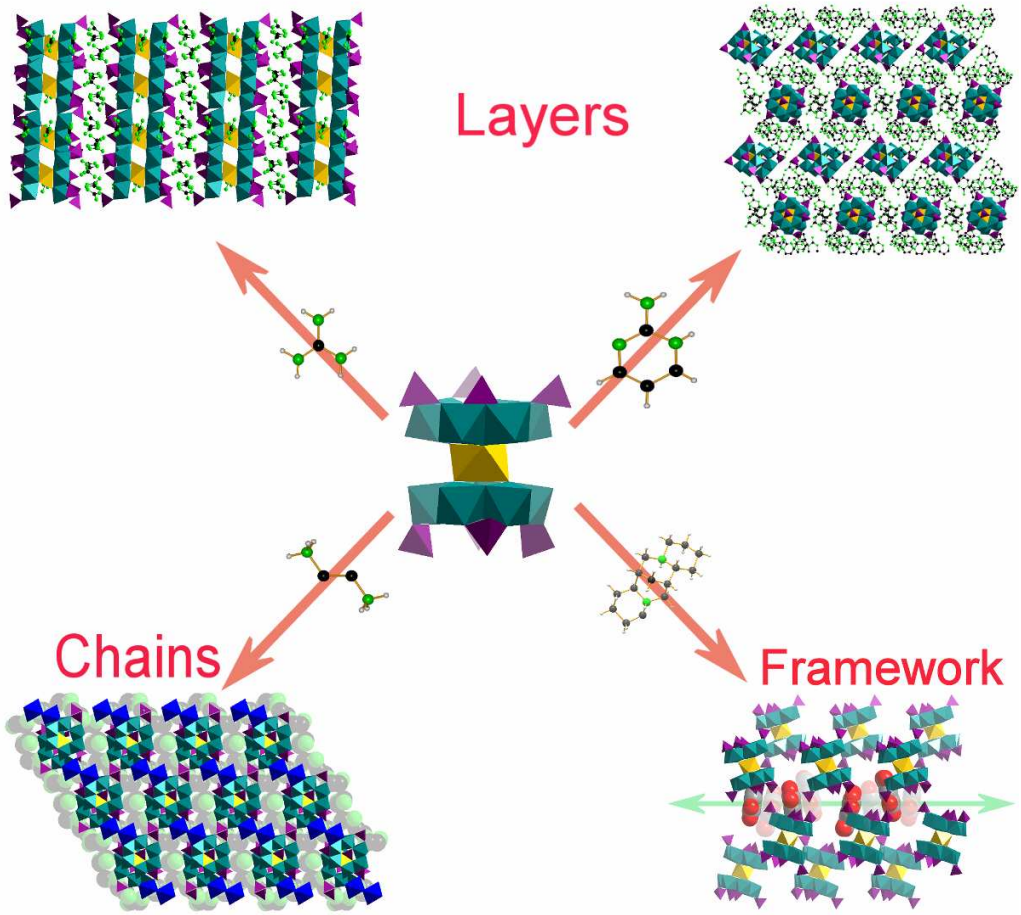

Figure 84: Illustration of the different assembly-types formed using $\{Mo_6\}_2$ anions, depending on the type of amine employed in the synthesis. Rigid planar amines result in the formation of layered structures; flexible amines gave 1D linear chains; a chiral bicyclic amine resulted in the formation of a porous framework structure.

In addition to the compounds above, a $\{Mo_5\}$-based cluster framework was formed where planar aromatic amines were employed to direct the structural arrangement of the cluster units. Supramolecular effects of the amine groups were observed and two types of π-π-

stacked columns were formed within the structure. These assemblies enabled the formation of a layered superstructure where the cluster anions adopt an ABAB-type arrangement.

Table 6: Summary of the $\{Mo_6\}_2$-based systems

Compound	Formula
13	$(GUA)_{12}[Mo_{12}O_{62}H_{11}Na_1P_8]\cdot 11H_2O$
14	$(APY)_{14}[Mo_{12}O_{62}H_9NaP_8]\cdot 13H_2O$
15	$(EN)_6[Mo_{12}O_{62}H_9Na_3P_8]\cdot 18H_2O$
16	$(APY)_5[Mo_5O_{15}H(PO_4)_2]\cdot 5H_2O$
17	$(SPA)_4(BTC)_1[H_{15}Mo_{12}NaO_{62}P_8]\cdot 10H_2O$

Future work will focus on exploiting this strategy by forming more sophisticated supramolecular frameworks which utilise the specific binding modes of organic amines to direct the assembly of the cluster anions. This might result in the assembly of frameworks which combine larger pore sizes with increased structural stability and might therefore be of interest for heterogeneous catalysis or sequestration processes.

4.2.2 Silver-linked polyoxometalate assemblies

Two silver-linked assemblies based on decavanadate building blocks $\{V_{10}\}$ were isolated from organic solution. In both cases, the principal connectors were trinuclear DMSO-linked silver units $\{Ag_3\}$ which allowed the formation of 1D zigzag chains and 2D planar networks. In case of the chain assemblies, the zigzag pattern is established by coordination of two $\{Ag_3\}$ groups to one $\{V_{10}\}$ cluster in an almost perpendicular fashion. In addition, the opposite cluster face is occupied by $\{Ag_1\}$ capping groups which inhibit further growth, thus allowing the isolation of polymeric chains of the type $[\{Ag_3\}\{V_{10}\}\{Ag_1\}]_\infty$, see Table 7. It is interesting to note that these chains are electrically neutral and can thus be densely packed in the crystal structure without having to accommodate any additional counterions to balance the charge.

The assembly of a 2D network structure was achieved by employing structurally identical $\{Ag_3\}$ units as linkers which coordinate to opposite faces of the $\{V_{10}\}$ cluster anion. By this means, a linear arrangement of cluster units is achieved and additional $\{Ag_1\}$ units are

accommodated in between two neighbouring sets of cluster chains so that in consequence, each cluster unit is connected in two dimensions and acts as a four-connected node.

A 3D porous framework was assembled using $\{W_{12}\}$ α-metatungstate clusters as inorganic building blocks which were cross-linked using dinuclear $\{Ag_2\}$ connectors. In the framework, the $\{W_{12}\}$ units act as eight-connected nodes resulting in a cubic arrangement of eight $\{Ag_2\}$ linkers is formed around each cluster. The $\{Ag_2\}$ linkers connect four $\{W_{12}\}$ units in a tetrahedral fashion. The stability of the silver assembly is provided by argentophilic interactions between the d^{10} closed-shell metal centres. In addition the spatial arrangement of tungstate clusters and silver linkers results in the formation of a 2D interconnected network of channels. This porous system is templated by silver cation complexes where the silver centre is coordinated tetrahedrally by four acetonitrile ligands.

The accessibility of the pore system was demonstrated by several sorption-desorption cycles using acetonitrile as a sorbent. In addition, various other small molecules were sorbed into the pores, although to a lesser degree than the original solvent acetonitrile. Crystallographic calculations based on the desolvated crystal structure showed an accessible pore volume of almost 40 vol.-% with an associated specific surface area of more than 1000 $m^2\ g^{-1}$. The uptake of cationic species was demonstrated by sorption of Cu^{2+} from methanolic solution which showed a saturation uptake of *ca.* 3.5 wt.-%.

These results will be further investigated using other isopolyoxometalates as building blocks for the assembly of silver-linked frameworks. The templating effect of the silver cation complexes will be studied and variation of the ligand size might eventually allow fine-tuning of the pore-size. In combination with a variation of the cluster anion this approach might provide a general route to functional silver-linked polyoxometalate frameworks.

Table 7: Summary of the silver-linked polyoxometalate assemblies

Compound	Cluster type	Formula
18	$[H_2V_{10}O_{28}]^{4-}$	$[Ag_3(DMSO)_6][Ag_1(DMSO)_3][H_2V_{10}O_{28}]$
19	$[H_2V_{10}O_{28}]^{4-}$	$[Ag_3(DMSO)_6][Ag_1(DMSO)_2][H_2V_{10}O_{28}]$
20	$[H_3W_{12}O_{40}]^{5-}$	$[Ag(CH_3CN)_4][Ag_2(CH_3CN)_4][H_3W_{12}O_{40}]$

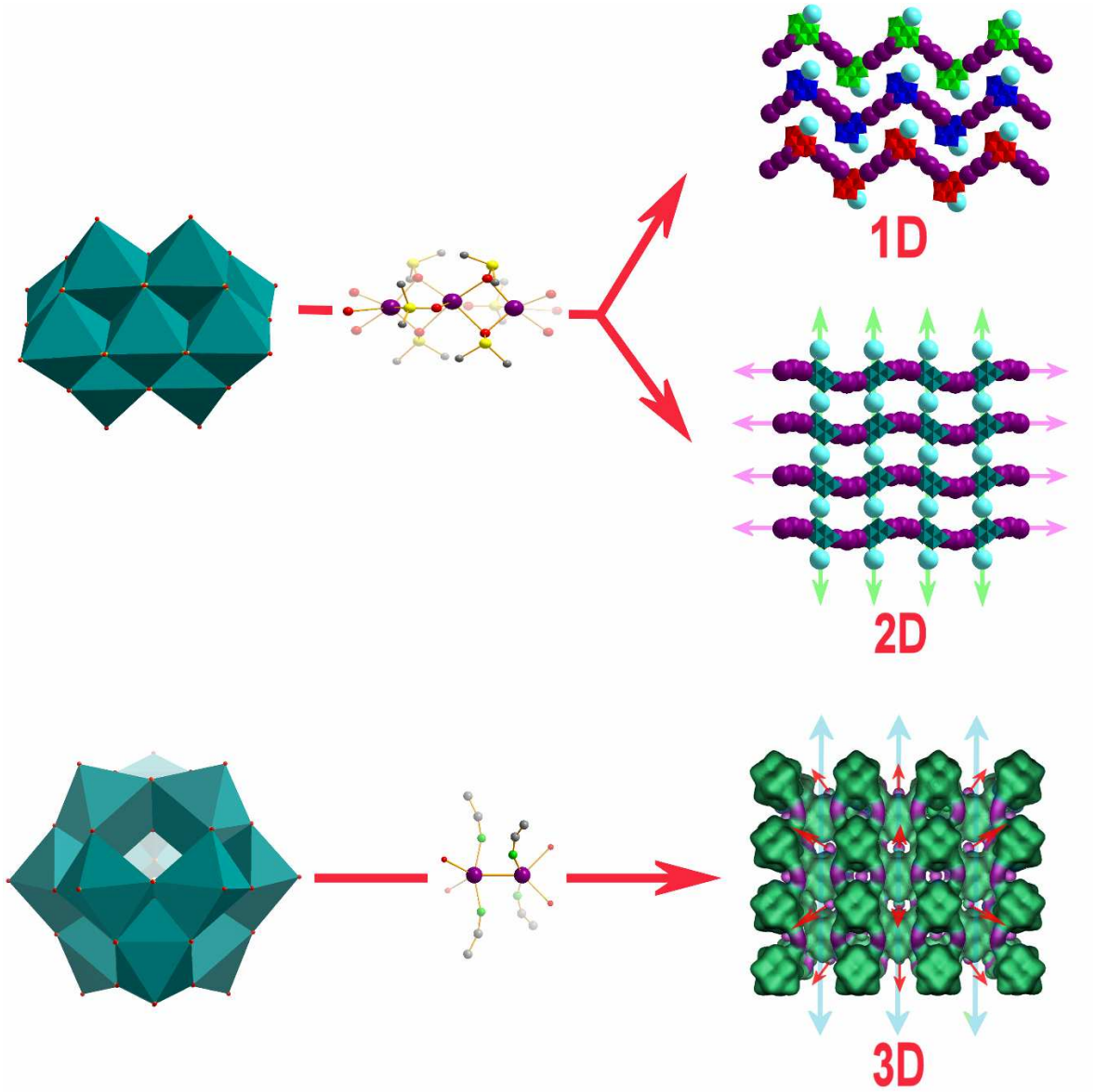

Figure 85: Illustration of the formation of 1D zigzag chains and a 2D planar network by cross-linking $\{V_{10}\}$ decavanadate units with supramolecular silver assemblies. A 3D porous framework was isolated by connecting $\{W_{12}\}$ metatungstate clusters with $\{Ag_2\}$ groups.

In conclusion, the formation of polyoxometalate frameworks based on two distinct linking modes has been studied. It has been shown that protonated amines can act as versatile linking groups and result in the formation of a variety of framework assemblies using specific hydrogen-bonding motifs as structural supports. The use of transition metals to link cluster units showed that depending on the conditions and cluster types, 1D chains, 2D networks and 3D porous frameworks can be isolated. Both approaches will be further exploited to allow the formation of a new family of polyoxometalate-based frameworks.

5 Experimental Section

5.1 Materials

All reagents and solvents were supplied by Sigma Aldrich Chemical Company Ltd., Thermo Fisher Scientific, and Lancaster Chemicals. Unless stated otherwise, the materials were used without further purification. Solvents were supplied by Thermo Fisher Chemicals.

5.2 Instrumentation

The following analytical instruments were used to analyse and characterise the products:

Fourier-transform infrared (FT-IR) spectroscopy: Unless stated otherwise, the materials were prepared as KBr pellets and FT-IR spectra were collected in transmission mode using a JASCO FT-IR-410 spectrometer or a JASCO FT-IR 4100 spectrometer; air was used as a background. Wavenumbers ($\tilde{\nu}$) are given in cm^{-1}; intensities as denoted as vs = very strong, s = strong, m = medium, w = weak, b = broad.

Microanalysis: Carbon, nitrogen and hydrogen content were determined by the microanalysis services within the Department of Chemistry, University of Glasgow using a EA 1110 CHNS, CE-440 Elemental Analyser.

Mass Spectrometry: Electrospray-ionisation mass spectrometry (ESI-MS) and coldspray-ionisation mass spectrometry (CS-MS) were performed using a Bruker micrOTOF-Q quadrupole time-of -flight mass spectrometer.

Single Crystal X-Ray Diffraction: Single crystal datasets were collected at 150(2) K unless stated otherwise on the following instruments:

Nonius Kappa CCD diffractometer (λ ($Mo_{K\alpha}$) = 0.71073 Å) equipped with a graphite monochromator.

Bruker AXS Apex II (λ ($Mo_{K\alpha}$) = 0.71073Å) equipped with a graphite monochromator.

Oxford Diffraction Gemini Ultra S (λ ($Mo_{K\alpha}$) = 0.71073Å and λ ($Cu_{K\alpha}$) = 1.5405 Å) equipped with a graphite monochromator.

Powder X-Ray Diffraction: Powder XRD patterns were collected on a Bruker AXS D8 powder diffractometer (λ ($Cu_{K\alpha}$) = 1.5405 Å) equipped with a graphite monochromator. Unless stated otherwise the datasets were collected in capillary mode at room temperature.

UV-Vis spectroscopy: UV-Vis spectra were collected using a Shimadzu PharmaSpec UV-1700 UV-Vis spectrophotometer in transmission mode using quartz cuvettes with 1.0 cm optical path length.

^{1}H-Nuclear magnetic resonance spectroscopy (^{1}H-NMR): ^{1}H-NMR spectroscopy was performed on a Bruker DPX 400 spectrometer using the solvent signal as internal standard. All δ values are given in ppm.

Thermogravimetric analysis (TGA): Thermogravimetric analysis was performed on a TA Instruments Q 500 Thermogravimetric Analyzer under nitrogen or air flow at a typical heating rate of 5 ° C min^{-1}.

Differential scanning calorimetric analysis (DSC): DSC analysis was performed on a TA Instruments Q 200 calorimeter under nitrogen flow at a typical heating rate of 20 ° C min^{-1}.

Flame Atomic Absorption Spectrometry (FAAS): FAAS was performed at the Environmental Chemistry Section, Department of Chemistry, University of Glasgow on a Perkin-Elmer 1100B Atomic Absorption Spectrophotometer.

pH measurements: The solution pH was determined using a Hanna HI-98160 pH meter equipped with a glass electrode and temperature probe. Two-point calibration was conducted at pH 4.01 and pH 7.01.

5.3 Synthesis and characterisation

5.3.1 Synthesis of compound 1 $(C_6H_{16}O_3N_1)_8[Mo_{36}O_{112}(H_2O)_{14}]\cdot 10H_2O$

$(C_6H_{16}O_3N_1)_6[Mo_{18}O_{54}(SO_3)_2] \rightarrow (C_6H_{16}O_3N_1)_8[Mo_{36}O_{112}(H_2O)_{14}]$

$(C_6H_{16}O_3N_1)_6[Mo_{18}O_{54}(SO_3)_2]\cdot 4H_2O$ (0.20g, 53.7 µmol) was dissolved in 40 ml water in a plastic flask to exclude any sources of sodium cations. The solution was kept in an open plastic vessel for several weeks. Due to oxidation by the air the dark blue solution colour gradually changed to colourless. Slow evaporation of the solution to near dryness over a

period of 1-2 months yielded colourless needle crystals of **1**. Yield: 0.11 g (16.0 µmol, 59.5 % based on Mo).

Characteristic IR-bands (in cm^{-1}): 3412 (s, b), 1617 (m), 1447 (m), 1397 (m), 1261 (w), 1207 (w), 1091 (m), 1066 (m), 979 (m), 957 (s), 877 (vs), 788 (s), 689 (s), 625 (s), 574 (s).

Elemental analysis in wt.-% for $C_{48}H_{176}Mo_{36}N_8O_{160}$ (calculated values in brackets) C 8.38 (7.72), H 2.58 (2.44), N 1.63 (1.50).

5.3.2 Synthesis of compound 2: $(C_6H_{16}O_3N_1)_6\{Na_2[Mo_{36}O_{112}(H_2O)_{14}]\}\cdot 28H_2O$

$36\ Na_2MoO_4 + 6\ C_6H_{16}O_3N_1 + 66\ H^+ \rightarrow (C_6H_{16}O_3N_1)_6\{Na_2[Mo_{36}O_{112}(H_2O)_{14}]\}\cdot 28H_2O$

$Na_2MoO_4\cdot 2H_2O$ (1.80 g, 7.4 mmol) and triethanolamine hydrochloride (2.24 g, 12.0 mmol) were dissolved in H_2O (40 ml). The pH of the clear solution was adjusted to 1.2 using dilute HCl (4 M) and the mixture was heated to 90 ° C for 2 h. The solution was then allowed to cool to room temperature, centrifuged and after 1-2 days, colourless crystals of **2** were isolated. Yield 0.42 g (60.4 µmol, 29.4 % based on Mo).

Characteristic IR-bands (in cm^{-1}): 3428 (s, b), 2963 (w), 2925 (w), 2874 (w), 1625 (m), 1448 (w), 1385 (w), 1261 (m), 1209 (w), 1095 (m), 1028 (w), 956 (m), 878 (s), 799 (s), 696 (w), 620 (m), 573 (s).

Elemental analysis in wt.-% for $C_{36}H_{180}Mo_{36}N_6Na_2O_{172}$ (calculated values in brackets): C 6.22 (6.51), H 2.61 (1.80), N 1.21 (1.08).

5.3.3 Computational methods used in the study of 1 and 2

Density Functional Theory (DFT) calculations on both $\{Mo_{36}\}$ cluster anions **1a** and **2a** were performed to establish charge densities. The calculations were performed by Prof. Dr. Paul Kögerler, Ames Laboratory, Iowa State University, USA.

Computational details: DFT calculations were performed on isolated cluster anions using the TURBOMOLE 5.7 program[175] employing TZVP basis sets and hybrid B3-LYP exchange/correlation functionals. In a first step, hydrogen positions of H_2O ligand groups

were modelled onto the crystallographic coordinates of the {Mo_{36}} anions **1a** and **2a** whereby molecular C_i symmetry was maintained. These coordinates were then allowed to relax until the total DFT energies converged; this resulted in maximum deviations smaller than 0.04 Å from the initial crystallographic coordinates. Atomic point charges were derived from the such-obtained final geometries using the Löwdin formalism. The use of the COSMO solvation model to account for continuum polarisation effects in aqueous solution significantly and evenly decreased the energies of the frontier orbitals but did not significantly affect the charge distributions.

First, it was investigated whether the actual coordination site of the sodium cation in **2a** is determined by the coordination site of the TEAH ligand. However, calculations on **1a** and on **2a** with the $[Na(OH_2)_3]^+$ group removed clearly indicate that, while small charge differences are observed for the three terminal oxo groups to which the Na^+ cation eventually binds (only taking Na-O contacts < 2.75 Å into account) in **2a**, their values add to the same total charge (Σ: –0.44) regardless of the site of the TEAH coordination. Although the Na^+ cation could also occupy other positions in the interior "pockets" of the two convex halves of the {Mo_{36}} framework that allow coordination to a different set of three terminal oxo groups, all of these sets yield a decreased total charge (with charge sums of up to –0.40) and thus a decreased electrostatic binding energy, rendering the Na^+ position observed in **2a** the energetic optimum. Calculations on **1a** and **2a** with the TEAH ligands replaced by water molecules then yield charge distributions for the molybdenum centres which indicate that the coordination sites of the $TEAH^+$ ligands are indeed subject to these charge variations: Out of all Mo positions to which water ligands can coordinate, the position to which TEAH coordinates in **2a**, is found to be most electrophilic with a charge of +0.465 in {**2a**+2H_2O}, compared to charges in the range of +0.338 to +0.391 for the other Mo(OH_2) positions. For {**1a**+2H_2O}, the spread of Mo charges is less pronounced but the TEAH coordinated Mo position is identified as the most electrophilic, with a charge of +0.402 compared to charges ranging from +0.339 to +0.369 for the remaining Mo positions that are available for an H_2O – TEAH exchange.

5.3.4 Synthesis of compound 3 $(TEAH)_9Na_2\{(H_2O)_4K\subset[H_{12}W_{36}O_{120}]\}\bullet17H_2O$

$36\ Na_2WO_4 + 9\ TEAH + K^+ + 62H^+ \rightarrow (TEAH)_9Na_2\{(H_2O)_4K\subset[H_{12}W_{36}O_{120}]\}\bullet17H_2O$

$Na_2WO_4\cdot2H_2O$ (2.00 g, 6.06 mmol) and triethanolamine hydrochloride (2.50 g, 13.47 mmol) were dissolved in H_2O (50 ml) in a plastic flask and the solution was adjusted to a pH of 2.2 using 2.0 ml HCl (4M). After heating the reaction mixture to 80° C in a water bath for 30 min, KCl (30mg, 0.40 mmol) were added to the hot solution and the mixture was allowed to cool to room temperature without further stirring. The sample was stored in a plastic vial for crystallisation, which yielded colourless needles of **3** over a period of 2-3 days. Yield: 0.869 g (83.8 µmol, 49.8 % based on W).

Characteristic IR-bands (in cm^{-1}): 3447 (m), 1622 (w), 1449 (w), 1401 (w), 1320 (m), 1256 (m), 1205 (m), 1093 (s), 1065 (vs), 950 (vs), 895 (s), 780 (s).

Elemental analysis in wt.-% for $C_{54}H_{198}KN_9Na_2O_{168}W_{36}$ (calculated values in brackets): C 6.69 (6.26), H 2.00 (1.93), K 0.38 (0.38), N 1.39 (1.22), Na 0.45 (0.44), W 61.7 (63.9).

5.3.5 Synthesis of compound 4: $(TEAH)_9Na_2\{(H_2O)_4Rb\subset[H_{12}W_{36}O_{120}]\}\bullet17H_2O$

$36\ Na_2WO_4 + 9\ TEAH + Rb^+ + 62H^+ \rightarrow (TEAH)_9Na_2\{(H_2O)_4Rb\subset[H_{12}W_{36}O_{120}]\}\bullet17H_2O$

$Na_2WO_4\cdot2H_2O$ (2.00 g, 6.06 mmol) and triethanolamine hydrochloride (2.50 g, 13.47 mmol) were dissolved in H_2O (50 ml) in a plastic flask and the solution was adjusted to a pH of 2.2 using ca. 2.0 ml HCl (4M). The reaction mixture was heated to ca. 80 – 85 ° C in a microwave and RbCl (48 mg, 0.40 mmol) was added to the hot solution under stirring. The mixture was allowed to cool to room temperature. The sample was stored in a plastic vial for crystallisation which gave colourless needles of **4** over a period of 1 week. Yield: 0.695 g (66.7 µmol, 39.6 % based on W).

Characteristic IR-bands (in cm^{-1}): 3443 (m), 1620 (w), 1449 (w), 1404 (m), 1321 (w), 1255 (w), 1203 (w), 1093 (s), 1065 (s), 950 (vs), 894 (vs), 778 (s).

Elemental analysis in wt.-% for $C_{54}H_{198}N_9Na_2O_{168}RbW_{36}$ (calculated values in brackets): C 6.96 (6.23), H 1.64 (1.92), N 1.35 (1.21), Na 0.44 (0.44), Rb 0.81 (0.82), W 64.7 (63.6).

5.3.6 Synthesis of compound 5: $(TEAH)_9Na_2\{(H_2O)_4Cs\subset[H_{12}W_{36}O_{120}]\}\bullet 15H_2O$

$36\ Na_2WO_4 + 9\ TEAH + K^+ + 62\ H^+ \rightarrow (TEAH)_9Na_2\{(H_2O)_4Cs\subset[H_{12}W_{36}O_{120}]\}\bullet 17H_2O$

$Na_2WO_4 \cdot 2H_2O$ (2.00 g, 6.06 mmol) and triethanolamine hydrochloride (2.50 g, 13.47 mmol) were dissolved in H_2O (50 ml) in a plastic flask and the solution was adjusted to a pH of 2.2 using ca. 2.0 ml HCl (4M). The reaction mixture was heated to ca. 80 – 85 ° C in a microwave and CsCl (67 mg, 0.40 mmol) was added to the hot solution under stirring. The mixture was allowed to cool to room temperature. The sample was stored in a plastic vial for crystallisation which yielded colourless needles of **5** over a period of one week. Yield: 0.689 g (65.6 µmol, 38.9 % based on W).

Characteristic IR-bands (in cm^{-1}): 3450 (m), 1620 (m), 1449 (m), 1404 (w), 1320 (w), 1255 (w), 1203 (w), 1093 (m), 1065 (s), 950 (vs), 894 (vs), 781 (m), 652 (m).

Elemental analysis in wt.-% for $C_{54}H_{194}CsN_9Na_2O_{166}W_{36}$ (calculated values in brackets): C 6.93 (6.22), H 1.58 (1.88), N 1.34 (1.28), Na 0.55 (0.44), Cs 0.81 (1.28), W 64.1 (63.5).

5.3.7 Synthesis of compound 6: $(TEA)(TEAH)_8\{(H_2O)_4Sr\subset[H_{12}W_{36}O_{120}]\}\bullet 17H_2O$

$36\ Na_2WO_4 + 9\ TEAH + Sr^+ + 62\ H^+ \rightarrow (TEAH)_9Na_2\{(H_2O)_4Sr\subset[H_{12}W_{36}O_{120}]\}\bullet 17H_2O$

$Na_2WO_4 \cdot 2H_2O$ (2.00 g, 6.06 mmol) and triethanolamine hydrochloride (2.50 g, 13.47 mmol) were dissolved in H_2O (50 ml) in a plastic flask and the solution was adjusted to a pH of 2.2 using ca. 2.0 ml HCl (4M). The reaction mixture was heated to ca. 80 – 85 ° C in a microwave and $SrCl_2 \cdot 6H_2O$ (107 mg, 0.40 mmol) was added to the hot solution under stirring. The mixture was allowed to cool to room temperature. The sample was stored in a plastic vial for crystallisation which gave colourless crystalline needles of **6** over a period of 2.3 days. Yield: 0.930 g (89.3 µmol, 53.1 % based on W).

Characteristic IR-bands (in cm^{-1}): 3433 (s), 1620 (m), 1449 (m), 1398 (w), 1320 (w), 1257 (w), 1204 (s), 1093 (vs), 1066 (s), 953 (vs), 898 (vs), 779 (vs), 660 (s).

Elemental analysis in wt.-% for $C_{54}H_{197}N_9Na_2O_{168}SrW_{36}$ (calculated values in brackets): C 6.76 (6.23), H 1.58 (1.21), N 1.29 (1.21), Na 0.48 (0.44), Sr 0.81 (0.84), W 64.0 (63.6).

5.3.8 Synthesis of compound 7: $(TEA)(TEAH)_8\{(H_2O)_4Ba_{1.5}\subset[H_{12}W_{36}O_{120}]\}\bullet 17H_2O$

$36\ Na_2WO_4 + 9\ TEAH + 1.5Ba^{+} + 62\ H^{+} \rightarrow (TEA)(TEAH)_8\{(H_2O)_4Ba_{1.5}[H_{12}W_{36}O_{120}]\}\bullet 17H_2O$

$Na_2WO_4 \cdot 2H_2O$ (1.00 g, 3.03 mmol) and triethanolamine hydrochloride (1.25 g, 6.73 mmol) were dissolved in H_2O (35 ml) and the solution was adjusted to pH 1.3 with ca. 3 ml HCl (4M). After heating the reaction mixture to 80° C microwave, $BaCl_2 \cdot 2H_2O$ (25 mg, 0.10 mmol) dissolved in H_2O (5 ml) were added dropwise to the vigorously stirred hot solution. The pH was then immediately adjusted to 2.2 with a few drops of aqueous triethanolamine solution (3M) and the mixture was allowed to cool to room temperature. The solution was filtered to remove any precipitate and the clear colourless solution was stored in a plastic vial and gave colourless crystalline needles of **7** over a period of 2-3 days. The crystals were washed with cold water, collected by filtration and dried. Yield: 0.422 g (40.2 μmol, 47.8 % based on W).

Characteristic IR-bands (in cm^{-1}): 3434 (s), 1618 (m), 1450 (w), 1386 (w), 1320 (w), 1257 (m), 1203 (m), 1093 (s), 1067 (s), 956 (vs), 895 (vs), 778 (s).

Elemental analysis in wt.-% for $C_{54}H_{197}Ba_{1.5}N_9O_{168}W_{36}$ (calculated values in brackets): C 6.29 (6.19), H 1.74 (1.89), N 1.20 (1.20), Na 0.45 (0.22), Ba 2.1 (1.96), W 60.1 (63.1).

5.3.9 Synthesis of compound 8 $(TEAH)_9Na_2\{(NH_4)\subset[H_{12}W_{36}O_{120}]\}\bullet 19H_2O$

$36\ Na_2WO_4 + 9\ TEAH + NH_4^{+} + 62\ H^{+} \rightarrow (TEAH)_9Na_2\{(H_2O)_4NH_4\subset[H_{12}W_{36}O_{120}]\}\bullet 17H_2O$

$Na_2WO_4 \cdot 2H_2O$ (2.00 g, 6.06 mmol) and triethanolamine hydrochloride (2.5 g, 13.47 mmol) were dissolved in H_2O (60 ml) in a plastic flask and the solution was adjusted to a pH of 1.8 using 2.5 ml HCl (4M). After heating the reaction mixture to ca. 80° C in microwave, NH_4Cl (27 mg, 0.50 mmol) dissolved in 5 ml H_2O was added dropwise to the vigorously stirred hot solution and the mixture was allowed to cool to room temperature under stirring. The clear solution was stored in a plastic vial and colourless crystalline needles of **8** were isolated after ca. 5 days. The crystals were washed with cold water, collected by filtration and dried. Yield: 0.662 g (38% based on W).

Characteristic IR-bands (in cm^{-1}): 3442 (m), 1623 (m), 1485 (w), 1456 (w), 1404 (w), 1321 (m), 1255 (w), 1197 (w), 1093 (s), 950 (s), 897 (vs), 781 (s), 666 (s).

Elemental analysis in wt.-% for $C_{54}H_{198}N_{10}Na_2O_{166}W_{36}$ (calculated values in brackets): C 6.29, H 1.94, N 1.36, Na 0.45, W 64.2; found: C 6.92 (6.29), H 1.66 (1.94), N 1.37 (1.36), Na 0.46 (0.45), W 66.5 (64.2).

5.3.10 Synthesis of compound 9: $(TEAH)_{11}\{(Ph(C_2H_4)NH_3)\subset[H_{12}W_{36}O_{120}]\}\bullet 17H_2O$

$36\ Na_2WO_4 + 11\ TEAH + Ph(C_2H_4)NH_3^+ + 62\ H^+ \rightarrow$
$(TEAH)_{11}(Ph(C_2H_4)NH_3)\subset[H_{12}W_{36}O_{120}]\}\bullet 17H_2O$

A solution of $Na_2WO_4\cdot 2H_2O$ (2.00 g, 6.06 mmol) and triethanolamine hydrochloride (2.5 g, 13.47 mmol) in 50 ml H_2O was adjusted to a pH of 2.2 using ca. 2 ml HCl (4M). After heating the reaction mixture to ca. 80-85 ° C in a microwave, phenethylamine (29 mg, 0.24 mmol) dissolved in 5 mL H_2O were added dropwise to the stirred hot solution and the mixture was allowed to cool down to room temperature. The clear colourless solution was kept in a plastic vial and after ca. 1 week large colourless crystalline rhombohedra of **9** were isolated. The crystals were collected on a filter paper, washed with cold water and dried. Yield: 0.867 g (82 µmol, 48.7 % based on W).

Characteristic IR-bands (in cm^{-1}): 3425 (m,b), 3058 (w), 1601 (w), 1444 (w), 1351 (w), 1212 (w), 1088 (w), 1051 (vs), 982 (vs), 948 (vs), 888 (vs), 771 (s).

Elemental analysis in wt.-% for $C_{74}H_{234}N_{12}O_{170}W_{36}$ (calculated values in brackets): C: 8.48 (8.36), H: 1.91 (2.21), N: 1.47 (1.58), W 61.8 (62.3).

5.3.11 Synthesis of compound 10: $(TEAH)_{11}\{(Ph(C_4H_8)NH_3)\subset[H_{12}W_{36}O_{120}]\}\bullet 17H_2O$

$36\ Na_2WO_4 + 11\ TEAH + Ph(C_4H_8)NH_3^+ + 62\ H^+ \rightarrow$
$(TEAH)_{11}(Ph(C_4H_8)NH_3)\subset[H_{12}W_{36}O_{120}]\}\bullet 17H_2O$

A solution of $Na_2WO_4\cdot 2H_2O$ (2.00 g, 6.06 mmol) and triethanolamine hydrochloride (2.5 g, 13.47 mmol) in 50 ml H_2O was adjusted to a pH of 2.2 using ca. 2 ml HCl (4M). After heating the reaction mixture to ca. 80-85 ° C in a microwave, 4-phenylbutylamine (33 mg,

0.22 mmol) dissolved in 5 mL H_2O were added dropwise to the stirred hot solution and the mixture was allowed to cool down to room temperature. The clear colourless solution was kept in a plastic vial and after ca. 1 week colourless crystalline needles of **10** were isolated. The crystals were collected on a filter paper, washed with cold water and dried. Yield: 0.658 g (62 µmol, 36.7 % based on W).

Characteristic IR-bands (in cm^{-1}): 3315 (m,b), 3049 (m), 1610 (w), 1471 (m), 1241 (w), 1051 (m), 1081 (vs), 985 (s), 951 (vs), 891 (vs), 785 (s).

Elemental analysis in wt.-% for $C_{76}H_{238}N_{12}O_{170}W_{36}$ (calculated values in brackets): C: 8.45 (8.56), H: 1.94 (2.25), N: 1.44 (1.58), W 61.5 (62.1).

5.3.12 Synthesis of compound 11: $(TEAH)_{10}Na\{(p\text{-}(CH_2NH_3)_2C_6H_4))\subset[H_{12}W_{36}O_{120}]\}\bullet 17H_2O$

$36\ Na_2WO_4 + 10\ TEAH + p\text{-}(CH_2NH_3)_2C_6H_4^{2+} + 61\ H^+ \rightarrow$
$(TEAH)_{10}Na((p\text{-}(CH_2NH_3)_2C_6H_4)\subset[H_{12}W_{36}O_{120}]\}\bullet 17H_2O$

A solution of $Na_2WO_4{\cdot}2H_2O$ (2.00 g, 6.06 mmol) and triethanolamine hydrochloride (2.5 g, 13.47 mmol) in 50 ml H_2O was adjusted to a pH of 2.2 using ca. 2 ml HCl (4M). After heating the reaction mixture to 80° C in a microwave, 14 mg (0.10 mmol) p-xylylene diamine (p-XDA) dissolved in 5 mL H_2O was added dropwise to the stirred hot solution. The reaction mixture was allowed to cool to room temperature and the clear colourless solution was stored in a plastic vial. After 3-4 days, colourless crystalline needles of **11** were isolated. The crystals were collected on a filter paper and dried. Yield: 0.573 g (0.055 mmol, 32 % based on W).

Characteristic IR-bands (in cm^{-1}): 3450 (m), 3150 (w), 1620 (w), 1474 (w), 1255 (w), 1201 (w), 1093 (s), 1065 (s), 1030 (s), 950 (vs), 898 (vs), 809 (s), 785 (s).

^{1}H-NMR (400 MHz, D_2O, in ppm): δ = 7.61 (b, 4H), 4.20 (b, 4H) 3.92 (m, 60H), 3.46 (m, 60H).

Elemental analysis in wt.-% for $C_{62}H_{204}N_{11}O_{137}W_{36}$ (calculated values in brackets): C 7.79 (7.49), H 1.70 (2.07), N 1.57 (1.55), W 66.02 (66.59), Na: 0.25 (0.23).

5.3.13 Synthesis of compound 12: $(TEAH)_{10}[(H_3N(C_6H_{12})NH_3)\subset[H_{12}W_{36}O_{120}]]\bullet 17H_2O$

$36\ Na_2WO_4 + 10\ TEAH + H_3N(C_6H_{12})NH_3^{2+} + 61\ H^+ \rightarrow$
$(TEAH)_{10}Na((p\text{-}(CH_2NH_3)_2C_6H_4)\subset[H_{12}W_{36}O_{120}]\}\bullet 17H_2O$

A solution of $Na_2WO_4 \cdot 2H_2O$ (2.00 g, 6.06 mmol) and triethanolamine hydrochloride (2.5 g, 13.47 mmol) in 50 ml H_2O was adjusted to a pH of 2.2 using ca. 2 ml HCl (4M). After heating the reaction mixture to 80° C in a microwave, 1,6-diaminohexane (23 mg, 0.20 mmol) dissolved in 5 mL H_2O were added dropwise to the stirred hot solution and the mixture was allowed to cool down to room temperature. The clear colourless solution was kept in a plastic vial and after ca. 2-4 days, colourless crystalline needles of **12** were isolated. The crystals were collected on a filter paper, washed with cold water and dried. Yield: 0.760 g (73 mmol, 43 % based on W).

Characteristic IR-bands (in cm^{-1}): 3438 (m,b), 3065 (w), 1614 (w), 1448 (w), 1395 (w), 1320 (m), 1256 (m), 1205 (m), 1092 (m), 1066 (s), 985 (vs), 950 (vs), 890 (s), 781 (s).

^{1}H-NMR (400 MHz, D_2O): δ = 3.94 (m, 60H), 3.48 (m, 60H) 3.10 (m, 2H), 1.81 (broad, 2H), 1.45 (broad, 2H).

Elemental analysis in wt.-% for $C_{66}H_{224}N_{12}O_{167}W_{36}$ (calculated values in brackets): C 7.43 (7.57), H 1.73 (2.16), N 1.61 (1.60), W 63.5 (63.2).

5.3.14 Synthesis of compound 13: $(CH_6N_3)_{12}[Mo_{12}O_{62}H_{11}NaP_8]\cdot 11H_2O$

$12\ Na_2MoO_4 + 2\ Na_2S_2O_4 + 12\ CH_6N_3^+ + 8\ PO_4^{3-} + 28\ H^+ \rightarrow$
$(CH_6N_3)_{12}[Mo_{12}O_{62}H_{11}NaP_8]\cdot 11H_2O + 4\ SO_4^{2-}$

Guanidine carbonate (1.0 g, 10.5 mmol) was dissolved in 22 ml of water. After adding $Na_2MoO_4 \cdot 2\ H_2O$ (0.50 g, 2.07 mmol), the pH of the clear solution was slowly adjusted to 6.0 using a 1:1 (v/v) mixture of sulphuric acid (9 %) and phosphoric acid (9 %). After the CO_2 – release ceased, $Na_2S_2O_4$ (0.10 g, 0.57 mmol) was added under vigorous stirring. The colour immediately changed to green-blue and after 15 min of stirring the mixture was filtered to remove any insoluble precipitate and a clear green-blue solution was obtained. The sample

was stored in a glass vial for one week and yielded 64 mg (20 µmol, 11.60% based on Mo) of **13** as red crystalline needles.

Characteristic IR-bands (in cm^{-1}): 3151 (m, b), 1650 (s), 1141 (m), 1007 (m), 916 (s), 725 (s).

Elemental analysis in wt.-% for $C_{12}H_{105}N_{36}Mo_{12}Na_1O_{73}P_8$ (calculated values in brackets): C: 4.32 (4.31), H: 2.85 (3.16), N: 14.77 (15.08).

5.3.15 Synthesis of compound 14: $(C_4H_6N_3)_{14}[Mo_{12}O_{62}H_9NaP_8]\cdot 13H_2O$ and compound 16 $(C_4H_6N_3)_5[Mo_5O_{23}P_2H_1]\cdot 5H_2O$

$12\ Na_2MoO_4 + 2\ Na_2S_2O_4 + 14\ C_4H_6N_3^+ + 8\ PO_4^{3-} + 26\ H^+ \rightarrow (C_4H_6N_3)_{14}[Mo_{12}O_{62}H_9NaP_8]\cdot 11H_2O + 4\ SO_4^{2-}$

$5\ Na_2MoO_4 + 1\ Na_2S_2O_4 + 5\ C_4H_6N_3^+ + 2\ PO_4^{3-} + 11\ H^+ \rightarrow (C_4H_6N_3)_{12}[Mo_5O_{23}H_1P_2]\cdot 5H_2O + 2\ SO_4^{2-}$

2–aminopyrimidine (3.0 g, 16.11 mmol) was dissolved in 23 ml of water. Subsequently, $Na_2MoO_4\cdot 2\ H_2O$ (0.50 g, 2.07 mmol) was added and the pH of the clear colourless solution was reduced to 3.5 using phosphoric acid (9 %). $Na_2S_2O_4$ (50 mg, 0.29 mmol) was added under vigorous stirring, resulting in an immediate colour-change to blue. After stirring for 10 min, the solution pH was adjusted to 3.4 using phosphoric acid (9 %) and the solution was filtered to remove any precipitate. Storage at room temperature in a glass sample vial for one week gave a mixture of light blue needles of **16** (130 mg, 87.7 mmol, 4.2 % based on Mo) and 52.0 mg (0.013 mmol, 7.5 % based on Mo) of red-brown plates of **14.**

Characteristic IR-bands (in cm^{-1}): 3394 (m, b), 1667 (s), 1626 (s), 1353 (m), 1067 (s), 959 (s), 731 (m), 492 (m).

Elemental analysis in wt.-% (calculated values in brackets) for $C_{56}H_{119}N_{42}Mo_{12}Na_1O_{75}P_8$: C: 16.72 (16.80), H: 2.85 (3.00), N: 14.37 (14.69).

5.3.16 Synthesis of compound 15: $(C_2H_{10}N_2)_6[Mo_{12}O_{62}H_{11}NaP_8]\cdot 11H_2O$

$12\ Na_2MoO_4 + 2\ Na_2S_2O_4 + 6\ C_2H_{10}N_2^{2+} + 8\ PO_4^{3-} + 28\ H^+ \rightarrow$
$(C2H_{10}N_2)_6[Mo_{12}O_{62}H_{11}NaP_8]\cdot 11H_2O + 4\ SO_4^{2-}$

$Na_2MoO_4 \cdot 2\ H_2O$ (0.50 g, 2.07 mmol) was added to a stirred solution of N,N,N',N'-tetrakis(hydroxyethyl) ethylenediamine (0.50 g, 2.12 mmol) in 20 ml of water at 65 °C. The resulting mixture was acidified to pH 6.0 with phosphoric acid (9 %). $Na_2S_2O_4$ (0.10 g, 0.57 mmol) were added under stirring. The solution instantly turned brown and the solution pH was adjusted to 5.9 using dilute phosphoric acid (9 %). The solution was allowed to cool to room temperature and was subsequently filtered, resulting in a brown solution and a brown precipitate. The clear brown solution was kept in a glass sample vial for ten days and large, red crystal needles of **15** were isolated. Yield: 55 mg (17 µmol, 10.0 %, based on Mo).

Characteristic IR-bands (in cm^{-1}): 3380-3180 (w, b), 1617 (w), 1508 (w), 1336 (w) 1000 (w), 898 (m), 723 (m).

Elemental analysis in wt.-% (calculated values in brackets) for $C_{12}H_{83}N_{12}Mo_{12}Na_1O_{73}P_8$: C: 4.83 (4.83), H: 3.10 (2.80), N: 5.62 (5.63).

5.3.17 Synthesis of compound 17: $(C_{15}H_{28}N_2)_4(C_9H_6O_6)_1[H_{15}Mo_{12}NaO_{62}P_8]\ 10H_2O$

$12\ Na_2MoO_4 + 2\ Na_2S_2O_4 + 4\ C_{15}H_{28}N_2^{2+} + C_9H_6O_6 + 8\ PO_4^{3-} + 32\ H^+ \rightarrow$
$(C_{15}H_{28}N_2)_4(C_9H_6O_6)_1[H_{15}Mo_{12}NaO_{62}P_8]\ 10H_2O + 4\ SO_4^{2-}$

$Na_2MoO_4 \cdot 2H_2O$ (1.33 g, 5.49 mmol) was dissolved in 100 ml of a saturated aqueous 1,3,5-benzenetricarboxylic acid (BTC) solution. 0.5 ml H_3PO_4 (9 %) and (-)-sparteine sulfate pentahydrate (1.25 g, 2.96 mmol) were added. The white precipitate which formed immediately was redissolved by adjusting the pH to 8.0 using concentrated aqueous NaOH solution. The pH was then lowered to 4.0 using H_3PO_4 (9%) and $Na_2S_2O_4$ (1.00 g, 5.70 mmol) was added. The pH was lowered to 3.5 using H_3PO_4 (9 %). After stirring for 2 h, the mixture was filtered and the clear red-brown solution was kept in a glass vial. After three days, red crystals of **17** were isolated. Yield: 0.344 g (94 µmol, 20.6 % based on Mo).

Characteristic IR-bands (in cm^{-1}): 3435(m, b), 2947(m), 1715(m), 1635(m), 1468(m) 1263(m), 1065(s), 966(s), 743(m).

Elemental analysis in wt.-% for the dehydrated material (calculated values in brackets): $C_{69}H_{133}N_8O_{68}Na_1Mo_{12}P_8$: C: 23.44 (23.12), H: 3.91 (3.74), N: 2.96 (3.13).

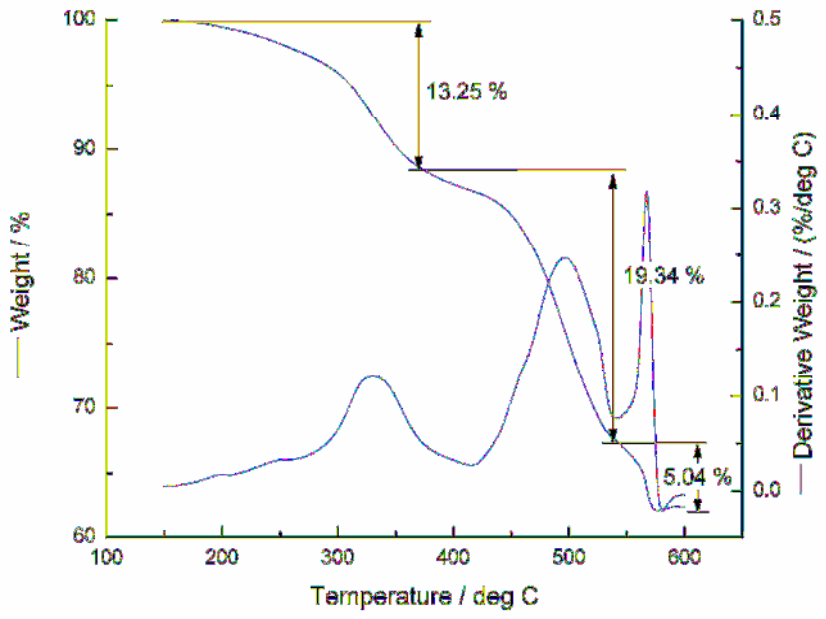

Figure 86: Thermogravimetric analysis of compound **17**.

Thermogravimetric analysis shows three distinct weight losses over the temperature range from 150 ºC to 600 ºC. The first two weight losses correspond to 13.25% and 19.34 % respectively and add up to 32.59 % which correlates to the calculated loss for all BTC and (-)-sparteine moieties (calc: 32.24 %). The third weight loss of 5.04 % can be assigned to a partial decomposition of the cluster with the loss of the phosphate moieties as volatile P_2O_5.

5.3.18 Synthesis of compound 18: $[Ag((CH_3)_2SO)_3][[Ag_3((CH_3)_2SO)_6][H_2V_{10}O_{29}] \bullet 1(CH_3)_2SO$

Synthesis of the precursor $(TBA)_3[H_3V_{10}O_{28}]$:

$10\ NaVo_3 + 7H^+\ 3\ TBA^+ \rightarrow (TBA)_3[H_3V_{10}O_{28}] + 2\ H_2O$

$NaVO_3$ (10.60 g, 87.0 mmol) was dissolved in H_2O by adjusting the pH to 12.5 using aqueous NaOH solution. The pH was lowered slowly to 5.0 by addition of HCl (4M). The clear, orange solution was subsequently added dropwise to an aqueous solution of *n*-Bu_4NBr (17.8 g, 55.2 mmol) in 100 ml water. The pH of the resulting suspension was kept at pH 4.5 using HCl (4M). The orange precipitate was filtered off, washed consecutively with water, EtOH and Et_2O and vacuum dried in a desiccator. The orange

powder was then re-dissolved in 200 ml acetonitrile and the solution was centrifuged to remove any insoluble precipitate. Orange crystals of $(TBA)_3[H_3V_{10}O_{28}]$ were obtained after ca. one week by diffusion of ethyl acetate into the acetonitrile solution. Yield: 6.89 g (4.1 mmol, 46.8 % based on V). Purity was confirmed by FT-IR, single-crystal and powder XRD analysis.

Synthesis of compound **18**:

$(TBA)_3[H_3V_{10}O_{28}] + 4\ Ag^+ + 7\ (CH_3)_2SO)_3 \rightarrow$
$[Ag((CH_3)_2SO)_3][[Ag_3((CH_3)_2SO)_6][H_2V_{10}O_{29}] \bullet 1(CH_3)_2SO$

$(TBA)_3[H_3V_{10}O_{28}]$ (220 mg, 131 µmol) was dissolved in 10 ml DMSO under stirring. 5 equivalents $AgNO_3$ (117 mg, 0.69 mmol) were dissolved in 5 ml of a 3:2 (v:v) mixture of DMSO and acetonitrile and added dropwise to the first solution under stirring. The reaction mixture was stirred for 48 h, centrifuged and setup for crystallisation. The diffusion of ethyl acetate into the reaction mixture resulted in the formation of **18** as orange hexagonal plates. NB: Compound **19** crystallises as a side product. Yield: 112 mg (52.1 µmol, 39.7 % based on V).

Characteristic IR-bands (in cm^{-1}): 3348(m, b), 2938 (s), 2870 (s), 1481 (w), 975 (vs), 891 (vs), 792 (vs).

Elemental analysis in wt.-% for $C_{20}H_{62}Ag_4O_{38}S_{10}V_{10}$ (calculated values in brackets): C 10.79 (11.06), H 2.85 (2.70).

5.3.19 Synthesis of compound 19: $[Ag((CH_3)_2SO)_2][[Ag_3((CH_3)_2SO)_6][H_2V_{10}O_{28}] \bullet 1(CH_3)_2SO$

$(TBA)_3[H_3V_{10}O_{28}] + 4\ Ag^+ + 8\ (CH_3)_2SO)_3 \rightarrow$
$[Ag((CH_3)_2SO)_3][[Ag_3((CH_3)_2SO)_6][H_2V_{10}O_{29}] \bullet 1(CH_3)_2SO$

$(TBA)_3[H_3V_{10}O_{28}]$ (230 mg, 137 µmol) was dissolved in 4 ml DMSO under stirring. 8 equivalents $AgNO_3$ (187 mg, 1.10 mmol) were dissolved in 3 ml of a 3:1 (v:v) mixture of DMSO and acetonitrile and added dropwise to the first solution under stirring. The reaction mixture was stirred for 24 h, centrifuged and setup for crystallisation. The diffusion of ethyl acetate into the reaction mixture resulted in the formation of **19** as red block crystals. NB: Compound **18** crystallises as a side product. Yield: 98 mg (43.0 µmol, 34.2 % based on V).

Characteristic IR-bands (in cm^{-1}): 3352(m, b), 2946 (s), 2872 (s), 1471 (w), 981 (vs), 881 (vs), 795 (vs).

Elemental analysis in wt.-% for $C_{18}H_{56}Ag_4O_{37}S_9V_{10}$ (calculated values in brackets): C 10.81 (10.32), H 2.85 (2.70).

5.3.20 Synthesis of compound 20: $[Ag(CH_3CN)_4]$ $[[Ag(CH_3CN)_2]_4H_3W_{12}O_{40}]$

$(n\text{-}C_4H_9)4N)_4H_4W_{12}O_{40}^{+}$ 5 Ag^+ + 12 $CH_3CN \rightarrow [Ag(CH_3CN)_4][[Ag(CH_3CN)_2]_4H_3W_{12}O_{40}]$

$(n\text{-}C_4H_9)_4N)_4H_4W_{12}O_{40}$ (500 mg, 131 µmol) and 10 equivalents of $AgNO_3$ (222 mg, 1.31 mmol) were dissolved in 25 ml acetonitrile. 1 ml HNO_3 (35%) was added and the mixture was heated to 80 °C for 24 h under stirring. After cooling to room temperature, a white precipitate was removed by centrifugation. Diffusion of acetone, ethyl acetate or ether into the clear solution gave large colourless block crystals of **20** after ca. 4 days. Yield: 297 mg (76.5 µmol, 59.7 % based on W).

Characteristic IR-bands (in cm^{-1}): 3454 (vs,b), 1623 (m), 1384 (w), 1262 (w), 945 (s), 892 (vs), 768 (vs).

Elemental analysis in wt.-% for $C_{24}H_{39}N_{12}O_{40}Ag_5W_{12}$ (calculated values in brackets): C: 6.67 (7.42); H: 0.88 (1.01); N: 3.78 (4.33), Ag 13.90 (13.66), W 56.84 (58.26), indicating the loss of 1.5 CH_3CN solvent molecules.

UV-VIS spectroscopy

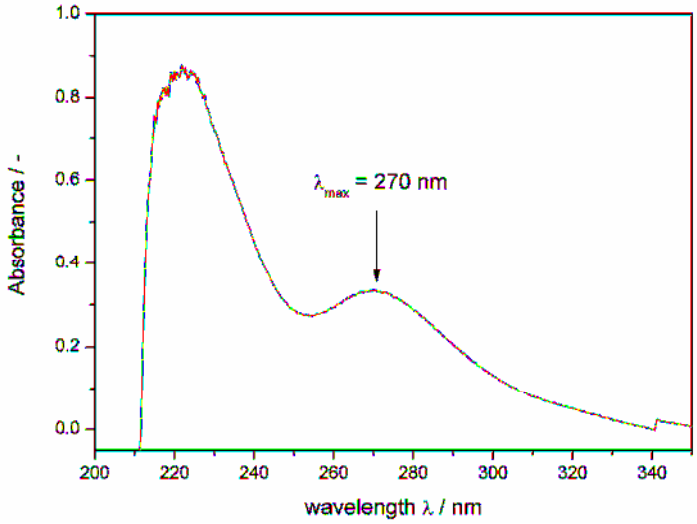

Figure 88: Solid-state UV-VIS spectrum of **20** recorded in transmission mode. The absorption peak at λ = 270 nm is indicative of the presence of argentophilic Ag-Ag-interactions.

Thermogravimetric analysis and differential scanning calorimetry

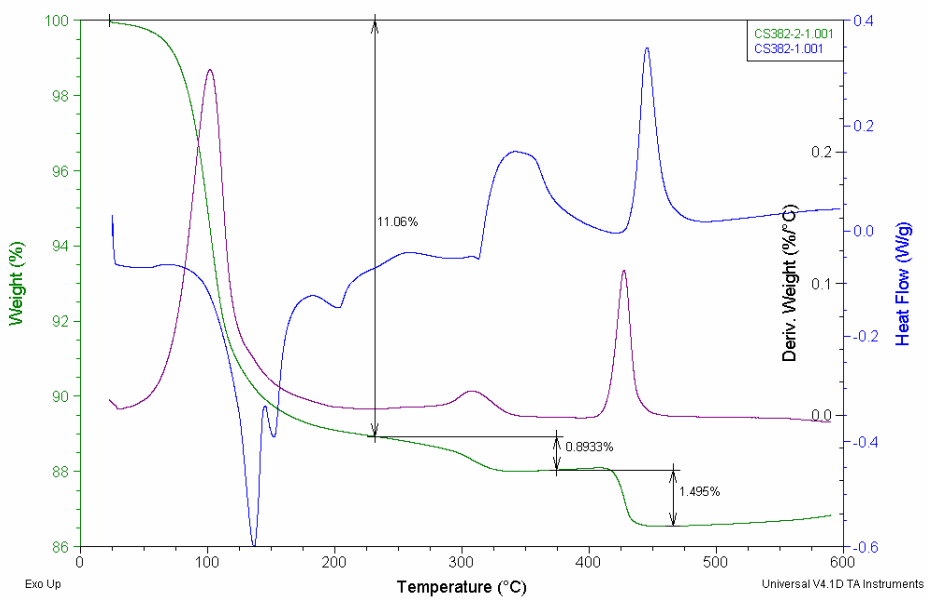

Figure 87: Thermogravimetric analysis (TGA) and differential scanning calorimetry analysis (DSC) of compound **20**.

Step 1: loss of 12 CH_3CN, between 20 and 220 °C, peak at 102 °C. Weight loss: 11.06 % (calc: 12.59 %) indicating the loss of some solvent acetonitrile molecules upon air-drying.

Step 2: loss of 1.5 H_2O (oxygen and protons from the cluster), between 220 and 375 °C, peak at 308 °C. Weight loss: 0.89 % (calc: 0.70).

Step 3: structural decomposition between 375 and 470 °C, peak at 427 °C

Weight loss: 1.49 % most likely due to the formation and decomposition of Ag_2O with the release of molecular O_2.

Thermogravimetric sorption studies

A crystalline sample of **1** was removed from the mother liquor, air dried, ground up and heated to 150 °C (rate: 20 °C min^{-1}) on a TA Instruments TGA 500. The sample was kept isothermal until no further weight loss was observed (ca. 20 min). The sample was then cooled to room temperature and stored in acetonitrile vapour for 24 h to allow re-adsorption of the solvent molecules. The thermogravimetric procedure described above was then repeated to determine the reversibility of the sorption process.

5.3.21 Synthesis of compound 21: (*n*-$Bu_4N)_4[H_4W_{12}O_{40}]$

$12\ Na_2WO_4 + 20H^+ + 4\ (n\text{-}Bu_4N) \rightarrow (n\text{-}Bu_4N)_4[H_4W_{12}O_{40}] + 8\ H_2O$

$Na_2WO_4 \cdot H_2O$ (12.0 g, 36.4 mmol) was dissolved in 100 ml warm H_2O. The clear solution (pH 8.5) was slowly acidified to pH 3.5 using ca. 25 ml of aqueous HCl (19 %). A pale yellow precipitate which appeared on addition of the acid was allowed to re-dissolve by vigorous stirring. The clear yellow solution was subsequently heated to 90 ° C for 48 h, cooled to room temperature and centrifuged to remove any precipitate which had formed over the course of the reaction. The solution pH was again adjusted to 3.5 using HCl (19 %) and 10 equivalents of *n*-tetrabutylammonium bromide (14.08 g, 43.7 mmol) dissolved in 20 ml of water were added to the tungstate solution under vigorous stirring. The solution pH was kept at 3.0 using HCl (19 %) and a white voluminous precipitate was filtered off, washed consecutively with water, EtOH and Et_2O and vacuum dried in a desiccator. The white powder was then redissolved in hot acetonitrile (ca. 200ml), centrifuged to remove any insoluble by-products and allowed to crystallise. Large colourless crystalline blocks of **21** were obtained after ca. one week. Yield: 10.16 g (2.62 mmol, 86.4 % based on W).Characteristic IR-bands (in cm^{-1}): 3443(m, b), 2960 (s), 2871 (s), 1634 (m), 1482 (s), 1380 (m), 1152 (w), 941 (vs), 879 (vs), 781 (vs). Elemental analysis in wt.-% for $C_{64}H_{148}N_4O_{40}W_{12}$ (calculated values in brackets): C 20.08 (20.12), H 3.87 (3.90), N 1.51 (1.47).

ESI-MS analysis

Crystals of compound 21 were dissolved in acetonitrile and diluted to a final concentration of *ca.* 2 x 10^{-6} mol L^{-1}.

Peak assignments for the native compound 21 in negative ion mode:

Peak m/z	Charge	Assignment
703.83	2-	W_6O_{19}
712.85	4-	$H_4W_{12}O_{40}$
944.78	3-	$H_3W_{12}O_{39}$
962.8	3-	$K_1H_4W_{12}O_{40}$
976.4	3-	$K_2H_3W_{12}O_{40}$
987.82	3-	$K_3H_2W_{12}O_{40}$
1030.55	3-	$(TBA)_1H_4W_{12}O_{40}$
1110.98	3-	$(TBA)_2H_3W_{12}O_{40}$
1404	1-	HW6O19

1547.32	2-	$(TBA)_1H_5W_{12}O_{40}$
1667.96	2-	$(TBA)_2H_4W_{12}O_{40}$
1788.09	2-	$(TBA)_3H_3W_{12}O_{40}$
2224.28	3-	$(TBA)_4(H_5W_{12}O_{40})(H_4W_{12}O_{40})$
2304.04	3-	$(TBA)_5(H_4W_{12}O_{40})_2$
2384.80	3-	$(TBA)_6(H_3W_{12}O_{40})(H_4W_{12}O_{40})$
2465.55	3-	$(TBA)_7(H_3W_{12}O_{40})_2$
2623.33	4-	$(TBA)_7(H_3W_{12}O_{40})_2$
3578.21	1-	$(TBA)_3H_4W_{12}O_{40}$
3819.49	1-	$(TBA)_4H_3W_{12}O_{40}$

Peak assignments for the deprotonated compound 21 in negative ion mode

Peak m/z	Charge	Assignment
712.85	4-	$H_4W_{12}O_{40}$
962.8	3-	$K_1H_4W_{12}O_{40}$
976.4	3-	$K_2H_3W_{12}O_{40}$
987.82	3-	$K_3H_2W_{12}O_{40}$
1030.55	3-	$(TBA)_1H_4W_{12}O_{40}$
1110.98	3-	$(TBA)_2H_3W_{12}O_{40}$
1404	1-	HW_6O_{19}
1667.96	2-	$(TBA)_2H_4W_{12}O_{40}$
1788.09	2-	$(TBA)_3H_3W_{12}O_{40}$
3578.21	1-	$(TBA)_3H_4W_{12}O_{40}$
3819.49	1-	$(TBA)_4H_3W_{12}O_{40}$

5.3.22 Synthesis of compound 22: $(n\text{-}Pr_4N)_5[H_3W_{12}O_{40}]$

$(n\text{-}C_4H_9)_4N)_4[H_4W_{12}O_{40}] + 4\ (n\text{-}Pr_4N) \rightarrow (n\text{-}Pr_4N)_5[H_3W_{12}O_{40}]$

$(n\text{-}C_4H_9)_4N)_4[H_4W_{12}O_{40}]$ (200 mg, 51.5 µmol) was dissolved in 10 ml acetonitrile. $(n\text{-}Pr_4N)Br$ (8 equivalents, 1.09 g, 4.12 mmol) and 100 µl aqueous nitric acid (35 %) were added under stirring. The solution was left to crystallise for eight weeks and produced colourless block crystals of **22**, $(n\text{-}Pr_4N)_4[H_4W_{12}O_{40}]$. Yield: 12 mg (3.19 µmol, 6.2 % based on W). The material was characterised by FT-IR and single-crystal XRD.Characteristic IR-bands (in cm^{-1}): 3342(m, b), 3011 (m), 2866 (s), 1474 (s), 1391 (m), 1144 (w), 943 (vs), 875 (vs), 779 (vs).

6 Crystallographic Section

21 single-crystal X-ray diffraction datasets are presented in this thesis. Due to the large amount of tabulated data such as atoms coordinates, anisotropic displacement parameters and atom coordinates, only tables with bond lengths and angles are listed in this section. For additional data, the reader is referred to the supplementary data which is deposited with this thesis and can be obtained from the University of Glasgow. Structures were solved using Patterson or Direct methods with SHELXS-97 or SIR-92 using WinGX routines. Refinement was accomplished by full matrix least-squares on F^2 *via* SHELXL-97. All non-hydrogen atoms were refined anisotropically unless stated otherwise. Hydrogen atom positions were calculated using standard geometric criteria and refined using a riding model. All data manipulation and presentation steps were performed using WinGX. Details of interest about the structure refinement are given in the tables. The following quantities are given in the information for each structure and were calculated as follows:

$$\text{Goodness-of-fit (GooF)} = \left(\sqrt{\sum \frac{w(F_0^2 - F_c^2)^2}{(n-p)}} \right)$$

$$\text{Weighting scheme } w = \frac{1}{[\sigma^2(\mathrm{F_0})^2 + (\mathrm{A\,P})^2 + (\mathrm{BP})]}$$

$$\text{With } P = \frac{[\max(I_{obs,O}) + 2F_c^2]}{3}$$

and p: number of parameters; n: number of data; A, B: weighting scheme parameters

$$\mathrm{R1} = \frac{\Sigma \,||\, \mathrm{F_0} \,| - |\, \mathrm{F_c} \,||}{\Sigma \,|\, \mathrm{F_o} \,|}$$

$$\mathrm{wR2} = \sqrt{\frac{\Sigma[\mathrm{w}(\mathrm{F_0^2} - \mathrm{F_c^2})^2]}{\Sigma \mathrm{w}(\mathrm{F_0^2})^2}}$$

$$\mathrm{R(int)} = \frac{\Sigma \left| F_0^2 - F_c^2(mean) \right|}{\Sigma \left| F_0^2 \right|}$$

6.1 Crystal data and structure refinement for compound 1

Identification code	DEQREX	
Empirical formula	C36 H182 Mo36 N6 O172	
Formula weight	6905.72	
Temperature	120(2) K	
Wavelength	0.71073 Å	
Crystal system	Triclinic	
Space group	*P*-1	
Unit cell dimensions	a = 16.3351(3) Å	α = 83.330(1)°.
	b = 16.5709(4) Å	β = 65.010(2)°.
	c = 18.5803(5) Å	γ = 85.107(2)°.
Volume	4524.08(18) $Å^3$	
Z	1	
Density (calculated)	2.535 g/cm^3	
Absorption coefficient	2.525 mm^{-1}	
F(000)	3328	
Crystal size	0.20 x 0.20 x 0.16 mm^3	
Theta range for data collection	1.66 to 25.98°.	
Index ranges	-18<=h<=20, -19<=k<=20, -22<=l<=22	
Reflections collected	63978	
Independent reflections	17591 [R(int) = 0.0465]	
Completeness to theta = 25.98°	99.2 %	
Absorption correction	Empirical	
Max. and min. transmission	0.6881 and 0.6321	
Refinement method	Full-matrix least-squares on F^2	
Data / restraints / parameters	17591 / 0 / 1016	
Goodness-of-fit on F^2	1.066	
Final R indices [I>2sigma(I)]	R1 = 0.0439, wR2 = 0.1182	
R indices (all data)	R1 = 0.0569, wR2 = 0.1279	
Largest diff. peak and hole	1.52 and -1.08 $e.Å^{-3}$	

Ortep representation of compound 1 at 50 % probability level

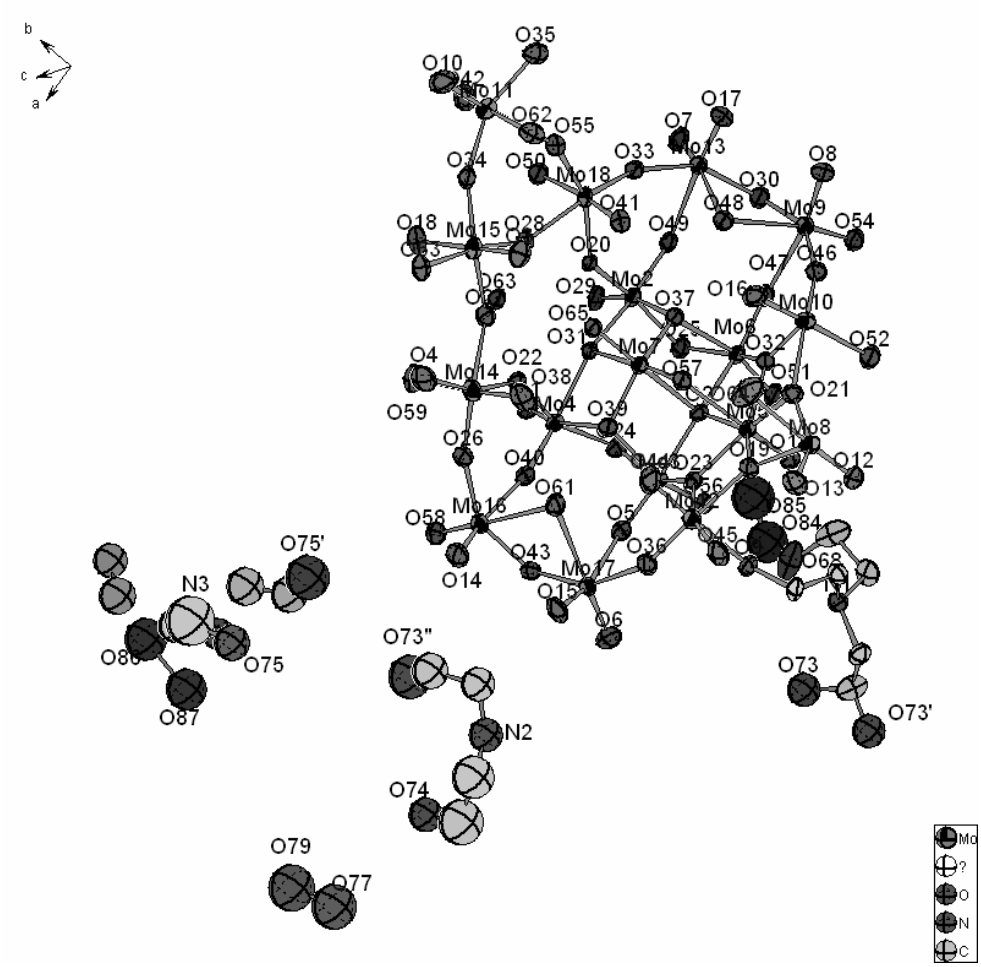

6.2 Crystal data and structure refinement for compound 2

Identification code	DEQRAT	
Empirical formula	C36 H180 Mo36 N6 Na2 O172	
Formula weight	6949.68	
Temperature	150(2) K	
Wavelength	0.71073 Å	
Crystal system	Triclinic	
Space group	*P*-1	
Unit cell dimensions	a = 15.8931(2) Å	α = 101.2100(10)°.
	b = 17.3089(2) Å	β = 95.4810(10)°.
	c = 18.1880(3) Å	γ = 116.5850(10)°.
Volume	4292.95(10) $Å^3$	
Z	1	
Density (calculated)	2.688 g/cm^3	
Absorption coefficient	2.666 mm^{-1}	
F(000)	3348	
Crystal size	0.25 x 0.20 x 0.18 mm^3	
Theta range for data collection	1.54 to 26.00°.	
Index ranges	-19<=h<=19, -21<=k<=20, 0<=l<=22	
Reflections collected	55854	
Independent reflections	16838 [R(int) = 0.044]	
Completeness to theta = 26.00°	99.7 %	
Absorption correction	Empirical	
Max. and min. transmission	0.645 and 0.555	
Refinement method	Full-matrix least-squares on F^2	
Data / restraints / parameters	16838 / 12 / 1213	
Goodness-of-fit on F^2	1.043	
Final R indices [I>2sigma(I)]	R1 = 0.0315, wR2 = 0.0665	
R indices (all data)	R1 = 0.0451, wR2 = 0.0706	
Largest diff. peak and hole	1.89 and -0.93 $e.Å^{-3}$	

Ortep representation of compound 2 at 50 % probability level

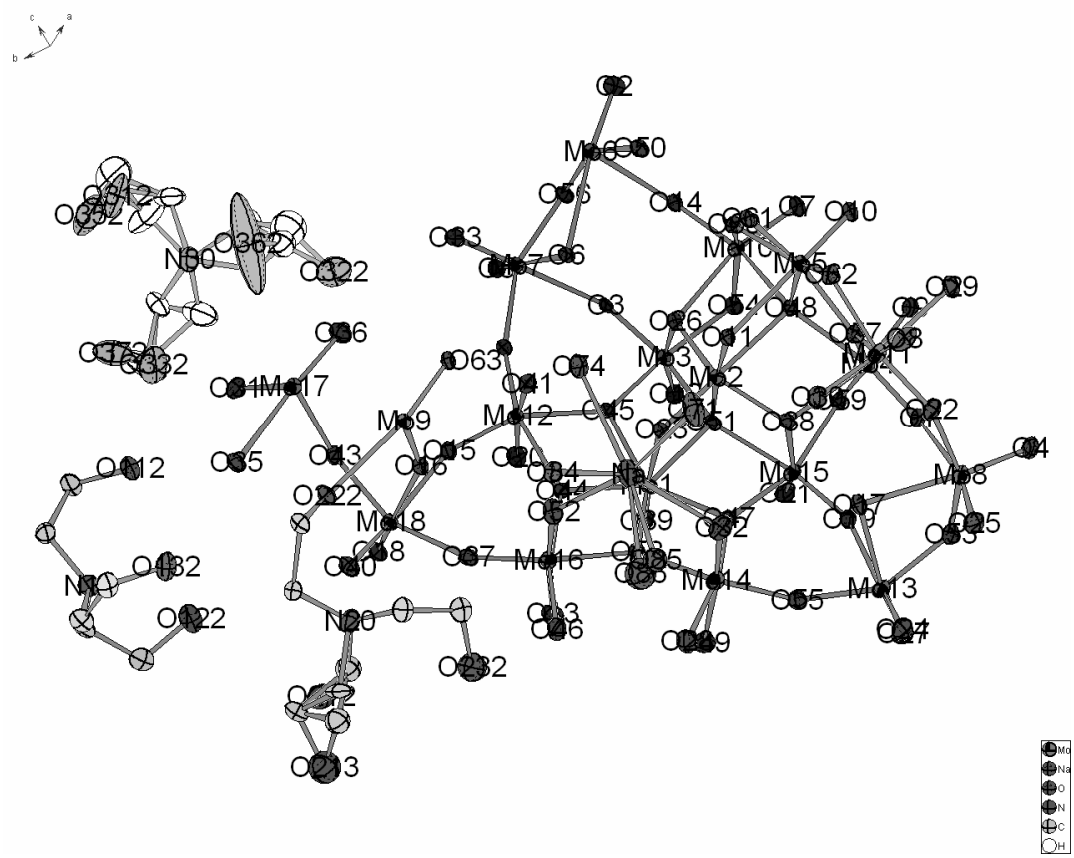

6.3 Crystal data and structure refinement for compound 4

Identification code	WEJVUD	
Empirical formula	C54 H198 N9 Na2 O168 Rb W36	
Formula weight	10412.26	
Temperature	150(2) K	
Wavelength	0.71073 Å	
Crystal system	Orthorhombic	
Space group	*P*nma	
Unit cell dimensions	a = 27.3088(3) Å	α= 90°.
	b = 35.1380(4) Å	β= 90°.
	c = 21.2632(3) Å	γ = 90°.
Volume	20403.7(4) $Å^3$	
Z	4	
Density (calculated)	3.39 g/cm^3	
Absorption coefficient	20.551 mm^{-1}	
F(000)	18608	
Crystal size	0.30 x 0.14 x 0.14 mm^3	
Theta range for data collection	1.68 to 23.50°.	
Index ranges	-30<=h<=30, -39<=k<=37, -23<=l<=23	
Reflections collected	111232	
Independent reflections	15357 [R(int) = 0.0830]	
Completeness to theta = 23.50°	99.9 %	
Absorption correction	Empirical	
Max. and min. transmission	0.1610 and 0.0632	
Refinement method	Full-matrix least-squares on F^2	
Data / restraints / parameters	15357 / 14 / 1121	
Goodness-of-fit on F^2	1.039	
Final R indices [I>2sigma(I)]	R1 = 0.0460, wR2 = 0.0992	
R indices (all data)	R1 = 0.0850, wR2 = 0.1146	
Largest diff. peak and hole	2.60 and -2.26 $e.Å^{-3}$	

ORTEP representation of compound 4 at 50 % probability level

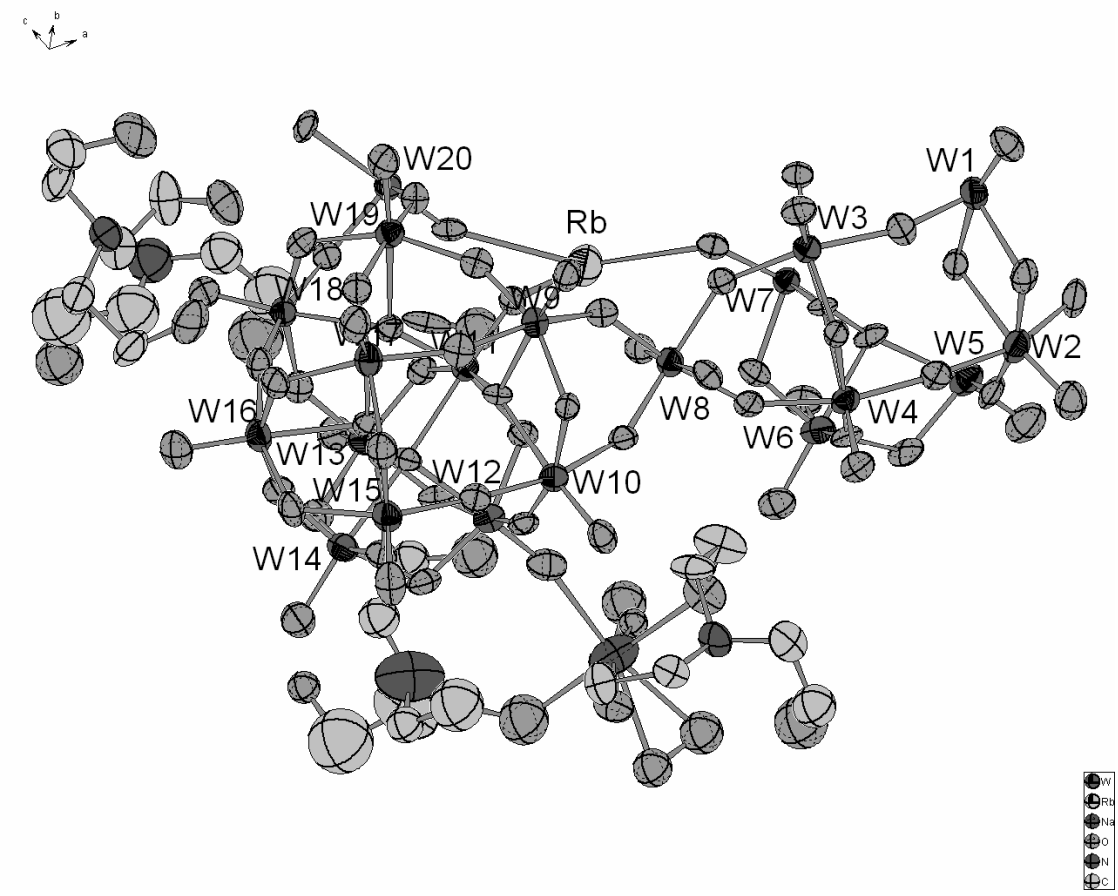

6.4 Crystal data and structure refinement for compound 5

Identification code	WEJWAK	
Empirical formula	C54 H194 Cs N9 Na2 O166 W36	
Formula weight	10423.67	
Temperature	100(2) K	
Wavelength	0.71073 Å	
Crystal system	Orthorhombic	
Space group	*P*nma	
Unit cell dimensions	a = 26.8369(10) Å	α= 90°.
	b = 34.8568(13) Å	β= 90°.
	c = 21.0337(8) Å	γ = 90°.
Volume	19675.9(13) $Å^3$	
Z	4	
Density (calculated)	3.519 g/cm^3	
Absorption coefficient	21.247 mm^{-1}	
F(000)	18600	
Crystal size	0.30 x 0.12 x 0.10 mm^3	
Theta range for data collection	1.13 to 25.00°.	
Index ranges	-31<=h<=31, -41<=k<=31, -22<=l<=19	
Reflections collected	79977	
Independent reflections	15583 [R(int) = 0.0642]	
Completeness to theta = 25.00°	88.4 %	
Absorption correction	Empirical	
Max. and min. transmission	0.2251 and 0.0607	
Refinement method	Full-matrix least-squares on F^2	
Data / restraints / parameters	15583 / 6 / 1112	
Goodness-of-fit on F^2	1.061	
Final R indices [I>2sigma(I)]	R1 = 0.0386, wR2 = 0.0870	
R indices (all data)	R1 = 0.0651, wR2 = 0.1013	
Largest diff. peak and hole	2.37 and -1.57 $e.Å^{-3}$	

ORTEP representation of compound 5 at 50 % probability level

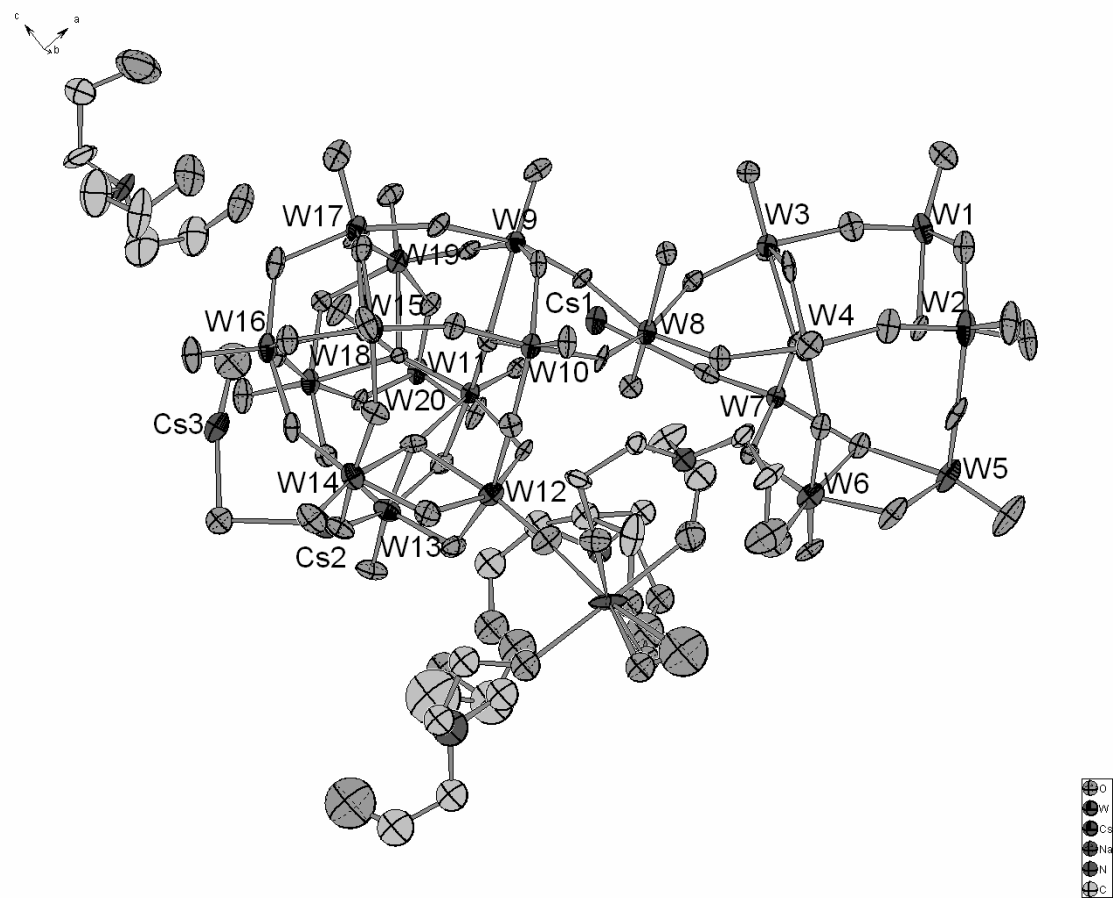

6.5 Crystal data and structure refinement for compound 6

Identification code	WEJWIS	
Empirical formula	C54 H197 N9 Na2 O168 Sr W36	
Formula weight	10413.41	
Temperature	150(2) K	
Wavelength	0.71073 Å	
Crystal system	Orthorhombic	
Space group	*P*nma	
Unit cell dimensions	a = 27.5918(3) Å	α= 90°.
	b = 34.9442(3) Å	β= 90°.
	c = 20.7727(2) Å	γ = 90°.
Volume	20028.5(3) $Å^3$	
Z	4	
Density (calculated)	3.453 g/cm^3	
Absorption coefficient	20.958 mm^{-1}	
F(000)	18608	
Crystal size	0.25 x 0.22 x 0.16 mm^3	
Theta range for data collection	1.87 to 24.00°.	
Index ranges	-31<=h<=29, -32<=k<=39, -23<=l<=20	
Reflections collected	96316	
Independent reflections	15960 [R(int) = 0.0554]	
Completeness to theta = 24.00°	99.6 %	
Absorption correction	Empirical	
Max. and min. transmission	0.1344 and 0.0774	
Refinement method	Full-matrix least-squares on F^2	
Data / restraints / parameters	15960 / 6 / 1178	
Goodness-of-fit on F^2	1.038	
Final R indices [I>2sigma(I)]	R1 = 0.0370, wR2 = 0.0726	
R indices (all data)	R1 = 0.0701, wR2 = 0.0833	
Largest diff. peak and hole	1.35 and -1.37 $e.Å^{-3}$	

ORTEP representation of compound 6 at 50 % probability level

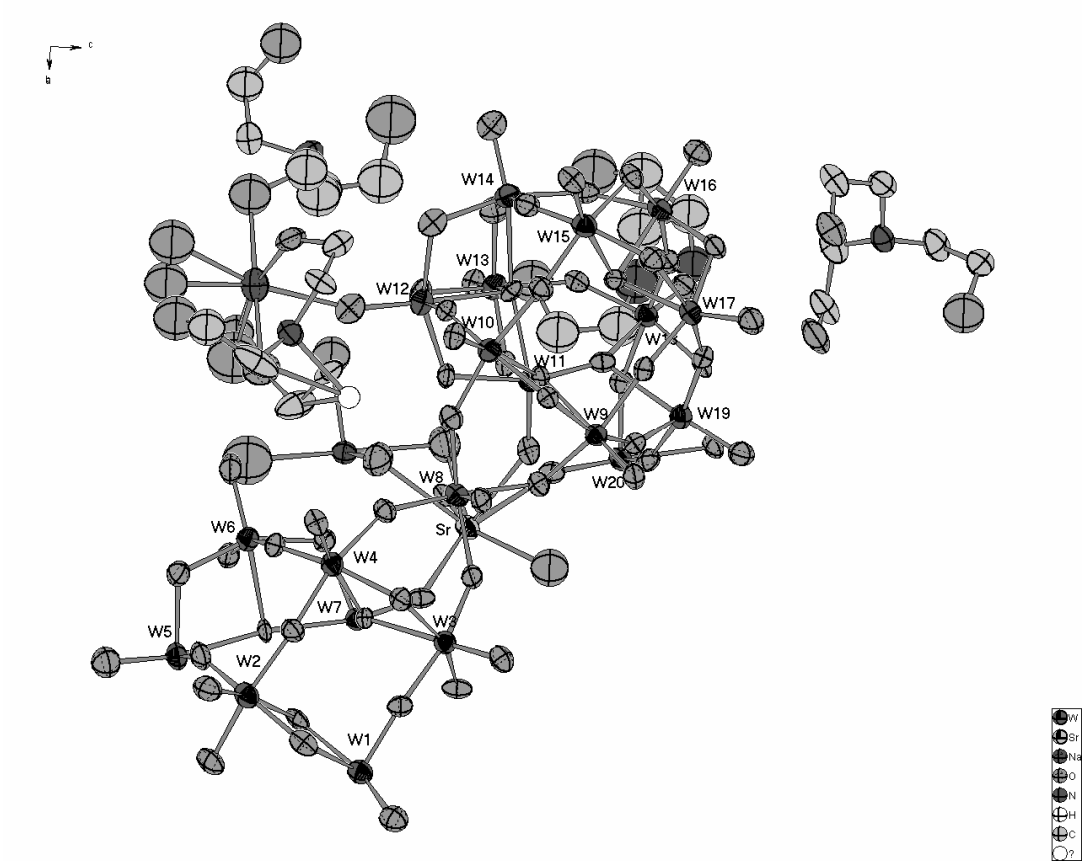

6.6 Crystal data and structure refinement for compound 7

Identification code	WEJWOY	
Empirical formula	C54 H192 Ba N9 Na O165 W36	
Formula weight	10387.10	
Temperature	150(2) K	
Wavelength	0.71073 Å	
Crystal system	Orthorhombic	
Space group	*P*nma	
Unit cell dimensions	a = 27.4259(9) Å	α= 90°.
	b = 35.3105(11) Å	β= 90°.
	c = 20.9978(9) Å	γ = 90°.
Volume	20334.7(13) $Å^3$	
Z	4	
Density (calculated)	3.393 g/cm^3	
Absorption coefficient	20.569 mm^{-1}	
F(000)	18520	
Crystal size	0.32 x 0.18 x 0.14 mm^3	
Theta range for data collection	1.59 to 24.73°.	
Index ranges	-32<=h<=32, -41<=k<=37, -23<=l<=24	
Reflections collected	78760	
Independent reflections	17546 [R(int) = 0.0715]	
Completeness to theta = 24.73°	99.2 %	
Absorption correction	None	
Max. and min. transmission	0.1609 and 0.0583	
Refinement method	Full-matrix least-squares on F^2	
Data / restraints / parameters	17546 / 15 / 1166	
Goodness-of-fit on F^2	1.037	
Final R indices [I>2sigma(I)]	R1 = 0.0407, wR2 = 0.0789	
R indices (all data)	R1 = 0.0689, wR2 = 0.0897	
Largest diff. peak and hole	1.737 and -2.332 e.$Å^{-3}$	

ORTEP representation for compound 7 at 50 % probability level

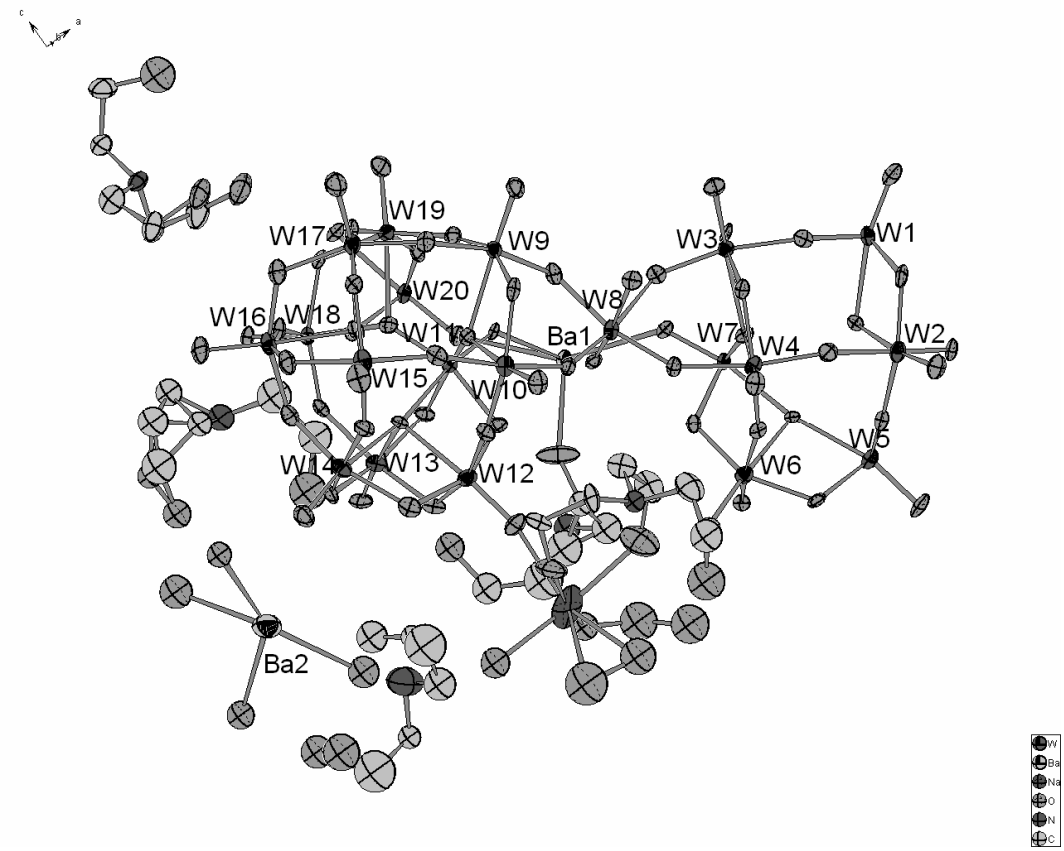

6.7 Crystal data and structure refinement for compound 8

Identification code	WEJWEO	
Empirical formula	C54 H198 N10 Na2 O166 W36	
Formula weight	10308.80	
Temperature	150(2) K	
Wavelength	0.71073 Å	
Crystal system	Orthorhombic	
Space group	*P*nma	
Unit cell dimensions	a = 27.0818(4) Å	α= 90°.
	b = 35.1386(4) Å	β= 90°.
	c = 21.2120(3) Å	γ = 90°.
Volume	20185.7(5) $Å^3$	
Z	4	
Density (calculated)	3.392 g/cm^3	
Absorption coefficient	20.533 mm^{-1}	
F(000)	18424	
Crystal size	0.30 x 0.09 x 0.08 mm^3	
Theta range for data collection	1.61 to 24.00°.	
Index ranges	-30<=h<=30, -40<=k<=35, -24<=l<=24	
Reflections collected	92755	
Independent reflections	15979 [R(int) = 0.0887]	
Completeness to theta = 24.00°	99.0 %	
Absorption correction	Empirical	
Max. and min. transmission	0.2904 and 0.0633	
Refinement method	Full-matrix least-squares on F^2	
Data / restraints / parameters	15979 / 15 / 1170	
Goodness-of-fit on F^2	1.009	
Final R indices [I>2sigma(I)]	R1 = 0.0474, wR2 = 0.0813	
R indices (all data)	R1 = 0.1107, wR2 = 0.1001	
Largest diff. peak and hole	1.42 and -1.35 $e.Å^{-3}$	

ORTEP representation of compound 8 at 50 % probability level

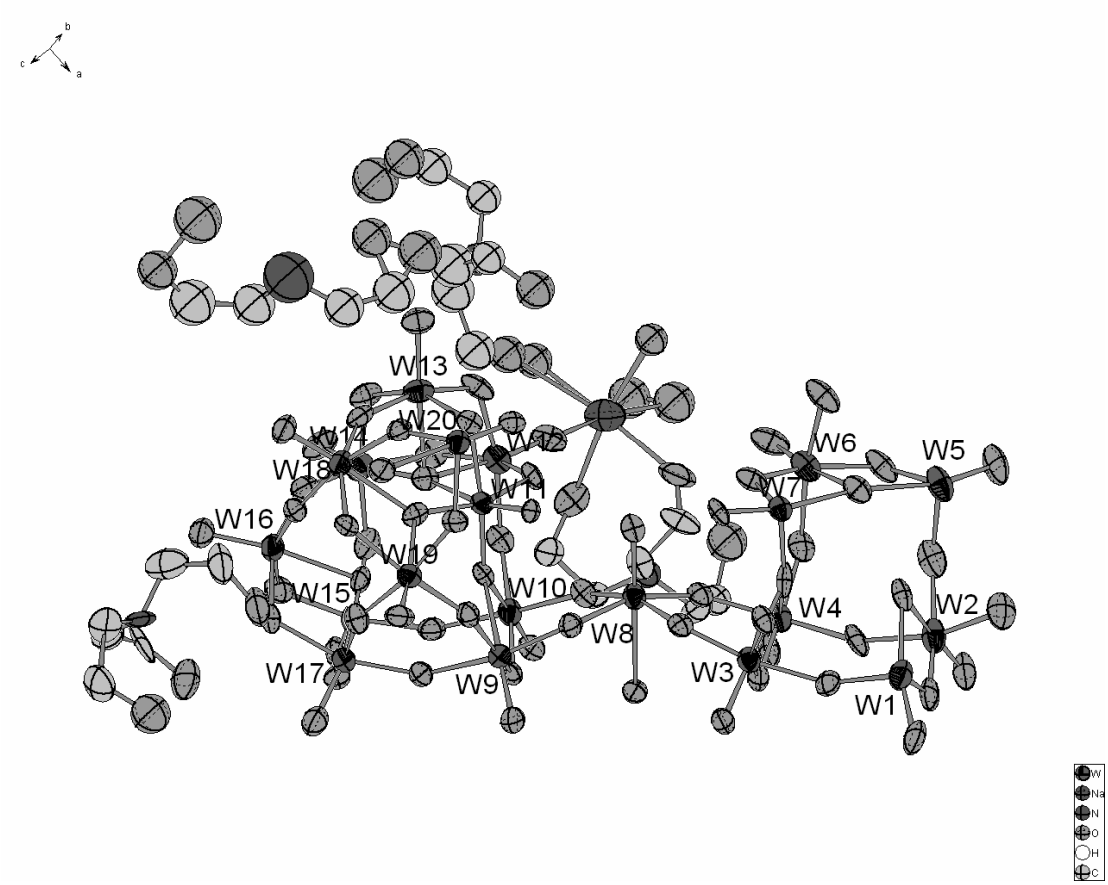

6.8 Crystal data and structure refinement for compound 9

Identification code	ob269a	
Empirical formula	C74 H234 N12 O170 W36	
Formula weight	10633.2416	
Temperature	150(2) K	
Wavelength	0.71073 Å	
Crystal system	Triclinic	
Space group	*P*-1	
Unit cell dimensions	a = 21.2201(6) Å	α= 95.793(2)°.
	b = 21.3592(8) Å	β= 91.268(2)°.
	c = 25.3862(8) Å	γ = 95.597(2)°.
Volume	11386.9(6) $Å^3$	
Z	4	
Density (calculated)	2.350 g/cm^3	
Absorption coefficient	12.136 mm^{-1}	
F(000)	7432	
Crystal size	0.10 x 0.12 x 0.20 mm^3	
Theta range for data collection	1.43 to 24.00°.	
Index ranges	-24<=h<=24, -24<=k<=24, -28<=l<=29	
Reflections collected	112861	
Independent reflections	35295 [R(int) = 0.0797]	
Completeness to theta = 24.00°	98.7 %	
Refinement method	Full-matrix least-squares on F^2	
Data / restraints / parameters	35295 / 9 / 2320	
Goodness-of-fit on F^2	1.005	
Final R indices [I>2sigma(I)]	R1 = 0.0545, wR2 = 0.1179	
R indices (all data)	R1 = 0.1098, wR2 = 0.1419	
Largest diff. peak and hole	2.134 and -1.984 $e.Å^{-3}$	

ORTEP representation of compound 9 at 50 % probability level

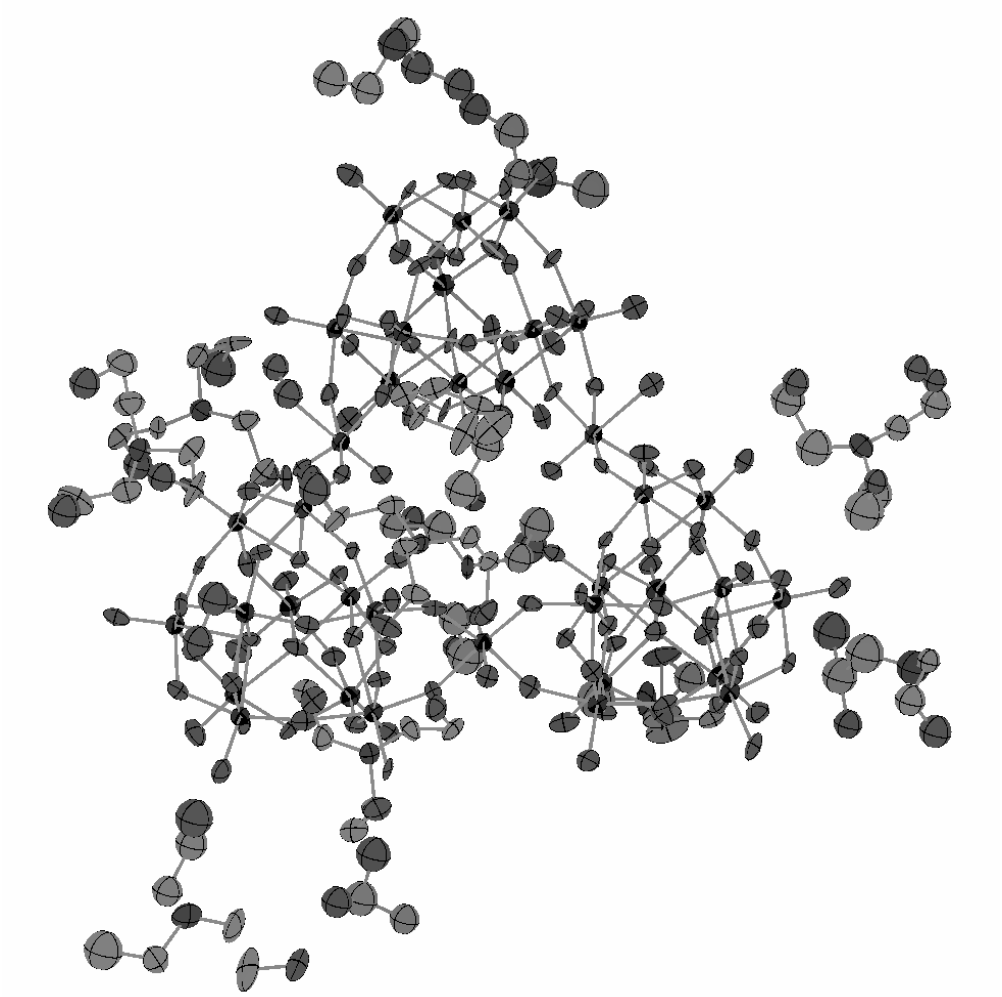

6.9 Crystal data and structure refinement for compound 10

Identification code	ob279b	
Empirical formula	C180 H120 N10 Na6 O50 W36	
Formula weight	9979.40	
Temperature	100(2) K	
Wavelength	0.71073 Å	
Crystal system	Monoclinic	
Space group	$P2_1/c$	
Unit cell dimensions	a = 20.8527(8) Å	α= 90°.
	b = 35.4301(14) Å	β= 93.393(2)°.
	c = 27.2308(10) Å	γ = 90°.
Volume	20083.2(13) $Å^3$	
Z	4	
Density (calculated)	3.301 g/cm^3	
Absorption coefficient	20.600 mm^{-1}	
F(000)	17600	
Crystal size	0.18 x 0.14 x 0.12 mm^3	
Theta range for data collection	1.15 to 25.72°.	
Index ranges	-25<=h<=25, -43<=k<=42, -33<=l<=31	
Reflections collected	151007	
Independent reflections	37929 [R(int) = 0.0664]	
Completeness to theta = 25.72°	98.9 %	
Max. and min. transmission	0.1913 and 0.1190	
Refinement method	Full-matrix least-squares on F^2	
Data / restraints / parameters	37929 / 0 / 2183	
Goodness-of-fit on F^2	1.039	
Final R indices [I>2sigma(I)]	R1 = 0.0469, wR2 = 0.1120	
R indices (all data)	R1 = 0.0834, wR2 = 0.1340	
Largest diff. peak and hole	2.140 and -1.689 $e.Å^{-3}$	

ORTEP representation of compound 10 at 50 % probability level

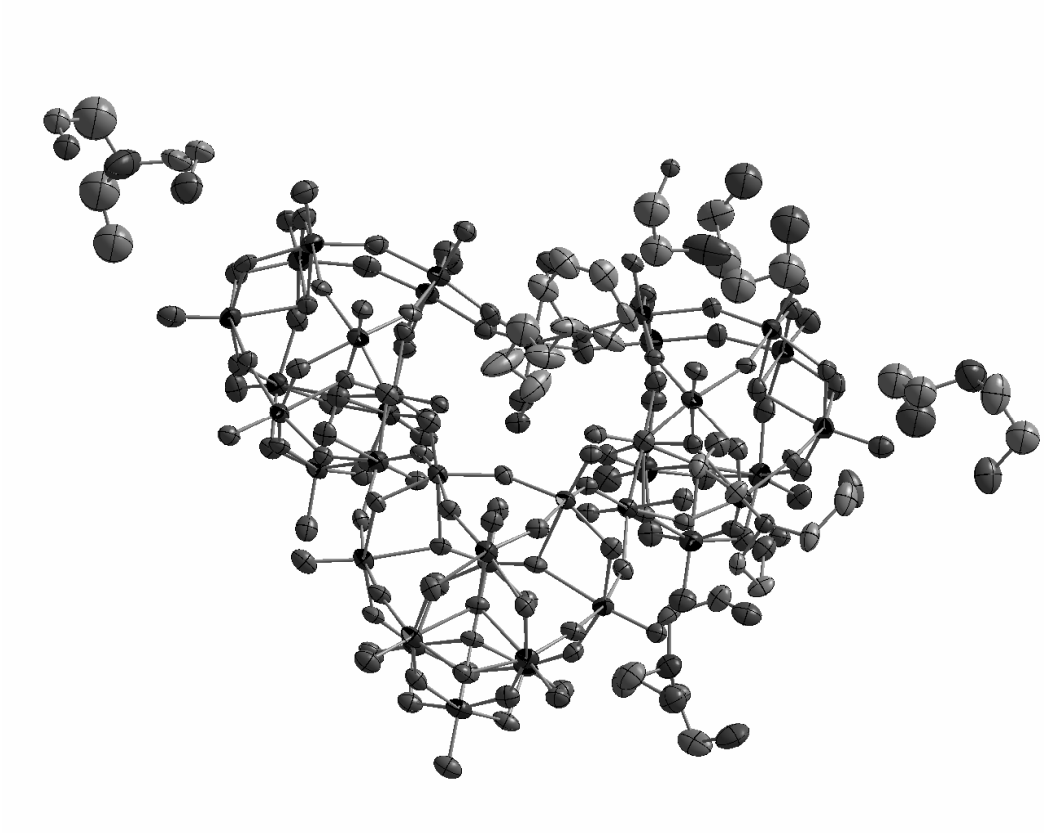

6.10 Crystal data and structure refinement for compound 11

Identification code	ob224e	
Empirical formula	C56 H178 N10 Na2 O160 W36	
Formula weight	10216.66	
Temperature	150(2) K	
Wavelength	0.71073 Å	
Crystal system	Orthorhombic	
Space group	*P*nma	
Unit cell dimensions	a = 26.9515(12) Å	α= 90°.
	b = 35.2430(15) Å	β= 90°.
	c = 21.4907(10) Å	γ = 90°.
Volume	20413.0(16) $Å^3$	
Z	4	
Density (calculated)	3.324 g/cm^3	
Absorption coefficient	20.300 mm^{-1}	
F(000)	18200	
Crystal size	0.30 x 0.06 x 0.06 mm^3	
Theta range for data collection	1.11 to 24.51°.	
Index ranges	-21<=h<=31, -40<=k<=41, -24<=l<=23	
Reflections collected	83614	
Independent reflections	16708 [R(int) = 0.0572]	
Completeness to theta = 24.51°	96.5 %	
Max. and min. transmission	0.3755 and 0.0642	
Refinement method	Full-matrix least-squares on F^2	
Data / restraints / parameters	16708 / 23 / 1110	
Goodness-of-fit on F^2	1.033	
Final R indices [I>2sigma(I)]	R1 = 0.0384, wR2 = 0.0829	
R indices (all data)	R1 = 0.0698, wR2 = 0.0946	
Largest diff. peak and hole	1.886 and -1.334 $e.Å^{-3}$	

Ortep representation of compound 11 at 50 % probability level

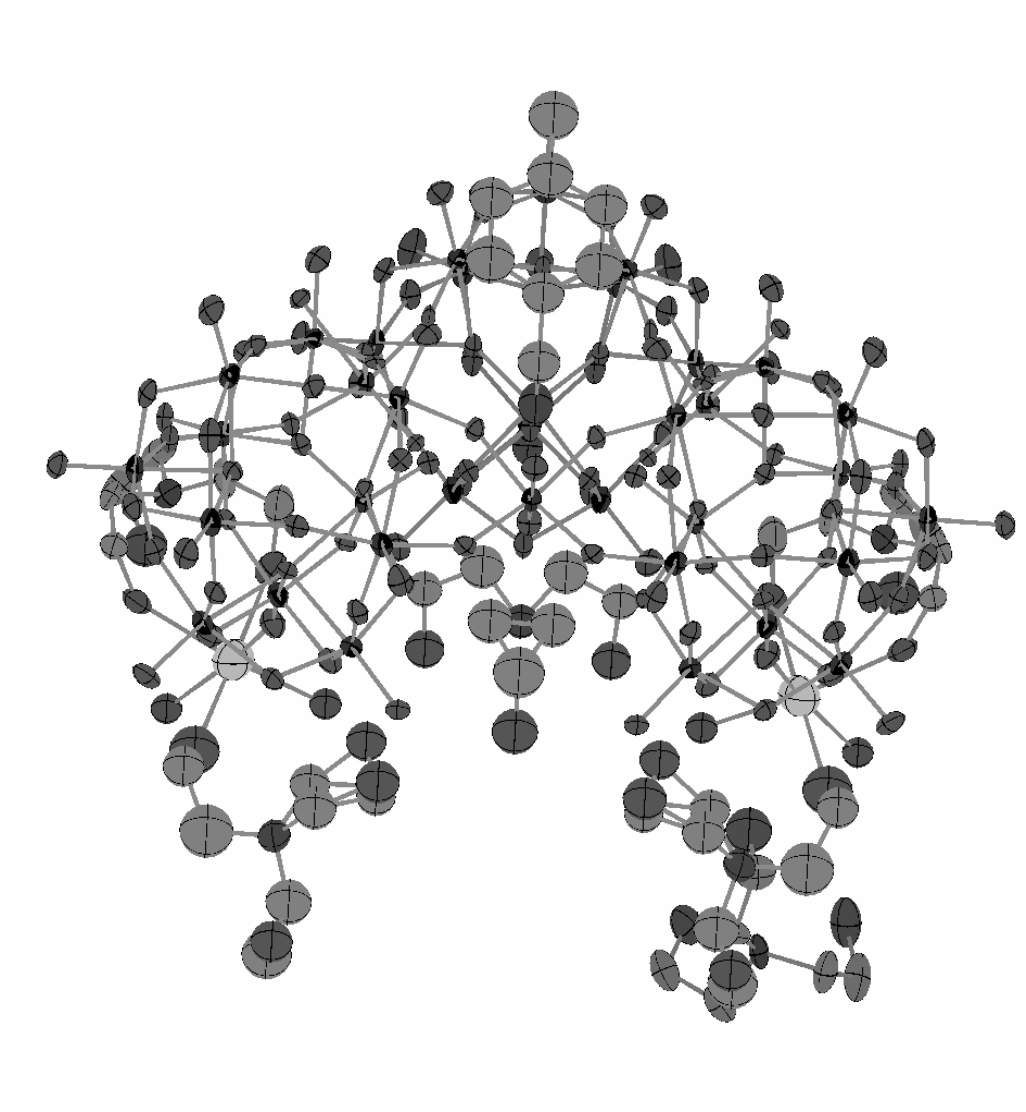

6.11 Crystal data and structure refinement for compound 12

Identification code	ob247b	
Empirical formula	C60 H191 N11 Na2 O160 W36	
Formula weight	10291.82	
Temperature	100(2) K	
Wavelength	0.71073 Å	
Crystal system	Orthorhombic	
Space group	*P*nma	
Unit cell dimensions	a = 27.175(2) Å	α = 90°.
	b = 35.099(3) Å	β = 90°.
	c = 21.202(2) Å	γ = 90°.
Volume	20223(3) $Å^3$	
Z	4	
Density (calculated)	3.380 g/cm^3	
Absorption coefficient	20.492 mm^{-1}	
F(000)	18376	
Crystal size	0.20 x 0.10 x 0.10 mm^3	
Theta range for data collection	1.87 to 23.78°.	
Index ranges	-22<=h<=29, -28<=k<=39, -24<=l<=22	
Reflections collected	71608	
Independent reflections	14839 [R(int) = 0.0642]	
Completeness to theta = 23.78°	94.1 %	
Max. and min. transmission	0.2337 and 0.1052	
Refinement method	Full-matrix least-squares on F^2	
Data / restraints / parameters	14839 / 22 / 1110	
Goodness-of-fit on F^2	1.020	
Final R indices [I>2sigma(I)]	R1 = 0.0336, wR2 = 0.0709	
R indices (all data)	R1 = 0.0499, wR2 = 0.0771	
Largest diff. peak and hole	1.67 and -1.24 e.$Å^{-3}$	

ORTEP representation for compound 12 at 50 % probability level

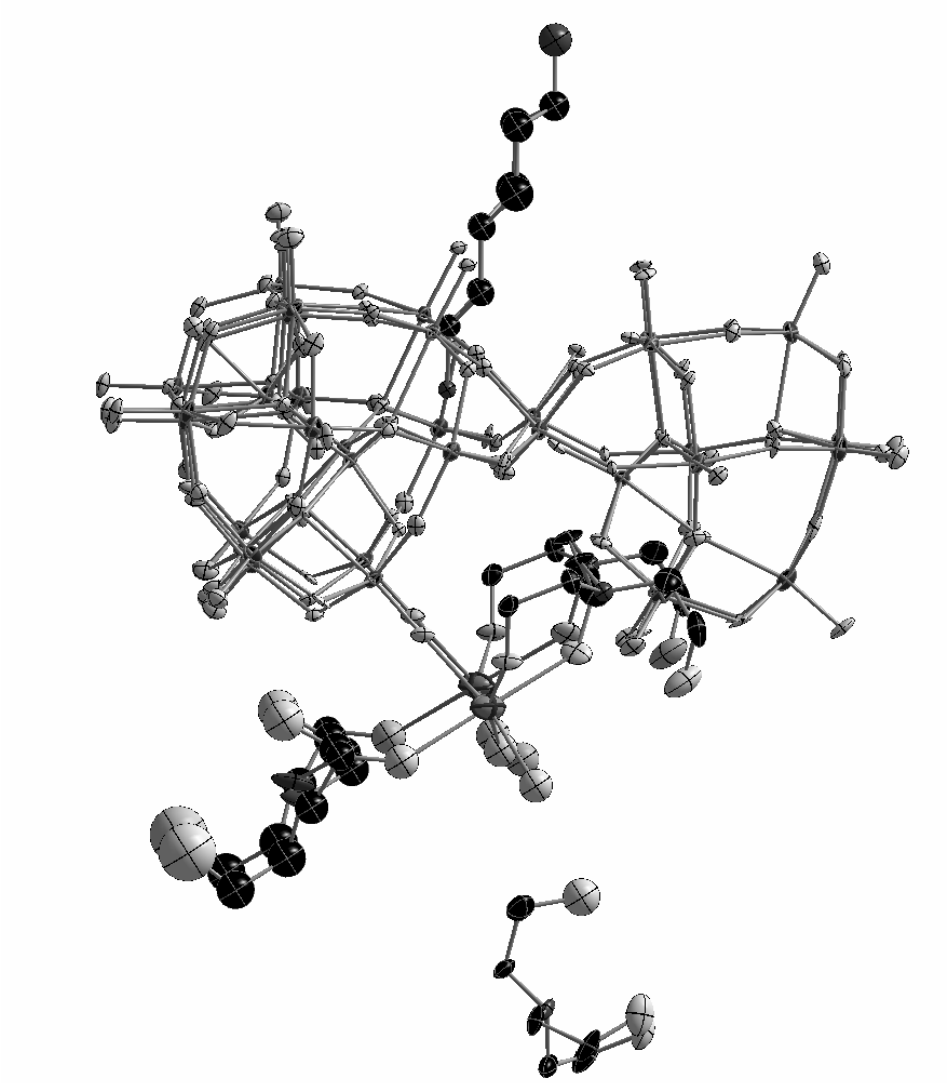

6.12 Crystal data and structure refinement for compound 13

Identification code	GENKIU (at CCDC)	
Empirical formula	C12 H105 Mo12 N36 Na O73 P8	
Formula weight	3344.35	
Temperature	150(2) K	
Wavelength	0.71073 Å	
Crystal system	Monoclinic	
Space group	$P2_1/c$	
Unit cell dimensions	a = 13.3317(3) Å	$\alpha = 90°$.
	b = 23.5623(3) Å	$\beta = 93.3190(10)°$.
	c = 29.9110(6) Å	$\gamma = 90°$.
Volume	9380.0(3) $Å^3$	
Z	4	
Density (calculated)	2.368 g/m^3	
Absorption coefficient	1.820 mm^{-1}	
F(000)	6592	
Crystal size	0.20 x 0.14 x 0.12 mm^3	
Theta range for data collection	1.76 to 26.00°.	
Index ranges	-16<=h<=16, 0<=k<=29, 0<=l<=36	
Reflections collected	62844	
Independent reflections	18356 [R(int) = 0.0618]	
Completeness to theta = 26.00°	99.6 %	
Absorption correction	Empirical	
Max. and min. transmission	0.8112 and 0.7123	
Refinement method	Full-matrix least-squares on F^2	
Data / restraints / parameters	18356 / 0 / 1298	
Goodness-of-fit on F^2	1.035	
Final R indices [I>2sigma(I)]	R1 = 0.0436, wR2 = 0.0977	
R indices (all data)	R1 = 0.0814, wR2 = 0.1096	
Largest diff. peak and hole	1.721 and -0.752 $e.Å^{-3}$	

ORTEP representation of compound 13 at 50 % probability level

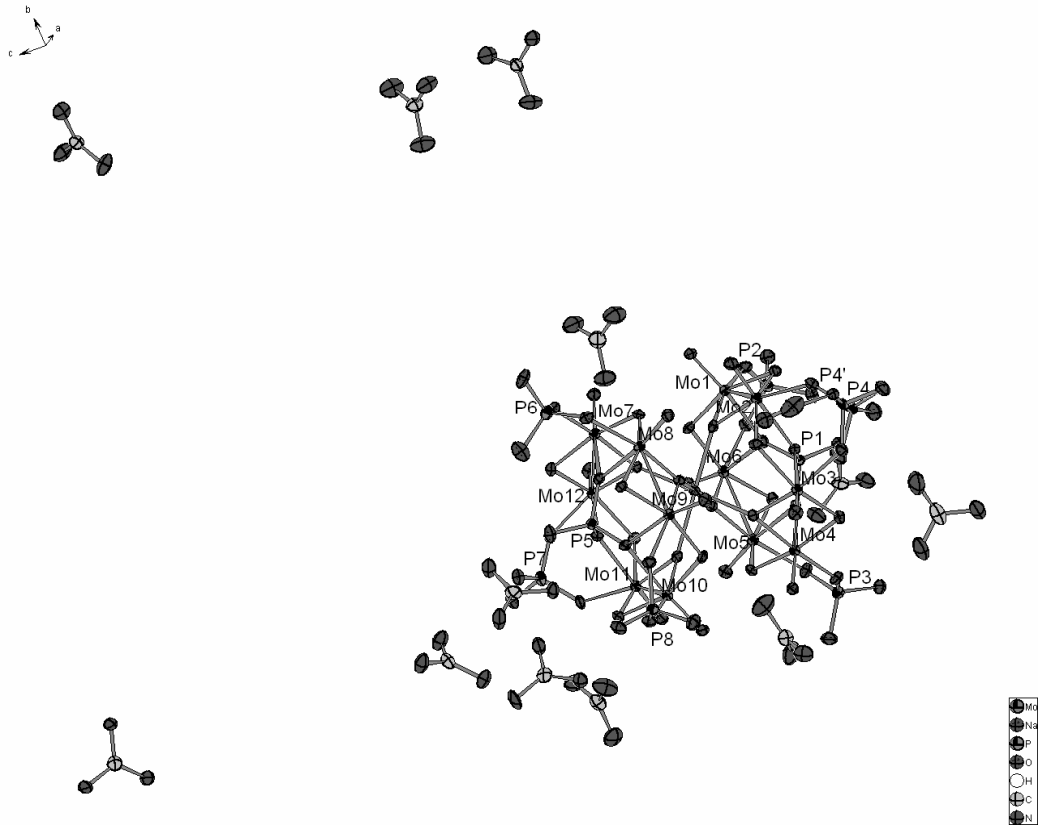

6.13 Crystal data and structure refinement for compound 14

Identification code	GENKOA	
Empirical formula	C56 H119 Mo12 N42 Na O75 P8	
Formula weight	4002.96	
Temperature	150(2) K	
Wavelength	0.71073 Å	
Crystal system	Triclinic	
Space group	*P*-1	
Unit cell dimensions	a = 16.9408(4) Å	α= 95.992(1)°.
	b = 17.8534(2) Å	β= 90.013(1)°.
	c = 26.8981(5) Å	γ = 113.569(1)°.
Volume	7408.1(2) $Å^3$	
Z	2	
Density (calculated)	1.795 g/cm^3	
Absorption coefficient	1.171 mm^{-1}	
F(000)	3968	
Crystal size	0.3 x 0.2 x 0.04 mm^3	
Theta range for data collection	1.86 to 21.13°.	
Index ranges	-17<=h<=17, -18<=k<=17, 0<=l<=27	
Reflections collected	62347	
Independent reflections	15944 [R(int) = 0.0724]	
Completeness to theta = 21.13°	98.5 %	
Absorption correction	Empirical	
Max. and min. transmission	0.907 and 0.747	
Refinement method	Full-matrix least-squares on F^2	
Data / restraints / parameters	15944 / 126 / 1614	
Goodness-of-fit on F^2	1.050	
Final R indices [I>2sigma(I)]	R1 = 0.0787, wR2 = 0.2098	
R indices (all data)	R1 = 0.1025, wR2 = 0.2252	
Largest diff. peak and hole	1.961 and -0.873 $e.Å^{-3}$	

ORTEP representation of compound 14 at 50 % probability level

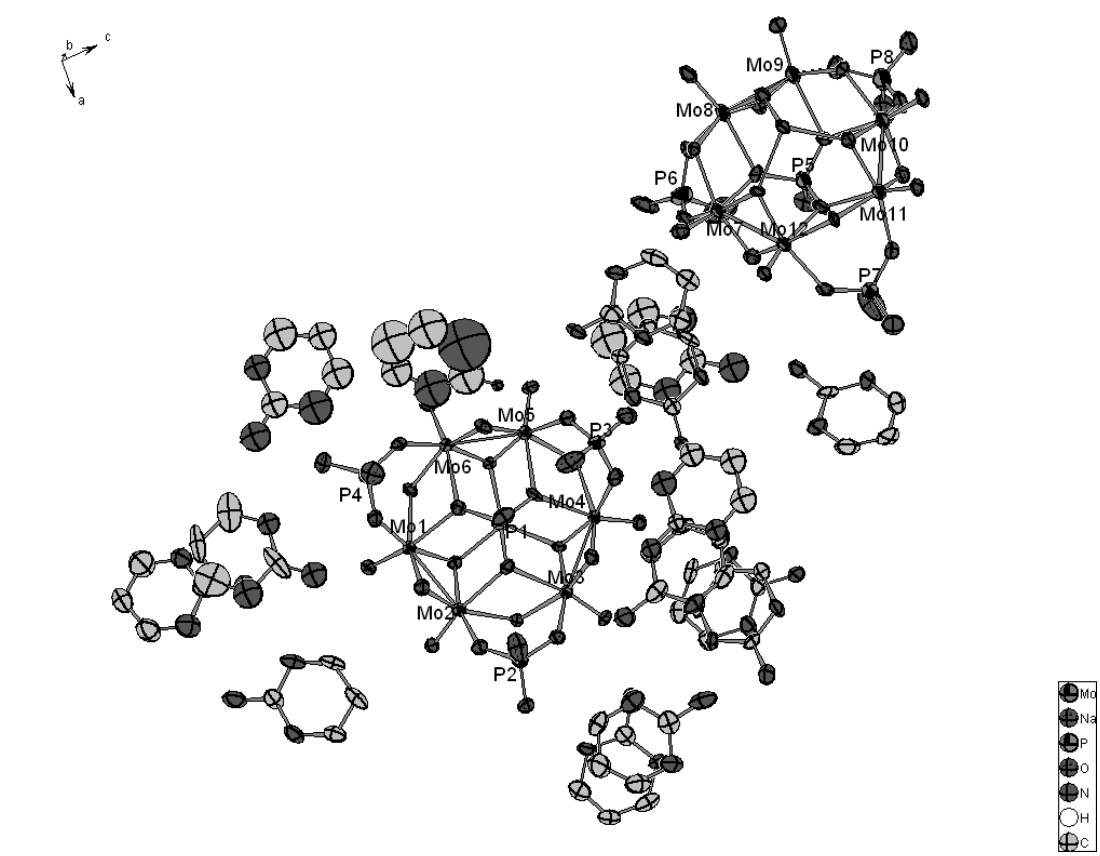

6.14 Crystal data and structure refinement for compound 15

Identification code	GENKUG	
Empirical formula	C12 H105 Mo12 N12 Na3 O80 P8	
Formula weight	3166.09	
Temperature	150(2) K	
Wavelength	0.71073 Å	
Crystal system	Triclinic	
Space group	*P*-1	
Unit cell dimensions	a = 13.4228(2) Å	α = 98.443(1)°.
	b = 13.4215(3) Å	β= 104.914(1)°.
	c = 14.7383(3) Å	γ = 119.049(1)°.
Volume	2123.70(7) $Å^3$	
Z	1	
Density (calculated)	2.476 g/cm^3	
Absorption coefficient	2.009 mm^{-1}	
F(000)	1558	
Crystal size	0.20 x 0.18 x 0.18 mm^3	
Theta range for data collection	1.76 to 27.49°.	
Index ranges	-17<=h<=16, -17<=k<=16, 0<=l<=19	
Reflections collected	26124	
Independent reflections	9255 [R(int) = 0.0350]	
Completeness to theta = 27.49°	94.9 %	
Absorption correction	Empirical	
Max. and min. transmission	0.714 and 0.689	
Refinement method	Full-matrix least-squares on F^2	
Data / restraints / parameters	9255 / 6 / 577	
Goodness-of-fit on F^2	1.074	
Final R indices [I>2sigma(I)]	R1 = 0.0336, wR2 = 0.0819	
R indices (all data)	R1 = 0.0384, wR2 = 0.0841	
Largest diff. peak and hole	1.08 and -0.92 $e.Å^{-3}$	

ORTEP representation of compound 15 at 50 % probability level

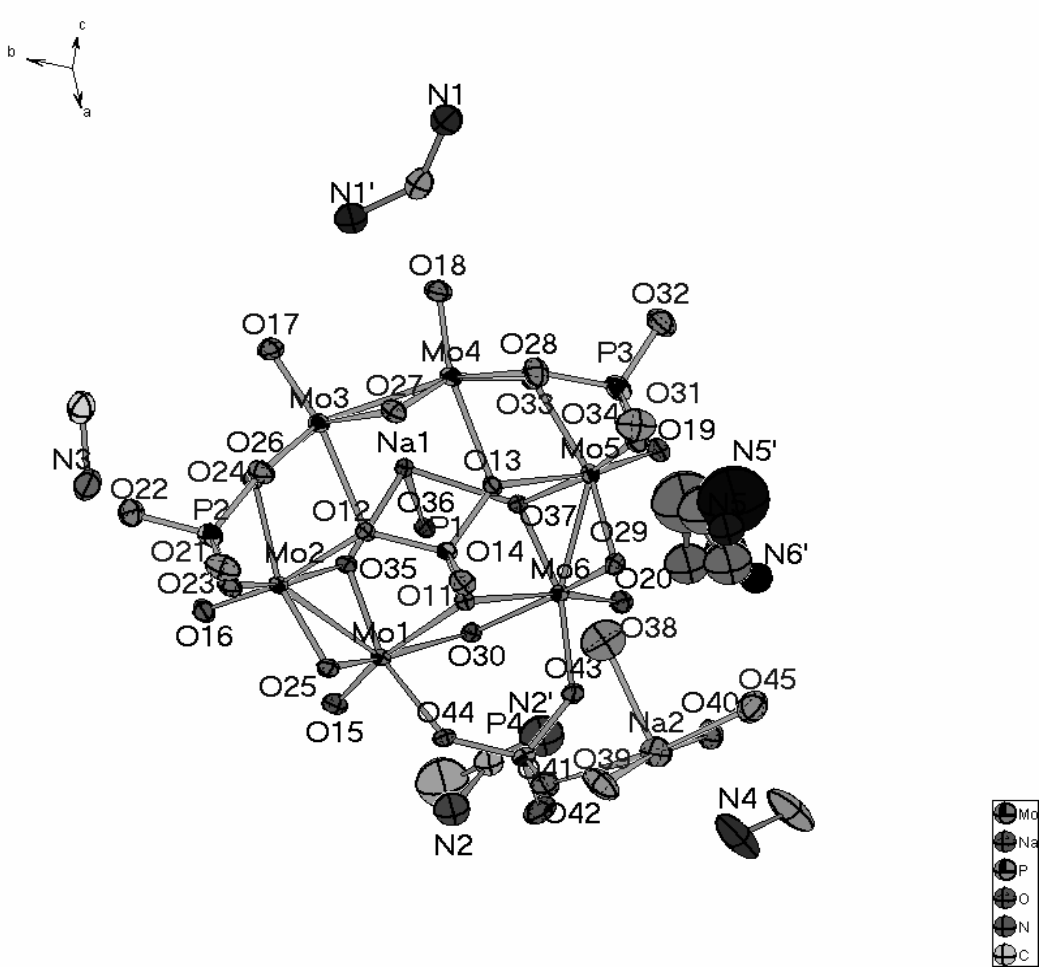

6.15 Crystal data and structure refinement for compound 16

Identification code	CS120A	
Empirical formula	C20 H41 Mo5 N15 O28 P2	
Formula weight	1481.32	
Temperature	150(2) K	
Wavelength	0.71073 Å	
Crystal system	Triclinic	
Space group	*P*-1	
Unit cell dimensions	a = 10.0547(3) Å	α= 91.377(2)°.
	b = 10.5462(3) Å	β= 91.7830(10)°.
	c = 21.3713(7) Å	γ = 104.366(2)°.
Volume	2193.08(12) $Å^3$	
Z	2	
Density (calculated)	2.243 g/cm^3	
Absorption coefficient	1.576 mm^{-1}	
F(000)	1460	
Crystal size	0.22 x 0.18 x 0.06 mm^3	
Theta range for data collection	1.99 to 26.00°.	
Index ranges	-12<=h<=12, -13<=k<=13, 0<=l<=26	
Reflections collected	34808	
Independent reflections	8600 [R(int) = 0.0548]	
Completeness to theta = 26.00°	99.8 %	
Absorption correction	Gaussian	
Max. and min. transmission	0.911 and 0.723	
Refinement method	Full-matrix least-squares on F^2	
Data / restraints / parameters	8600 / 15 / 661	
Goodness-of-fit on F^2	1.041	
Final R indices [I>2sigma(I)]	R1 = 0.0297, wR2 = 0.0725	
R indices (all data)	R1 = 0.0395, wR2 = 0.0760	
Largest diff. peak and hole	0.77 and -0.82 e.$Å^{-3}$	

ORTEP representation of compound 16 at 50 % probability level

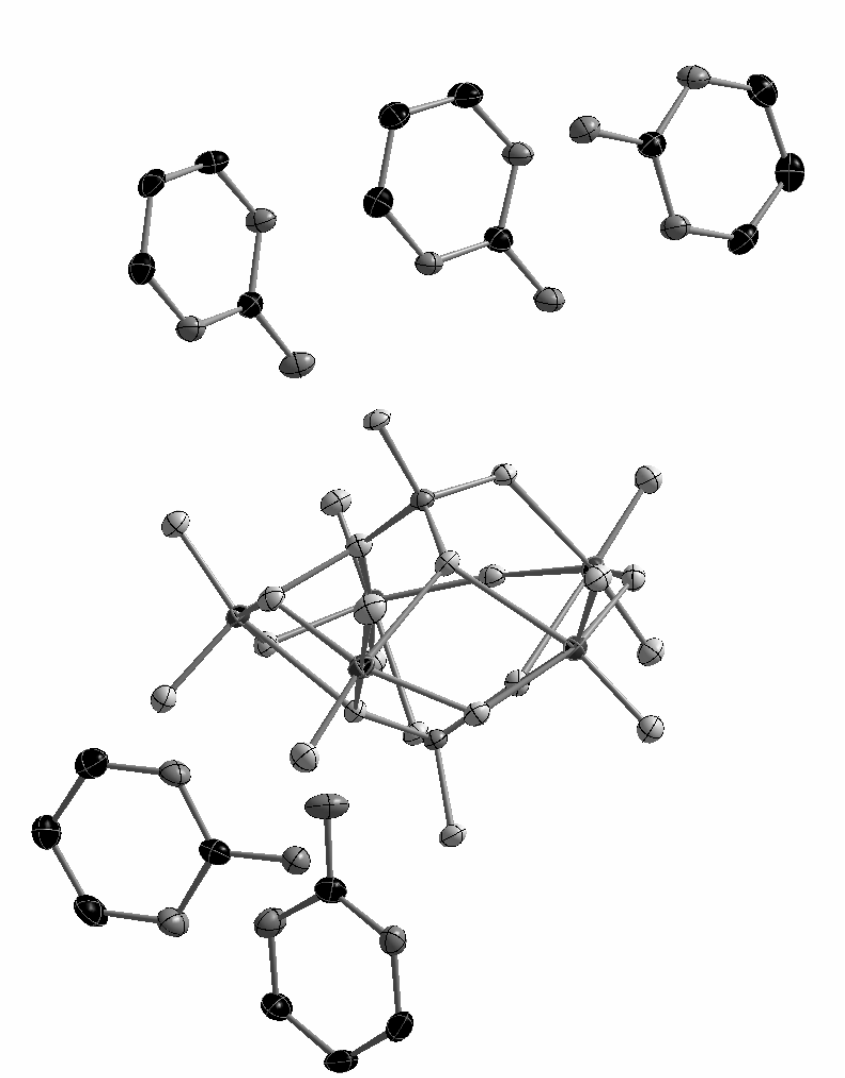

6.16 Crystal data and structure refinement for compound 17

Identification code	HEVVUA	
Empirical formula	C69 H153 Mo12 N8 Na O78 P8	
Formula weight	3765.02	
Temperature	123(2) K	
Wavelength	0.71073 Å	
Crystal system	Orthorhombic	
Space group	$P2_12_12_1$	
Unit cell dimensions	a = 14.5405(3) Å	α= 90°.
	b = 25.0846(3) Å	β= 90°.
	c = 38.3524(8) Å	γ = 90°.
Volume	13988.8(4) $Å^3$	
Z	4	
Density (calculated)	1.788 g/cm^3	
Absorption coefficient	1.229 mm^{-1}	
F(000)	7528	
Crystal size	0.20 x 0.10 x 0.06 mm^3	
Theta range for data collection	1.70 to 25.15°.	
Index ranges	0<=h<=17, 0<=k<=29, -45<=l<=45	
Reflections collected	47099	
Independent reflections	22764 [R(int) = 0.0716]	
Completeness to theta = 25.15°	95.3 %	
Absorption correction	Gaussian	
Max. and min. transmission	0.9299 and 0.7912	
Refinement method	Full-matrix least-squares on F^2	
Data / restraints / parameters	22764 / 14 / 1504	
Goodness-of-fit on F^2	1.028	
Final R indices [I>2sigma(I)]	R1 = 0.0649, wR2 = 0.1465	
R indices (all data)	R1 = 0.0992, wR2 = 0.1652	
Largest diff. peak and hole	1.96 and -0.92 e.$Å^{-3}$	

ORTEP representation of compound 17 at 50 % probability level

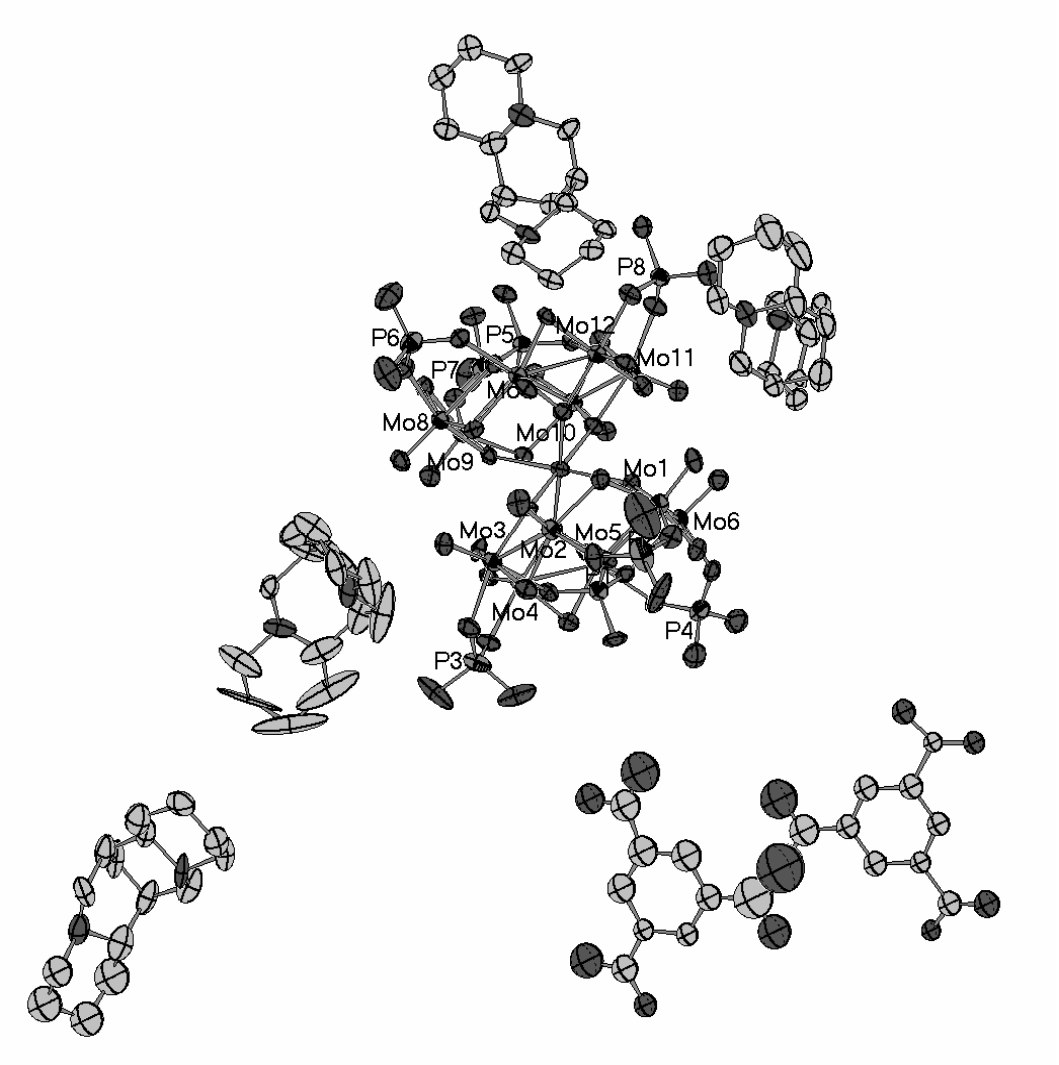

6.17 Crystal data and structure refinement for compound 18

Identification code	cs502-2	
Empirical formula	C20 H63 Ag4 O38 S10 V10	
Formula weight	2173.18	
Temperature	150(2) K	
Wavelength	0.71073 Å	
Crystal system	Monoclinic	
Space group	*P*21	
Unit cell dimensions	a = 10.8165(2) Å	α= 90°.
	b = 22.5042(4) Å	β= 91.113(2)°.
	c = 12.6180(2) Å	γ = 90°.
Volume	3070.85(9) $Å^3$	
Z	2	
Density (calculated)	2.243 g/cm^3	
Absorption coefficient	3.522 mm^{-1}	
F(000)	1944	
Crystal size	0.1 x 0.15 x 0.15 mm^3	
Theta range for data collection	2.66 to 28.56°.	
Index ranges	-14<=h<=14, -30<=k<=29, -14<=l<=15	
Reflections collected	15782	
Independent reflections	11394 [R(int) = 0.0222]	
Completeness to theta = 27.50°	99.2 %	
Absorption correction	None	
Refinement method	Full-matrix least-squares on F^2	
Data / restraints / parameters	11394 / 1 / 739	
Goodness-of-fit on F^2	0.994	
Final R indices [I>2sigma(I)]	R1 = 0.0308, wR2 = 0.0720	
R indices (all data)	R1 = 0.0384, wR2 = 0.0737	
Absolute structure parameter	0.200(18)	
Largest diff. peak and hole	0.777 and -0.553 $e.Å^{-3}$	

ORTEP representation of compound 18 at 50 % probability level

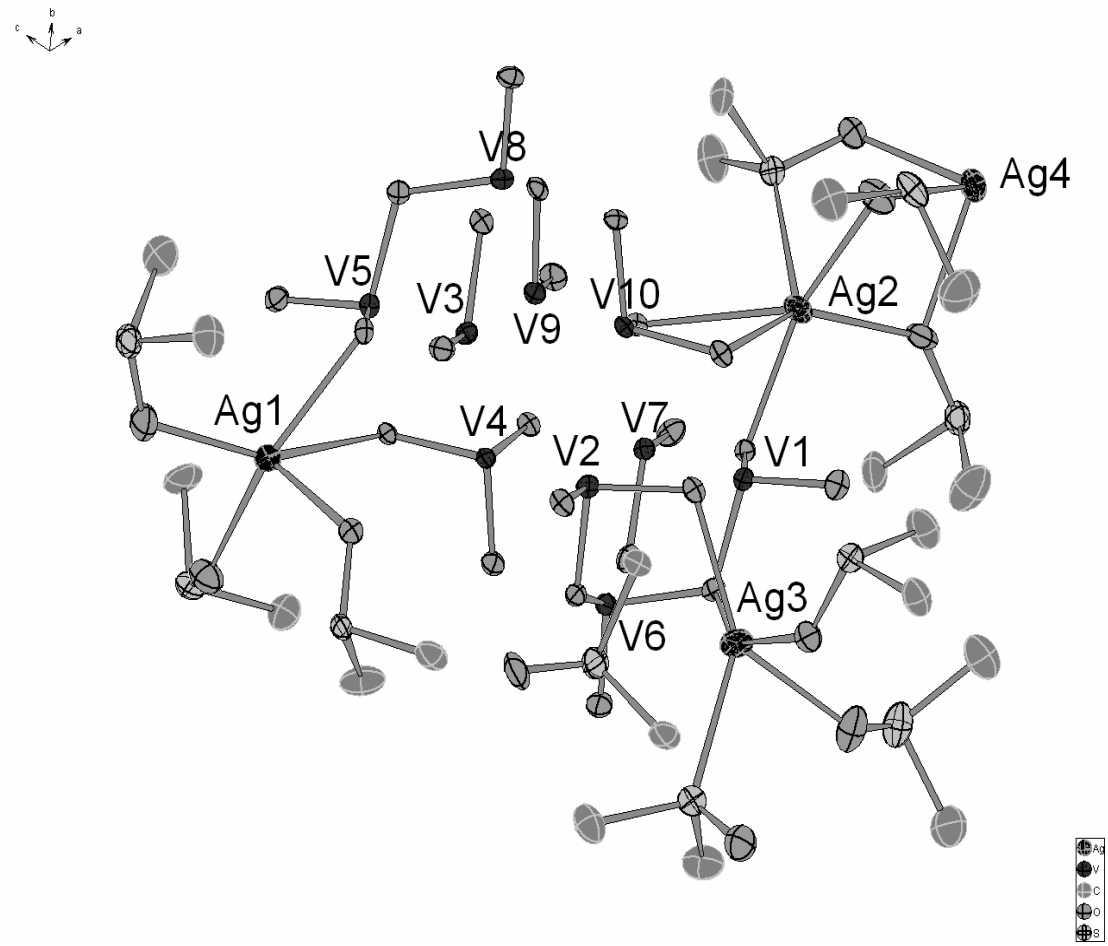

6.18 Crystal data and structure refinement for compound 19

Identification code	cs502-3	
Empirical formula	$C_{10}H_{33}Ag_3O_{19}S_5V_5$	
Formula weight	1196.00	
Temperature	150 (2) K	
Wavelength	0.71073 Å	
Crystal system	monoclinic	
Space group	*C*2/c	
Unit cell dimensions	a = 23.2469(6) Å	α= 90°.
	b = 11.2516(3) Å	β= 95.121(2)°.
	c = 23.2770(6) Å	γ = 90°.
Volume	6064.1(3) $Å^3$	
Z	5	
Density (calculated)	1.854 g/cm^3	
Absorption coefficient	2.345 mm^{-1}	
F(000)	3350	
Crystal size	0.1 x 0.15 x 0.15 mm^3	
Theta range for data collection	2.72 to 26.55°.	
Index ranges	-28<=h<=29, -14<=k<=13, -30<=l<=27	
Reflections collected	17462	
Independent reflections	6912 [R(int) = 0.0416]	
Completeness to theta = 26.55°	99.4 %	
Refinement method	Full-matrix least-squares on F^2	
Data / restraints / parameters	6912 / 0 / 435	
Goodness-of-fit on F^2	0.967	
Final R indices [I>2sigma(I)]	R1 = 0.0428, wR2 = 0.1154	
R indices (all data)	R1 = 0.0702, wR2 = 0.1228	
Largest diff. peak and hole	0.966 and -1.158 e.$Å^{-3}$	

ORTEP representation of compound 19 at 50 % probability level

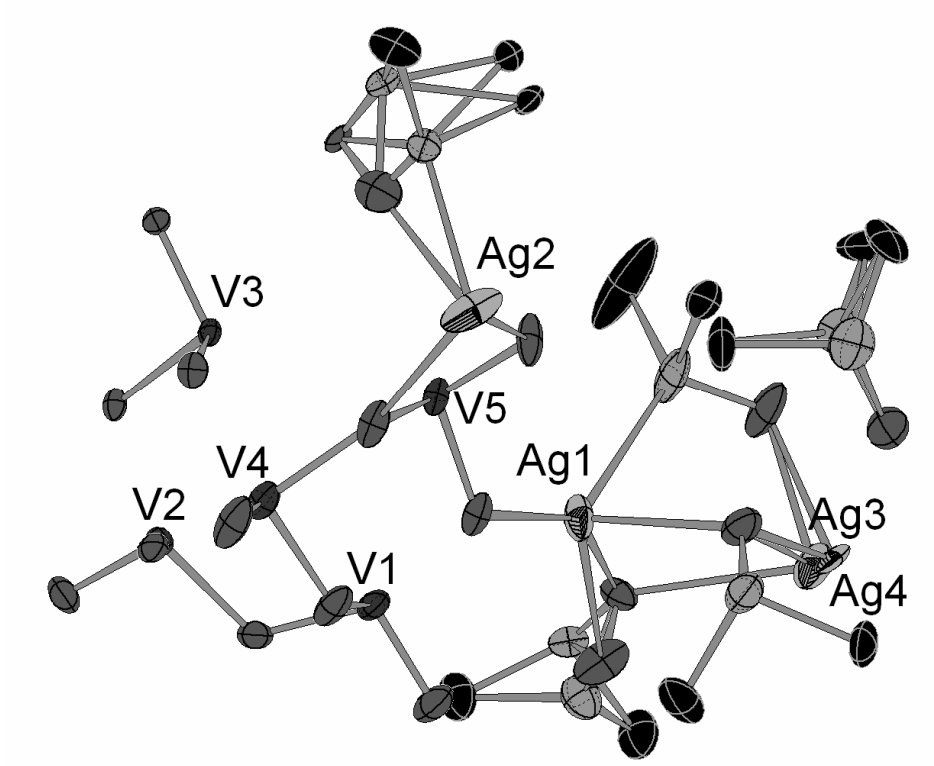

6.19 Crystal data and structure refinement for compound 20

Identification code	cs272	
Empirical formula	C24 H39 Ag5 N12 O40 W12	
Formula weight	3881.22	
Temperature	150(2) K	
Wavelength	0.71073 Å	
Crystal system	Tetragonal	
Space group	*P*4/mnc	
Unit cell dimensions	a = 13.4833(9) Å	α= 90°.
	b = 13.4833(9) Å	β= 90°.
	c = 18.190(2) Å	γ = 90°.
Volume	3307.0(5) $Å^3$	
Z	2	
Density (calculated)	3.898 g/cm^3	
Absorption coefficient	22.306 mm^{-1}	
F(000)	3420	
Crystal size	0.18 x 0.12 x 0.09 mm^3	
Theta range for data collection	2.24 to 24.79°.	
Index ranges	-15<=h<=13, -15<=k<=15, -21<=l<=13	
Reflections collected	12046	
Independent reflections	1474 [R(int) = 0.0316]	
Completeness to theta = 24.79°	99.1 %	
Absorption correction	Empirical	
Max. and min. transmission	1.000 and 0.140	
Refinement method	Full-matrix least-squares on F^2	
Data / restraints / parameters	1474 / 0 / 174	
Goodness-of-fit on F^2	1.221	
Final R indices [I>2sigma(I)]	R1 = 0.0466, wR2 = 0.1173	
R indices (all data)	R1 = 0.0505, wR2 = 0.1201	
Largest diff. peak and hole	1.56 and -1.07 $e.Å^{-3}$	

ORTEP representation of compound 20 at 50 % probability level

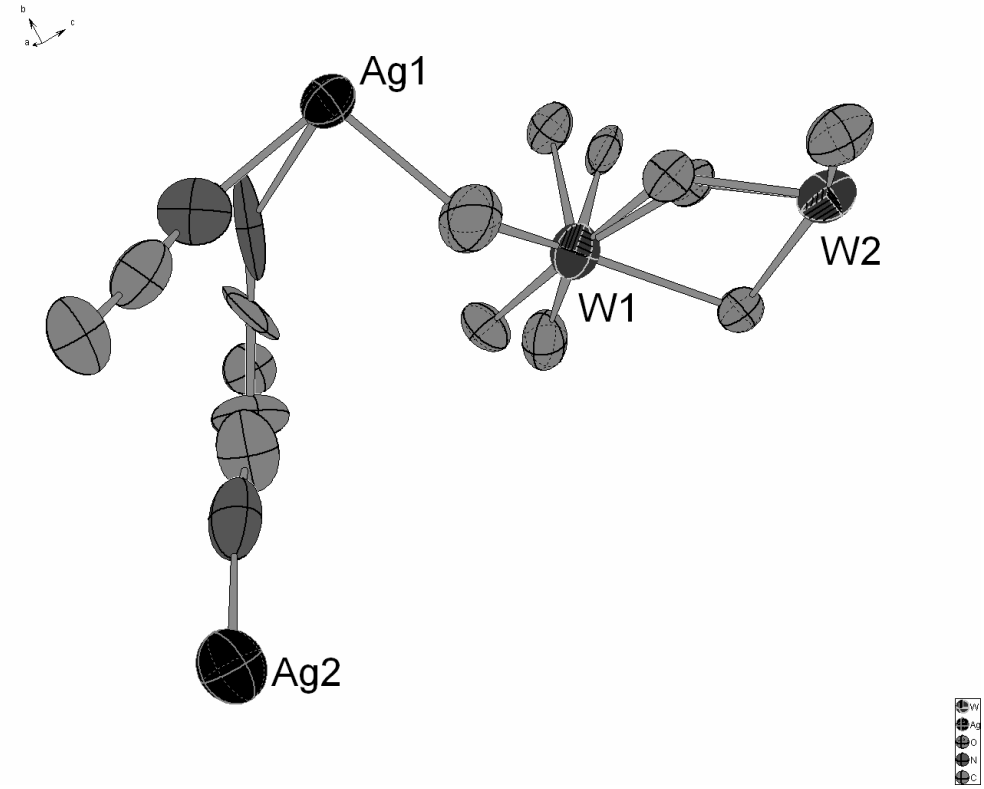

6.20 Crystal data and structure refinement for compound 22

Identification code	cs467-5	
Empirical formula	C48 H116 N4 O40 W12	
Formula weight	3653.43	
Temperature	150(2) K	
Wavelength	0.71073 Å	
Crystal system	Triclinic	
Space group	*P*-1	
Unit cell dimensions	a = 13.5966(3) Å	α= 79.6615(17)°.
	b = 14.3250(3) Å	β= 87.0711(17)°.
	c = 22.2445(5) Å	γ = 87.3499(16)°.
Volume	4253.65(16) $Å^3$	
Z	2	
Density (calculated)	2.775 g/cm^3	
Absorption coefficient	16.232 mm^{-1}	
F(000)	3124	
Crystal size	0.15 x 0.12 x 0.10 mm^3	
Theta range for data collection	2.88 to 24.71°.	
Index ranges	-15<=h<=15, -16<=k<=16, -26<=l<=25	
Reflections collected	39345	
Independent reflections	14390 [R(int) = 0.0307]	
Completeness to theta = 24.71°	99.3 %	
Refinement method	Full-matrix least-squares on F^2	
Data / restraints / parameters	14390 / 0 / 977	
Goodness-of-fit on F^2	1.037	
Final R indices [I>2sigma(I)]	R1 = 0.0276, wR2 = 0.0692	
R indices (all data)	R1 = 0.0379, wR2 = 0.0733	
Largest diff. peak and hole	1.815 and -1.219 $e.Å^{-3}$	

ORTEP representation of compound 22 at 50 % probability level

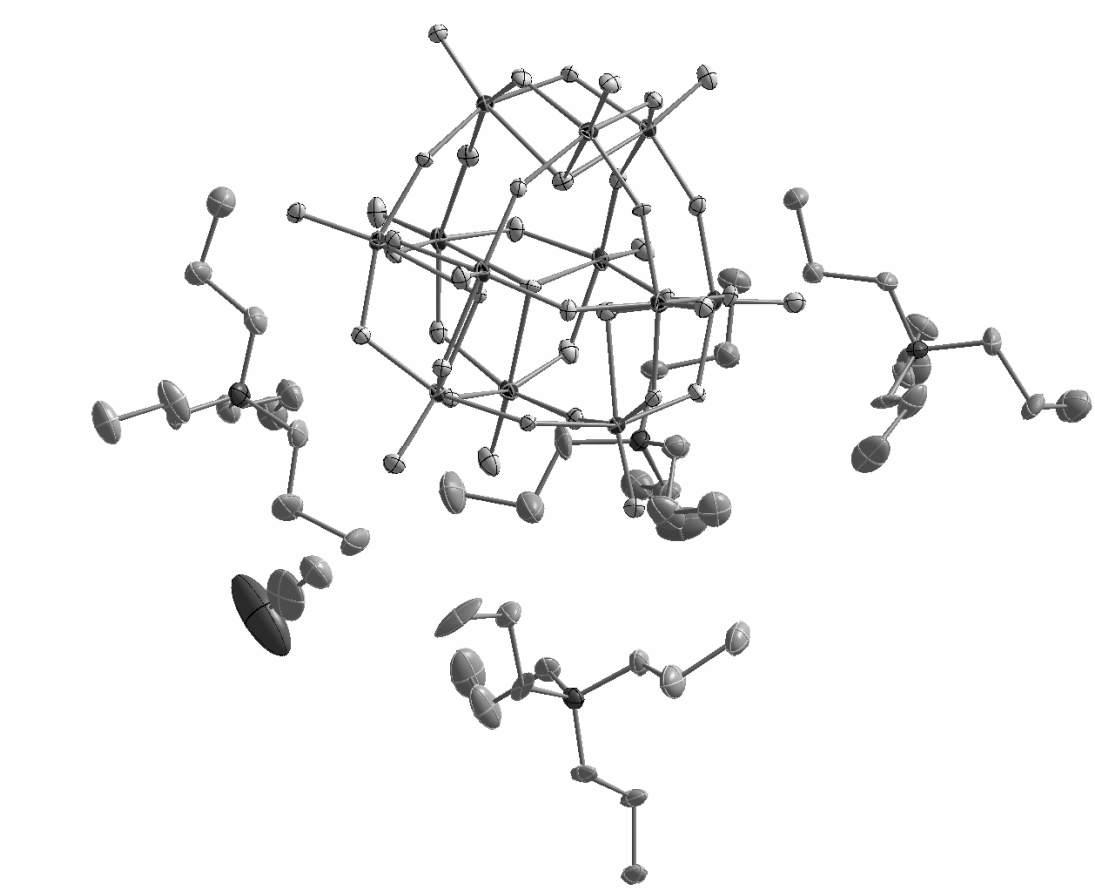

7 Literature references

[1] http://nobelprize.org/nobel_prizes/chemistry/laureates/1987/index.html
[2] J. M. Berg, J. L. Tymoczko, L. Stryer, *Biochemistry: International Edition*, 6 rev. ed., W. H. Freeman & Co, San Fransisco, **2006**.
[3] A. Müller, M. Koop, H. Bögge, M. Schmidtmann, C. Beugholt, *Chem. Commun.* **1998**, 1501.
[4] D. L. Long, C. Streb, P. Kögerler, L. Cronin, *J. Clust. Sci.* **2006**, *17*, 257.
[5] A. Rodriguez-Fortea, C. de Graaf, J. M. Poblet, *Chem. Phys. Lett.* **2006**, *428*, 88.
[6] X. Lopez, C. de Graaf, J. M. Maestre, M. Beard, M. M. Rohmer, C. Bo, J. M. Poblet, *J. Chem. Theory. Comp* **2005**, *1*, 856.
[7] L. K. Yan, G. C. Yang, W. Guan, Z. M. Su, R. S. Wang, *J. Phys. Chem. B* **2005**, *109*, 22332.
[8] S. P. de Visser, D. Kumar, R. Neumann, S. Shaik, *Angew. Chem. Int. Ed. Engl.* **2004**, *43*, 5661.
[9] J. M. Poblet, X. Lopez, C. Bo, *Chem. Soc. Rev.* **2003**, *32*, 297.
[10] D. Volkmer, B. Bredenkotter, J. Tellenbroker, P. Kögerler, D. G. Kurth, P. Lehmann, H. Schnablegger, D. Schwahn, M. Piepenbrink, B. Krebs, *J. Am. Chem. Soc.* **2002**, *124*, 10489.
[11] X. Lopez, C. Bo, J. M. Poblet, *J. Am. Chem. Soc.* **2002**, *124*, 12574.
[12] M. M. Rohmer, M. Benard, J. P. Blaudeau, J. M. Maestre, J. M. Poblet, *Coord. Chem. Rev.* **1998**, *180*, 1019.
[13] Y. Y. Chen, X. W. Han, *Prog. Chem.* **2006**, *18*, 399.
[14] V. Nardello, J. M. Aubry, D. E. De Vos, R. Neumann, W. Adam, R. Zhang, J. E. ten Elshof, P. T. Witte, P. L. Alsters, *J. Mol. Cat. A* **2006**, *251*, 185.
[15] N. Mizuno, K. Yamaguchi, K. Kamata, *Coord. Chem. Rev.* **2005**, *249*, 1944.
[16] P. T. Witte, P. L. Alsters, W. Jary, R. Mullner, P. Pochlauer, D. Sloboda-Rozner, R. Neumann, *Org. Proc. Res. Developm.* **2004**, *8*, 524.
[17] A. R. Gaspar, D. V. Evtuguin, C. P. Neto, *Ind. Eng. Chem. Res.* **2004**, *43*, 7754.
[18] J. H. Holles, C. J. Dillon, J. A. Labinger, M. E. Davis, *J. Catal.* **2003**, *218*, 42.
[19] K. Kamata, K. Yonehara, Y. Sumida, K. Yamaguchi, S. Hikichi, N. Mizuno, *Science* **2003**, *300*, 964.
[20] J. J. Berzelius, *Poggendorffs Ann. Phys. Chem.* **1826**, *6*, 369.
[21] L. Pauling, *J. Am. Chem. Soc.* **1929**, *51*, 2868.
[22] P. Gouzerh, M. Che, *L'actualite chimique* **2006**, 1.
[23] A. Werner, *Ber. Deutschen Chem. Ges.***1907**, *40*, 40.
[24] M. v. Laue, *Physikalische Zeitschrift* **1913**, *14*, 1075.
[25] W. L. Bragg, *Nature* **1912**, *90*, 410.
[26] J. F. Keggin, *Proc. Royal Chem. Soc. London A* **1934**, *144*, 0075.
[27] J. F. Keggin, *Nature* **1933**, *132*, 351.
[28] M. T. Pope, in *Encyclopedia of Inorg. Chem.*, 2 ed. (Ed.: R. B. King), John Wiley & Sons, Chichester, **2005**, pp. 1.
[29] A. Müller, S. Roy, *Coord. Chem. Rev.* **2003**, *245*, 153.
[30] L. C. W. Baker, D. C. Glick, *Chem. Rev.* **1998**, *98*, 3.
[31] R. D. Shannon, *Acta Cryst. Section A* **1976**, *32*, 751.
[32] K. H. Tytko, O. Glemser, in *Adv. Inorg. Chem. Radiochem., Vol. 19* (Eds.: H. J. Emeleus, A. G. Sharpe), Academic Press, New York, **1976**, p. 306.

[33] V. W. Day, M. F. Fredrich, W. G. Klemperer, W. Shum, *J. Am. Chem. Soc.* **1977**, *99*, 6146.
[34] F. A. Cotton, G. Wilkinson, C. A. Murillo, M. Bochmann, *Adv. Inorg. Chem.*, 6 ed., Wiley Interscience, New York, **1999**.
[35] J. J. Hastings, O. W. Howarth, *J. Chem. Soc.-Dalton Trans.* **1992**, 209.
[36] C. R. Sprangers, J. K. Marmon, D. C. Duncan, *Inorg. Chem.* **2006**, *45*, 9628.
[37] R. I. Maksimovskaya, G. M. Maksimov, *Inorg. Chem.* **2001**, *40*, 1284.
[38] Y. Lin, K. Nomiya, R. G. Finke, *Inorg. Chem.* **1993**, *32*, 6040.
[39] Y. Lin, T. J. R. Weakley, B. Rapko, R. G. Finke, *Inorg. Chem.* **1993**, *32*, 5095.
[40] D. K. Lyon, W. K. Miller, T. Novet, P. J. Domaille, E. Evitt, D. C. Johnson, R. G. Finke, *J. Am. Chem. Soc.* **1991**, *113*, 7209.
[41] L. Pettersson, I. Andersson, F. Taube, I. Toth, M. Hashimoto, O. W. Howarth, *J. Chem. Soc. - Dalton Trans.* **2003**, 146.
[42] L. Pettersson, I. Andersson, O. W. Howarth, *Inorg. Chem.* **1992**, *31*, 4032.
[43] O. W. Howarth, P. Kelly, L. Pettersson, *J. Chem. Soc.-Dalton Trans.* **1990**, 81.
[44] O. W. Howarth, P. Kelly, *J. Chem. Soc.-Chem. Commun.* **1988**, 1236.
[45] M. T. Pope, A. Müller, *Angew. Chem. Int. Ed. Engl.* **1991**, *30*, 34.
[46] W. G. Klemperer, *Inorganic Syntheses* **1990**, *27*, 71.
[47] M. I. Khan, Q. Chen, H. Hope, S. Parkin, C. J. Oconnor, J. Zubieta, *Inorg. Chem.* **1993**, *32*, 2929.
[48] Q. Chen, J. Zubieta, *Inorg. Chim. Acta* **1992**, *200*, 95.
[49] M. I. Khan, Q. Chen, J. Zubieta, D. P. Goshorn, *Inorg. Chem.* **1992**, *31*, 1556.
[50] G. Suss-Fink, L. Plasseraud, V. Ferrand, S. Stanislas, A. Neels, H. Stoeckli-Evans, M. Henry, G. Laurenczy, R. Roulet, *Polyhedron* **1998**, *17*, 2817.
[51] Y. Hayashi, Y. Ozawa, K. Isobe, *Inorg. Chem.* **1991**, *30*, 1025.
[52] H. K. Chae, W. G. Klemperer, V. W. Day, *Inorg. Chem.* **1989**, *28*, 1423.
[53] R. N. Devi, J. Zubieta, *Inorg. Chim. Acta* **2002**, *332*, 72.
[54] I. Correia, F. Avecilla, S. Marcao, J. C. Pessoa, *Inorg. Chim. Acta* **2004**, *357*, 4476.
[55] M. delArco, M. V. G. Galiano, V. Rives, R. Trujillano, P. Malet, *Inorg. Chem.* **1996**, *35*, 6362.
[56] D. C. Crans, M. Mahrooftahir, O. P. Anderson, M. M. Miller, *Inorg. Chem.* **1994**, *33*, 5586.
[57] S. Nakamura, T. Ozeki, *J. Chem. Soc.-Dalton Trans.* **2001**, 472.
[58] J. M. Arrieta, *Polyhedron* **1992**, *11*, 3045.
[59] J. Y. Kempf, M. M. Rohmer, J. M. Poblet, C. Bo, M. Benard, *J. Am. Chem. Soc.* **1992**, *114*, 1136.
[60] V. W. Day, W. G. Klemperer, D. J. Maltbie, *J. Am. Chem. Soc.* **1987**, *109*, 2991.
[61] H. T. Evans, *Inorg. Chem.* **1966**, *5*, 967.
[62] F. J. C. Rossotti, H. Rossotti, *Journal J. Inorg. Nucl. Chem.* **1956**, *2*, 201.
[63] F. J. C. Rossotti, H. Rossotti, *Acta Chemica Scandinavica* **1956**, *10*, 957.
[64] H. Dong, K. S. Hagen, C. L. Hill, *J. Chem. Soc.-Chem. Commun.* **1993**, 426.
[65] T. Drezen, O. Joubert, M. Ganne, L. Brohan, *J. Solid State Chem.* **1998**, *136*, 298.
[66] H. N. Miras, R. G. Raptis, N. Lalioti, M. P. Sigalas, P. Baran, T. A. Kabanos, *Chem. Eur. J.* **2005**, *11*, 2295.
[67] C. D. Wu, C. Z. Lu, X. Lin, H. H. Zhuang, J. S. Huang, *Inorg. Chem. Commun.* **2002**, *5*, 664.
[68] G. B. Karet, Z. M. Sun, W. E. Streib, J. C. Bollinger, D. N. Henderickson, G. Christou, *Chem. Commun.* **1999**, 2249.
[69] T. Drezen, M. Ganne, *J. Solid State Chem.* **1999**, *147*, 552.

[70] A. Müller, E. Krickemeyer, M. Penk, R. Rohlfing, A. Armatage, H. Bögge, *Angew. Chem. Int. Ed. Engl.* **1991**, *30*, 1674.
[71] A. Müller, R. Sessoli, E. Krickemeyer, H. Bögge, J. Meyer, D. Gatteschi, L. Pardi, J. Westphal, K. Hovemeier, R. Rohlfing, J. Doring, F. Hellweg, C. Beugholt, M. Schmidtmann, *Inorg. Chem.* **1997**, *36*, 5239.
[72] W. G. Klemperer, T. A. Marquart, O. M. Yaghi, *Angew. Chem. Int. Ed. Engl.* **1992**, *31*, 49.
[73] W. G. Klemperer, T. A. Marquart, O. M. Yaghi, *Mat. Chem. Phys.* **1991**, *29*, 97.
[74] V. W. Day, W. G. Klemperer, O. M. Yaghi, *J. Am. Chem. Soc.* **1989**, *111*, 5959.
[75] B. Dietrich, in *Comprehensive Supramolecular Chemistry, Vol. 1* (Ed.: G. W. Gockel), Elsevier, Oxford, **1996**, pp. 153.
[76] A. Müller, C. Serain, *Acc. Chem. Res.* **2000**, *33*, 2.
[77] M. T. Pope, *Heteropoly and Isopoly Oxometalates*, Springer-Verlag, Berlin, **1983**.
[78] H. Vivier, J. Bernard, H. Djomaa, *Rev. Chim. Minerale* **1977**, *14*, 584.
[79] L. O. Atovmyan, O. N. Kraschoka, *Zh. Strukt. Khim* **1972**, *13*, 342.
[80] I. Lindqvist, *Arkiv. Kemi* **1950**, *2*, 349.
[81] K. Pavani, S. E. Lofland, K. V. Ramanujachary, A. Ramanan, *Eur. J. Inorg. Chem.* **2007**, 568.
[82] J. H. Luo, M. C. Hong, R. H. Wang, Q. Shi, R. Cao, J. B. Weng, R. Q. Sun, H. H. Zhang, *Inorg. Chem. Commun.* **2003**, *6*, 702.
[83] H. Jin, Y. F. Qi, E. B. Wang, Y. G. Li, X. L. Wang, C. Qin, S. Chang, *Crystal Growth & Design* **2006**, *6*, 2693.
[84] A. Kitamura, T. Ozeki, A. Yagasaki, *Inorg. Chem.* **1997**, *36*, 4275.
[85] Y. F. Song, H. Abbas, C. Ritchie, N. McMillian, D. L. Long, N. Gadegaard, L. Cronin, *J.l Mat. Chem.* **2007**, *17*, 1903.
[86] H. Abbas, A. L. Pickering, D. L. Long, P. Kögerler, L. Cronin, *Chem. Eur. J.* **2005**, *11*, 1071.
[87] D. G. Allis, R. S. Rarig, E. Burkholder, J. Zubieta, *J. Mol. Struc* **2004**, *688*, 11.
[88] K. H. Tytko, Schönfeld.B, B. Buss, O. Glemser, *Angew. Chem. Int. Ed. Engl.* **1973**, *12*, 330.
[89] I. Paulat-Böschen, B. Krebs, *Acta Cryst. Section B* **1982**, *38*, 1710.
[90] I. Paulat-Böschen, *J. Chem. Soc.-Chem. Commun.* **1979**, 780.
[91] B. Z. Lin, Y. M. Chen, P. D. Liu, *Dalton Trans.* **2003**, 2474.
[92] L. Lisnard, A. Dolbecq, P. Mialane, J. Marrot, F. Secheresse, *Inorg. Chim. Acta* **2004**, *357*, 845.
[93] J. Y. Niu, Z. L. Wang, J. P. Wang, *J. Coord. Chem.* **2004**, *57*, 411.
[94] J. P. Launay, *J. Inorg. Nucl. Chem.* **1976**, *38*, 807.
[95] T. Lehmann, J. Fuchs, *Z. Naturforsch. B* **1988**, *43*, 89.
[96] D. L. Long, H. Abbas, P. Kögerler, L. Cronin, *J. Am. Chem. Soc.* **2004**, *126*, 13880.
[97] F.-Q. Zhang, H.-S. Wu, D.-B. Cao, X.-M. Zhang, Y.-W. Li, H. Jiao, *J. Mol. Struc: THEOCHEM* **2005**, *755*, 119.
[98] A. Teze, G. Herve, *J. Inorg. Nucl. Chem.* **1977**, *39*, 999.
[99] K. Y. Matsumoto, A. Kobayashi, Y. Sasaki, *Bull. Chem. Soc. Japan* **1975**, *48*, 3146.
[100] A. Teze, E. Cadot, V. Bereau, G. Herve, *Inorg. Chem.* **2001**, *40*, 2000.
[101] J. Rowsell, L. F. Nazar, *J. Am. Chem. Soc.* **2000**, *122*, 3777.
[102] P. Mialane, A. Dolbecq, L. Lisnard, A. Mallard, J. Marrot, F. Secheresse, *Angew. Chem. Int. Ed. Engl.* **2002**, *41*, 2398.
[103] Z. G. Han, Y. L. Zhao, J. Peng, A. X. Tian, Y. H. Feng, Q. Liu, *J. Solid State Chem.* **2005**, *178*, 1386.

[104] L. A. Allaoui, A. Aouissi, *J. Mol. Cat. A* **2006**, *259*, 281.
[105] A. Teze, G. Herve, in *Inorganic Syntheses, Vol. 27* (Ed.: A. P. Ginsburg), John Wiley & Sons, New York, **1990**, p. 89.
[106] Y. G. Chen, J. Gong, L. Y. Qu, *Coord. Chem. Rev.* **2004**, *248*, 245.
[107] J. M. Clemente-Juan, E. Coronado, J. R. Galan-Mascaros, C. J. Gomez-Garcia, *Inorg. Chem.* **1999**, *38*, 55.
[108] M. Nyman, A. J. Celestian, J. B. Parise, G. P. Holland, T. M. Alam, *Inorg. Chem.* **2006**, *45*, 1043.
[109] L. Lisnard, P. Mialane, A. Dolbecq, J. Marrot, J. M. Clemente-Juan, E. Coronado, B. Keita, P. de Oliveira, L. Nadjo, F. Secheresse, *Chem. Eur. J.* **2007**, *13*, 3525.
[110] S. T. Zheng, D. Q. Yuan, H. P. Jia, J. Zhang, G. Y. Yang, *Chem. Commun.* **2007**, 1858.
[111] K. Hayashi, H. Murakami, K. Nomiya, *Inorg. Chem.* **2006**, *45*, 8078.
[112] L. H. Bi, U. Kortz, B. Keita, L. Nadjo, *Dalton Trans.* **2004**, 3184.
[113] B. Dawson, *Acta Cryst.* **1953**, *6*, 81.
[114] G. Herve, A. Teze, R. Contant, in *Polyoxometalate Molecular Science* (Eds.: J. Borras-Almenar, E. Coronado, A. Müller, M. T. Pope), Kluwer Academic Publishers, Dordrecht, **2003**, p. 33.
[115] M. N. Timofeeva, M. M. Matrosova, T. Reshetenko, L. B. Avdeeva, A. A. Budneva, A. B. Ayupov, E. A. Paukshtis, A. L. Chuvilin, A. V. Volodin, V. A. Likholobov, *J. Mol. Cat. A* **2004**, *211*, 131.
[116] Y. Shen, J. Y. Liu, J. G. Jiang, B. F. Liu, S. J. Dong, *J. Phys. Chem. B* **2003**, *107*, 9744.
[117] B. B. Xu, L. Xu, G. G. Gao, Y. N. Jin, *Appl. Surf. Sci.* **2007**, *253*, 3190.
[118] Y. N. Jin, L. Xu, L. D. Zhu, W. J. An, G. G. Gao, *Thin Solid Films* **2007**, *515*, 5490.
[119] M. Inoue, T. Suzuki, Y. Fujita, M. Oda, N. Matsumoto, T. Yamase, *J. Inorg. Biochem.* **2006**, *100*, 1225.
[120] M. Inoue, T. Suzuki, Y. Fujita, M. Oda, N. Matsumoto, J. Iijima, T. Yamase, *Biomedicine & Pharmacotherapy* **2006**, *60*, 220.
[121] D. L. Long, P. Kögerler, L. Cronin, *Angew. Chem. Int. Ed. Engl.* **2004**, *43*, 1817.
[122] A. J. Gaunt, I. May, D. Collison, K. T. Holman, M. T. Pope, *J. Mol. Struc* **2003**, *656*, 101.
[123] http://www.ub.uni-bielefeld.de/cgi-bin/neubutton.cgi?pfad=/diglib/aufkl/nadb/255951&seite=00000407.TIF.
[124] C. W. Scheele, *Sämtliche physische und chemische Werke*, (reprint, original: 1793) ed., Martin Sändig, Wiesbaden, **1971**.
[125] A. Müller, E. Krickemeyer, S. Dillinger, H. Bögge, W. Plass, A. Proust, L. Dloczik, C. Menke, J. Meyer, R. Rohlfing, *Z. Anorg. Allg. Chem.* **1994**, *620*, 599.
[126] A. Müller, E. Krickemeyer, S. Dillinger, H. Bögge, A. Proust, W. Plass, R. Rohlfing, *Naturwissenschaften* **1993**, *80*, 560.
[127] A. Müller, W. Plass, E. Krickemeyer, S. Dillinger, H. Bögge, A. Armatage, C. Beugholt, U. Bergmann, *Monatshefte Fur Chemie* **1994**, *125*, 525.
[128] A. Müller, W. Plass, E. Krickemeyer, S. Dillinger, H. Bögge, A. Armatage, A. Proust, C. Beugholt, U. Bergmann, *Angew. Chem. Int. Ed. Engl.* **1994**, *33*, 849.
[129] A. Müller, W. Plass, E. Krickemeyer, R. Sessoli, D. Gatteschi, J. Meyer, H. Bögge, M. Krockel, A. X. Trautwein, *Inorg. Chim. Acta* **1998**, *271*, 9.
[130] A. Müller, J. Meyer, E. Krickemeyer, C. Beugholt, H. Bögge, F. Peters, M. Schmidtmann, P. Kögerler, M. J. Koop, *Chem. Eur. J.* **1998**, *4*, 1000.
[131] T. B. Liu, E. Diemann, H. L. Li, A. W. M. Dress, A. Müller, *Nature* **2003**, *426*, 59.

[132] A. Müller, H. Bögge, F. L. Sousa, M. Schmidtmann, D. G. Kurth, D. Volkmer, J. van Slageren, M. Dressel, M. L. Kistler, T. B. Liu, *Small* **2007**, *3*, 986.
[133] T. B. Liu, *J. Am. Chem. Soc.* **2003**, *125*, 312.
[134] T. B. Liu, *J. Am. Chem. Soc.* **2002**, *124*, 10942.
[135] A. Müller, E. Krickemeyer, H. Bögge, M. Schmidtmann, C. Beugholt, P. Kögerler, C. Z. Lu, *Angew. Chem. Int. Ed. Engl.* **1998**, *37*, 1220.
[136] A. Tsuda, E. Hirahara, Y. S. Kim, H. Tanaka, T. Kawai, T. Aida, *Angew. Chem. Int. Ed. Engl.* **2004**, *43*, 6327.
[137] A. Müller, S. Q. N. Shah, H. Bögge, M. Schmidtmann, *Nature* **1999**, *397*, 48.
[138] A. Müller, P. Kögerler, A. W. M. Dress, *Coord. Chem. Rev.* **2001**, *222*, 193.
[139] A. Müller, P. Kögerler, *Coord. Chem. Rev.* **1999**, *182*, 3.
[140] A. F. Holleman, E. Wiberg, N. Wiberg, *Lehrbuch der Anorganischen Chemie*, 101 ed., Walter de Gruyter, Berlin, **1995**.
[141] A. Müller, S. K. Das, S. Talismanov, S. Roy, E. Beckmann, H. Bögge, M. Schmidtmann, A. Merca, A. Berkle, L. Allouche, Y. S. Zhou, L. J. Zhang, *Angew. Chem. Int. Ed. Engl.* **2003**, *42*, 5039.
[142] A. Müller, E. Krickemeyer, H. Bögge, M. Schmidtmann, B. Botar, M. O. Talismanova, *Angew. Chem. Int. Ed. Engl.* **2003**, *42*, 2085.
[143] A. Müller, D. Rehder, E. T. K. Haupt, A. Merca, H. Bögge, M. Schmidtmann, G. Heinze-Bruckner, *Angew. Chem. Int. Ed. Engl.* **2004**, *43*, 4466.
[144] A. Müller, Y. S. Zhou, L. J. Zhang, H. Bögge, M. Schmidtmann, M. Dressel, J. van Slageren, *Chem. Commun.* **2004**, 2038.
[145] A. Müller, S. Sarkar, S. Q. N. Shah, H. Bögge, M. Schmidtmann, S. Sarkar, P. Kögerler, B. Hauptfleisch, A. X. Trautwein, V. Schunemann, *Angew. Chem. Int. Ed. Engl.* **1999**, *38*, 3238.
[146] A. Müller, F. Peters, M. T. Pope, D. Gatteschi, *Chem. Rev.* **1998**, *98*, 239.
[147] A. Müller, S. K. Das, P. Kögerler, H. Bögge, M. Schmidtmann, A. X. Trautwein, V. Schunemann, E. Krickemeyer, W. Preetz, *Angew. Chem. Int. Ed. Engl.* **2000**, *39*, 3414.
[148] A. Müller, E. Krickemeyer, S. K. Das, P. Kögerler, S. Sarkar, H. Bögge, M. Schmidtmann, S. Sarkar, *Angew. Chem. Int. Ed. Engl.* **2000**, *39*, 1612.
[149] T. M. Reineke, M. Eddaoudi, D. Moler, M. O'Keeffe, O. M. Yaghi, *J. Am. Chem. Soc.* **2000**, *122*, 4843.
[150] M. Eddaoudi, J. Kim, J. B. Wachter, H. K. Chae, M. O'Keeffe, O. M. Yaghi, *J. Am. Chem. Soc.* **2001**, *123*, 4368.
[151] M. Eddaoudi, J. Kim, M. O'Keeffe, O. M. Yaghi, *J. Am. Chem. Soc.* **2002**, *124*, 376.
[152] H. K. Chae, M. Eddaoudi, J. Kim, S. I. Hauck, J. F. Hartwig, M. O'Keeffe, O. M. Yaghi, *J. Am. Chem. Soc.* **2001**, *123*, 11482.
[153] K. S. Park, Z. Ni, A. P. Cote, J. Y. Choi, R. D. Huang, F. J. Uribe-Romo, H. K. Chae, M. O'Keeffe, O. M. Yaghi, *Proc. Nat. Acad. Sci.* **2006**, *103*, 10186.
[154] M. Eddaoudi, J. Kim, D. Vodak, A. Sudik, J. Wachter, M. O'Keeffe, O. M. Yaghi, *Proc. Nat. Acad. Sci.* **2002**, *99*, 4900.
[155] N. L. Rosi, J. Eckert, M. Eddaoudi, D. T. Vodak, J. Kim, M. O'Keeffe, O. M. Yaghi, *Science* **2003**, *300*, 1127.
[156] H. M. El-Kaderi, J. R. Hunt, J. L. Mendoza-Cortes, A. P. Cote, R. E. Taylor, M. O'Keeffe, O. M. Yaghi, *Science* **2007**, *316*, 268.
[157] A. P. Cote, A. I. Benin, N. W. Ockwig, M. O'Keeffe, A. J. Matzger, O. M. Yaghi, *Science* **2005**, *310*, 1166.

[158] B. L. Chen, M. Eddaoudi, S. T. Hyde, M. O'Keeffe, O. M. Yaghi, *Science* **2001**, *291*, 1021.
[159] F. Schüth, K. S. W. Sing, J. Weitkamp, (eds.), *Handbook of Porous Solids, Vol. 1-5*, Wiley VCH, Weinheim, **2002**.
[160] Y. Ishii, Y. Takenaka, K. Konishi, *Angew. Chem. Int. Ed. Engl.* **2004**, *43*, 2702.
[161] X. L. Wang, C. Qin, E. B. Wang, Z. M. Su, Y. G. Li, L. Xu, *Angew. Chem. Int. Ed. Engl.* **2006**, *45*, 7411.
[162] R. Kawamoto, S. Uchida, N. Mizuno, *J. Am. Chem. Soc.* **2005**, *127*, 10560.
[163] N. Mizuno, S. Uchida, *Chemistry Letters* **2006**, *35*, 688.
[164] S. Uchida, R. Kawamoto, N. Mizuno, *Inorg. Chem.* **2006**, *45*, 5136.
[165] S. Uchida, N. Mizuno, *J. Am. Chem. Soc.* **2004**, *126*, 1602.
[166] S. Uchida, R. Kawamoto, T. Akatsuka, S. Hikichi, N. Mizuno, *Chem. Mater.* **2005**, *17*, 1367.
[167] R. Atencio, A. Briceno, X. Galindo, *Chem. Commun.* **2005**, 637.
[168] G. Cao, R. C. Haushalter, K. G. Strohmaier, *Inorg. Chem.* **1993**, *32*, 127.
[169] R. C. Haushalter, L. A. Mundi, *Chem. Mater.* **1992**, *4*, 31.
[170] X. He, P. Zhang, T. Y. Song, Z. C. Mu, J. H. Yu, Y. Wang, J. N. Xu, *Polyhedron* **2004**, *23*, 2153.
[171] L. A. Meyer, R. C. Haushalter, *Inorg. Chem.* **1993**, *32*, 1579.
[172] P. Pyykkö, *Chem. Rev.* **1997**, *97*, 597.
[173] H. Kuppers, F. Lieba, A. L. Spek, *J. Appl. Crystallogr.* **2006**, *39*, 338.
[174] A. L. Spek, *J. Appl. Crystallogr.* **2003**, *36*, 7.
[175] O. Treutler, R. Ahlrichs, *J. Chem. Phys.* **1995**, *102*, 346.